THE SONOCHEMISTRY OF AQUEOUS SOLUTIONS

Thesis by

Inez Hua

In Partial Fulfillment of the Requirements

for the Degree of

Doctor of Philosophy

California Institute of Technology

Pasadena, CA

1996

(Submitted December 5, 1995)

c 1996

Inez Hua

All rights Reserved

Acknowledgments

The production of a thesis involves various tasks: designing experiments, collecting and analyzing experimental data, discussing and reporting the results, and of course, writing, writing and more writing. Many wonderful people and fortunate circumstances during my five years at Caltech made the learning process bearable and sometimes fun.

First, I wish to thank my advisor, Michael R. Hoffmann, for accepting me into his research group and allowing me to choose a project which interested me. I have been able to steer the project in directions which I found most enlightening, and that is a freedom not to be taken for granted. I also wish to thank my Ph.D examining committee, Professors Michael Hoffmann, Jim Morgan, Janet Hering, Chris Brennen and Harry Gray.

I am also grateful to my colleagues in Environmental Engineering Science, and especially to the other members of my research group. Through the years, numerous people have provided scientific guidance (when I was interpreting my results), as well as encouragement (when data points were scarce). Anastassia Kotronarou started me off on the sonochemistry project during her last summer at Caltech. Mark Schlautman, Beth Carraway, and Amy Hoffmann provided 'seniority' role-models for me to follow during my first and second years as a graduate student. Sayuri Desai performed many of the preliminary experiments described in Chapter 3 of this thesis. Linda Weavers has spent many hours talking with me across our shared lab bench, about topics ranging from ozone flow rates to pasta recipes. Dean Willberg has always been willing to lend a helping hand or extend a patient silence as I proposed various experimental schemes (some successful, others not so). The rest of the group, including Simo Pehkonen, Ron Siefert, Anne Johannsen, Nicola Peill, Janet Kesselmann, Won-Yong Choi, Pat Lang, and Scot Martin have always been friendly and generous whenever I have asked for computer time, help with instrumentation, the whereabouts of miscellaneous equipment, etc.

And to my great friend and colleague, Ralf Höchemer, I extend a special thanks. Ralf has been my co-worker in lab on two significant projects. We have spent many late

nights bolting and unbolting reactor systems; fixing analytical equipment; struggling with computer graphics; and troubleshooting almost everything in lab before it works. I know that had I done those projects by myself, they would probably have been longer and more tedious. I have found his insight into chemical systems to be helpful on many occasions. We have also visited almost every lunch buffet in Pasadena (both elegant and low-brow) and have had many good conversations and laughs during those meals.

There are many people working in Keck who have been helpful over the years. Peter Green was always willing to offer advice about analytical techniques; Rich Eastvedt and Joe Fontana provided invaluable assistance with building equipment. Shirley Anderson, Linda Scott, Fran Matzen, Susan Leising, and Rayma Harrison made my life easier in assorted different ways as I went about the business of being a graduate student here.

Finally, I wish to thank my family. My brother and sister, Lawrence and Vanessa, have cheered me on from afar during my graduate career, and my parents, Lo-Ching and Sui-Sheng, have always provided encouragement by refusing to believe that I could ever go wrong.

Abstract

The ultrasonic irradiation of organic compounds in aqueous solution is studied under various physical conditions. The observed sonochemical rate constants can be analyzed to yield information about the nature of the bubbles which exist during acoustic cavitation and to determine which parameters are significant for enhancing cavitation chemistry. Aqueous solutions of *p*-nitrophenylacetate (PNPA), *p*-nitrophenol (PNP), and carbon tetrachloride (CCl_4) were sonicated in various reactor configurations and with different saturating gases. The production of hydroxyl radical ($^{\bullet}OH$) and hydrogen peroxide (H_2O_2) was quantified at four different ultrasonic frequencies.

The most signficant features of the sonolytic hydrolysis of PNPA at 20 kHz are that the observed first order rate constants are independent of pH in the range of 3 to 8, but significantly influenced by the saturating gas (Kr, Ar, or He). Furthermore, the apparent activation parameters for hydrolysis of PNPA ($\Delta G^{\neq}$, $\Delta S^{\neq}$, $\Delta H^{\neq}$) are significantly different in sonicated systems than in solutions under ambient conditions. These changes are attributed to changes in the physical nature of the solvent when a layer of transient supercritical water is formed around the cavitation bubbles.

The psuedo-first order degradation rate constants for the transformation of PNP in a near-field acoustical processor (NAP) increases with increasing power-to-volume ratio over the range of 0.98-7.27 W/cm^3. An increase in the power-to-area ratio results in an increasingly fast degradation rate up to 1.2 W/cm^2 and a slight decrease thereafter. The nature of the background gas influences the degradation rate constant and product distribution. The fastest rate is observed when a mixture of Ar and O_2 is used to saturate the solution.

The sonolytic degradation of CCl_4 is investigated in Ar- and O_3-saturated aqueous solutions. The chlorine mass balance is typically >70%, mostly in the form of chloride ion

(Cl-). The reactive intermediate, dichlorocarbene, is identified and quantified by means of trapping with 2,3-dimethyl-2-butene. Low concentrations (0.01-0.1 μM) of hexachloroethane and tetrachloroethylene are detected. Ultrasonic irradiation of a mixture of PNP and CCl_4 results in the acceleration of the sonochemical degradation rate of p-NP.

Both the ultrasonic frequency and the saturating gas influence the production of $^{\bullet}OH$ and H_2O_2 during sonolysis of buffered, aqueous solutions. Ultrasonic frequencies of 20,40,80 and 500 kHz are used, and the background gas in solution are Kr, Ar, He or O_2. Both species are formed at the highest rates during sonolysis of a Kr-saturated solution at 500 kHz, whereas the lowest rates of production are observed during sonolysis of a He-saturated solution at 20 kHz. A range of rate constants for the production of $^{\bullet}OH$ and H_2O_2 are observed at each frequency because each of the four saturating gases has different physical properties (e.g., thermal conductivity.) However, the range narrows at the higher ultrasonic frequencies (80 and 500 kHz) compared to that observed at the lower frequencies (20 and 40 kHz).

Thesis Overview

The first chapter contains an introduction to the field of sonochemistry as well as basic mathematical equations which describe the physics of acoustic cavitation. The research objectives of the work contained in this thesis are described in chapter one.

The second chapter reports on the possible existence of supercritical water (SCW) during acoustic cavitation as investigated by studying the kinetics of *p*-nitrophenylacetate (PNPA) hydrolysis. Ultrasonic irradiation at 20 kHz accelerates the rate of hydrolysis (k_{obs}) in aqueous solution by two orders of magnitude over the pH range of 3 to 8. In the presence of ultrasound, the observed first-order rate constant for the hydrolysis of PNPA is independent of pH and ionic strength but strongly influenced by the nature of the saturating gas. In a Kr-saturated solution $k_{obs}=7.4\times10^{-4}$ s^{-1}, whereas in Ar- and He-saturated solutions, the corresponding rate constants are 4.6×10^{-4} s^{-1} and 1.2×10^{-4} s^{-1}. The apparent activation parameters ($\Delta G^{\neq}$, $\Delta S^{\neq}$, $\Delta H^{\neq}$) for the hydrolysis of *p*-nitrophenylacetate are different from those observed for hydrolysis under ambient conditions. The apparent activation entropy, $\Delta S^{\neq}$, is substantially decreased while $\Delta G^{\neq}$ and $\Delta H^{\neq}$ are increased. The decrease in $\Delta S^{\neq}$ is attributed to differential solvation effects due to the existence of SCW (e.g., lower ρ and ε) while the increases in $\Delta G^{\neq}$ and $\Delta H^{\neq}$ are attributed to changes in the heat capacity of water due to the formation of the transient supercritical state.

In chapter three, the potential application of large-scale, high-power ultrasound to the remediation of hazardous compounds is demonstrated by investigating the sonochemical degradation of *p*-nitrophenol (PNP) in a near-field acoustical processor (NAP) at 20 and 16 kHz. A mathematical model for a continuous-flow loop reactor is required in order to extract k from the experimentally observed rate constant, k_{obs}. The psuedo-first order rate constant of degradation is maximized by varying both the power-to-

volume ratio and the power-to-area ratio. The nature of the cavitating gas influences the degradation rate and product distribution, at given power-to-volume and power-to-area ratios. The rate constant for PNP degradation in an O_2-saturated solution, k_{O_2} = 5.19×10^{-4} s^{-1} is lower than in the presence of pure Ar ($k_{Ar}=7.94\times10^{-4}$ s^{-1}) or an Ar/O_2 mixture ($k_{Ar/O_2}=1.2\times10^{-3}$ s^{-1}). Furthermore, the production of 4-nitrocatechol (4NC), an intermediate in the degradation of PNP, is minimized in an O_2-saturated solution; less than 10% of PNP is transformed to 4NC during the course of the irradiation.

Chapter four contains results from the investigation of CCl_4 degradation in Ar- or O_3-saturated solutions sonicated at 20 kHz. The observed first-order rate constant is 3.3×10^{-3} s^{-1} for initial concentration of 19.5 and 3.9×10^{-3} s^{-1} when the initial concentration is 195 μM. >70% of the theoretical chlorine is recovered as chloride ion (Cl^-) or hypochlorous acid (HOCl). Low concentrations (0.01-0.1 μM) of hexachloroethane and tetrachloroethylene are detected. Furthermore, the reactive intermediate, dichlorocarbene, is identified and quantified by means of trapping with 2,3-dimethyl-2-butene. The mechanisms by which these by-products are formed is discussed. O_3 does not accelerate the sonolytic degradation of CCl_4 but does inhibit the accumulation of hexachloroethane and tetrachloroethylene by approximately an order of magnitude compared to sonolysis in an Ar-saturated solution. The sonolytic rate of degradation of PNP is enhanced by a factor of ~4.5 when CCl_4 is present in solution.

Chapter five contains a discussion of the sonolytic production of hydroxyl radical ($^{\bullet}OH$) and hydrogen peroxide (H_2O_2) is investigated at 20, 40, 80 and 500 kHz and with four different saturating gases (Kr, Ar, He, O_2) at each frequency. Sonolysis of a Kr-saturated solution at 500 kHz results in the fastest production rates of both $^{\bullet}OH$ and H_2O_2 (0.47 μM min^{-1} and 3.57 μM min^{-1}). Irradiation of a He-saturated solution at 20 kHz yields the slowest production rate constants: 0.031 μM min^{-1} and 0.05 μM min^{-1}, respectively. At a given frequency, the effective difference between saturating gases will vary. At 20 kHz, the rate constants for production of H_2O_2 vary by an order of magnitude

(0.05 μM min^{-1} to 1.31 μM min^{-1}) in the following order: $k_{Kr} > k_{Ar} > k_{O_2} > k_{He}$. In contrast, at 80 kHz, the rate constants range from 0.76 μM min^{-1} to 2.24 μM min^{-1}. Similar trends are observed for the production of $^{\bullet}OH$ at the same frequencies and under the same saturating gases. There is a positive correlation between production rates for each species and the ultrasonic frequency. The data can be interpreted, in part, by considering the different resonant radii of the bubbles at each frequency (177, 88, 44 and 7 μm) at 20, 40, 80 and 500 kHz, respectively.

Chapter 6 is meant to summarize the observations in the rest of the thesis. Highlights of each chapter will be presented. Different sonochemical effects for various compounds will be compared, and the influence of different reactor configurations will be defined.

Table of Contents

Chapter 1:

Introduction

MOTIVATION

The development of novel, oxidative treatment methods for water and wastewater has recently expanded. These types of processes include the use of hydrogen peroxide with ultraviolet light (H_2O_2/UV) to treat hazardous compounds in aqueous solution (1-3). The optimization of ozonolysis has also been explored (4,5), and applied to disinfection (6) and de-colorization of groundwater (7). Various sequential or parallel process combinations have been reported, including ozone and radiolysis (8) or sonolysis (9). Other processes include electrolysis (10), semi-conductor photocatalysis(11), and sonolysis (12-23). The effective transformation of chemical compounds with various chemical structures and physical properties is possible during sonolysis Ultrasonic irradiation also inactivates aqueous suspensions of certain viruses and bacteria (24). Sonolysis is more convenient than H_2O_2/UV or ozonolyis because it does not require the addition of a separately generated chemical oxidant to the treated solution. Furthermore, because localized high temperatures and pressures occur during sonolysis in addition to the generation of free-radicals, contaminant degradation can occur via several simultaneous pathways.

Despite the potential of ultrasonic irradiation as a method for hazardous wastewater treatment, further examination of fundamental parameters is required for optimization of the degradation rates. For example, most investigators in the area of environmental sonochemistry use a conventional probe-type reactor, operating at frequencies between 16-40 kHz. The influence of ultrasonic frequency on sonochemical effects has not been systematically studied, especially in the frequency range >100 kHz. Although sonolysis has been utililized in various industries (25-33), no large-scale ultrasonic treatment facilities have been designed specifically for contaminant degradation. Few attempts have been made to maximize degradation rate constants by exploring different reactor configurations or ultrasonic frequencies. Furthermore, a better

understanding of the physics of collapsing bubbles would allow for better exploitation of acoustic cavitation for contaminant degradation.

RESEARCH OBJECTIVES

The most significant goals of the research contained in this thesis are:

- To better understand the physical conditions during a cavitation event. Investigation of the possible existence of transient supercritical water in cavitating solutions is done by examining the kinetics of *p*-nitrophenylacetate hydrolysis.

- To more clearly elucidate reaction mechanisms which occur during the sonolysis of chemical compounds of environmental interest. Carbon tetrachloride is chosen as a structurally simple representative of halogenated hydrocarbons.

- To optimize reactor conditions for sonolytic degradation of organic compounds. The performance of a parallel-plate, flow-though reactor was compared to that of an immersed, vibrating horn during sonolysis of *p*-nitrophenol. The influence of various gases and gas mixtures is also examined.

- To investigate the influence of ultrasonic frequency on the nature of reactions within the gas-phase and interfacial region of a cavitation bubble. Also, it should be determined if there is an optimal ultrasonic frequency for sonochemical effects.

MECHANICS OF ULTRASONIC WAVES

Understanding how ultrasonic waves propagate through various media as well as how they are reflected and transmitted at interfaces will aid in the design of sonochemical reactors. The equations are developed in detail in several references (34,35) and are presented in this section. The general equation for three-dimensional wave propagation is (34):

$$\frac{\partial^2 \xi}{\partial t^2} = \frac{1}{\rho_o \beta_s} \nabla^2 \xi \tag{1}$$

where ξ = instantaneous displacement of a volume element in the medium; ρ_o and β_s are the density and the adiabatic compressibility of the medium. However, for a wave travelling in one-dimension in a fluid medium, the equation is simplified to:

$$\frac{\partial^2 q}{\partial t^2} = \left(\frac{1}{v^2}\right) \frac{\partial^2 q}{\partial x^2} \tag{2}$$

where q respresents the instantaneous displacement of a volume element in one-dimension and v is the speed of the wave travelling through the medium (i.e. the speed of sound for ultrasonic waves). The solution to Eqn. (2) expresses how physical variables (such as pressure, temperature, and density) will change as the wave propagates:

$$q = Q \cos \omega \left(t - \frac{x}{v} \right) \tag{3}$$

In this equation, q represents any of the physical variables which are sinusoidally changing; $\omega = 2\pi f$, the angular frequency; f = the frequency; and t and x are time and

space coordinates. Q is the amplitude of cyclic change for the variable q. All these equations assume a perfectly elastic fluid medium.

Wave propagation will be determined in part by the acoustic impedance of a medium. The characteristic acoustic impedance, Z_o, of a medium is given by:

$$Z_o = \rho_o v \tag{4}$$

where ρ_o and v are defined as before. For an ultrasonic wave, Z_o can be thought of as the ratio of the pressure to the particle velocity at any point in the sound field.

The two simplest cases for reflection and transmission involve a single interface, for a soundwave travelling through medium 1 at normal incidence or at an incident angle θ_1 to medium 2. These conditions are common for the interface between the sonicated liquid and the reactor wall, or in an open reactor, between the liquid and the atmosphere. The reflection and transmission coefficients R_a and T_a are functions only of the characteristic impedances of media 1 and 2:

$$R_a = \frac{1 - r_{2/1}}{1 + r_{2/1}} \tag{5}$$

$$T_a = \frac{2r_{2/1}}{1 + r_{2/1}} \tag{6}$$

$$r_{2/1} = \frac{\rho_2 v_2}{\rho_1 v_1} \tag{7}$$

for a wave at normal incidence. For a wave at an incident angle of θ_1 and travelling away from medium 2 at an angle of θ_2 , the corresponding equations are:

$$R_a = \frac{\left(\frac{\cos\theta_2}{\cos\theta_1}\right) - r_{2/1}}{\left(\frac{\cos\theta_2}{\cos\theta_1}\right) + r_{2/1}} \tag{8}$$

$$T_a = \frac{2r_{2/1}\cos\theta_1}{\cos\theta_2 + r_{2/1}} \tag{9}$$

Eqns. 8-9 are valid only when both media are fluids (i.e. the interface between the liquid and the atmosphere in an open reactor).

During sonolysis of a liquid in which the ultrasonic source is emitted directly into the liquid, the energy losses through the walls or into the atmosphere can be minimized by maximizing the reflection coefficient, R_a and minimizing the transmission coefficient, T_a. This is most easily accomplished by choosing appropriate materials for the reactor. Table I contains acoustic impedance values for various materials.

Because the acoustic impedance of gases is so much lower than that of liquids or solids, the water-air interface in an open sonochemical reactor can be considered almost perfectly reflecting, for sound waves travelling through the water towards the interface. Also, stainless steel (R_a = -0.936) is a better material than glass (R_a = -0.794) for reflecting normal incident waves back into solution.

Also of interest during sonochemical treatment is the variation in sound intensity at different regions within the solution. The intensity I of an ultrasonic wave at a distance d from the emitter is given by (36):

$$I = I_o \exp(-2\alpha d) \tag{10}$$

where α = absorption coefficient. The absorption coefficient is inversely related to the square of the ultrasonic frequency by a constant:

$$\frac{\alpha}{f^2} = k \tag{11}$$

An experimentally determined value (37) for k is 21.5×10^{-17} cm^{-1} s^{-2} in water over a wide range of frequencies. Thus, for an ultrasonic frequency of 20 kHz, $\alpha = 8.6 \times 10^{-8}$ cm^{-1} and at 500 kHz, 5.37×10^{-5} cm^{-1}. Distances of 267 km and 0.42 km are required for the intensity to decay by 99% at 20 and 500 kHz, respectively. This difference is not significant for the length scales of bench-top chemical reactors. It should be noted that there is a subtle difference between sound absorption and sound attenuation by the medium. Attenuation refers to a process which decreases the energy of the travelling wave, but does not dissipate the energy as heat. A common attenuation mechanism in liquids is acoustic scattering by inhomogeneities: e.g. bubbles, particles. Absorption refers to the conversion of the wave energy to heat, and is a relaxation process in the liquid.

ACOUSTIC CAVITATION

Ultrasonic waves travelling through a solution impose upon the liquid a sinusoidal pressure variation, alternately compressing the liquid molecules or pulling them apart by overcoming the intermolecular forces. At an ultrasonic frequency of 20 kHz, the liquid will be compressed and rarefied 2×10^4 times each second. Acoustic cavitation refers to the expansion and collapse of bubbles in a liquid which is exposed to ultrasonic waves. The bubbles generally occur in clouds within the solution, although the lifetime of a single bubble is on the order of microseconds and its radius is on the order of micrometers. Both stable and transient cavitation will be discussed.

An understanding of the various stages of acoustic cavitation, including nucleation, growth by rectified diffusion, and collapse of transient bubbles is important

for interpreting sonochemistry observed under different bulk conditions. Furthermore, consideration of the forces which bubbles exert on each other, Bjerknes forces, is important for determining how cavitation bubbles in a cloud will differ from single bubbles. The phenomena of sonoluminescence, the emission of light from cavitating bubbles, can be used to determine the physical conditions within the imploding bubble. Optimal conditions for sonoluminescence can be used to predict optimal conditions for sonochemistry.

• Nucleation and Cavitation Threshold

The nucleation of bubbles can occur by either a homogeneous or a heterogeneous process. Homogeneous nucleation involves a phase-transition in the liquid, resulting from microscopic variations in the density due to thermal fluctuations. The formation of a vaporous pocket can then occur, which may grow into an observable bubble. The energy of formation, F, of the bubble under these circumstances is given by (38):

$$F = 4\pi r^2\alpha - 4\pi r^3|P| \qquad (12)$$

where r = radius of the bubble, α = surface energy, P = pressure in the liquid. Most cavitation studies utilize negative pressures (i.e. tension) on the liquid. The first term of Eqn. 12 results from the energetics of forming an interface between two phases and the second term reflects energy gained during the transition from liquid to gas. As the value of P rises, the nucleation barrier decreases. Homogeneous nucleation studies are often done in liquid He (39-41) because of the high purity which can be achieved in this liquid.

Most investigations of heterogeneous nucleation have been done with water. Heterogeneous nucleation refers to the stabilization of pockets of gas by foreign substances in the liquid, such as surfactants or organic substances (42-44), ions (45-47) or

solid particles (45,46). This stabilization process weakens the liquid; most experimental measurements of the tensile strength of water yield values which are far below the theoretical prediction (48). Gas-pocket stabilization by entrapment in crevices on solid particles was proposed by Harvey et al. (49) and investigated more recently by other researchers (45,50,51). The pressure within the gas-pocket must balance the external, crushing forces:

$$P_L + \frac{2\sigma}{R} = P_g + P_v \qquad (13)$$

where P_L = presssure exerted on the interface by the liquid, σ = surface tension, P_g and P_v are the partial pressure of the gas and the vapor pressure of the liquid, respectively. If an acoustic pressure, P_A is applied to the liquid, the gas-pocket is stabilized during the compression cycle, but during the rarefaction cycle, the interface moves away from the apex of the crevice until the angle of contact is small enough such that the pocket can break away as a bubble (Fig 1).

The cavitation threshold is defined as the acoustic pressure amplitude at which a cavitation event is first detected (52). For liquids saturated with gas, thresholds for transient cavitation are 1-2 bar, and are effected by various bulk parameters. In most applications of ultrasound to sonochemistry, the sound intensity is high enough to ensure that the acoustic amplitude is above the threshold.

•Bubble Dynamics

The resonant radius of an oscillating bubble is the radius at which the bubble most efficiently absorbs energy from the ultrasonic field. The ultrasonic frequency will affect the resonant bubble radius (53):

$$\rho\omega_r^2 R_r^2 = 3KP_o \tag{14}$$

where ρ = density of water, ω_r = resonance frequency, R_r = resonant radius, P_o = pressure in the liquid, usually taken to be 1 atm, and K = polytropic index, as defined before. This expression is valid when surface tension effects are small.

For a spherical bubble containing gas and vapor, in an infinite liquid, the equations of motion must be determined by solving the equations of mass, momentum and energy conservation for the gas and liquid. The boundary condition is that these equations match at the bubble interface. The solution can be reached by approximating the above equations, and one of the most well-known expressions (54) is the Rayleigh-Plesset Equation:

$$R\frac{dR^2}{dt^2} + \frac{3}{2}\left(\frac{dR}{dt}\right)^2 = \frac{1}{\rho}\left[\left(P_o + \frac{2\sigma}{R_o}\right)\left(\frac{R_o}{R}\right)^{3K} - \frac{2\sigma}{R} - P_\infty\right] \tag{15}$$

where R = bubble radius, P_∞ = pressure in the liquid at infinity, P_o = pressure in the gas, R = instantaneous radius, R_o = initial radius. $K = C_p/C_v$, the polytropic index of the gas, σ = surface tension of the liquid.

The equations of motion for a bubble undergoing stable oscillation in a sound field can be derived from Eqn. 14 by assuming a small, linear variation of the radius with time (55). Stable cavitation is usually induced by lower acoustic pressure amplitudes than transient cavitation, and stable bubbles oscillate for many acoustic cycles The estimate for the temperature (36) within a bubble undergoing stable oscillation is given by:

$$\frac{T_o}{T_{max}} = \left\{1 + Q\left[\left(\frac{P_h}{P_m}\right)^{\frac{1}{3K}} - 1\right] - 1\right\}^{3(K-1)} \tag{16}$$

where Q = ratio of the resonance amplitude to the static amplitude of vibration of the bubble, P_m = the peak pressure of the bubble, the sum of the hydrostatic and acoustic pressures, and T_o = ambient temperature of the liquid.

The equations of motion for transient cavitation were developed by Noltingk and Neppiras (54,56), and reviewed by Flynn (57). Transient cavitation is characterized by the increase of the bubble radius to a size greater than reached during stable cavitation (at least twice the radius of the initial size) and a rapid, violent collapse during which the bubble wall approaches the speed of sound. Also, transient cavities exist for one or a few acoustic cycles. The maximum temperature,T_{max} and pressure,P_{max} can be estimated with Eqns. 17-18:

$$T_{max} = T_o\left\{\frac{P_m(K-1)}{P}\right\} \tag{17}$$

$$P_{max} = P\left\{\frac{P_m(K-1)}{P}\right\}^{\left(\frac{K}{K-1}\right)} \tag{18}$$

where P_m = pressure in the liquid at the time of collapse, P = pressure in the bubble at its maximum size (assumed to be the vapor pressure of the liquid), and K is defined as before. For a bubble containing Ar in water at 1 atm, the predicted temperature is ~6500 K. Experimentally, the temperature of the hot-gas phase region has been estimated by different methods to be 3300 K (58) and ~2000-4000 K (59).

The temperatures and pressures developed during bubble collapse depend on how completely the bubble implodes during the compression cycle. Thus, it is important to

know how the required collapse time compares with the length of the compression cycle. The bubble collapse time τ, for an empty void in an incompressible liquid is:

$$\tau = 0.915 R_m \left(\frac{\rho}{P_o} \right)^{0.5} \tag{19}$$

where R_m = radius at the start of collapse and ρ = density of the liquid and P_o = pressure in the liquid. For example, a bubble in water with a radius of 177 μm under an ambient pressure of 1 atm would collapse in ~16 μs. At an ultrasonic frquency of 20 kHz, the compression half-cycle is 25 μs. For a bubble which is not completely empty and which is acted upon by a sound field, Eqn. 18 can be modified to yield:

$$\tau = 0.915 R_m \left(\frac{\rho}{P_m} \right)^{0.5} \left(1 + \frac{P_{vg}}{P_m} \right) \tag{20}$$

where P_m and P_{vg} are pressure in the liquid and in the bubble at the start of collapse. At the beginning of the compression cycle, P_m is the sum of the hydrostatic pressure and the acoustic pressure amplitude. P_{vg} is due to gas and vapor in the bubble. In this situation, the time required to reach a minimum radius from the same initial radius, R_m, will be longer than in the more idealized situation described by Eqn. 19.

• The Transient Cavitation Cycle

Transient cavitation is the type most commonly observed in sonochemical systems. The 'transient cavitation cycle' was first proposed by Neppiras (60) and describes the behavior of a bubble in a solution exposed to ultrasonic irradiation above a certain intensity. A stable bubble in solution can grow by the process of rectified diffusion and reach the transient threshold, after which the bubble greatly increases in

size over a short period of time and then implodes and disintegrates into smaller bubbles. These smaller nuclei can then either dissolve or undergo the same cycle of behavior.

The process of rectified diffusion was first named by Blake (61), and is a means by which a bubble in an acoustic field can increase in size. When the bubble expands during a rarefaction half-cycle, the gas expands and there is a flux of gas from the surrounding liquid into the bubble. During the compression half-cycle, the gas is compressed and results in an outward flux of gas into the bulk liquid. Because the surface area of the bubble during the expansion cycle is larger than during the compression cycle, there is a net increase of gas within the bubble at the end of each acoustic cycle.

The second effect contributing to overall bubble growth is the 'shell' effect. The diffusion rate of the gas into the bubble is a function of the concentration gradient. When the bubble contracts, the spherical shell around the bubble expands, and the concentration of gas on the outer side of the bubble wall decreases. Thus, the rate of diffusion out of the bubble is greater than when the bubble is at its equilibrium radius. However, during bubble expansion, the shell thickness decreases, the concentration of gas near the outer side of the bubble wall increases, and hence there is a greater inflow of gas during expansion than during compression. The growth of bubbles by rectified diffusion has been experimentally observed (62). The radial growth rate and the threshold for rectified diffusion can be derived (63) from the equation of motion for a gas bubble.

The mathematical expressions required to describe cavitation bubble dynamics are often quite complex. Most of the equations in this section are based on certain physical conditions (e.g., incompressibility of the liquid or spherical symmetry of the bubble) which may be violated when the bubble is close to total collapse. However, discussion of these equations allows for the estimate of important physical quantities such as temperature, pressure, and collapse time.

BJERKNES FORCES

Acoustic cavitation usually refers to the formation of a cloud of bubbles, except in the case of acoustically levitated single bubbles. Thus, an understanding of how bubbles interact with each other while subject to a sound field is important and may ultimately effect the interpretation of cavitation chemistry. Bjerknes (64) showed that two bubbles of volumes V_1 and V_2, a distance, d, apart in a sound field will be subject to a force, F:

$$F \propto \frac{V_1 V_2}{d^2} \tag{21}$$

These forces can result in deviations from sphericity of the bubble shape (65). It has been calculated (66) that two bubbles of unequal size will move towards each other unless the driving frequency is between that of the two resonance frequencies for each bubble. Regardless of the driving frequency, two bubbles of equal size will always move towards each other in an acoustic field.

Furthermore, if a bubble is larger or smaller than its resonant size, it can be forced towards a pressure antinode or node, respectively (67). Thus, smaller bubbles will be forced into a region where they can expand to resonance size. Coalescence of smaller bubbles as they are translating towards the antinode is possible, as is growth by rectified diffusion, as the bubbles are oscillating as well as translating. Experimental observations of attractive Bjerknes forces have been reported during transient cavitation (68) and during the vaporization of a superheated droplet in the presence of a sound field (69). In a standing wave field, larger bubbles directed to pressure nodes have been observed to follow elliptical orbits (70) once they reach the nodes. The differential behavior displayed by bubbles of different sizes is an important component of the transient cavitation cycle.

SONOLUMINESCENCE

Sonoluminescence refers to the emission of light during acoustic cavitation and was first observed during the underwater exposure of photographic plates in solutions irradiated with ultrasound (71). Both multiple-bubble sonoluminescence (MBSL) (72-75) and single-bubble sonoluminescence (SBSL) (76-80) yield information about the conditions within the imploding cavitation bubbles. Commonly proposed mechanisms of sonoluminescence include shock-waves converging at the center of the bubble during implosion (81), and emission from excited state chemical species, such as hydroxyl radical (80). However, the nature of the emissions can be significantly influenced by small changes in bulk parameters.

Low percentages of noble gases mixed with nitrogen have been reported to enhance SBSL intensity and to change the spectral features of emission (78). A change in temperature from 40 ^{O}C to 1 ^{O}C resulted in a hundred-fold increase in the light intensity (76). SBSL measurements indicate more extreme conditions within the bubble interior than those indicated MBSL (77). The black body temperature of a single cavitating bubble in water has been estimated to be 1.6-3.0 $\times 10^4$ K. Furthermore, a comparison of the spectra of SBSL and MBSL indicates that liquid or dissolved species at the surface of cavitation bubbles in MBSL could be transported to the hot center of the bubble via surface waves and microjets whereas a single bubble may maintain a high degree of spherical symmetry (80,82). However, the sonoluminescence intensity during MBSL also increases with decreasing bulk liquid temperature (74). The physical conditions (liquid temperature, acoustic pressure amplitude, saturating gas) for optimal MBSL intensity are probably similar to those for optimal sonochemistry, because of the strong correlation between sonoluminescence and sonochemistry (83).

CAVITATION DETECTION AND CHARACTERIZATION

The accurate characterization of single cavitation bubbles as well as bubble clouds is crucial. Modern techniques include high-speed photgraphy (84-87), holography (88-91), Mie Scattering (92,93), and single- and multiple-bubble sonoluminescence. High-speed photography is useful for observing radial oscillations of a bubble and is most appropriate for single bubbles in unbounded fluids (i. e. no other bubbles with which to interact) or single bubbles near interfacial surfaces (i.e. liquid-solid interface). Bubble distribution profiles within a bubble cloud can be discerned from three-dimensional images generated by high-speed holography. Recent images suggest that the bubble density increases towards the center of the cloud (88).

Mie scattering is the scattering of light by bubbles with radii similar to the wavelength of the incoming light and can be used to determine the size of a bubble, given a consant scattering angle and fixed distance of the light source from the bubble. This method requires calibration by using an independent determination of bubble radius, the rise-time method. The scattered light-intensity is well correlated to bubble size for radii up to 50 μm (93). For radii between 60-100 μm the correlation exists; but there is a greater deviation of the radius measured by scattering intensity compared to that measured by the rise-time. Mie scattering, like high-speed photography, can only be used for low bubble density systems.

More qualitative and instrumentally simpler methods of detecting cavitation in solution include visually inspecting the chemiluminescence of luminol (5-amino-2,3-dihydro-1,4-phthalazinedione). Luminol reacts with various oxidants in alkaline solution to yield a blue light (94). Investigators sonicated aqueous solutions of luminol and determined that the most chemically active region during sonication at 20 kHz extended from the ultrasonic emitter in a cone shape whereas at 487 kHz, the luminescence orginated from a larger volume near the air-liquid interface of the solution (20).

Furthermore, zones of maximum luminous intensity and of maximum acoustic energy were observed to occupy different regions of the solution during irradiation at 500 kHz (95).

SONOCHEMISTRY IN AQUEOUS SOLUTION

The reactive species formed during the sonolysis of water are similar to those observed during radiolysis (Table II). The relative predominance of the different reactions is dicussed in greater detail in Chapter 5 of this thesis. Among the most extensively studied species are $^{\bullet}OH$ and H_2O_2, produced by the thermolysis of water molecules in the gas-phase of the bubble, and recombination of the resulting free-radicals. H_2O_2 is formed in the cooler interfacial area of the cavitation bubble (96) .

Chemical transformations which occur during sonolysis may occur in several different regions of the cavitation bubble (Fig. 2). Attack by oxidizing species such as hydroxyl radical ($^{\bullet}OH$) or oxygen atom ($O^{\bullet}$) or thermolysis of chemical bonds within the substrate can occur in either the gas-phase or interfacial region. $^{\bullet}OH$ is most concentrated in the gas-phase of the cavitation bubble although non-volatile compounds which have a high-boiling point such as nucleic acids (97), benzoic acid (98) and dimethyl sulfoxide (99) can be hydroxylated during sonolysis. It is presumed that aromatic substrates are attacked by addition of $^{\bullet}OH$ whereas non-aromatic molecules are attacked by hydrogen-atom abstraction (100) due to the much stronger C-H bond in aromatic systems. Rate constants for the reaction of $^{\bullet}OH$ with a wide range of organic compounds in both the gas-phase (101) and in aqueous solution (102) have been compiled.

The bond strengths of several organic functional groups are listed in Table III. These bond strengths can be compared to the O-H and O-O bond strength in water and oxygen molecules (119 kcal mol^{-1}) in order to estimate the relative importance of

thermolysis versus radical attack in the gas-phase of the bubble during the sonolytic degradation of a substrate. Further transformation in the bulk solution may result from reaction with H_2O_2, which is a longer-lived species than $^{\bullet}OH$ and more likely able to diffuse away from the bubble. Hydrolysis reactions are also enhanced (18,103) during ultrasonic irradiation and are thought to occur in the interfacial region.

The sonochemistry of a large number of chemical compounds in aqueous solutions has been studied. The degradation products of organic substrates include short-chain carboxylic acids and the appropriate inorganic ions. For example, decomposition of parathion (*O,O*-diethyl *O*, -p-nitrophenyl thiophosphate) (18) yielded sulfate, nitrite, nitrate, phosphate, *p*-nitrophenol, and oxalate. Exposure of an air-saturated 100 μM solution of pentachloropehenol to ultrasonic irradiation results in a non-linear reduction in the concentration to ~1 μM after 100 min and the formation of Cl^- (90% theoretical yield after 150 min sonication). Inorganic compounds (e.g., Tl^+) are oxidized (104) or reduced (105) (e.g., OsO_4) during sonolysis, depending on the nature of the saturating gas.

Physical properties of the solute such as its hydrophobicity (indicated by the octanol-water partition coefficient, K_{OW}) can determine which reaction routes a particular substrate will follow during sonochemical transformation. Hydrophobic compounds are known to partition to the interface of cavitating bubbles (96,106). Thus, the degradation rate constant during sonication can be pH-dependent. For example, the observed degradation rate constant of *p*-nitrophenol (pK_a=7.08) increases when the bulk solution pH is decreased (17).

Volatility is also important because a greater fraction of the dissolved reactant can reach the more extreme region of the bubble if the reactant is volatile, although the final collapse conditions may be less extreme due to a decrease in the effective polytropic index of the compressed medium. For example, the by-products of methanol degradation are produced most quickly in an Ar-saturated 10-15% (v/v) solution of methanol in water,

whereas in an 80% (v/v) solution, almost no chemical reaction occurs (107). However, as the concentration of methanol increases in the solution and in the gas-phase of the cavitating bubble, the effective polytropic index decreases, and the final temperature of bubble collapse is probably lower than in a bubble filled only with Ar and water vapor. Decomposition products of methanol formed in the most significant quantities are H_2, CH_2O, CO and CH_4 during sonolysis of an Ar-saturated solution and CO_2, CO, HCOOH, CH_2O and H_2O_2 during sonolysis of an O_2-saturated solution. The presence of $^{\bullet}CH_2OH$ has also been detected by spin-trapping (108).

The connections between sonochemistry and cavitation bubble dynamics need to be clarified in order to optimize sonochemical effects. In particular, the number of bubbles in solution needs to be more definitively determined, as well as the number of chemical reactions per cavitation event. To this end, both physical and chemical measurements are need.

List of Figure Captions

Fig. 1a: Stabilization of a gas-pocket by conical crevice on a solid particle during positive applied pressure to the solution.

Fig. 1b: Growth of the gas-liquid interface away from the apex during negative applied pressure (tension) on the liquid.

Fig. 2: Schematic of the reactive regions of a cavitation bubble in aqueous solution.

References

1. Beltran, F. J., Overjero, G., Acedo, B., *Wat. Res.*, **1993**, *27*, 1013-1021.

2. Scheck, C. K., Frimmel, F. H., *Wat. Res.*, **1995**, *29*, 2346-2352.

3. Shu, H. Y., Huang, C. R., Chang, M. C., *Chemosphere,* **1994**, *29*, 2597-2607.

4. Bhattacharyya, D., Vandierdonck, T. F., West, S. D., Freshour, A. R., *J. Haz. Mat.,* **1995**, *41*, 73-93.

5. Hausler, R., Briere, F. G., Beron, P., *Ozone Sci. Eng.,* **1993**, *15*, 201-211.

6. Scott, K. N., Wolfe, R. L., Stewart, M. H., *Ozone Sci. Eng.,* **1992**, *14*, 71-90.

7. Tan, L., Amy, G., Rigby, M., Renna, J., Kemp, K., *Oz. Sci. Eng.,* **1991**, *13*, 109-125.

8. Gehringer, P., Eschweiler, H., Szinovatz, W., Fiedler, H., Steiner, R., Sonneck, G., *Rad. Phys. Chem.,* **1993**, *42*, 711-714.

9. Olson, T. M., Barbier. P. F., *Wat. Res.,* **1994**, *28*, 1383-1391.

10. Nagaoka, T., Yamashita, J., Kaneda, M., Ogura, K., *J. Electroanal. Chem.,* **1992**, *335*, 187-195.

11. Hoffmann, M. R., Martin, S. T., Choi, W. Y., Bahnemann, D. W., *Chem. Rev.,* **1995**, *95*, 69-96.

12. Cost, M.; Mills, G.; Glisson, P.; Lakin, J., *Chemosphere,* **1993**, *27*, 1737-1743.

13. Hua, I.; Höchemer, R. H.; Hoffmann, M. R., *J. Phys. Chem.,* **1995**, *99*, 2335-2342.

14. Hua, I., Höchemer, R. H., Hoffmann, M. R., *Environ. Sci. Technol.,* **1995**, *29*, 2790-2796.

15. Koskinen, W. C.; Sellung, K. E.; Baker, J. M.; Barber, B. L.; Dowdy, R. H., *J. Environ. Sci. Health Part B,* **1994**, *29*, 581-590.

16. Kotranarou, A.; Mills, G.; Hoffmann, M. R., *Environ. Sci. Technol.,* **1992**, *26*, 2420-2428.

17. Kotronarou, A.; Mills, G.; Hoffmann, M. R., *J. Phys. Chem.,* **1991**, *95*, 3630-3638.

18. Kotronarou, A.; Mills, G.; Hoffmann, M. R., *Environ. Sci. Technol.,* **1992**, *26*, 1460-1462.

19. Petrier, C.; Micolle, M.; Merlin, G.; Luche, J. L.; Reverdy, G., *Environ. Sci. Technol.,* **1992**, *26*, 1639-1642.

20. Petrier, C.; Lamy, M. F.; Francony, A.; Benahcene, A.; David, B.; Renaudin, V.; Gondrexon, N., *J. Phys. Chem.,* **1994**, *98*, 10514-10520.

21. Serpone, N.; Terzian, R.; Colarusso, P.; Minero, C.; Pelizzetti, E.; Hidaka, H., *Res. Chem. Intermed.,* **1992**, *18*, 183-202.

22. Wu, J. M., Huang, H. S., Livengood, C. D., *Environ. Prog.,* **1992**, *11*, 195-201.

23. Price, G., Matthias, P., Lenz, EJ, *Process Safety and Environmental Protection: Transactions of the Institution of Chemical Engineers Part B,* **1994**, *72*, 27-31.

24. Scherba, G., Weigel, R. M., O'Brien, Jr.,W. D., *Appl. Environ. Microbiol.,* **1991**, *57*, 2079-2084.

25. Berlan, J.; Mason, T. J., *Ultrasonics,* **1992**, *30*, 203-212.

26. Bién, J., *Acustica,* **1991**, *74*, 279-283.

27. Bjorno, L., Gram, S., Sttenstrup, P. R., *Ultrasonics,* **1978**, 103.

28. Hunicke, R. L., *Ultrasonics,* **1990**, *28*, 291-294.

29. Hutchinson, J. M., Sayles, R. S., *Ultrasonics,* **1987**, *25*, 351-351.

30. Lin, J.-R.; Yen, T. F., *Energy and Fuels,* **1993**, *7*, 111-118.

31. Namgoong, E., Chun, J. S., *Thin Solid Films,* **1984**, *120*, 153-169.

32. Sadeghi, K. M.; Lin, J. R.; Yen, T. F., *Energy Sources,* **1994**, *16*, 439-449.

33. Umemura, S., Yumita, N., Nishigaki, R., *Jpn. J. Cancer Res.,* **1993**, *84*, 582-588.

34. *Ultrasonics*; Edmonds, P. D., Ed.; Academic Press: New York, 1981; Vol. 19, pp 619.

35. Shutilov, V. A. *Fundamental Physics of Ultrasound*; Gordon and Breach Science Publishers: New York, 1988, pp. 378.

36. Mason, T. J.; Lorimer, J. P. *Sonochemistry: Theory, Applications and Uses of Ultrasound in Chemistry*; Ellis Horwood Ltd.: Chichester, 1988, pp. 252.

37. Fox, F. E., Rock, G. D., *J. Acoust. Soc. Am.,* **1941**, *12*, 505-510.

38. Pettersen, M. S., Balibar, S., Maris, H., *Phys. Rev. B,* **1994**, *49*, 63-70.

39. Xiong, Q., Maris, H. J.,, *J. Low Temp. Phys.,* **1991**, *82*, 105-118.

40. Nissen, J. A., Bodegom, E., Brodie, L. C., Semura, J. S., *Phys. Rev. B,* **1989**, *40*, 6617-6624.

41. Maris, H. J., *J. Low Temp. Phys.,* **1994**, *94*, 125-144.

42. Fox, F. F., Herzfield, K. F.,, *J. Acoust. Soc. Am.,* **1954**, *26*, 984-989.

43. Iyengar, K. S., Richardson, E. G., *Br. J. Appl. Physics.*, **1958**, *9*, 154-158.

44. Haywood, A. T. J., *J. Phys. D: Appl. Physics,* **1970**, *3*, 574-579.

45. Apfel, R. E., *J. Acoust. Soc. Am.*, **1970**, *48*, 1179-1186.

46. Crum, L. A., *Appl. Sci. Res.*, **1982**, *38*, 101-115.

47. Akulichev, V., *Sov. Phys. Acoust.*, **1966**, *12*, 144-149.

48. Greenspan, M., Tschiegg, C. E., *J. Res. Natl. Bur. Stand. Sect. C,* **1967**, *71C*, 299-312.

49. Harvey, E. N., Barnes, K. K., McElroy, W. D., Whitely, A. H., Pease, D. C., Cooper, K. W.,, *J. Cell. Comp. Physiol.*, **1944**, *24*, 1.

50. Crum, L., *Nature (London),* **1979**, *278*, 148-149.

51. Winterton, R., *J. Phys. D: Appl. Phys.*, **1977**, *10*, 2041-2056.

52. Atchley, A. A., Crum, L. A. In *Ultrasound: Its Chemical, Physical and Biological Effects*; K. S. Suslick, Ed.; VCH Publishers: New York, 1988; pp 1-64.

53. Minnaert, M., *Phil. Mag.*, **1933**, *16*, 235.

54. Neppiras, E. A., Noltingk, B. E., *Proc. Phys. Soc. B (London),* **1951**, *64B*, 1032-1038.

55. Young, F. R. *Cavitation*; McGraw-Hill Book Company (UK) Limited: Berkshire, 1989, pp. 418.

56. Noltingk, B. E., and Neppiras, E. A., *Proc. Phys. Soc. B. (London),* **1950**, *63B*, 674-685.

57. Flynn, H. G. In *Physical Acoustics*; W. P. Mason, Ed.; Academic Press: 1964; Vol. 1B; pp 85.

58. Seghal, C., Steer, R. P., Sutherland, R. G., Verrall, R. E., *J. Chem. Phys.*, **1979**, *70*, 2242-2248.

59. Misik, V., Miyoshi, N., Riesz, P., *J. Phys. Chem.*, **1995**, *99*, 3605-3611.

60. Neppiras, E. A., *Ultrasonics,* **1980**, *18*, 201.

61. Blake, F. G. "Technical Memo 12," Acoustics Research Laboratory, Harvard University, 1949.

62. Crum, L. A., *J. Acoust. Soc. Am.*, **1980**, *68*, 203-211.

63. Crum, L. A., *Ultrasonics,* **1984**, *22*, 215-223.

64. Bjerknes, V. F. K. *Fields of Force*; Columbia University Press: New York, 1906.

65. Hall, P., Seminaras, G., *J. Fluid Mech.*, **1980**, *101*, 423-444.

66. Pelekasis, N. A., Tsamopoulos, J. A., *J. Fluid. Mech.*, **1993**, *254*, 501-527.

67. Walton, A. J., Reynolds, G. T., *Adv. Phys.*, **1984**, *33*, 595-669.

68. Crum, L. A., Nordling, D. A., *J. Acoust. Soc. Am.*, **1972**, *52*, 294-301.

69. Apfel, R. E., Harbison, J. P., *J. Acoust. Soc. Am.*, **1975**, *57*, 1371-1373.

70. Miller, D. L., *J. Acoust. Soc. Am.*, **1977**, *62*, 12-19.

71. Frenzel, H., Shultes, H., *Z. Phys. Chem.*, **1934**, *B27*, 421-424.

72. Finch, R. D., *Ultrasonics,* **1963**, *2*, 87-98.

73. Didenko, Y. T., Gordeychuk, T. V., Koretz, V. L., *J. Sound Vibr.*, **1991**, *32*, 71-76.

74. Didenko, Y. T., Nastitch, D. N., Pugach, S. P., Polovinka, Y. A., Kvochka, V. I., *Ultrasonics,* **1994**, *32*, 71-76.

75. Henglein, A., Guitierrez, M., *J. Phys. Chem.,* **1993**, *97*, 158-162.

76. Barber, B. P., Wu, C. C., Lofstedt, R., Roberts, P. H., Putterman, S. J., *Phys. Rev. Letts.,* **1994**, *72*, 1380-1383.

77. Crum, L. A., Roy, R. A., *Science,* **1994**, *266*, 233-234.

78. Hiller, R., Weninger, K., Putterman, S. J., Barber, B. P., *Science,* **1994**, *266*, 248-250.

79. Holt, R. G., Gaitan, D. F., Atchley, A. A., Holzfuss, J., *Phys. Rev. Letts.,* **1994**, *72*, 1376-1379.

80. Matula, T. J., Roy, R. A., Mourad, P. D., McNamara III, W. B., Suslick, K. S., *Phys. Rev. Lett.,* **1995**, *75*, 2602-2605.

81. Greenspan, H. P., Nadim, A., *Phys. Fluids A,* **1993**, *5*, 1065-1067.

82. Crum, L. A., *J. Acoust. Soc. Am.,* **1994**, *95*, 559-562.

83. Chendke, P. K., Fogler, H. S., *J. Phys. Chem.,* **1983**, *87*, 1362-1369.

84. Philipp, A., Delius, M., Scheffczyk, C., Vogel, A., Lauterborn, W., *J. Acoust. Soc. Am.,* **1993**, *93*, 2496-2509.

85. Ohl, C. D., Philipp, A., Lauterborn, W., *Annalen Der Physik,* **1995**, *4*, 26-34.

86. Lauterborn, W., Hentschel, W., *Ultrasonics,* **1985**, *23*, 260-268.

87. Lauterborn, W., Hentschel, W., *Ultrasonics,* **1986**, *24*, 59-65.

88. Lauterborn, W., Judt, A., Schmitz, E., *Opt. Letts.,* **1993**, *18*, 4-6.

89. Hentschel, W., Zarschizky, H., Lauterborn, W., *Opt. Comm.,* **1985**, *53*, 69-73.

90. Nyga, R., Schmitz, E., Lauterborn, W., *Appl. Opt.,* **1990**, *29*, 3365-3368.

91. Hentschel, W., Lauterborn, W., *Optic. Eng.,* **1985**, *24*, 687-691.

92. Aragon, S. R., Elvenspoek, M.,, *J. Chem Phys.,* **1982**, *77*, 3406-3413.

93. Hansen, G. M., *Appl. Opt.,* **1985**, *24*, 3214-3220.

94. Isacsson, U., Wettermark, G., *Anal. Chim. Acta,* **1974**, *68*, 339-362.

95. Renaudin, V., Gondrexion, N., Boldo, P., Petrier, C., Bernis, A., Gonthier, Y., *Ultrasonics Sonochemistry,* **1994**, *1*, s81-s85.

96. Henglein, A., Kormann, C., *Int. J. Radiat. Biol.,* **1985**, *48*, 251-258.

97. Yu, T. J., Sutherland, R. G., Verrall, R. E., *Can. J. Chem.,* **1980**, *58*, 1909-1915.

98. Parke, A. V. M., Taylor, D., *J. Chem. Soc.,* **1956**, 4442-4450.

99. Kondo, T., Kirschenbaum, L. J., Kim, H., Riesz, P., *J. Phys. Chem.,* **1993**, *97*, 522-527.

100. Sawyer, D. T. *Oxygen Chemistry*; Oxford University Press: New York, 1991; Vol. 26, pp. 223.

101. Atkinson, R., *Chem. Rev.,* **1985**, *85*, 69-201.

102. Buxton, G. V., Greenstock, C. L., Helman, W. P., Ross, A. B., *J. Phys. Chem. Ref. Data,* **1988**, *17*, 513-886.

103. Doulah, M. S., *Ind. Eng. Chem. Fundam.,* **1979**, *18*, 76-78.

104. Anbar, M., Pecht, I., *J. Phys. Chem.,* **1964**, *68*, 353-355.

105. Wawrzyczek, W., Tyzanouska, D., *Nature (London),* **1962**, *194*, 571-572.

106. Kondo, T., Riesz, P., *Free Rad. Biol. Med.,* **1989**, *7*, 259-268.

107. Buttner, J., Gutierrez, M., Henglein, A., *J. Phys. Chem.,* **1991**, *95*, 1528-1530.

108. Krishna, C. M., Kondo, T., Riesz, P., *J. Phys. Chem.,* **1989**, *93*, 5166-5172.

109. *CRC Handbook of Chemistry and Physics*; 71 ed.; Lide, D. R., Ed.; CRC Press: Boca Raton, 1990.

Table I

Acoustic Impedance Values of Selected Materials

Material	Temperature, °C	Acoustic Impedance, $kgm^{-2}\ s^{-1}$
Water, degassed/distilled	30	1.503×10^6
Pyrex glass	-	13.1×10^6
Stainless steel (347)	-	45.8×10^6
Air	30	405

*Data taken from CRC Handbook, 71st Ed.(109).

Table II

Chemical Reactions of Water During Acoustic Cavitation

a. Saturating Gas is Monoatomic and Inert (Kr, Ar, He)

$$H_2O \rightarrow H^{\bullet} + {}^{\bullet}OH$$

$$H^{\bullet} + {}^{\bullet}OH \rightarrow H_2O$$

$$2\ {}^{\bullet}OH \rightarrow O^{\bullet} + H_2O$$

$$2\ {}^{\bullet}OH \rightarrow H_2O_2$$

$$2\ H^{\bullet} \rightarrow H_2$$

b. Saturating Gas is Polyatomic and Reactive (O_2)

$$O_2 \rightarrow 2\ O^{\bullet}$$

$$O_2 + O^{\bullet} \rightarrow O_3$$

$$H^{\bullet} + O_2 \rightarrow HOO^{\bullet}$$

$$2\ HOO^{\bullet} \rightarrow H_2O_2$$

Table III

Bond Strengths of Selected Organic Compounds

Molecule	*Bond Strength, kcal mol^{-1}
C_2H_5-OH	94
C_6H_5-OH	111
C_6H_5-Cl	96
C_6H_5-NH_2	102
Cl-CCl_3	73
H-CCl_3	96

*At 298 K

Data taken from the CRC Handbook, 71st Edition (109)

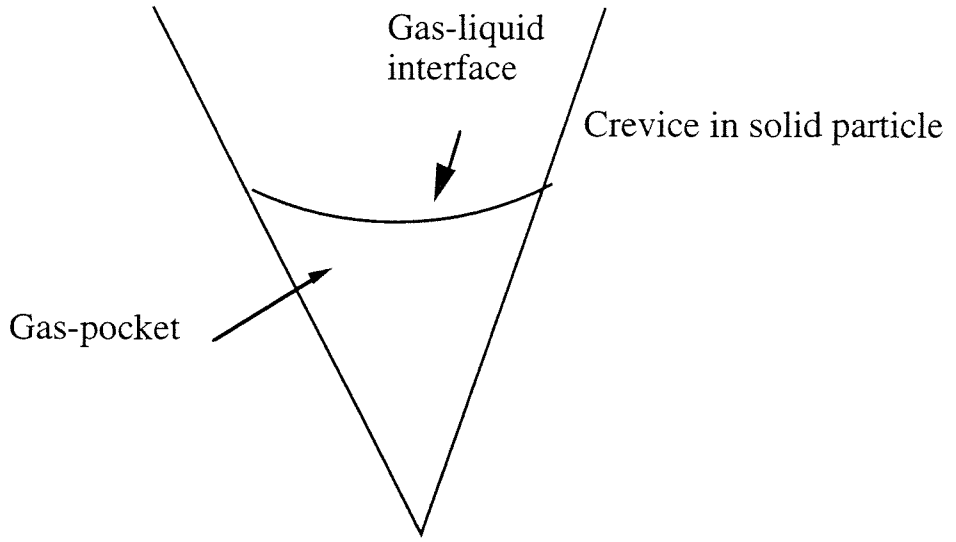

a.

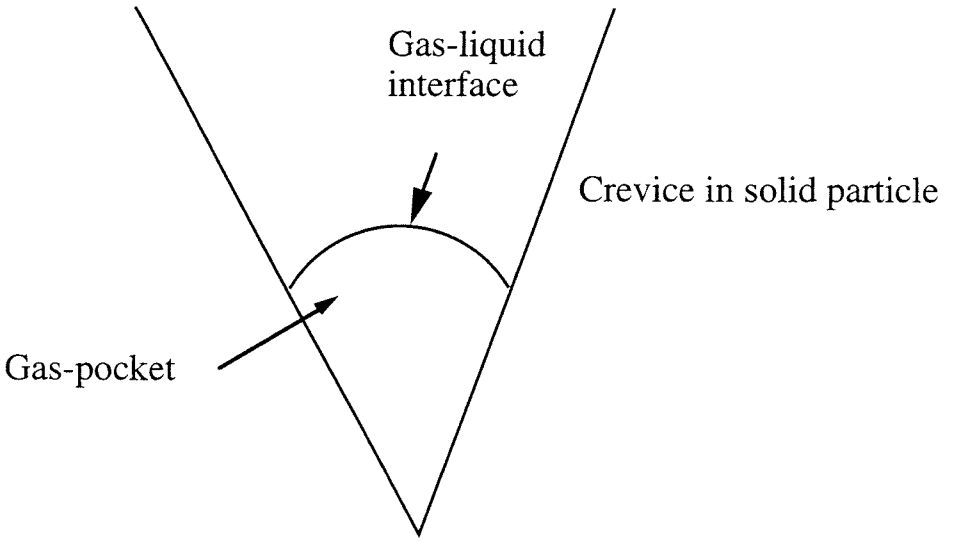

b.

Fig. 1a: Stabilization of a gas-pocket by conical crevice on a solid particle during positive applied pressure to the solution. 1b: Growth of the gas-liquid interface away from the apex during negative applied pressure (tension) on the liquid.

Bulk Solution
T = 298 K
P = 1 atm
No concentration gradients

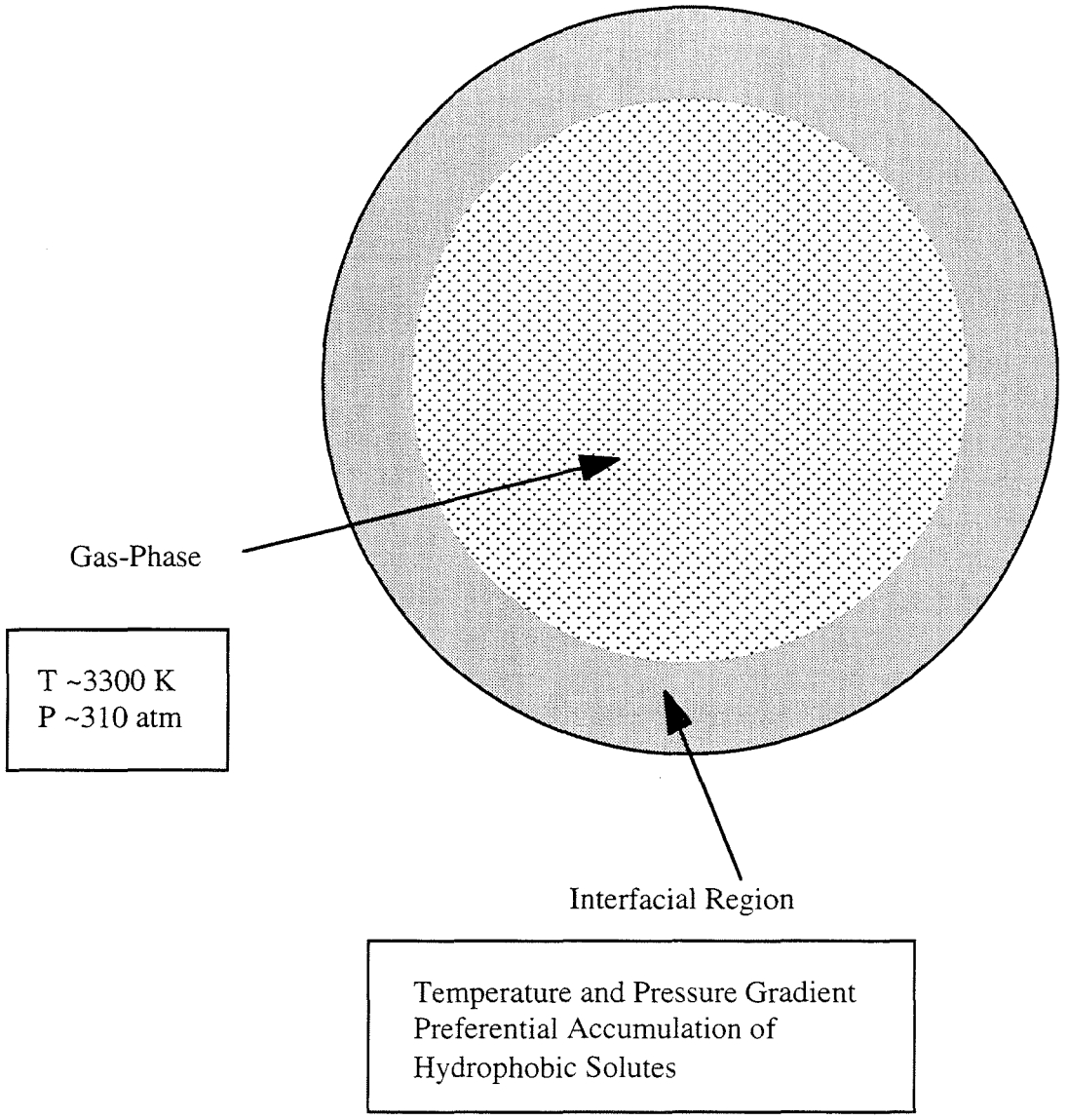

Fig. 2: Schematic of the reactive regions of a cavitation bubble in aqueous solution.

Chapter 2:
The Sonolytic Hydrolysis of *p*-Nitrophenylacetate:
The Role of Supercritical Water

The text of this chapter appears in [Hua, I., Höchemer, R. H., Hoffmann, M R.,*The Journal of Physical Chemistry*, 1995,99, 8, 2335-2342.]

Abstract

Ultrasonic irradiation is shown to accelerate the rate of hydrolysis of p-nitrophenylacetate (PNPA) in aqueous solution at 25 ^{O} C by two orders of magnitude over the pH range of 3 to 8. In the presence of ultrasound, the observed first-order rate constant for the hydrolysis of PNPA is found to be independent of pH and ionic strength with $k_{obs} = 7.5 \times 10^{-4}$ s^{-1} with Kr as the cavitating gas, $k_{obs} = 4.6 \times 10^{-4}$ s^{-1} with Ar as the cavitating gas, and $k_{obs} = 1.2 \times 10^{-4}$ s^{-1} with He as the cavitating gas. The apparent activation parameters for sonolytic catalysis are $\Delta H^{\neq}$(sonified) = 211 kJ/mol, $\Delta S^{\neq}$(sonified) = - 47 J/(mol K), and $\Delta G^{\neq}$(sonified) = 248 kJ/mol. Under ambient conditions and in the absence of ultrasound, k_{obs} is a strong function of pH where $k_{obs} = k_{H_2O}[H_2O] + k_{OH^-}[OH^-]$ with $k_{H_2O} = 6.0 \times 10^{-7}$ s^{-1} and $k_{OH^-} = 11.8$ $M^{-1}s^{-1}$ at 25 ^{o}C. The corresponding activation parameters are $\Delta H^{\neq}$ = 71.5 kJ/mol, $\Delta S^{\neq}$ = -107 J/(mol K) and $\Delta G^{\neq}$ = 155 kJ/mol.

During cavitational bubble collapse high temperatures and pressures exceeding the critical values of water ($T > T_c = 647$ K and $P > P_c = 221$ bar) occur in the vapor phase of the cavitating bubbles and at the interfaces between the hot vapors and the cooler bulk aqueous phase. The formation of transient supercritical water (SCW) appears to be an important factor in the acceleration of chemical reactions in the presence of ultrasound.

The apparent activation entropy, $\Delta S^{\neq}$, is decreased substantially during the sonolytic catalysis of PNPA hydrolysis, while $\Delta G^{\neq}$ and $\Delta H^{\neq}$ are increased. The decrease $\Delta S^{\neq}$ is attributed to differential solvation effects due to the existence of supercritical water (e.g., lower ρ and ε) while the increases in $\Delta G^{\neq}$ and $\Delta H^{\neq}$ are attributed to changes in the heat capacity of the water due to the formation of a transient supercritical state.

A dynamic heat-transfer model for the formation, lifetime and spatial extent of transient supercritical water at cavitating bubble interfaces is presented.

INTRODUCTION

The application of ultrasonic irradiation for the controlled degradation of chemical contaminants in water has been investigated recently using several model compounds (1-5). Upon the passage of ultrasonic waves, water molecules are exposed to alternative compression and rarefaction cycles. During a rarefaction cycle, the liquid density is low enough to form a cavitation bubble containing water vapor, dissolved gases, and high vapor-pressure solutes. During a compression cycle, a pre-existing cavity is compressed resulting in localized high temperatures and pressures. Equations describing the inception and dynamics of a cavitation bubble have been developed (6-8). With these equations, a theoretical temperature of 4200 K and a pressure of 975 atm have been predicted for a collapsing cavitation bubble in an aqueous solution saturated with N_2 (9). Experimental values of P = 313 atm and T = 3360 K have been reported (10). Cavitation temperatures in excess of 5000 K in organic and polymeric liquids have been reported (11,12).

Two distinct sites for chemical reaction exist during a single cavitation event (13). They are the gas-phase in the center of a collapsing cavitation bubble and a thin shell of superheated liquid surrounding the vapor phase. The volume of the gaseous region is estimated to be larger than that of the thin liquid shell by a factor of ~2 x 10^4 (14) in organic liquids.

Chemical transformations are initiated predominantly by pyrolysis at the bubble interface or in the gas-phase, and attack by hydroxyl radicals generated from the decomposition of water. The concentration of $^{\bullet}OH$ at a bubble interface in water has been estimated to be 4 x 10^{-3} M (15). Depending on its physical properties, a molecule can simultaneously or sequentially react in both the gas and interfacial liquid regions.

P-nitrophenol (p-NP) is degraded completely by sonolysis to yield short-chain carboxylic acids, CO_2, NO_3^- and NO_2^- (1). Intermediate products resulting from both

hydroxyl radical attack and thermal bond cleavage are detected. Hydroxyl radical attack on p-NP is thought to occur in a region of the bubble interface with T < 440 K, while pyrolysis occurs in a hotter interfacial region with an average temperature of 900 K (1). On the other hand, H_2S (2) appears to be degraded primarily by pyrolytic decomposition within the compressed vapor phase.

Even though the basic physical and chemical consequences of cavitation are understood, many fundamental questions about the cavitation site in aqueous solution remain unanswered. In particular, the dynamic temperature and pressure changes at the bubble interface and their effects on chemical reactions need to be explored. Since this region is likely to have transient temperatures and pressures in excess of 647 K and 221 bar for periods of microseconds to milliseconds, we propose that supercritical water (SCW) provides an additional phase for chemical reaction. This phase of water exists above the critical temperature, T_c, of 647 K and the critical pressure, P_c, of 221 bar and has physical characteristics intermediate between those of a gas and a liquid (16). The physicochemical properties of water such as viscosity, ion-product, density, and heat capacity change dramatically in the supercritical region (16,17). These changes favor substantial increases for rates of most chemical reactions. SCW has been used in industrial applications such as extraction (18), hydrolysis (19,20) and for environmental applications such as the destruction of hydrocarbons (21), and phenols (22,23).

In this paper, we present experimental results on the kinetics of p-nitrophenylacetate (p-NPA) hydrolysis in support of our hypothesis of the existence of transient SCW during ultrasonic irradiation in water. In addition, we present an elementary heat transfer model for the estimation of the lifetime and spatial extent of supercritical water during cavitational bubble collapse.

EXPERIMENTAL METHODS

Sonication was performed with a direct immersion-probe system (VCX-400 from Sonics and Materials). The irradiation horn was immersed reproducibly (3 cm below the surface) into the sample solution. The average power delivered to the aqueous phase was 115 W, which corresponds to an intensity of approximately 96 W/cm^2. Solutions of 100 μM p-NP were adjusted to pH 4.8-5.2 with phosphoric acid and sonolysis reactions were performed in a modified stainless-steel cell on a total volume of 25 mL. The cell was modified by the addition of stainless-steel gas dispersion and sampling tubes. A small Teflon tube with "luer-lok" connection (Aldrich) was inserted through the sampling tube. The reaction chamber was stirred with a magnetic stirring-bar and stirring motor. Compressed air was blown continuously through the converter to minimize changes in temperature of the piezoelectric crystal. pH was adjusted to the range pH 4.8-5.2 to ensure that all of the p-NP (pK_a = 7.16 at I = 0.05 M) (1) was in the neutral form such that it would preferentially partition to the gas bubble interfaces. The reaction solution was sparged for 15 min at a flow-rate of 10-15 mL/min with the appropriate gas. Constant temperature was maintained with a Haake A80 temperature - control system. The sonicated solution was at 25 °C. 0.5 mL aliquots were withdrawn via syringe through the sampling tube at variable time-intervals. Even though the total reaction volume was not maintained constant during sonication, dV/dt was determined to be small and thus did not have an effect on the value of the measured rate constant. The pH of the sample aliquots was adjusted to ~12 with 5 N NaOH and then filtered through 0.2 μm syringe filters (PFTE, Gelman). The degradation of p-NP was monitored spectrophotometrically at λ = 400 nm (ε = 17,900 M^{-1} cm^{-1}) with an HP8542a UV/VIS Spectrophotometer.

The rates of p-NPA hydrolysis in the absence of ultrasound were determined in a

temperature-controlled optical cell using an HP8450a UV/VIS Spectrophotometer. The appearance of p-nitrophenolate ion was monitored at λ = 360 nm or 400 nm. p-NPA was dissolved in a small volume of methanol before dilution in water; and solutions were used immediately after preparation. The ionic strength was maintained at μ = 0.4 M with NaCl and over the pH range of 2 to 11, three different buffers (i. e., $CH_3COOH/CH_3COO^-, CO_2 \cdot H_2O/CO_3^-$; HCO_3^- / CO_3^{2-}) and concentrations were used at each pH and the observed rate constants were extrapolated to zero buffer concentration to correct for the influence of general acid and base catalysis on the hydrolysis rate. Experiments were carried out in duplicate with an uncertainty of $\leq$ 5 %. The temperature of the solutions was maintained at 25 ^{o} C.

Solutions of 100 μM p-NPA were sonicated and analyzed in an identical fashion as p-NP. However, in the case of the p-NPA, the aliquots were adjusted to pH 7 by the addition of 0.2 mL pH 7 buffer to 0.5 mL of sample. The samples were filtered and the absorbance at λ = 272nm (ε = 8452 M^{-1} cm^{-1}) was measured. The contribution to the absorbance at 272 nm by p-NP (ε=1777 $M^{-1}cm^{-1}$) was subtracted from the total absorbance. The use of methanol as a co-solvent was shown to substantially decrease the observed rate constant. Thus, no further experiments were done with this co-colvent. P-NPA dissolved in water after approximately two hours of stirring and mild heating. The pH dependency of the reaction rate was established by a variation in buffer concentration or by using phosphoric acid. Ionic strength was varied with NaCl. NO_3^- and NO_2^- concentrations were determined by capillary electrophoresis (Dionex Capillary Electrophoresis System I) using a silica column (~60 cm) and a standard method for anion analysis (24).

Water with 18.2 mΩ resistivity (MilliQ UV Plus System) was used in the preparation of all aqueous solutions. P-NP and p-NPA (Aldrich, 99 %+ and 97 % purity respectively) were used without further purification. Phosphoric acid, sodium chloride, and potassium phosphate monobasic were reagent grade and used without further

purification.

RESULTS AND DISCUSSION

Comparative rate thermometry employing p-NP as a probe molecule can be used in order to estimate the effective temperatures achieved during bubble collapse (25). P-NP (1) is a suitable probe molecule since its kinetics and mechanism of degradation are well understood. The primary step during the sonolytic degradation of p-NP has been shown to be (1):

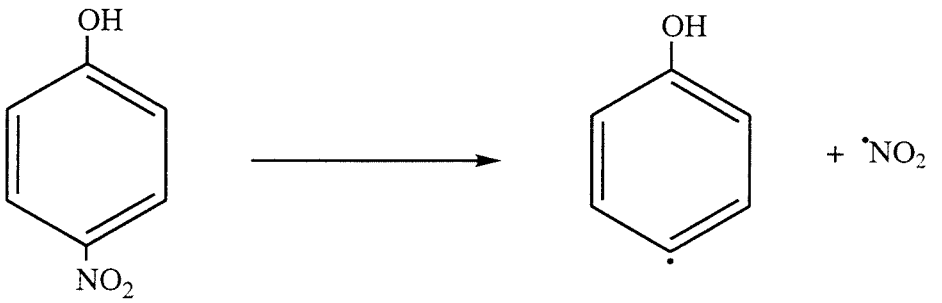

(1)

The activation energy for this pathway of degradation, which involves carbon-nitrogen bond cleavage, can be estimated from shock-tube studies of nitrobenzene decomposition (25). The reaction rate constant for carbon-nitrogen bond-cleavage in nitrobenzene has been determined to be:

$$k = A\exp\left\{\frac{-E_a}{RT}\right\} \qquad (2)$$

where $A = 1.9 \times 10^{15}\ s^{-1}$ and $E_a/R = 33026$ K, and the stoichiometry is given by:

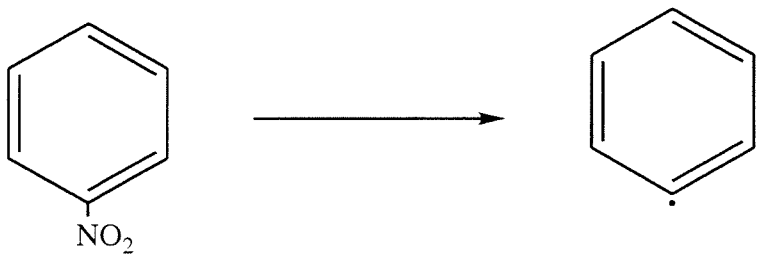

(3)

Using these values for A and E_a/R, we can estimate the effective temperature of the cavitation as follows:

$$T_{eff} = \frac{-E_a / R}{\ln\left(\frac{k}{A}\right)} = \frac{-33026}{\ln\left(\frac{k}{1.9x10^{15}}\right)} \quad [K] \tag{4}$$

The relative temperature of bubble collapse can be adjusted by saturating the solution with gases characterized by substantially different specific heats, thermal conductivities, and solubilities. An important factor controlling bubble collapse temperature is the polytropic factor, K, of the saturating gas (9). From a knowledge of K we can estimate the maximum temperature obtained during bubble collapse from Eq. 5:

$$T_{max} = T_0\left\{(K-1)\frac{P_m}{P}\right\} \tag{5}$$

where T_{max} = temperature of bubble upon collapse, T_0 = temperature of the bulk solution, P = pressure in the bubble at its maximum size (i. e., the vapor pressure of the solvent); P_m = pressure in liquid at moment of transient collapse and $K = C_p/C_v$. The value of K is associated with the amount of heat released from the gas inside the bubble during adiabatic compression. As K increases, the heat released upon bubble collapse also increases. Additional physicochemical properties that may influence the temperature attained during bubble collapse include thermal conductivity, λ, and gas solubility.

Values for the relevant physical properties (26,27) of gases used in this study are listed in Table I.

Thermal conductivities of the dissolved gases have been inversely correlated to sonoluminescence intensity (28) as well as with variable rates of free-radical formation (29,30) during sonolysis. A low thermal conductivity favors high collapse temperatures because the heat of collapse will dissipate less quickly from the cavitation site. Highly soluble gases should result in the formation of a larger number of cavitation nuclei and more extensive bubble collapse since gases with higher solubilities are more readily forced back into the aqueous phase. Thus, a gas with both a low thermal conductivity and high water solubility should yield the highest temperature upon cavitational bubble collapse. Based on physical properties, we predict that krypton will yield the highest rate of p-NP degradation, while helium should yield the lowest relative rate.

The sonolytic degradation of p-NP is found to be a first-order reaction for all gases as shown in Fig. 1. Using the rate constants obtained from this data and Eq. 3 we estimate the effective average temperatures at the interface of the collapsing bubbles for each gas (Table II). The highest effective temperature is achieved in a Kr-saturated solution, whereas a He-saturated solution results in the lowest effective temperature, as predicted above. Although the value of K is similar for all three gases, helium has an unusually high thermal conductivity and a relatively low solubility in comparison to Ar and Kr. Thus, the difference in the resulting effective temperature is also larger than that between Ar and Kr.

Probing for Supercritical Water During Cavitation

Given the typical temperatures and pressures attained during bubble collapse, we postulate the existence of microscopic domains of supercritical water that are continuously variable in time and space. Because of the transient nature of the

supercritical phase, indirect methods are required to determine its existence in an ultrasonically irradiated system. Examination of reaction rate data in the context of activated complex theory (ACT) may give us some indication of a change in the reaction environment. The hydrolysis of p-NPA was chosen as a model reaction to probe for supercritical water at the bubble interface. The reaction is most likely accelerated in that region because the compound is not volatile. Furthermore, the reaction does not involve hydroxyl radical and thus the interpretation of the observed reaction rate constants should not be complicated by formation rates of radicals produced during cavitation. Observed rate constants are highly pH dependent and range from 10^{-6} to 10^{-3} s^{-1} in the pH range 2-10 for this reaction under ambient conditions (Fig. 2). Above pH 6.5, the hydrolysis of p-NPA is base-catalyzed:

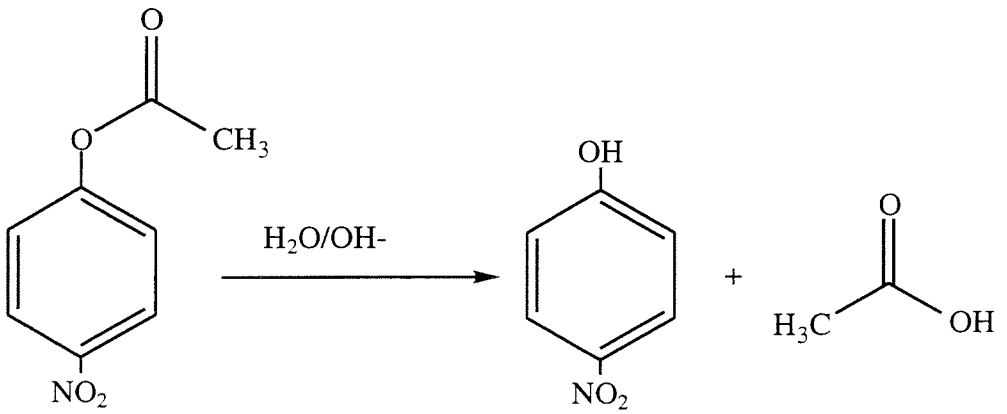

(6)

The rate law for p-NPA hydrolysis is written as:

$$v = k_{obs}\,[\text{p-NPA}] = \frac{-d[\text{p-NPA}]}{dt} \tag{7}$$

where

$$k_{obs} = k_{H_2O}[H_2O] + k_{OH^-}[OH^-] + k_{H^+}[H^+] \tag{8}$$

with $k_{H^+} \approx 0$.

The pH dependency of the control reaction is shown in Fig. 2.

The overall first-order rate constant for p-NPA hydrolysis contains two terms that account for the uncatalyzed reaction with water and for the base - catalyzed pathway. Under normal conditions, the concentration of the water and OH^- (at a constant pH) remain constant and thus the overall rate constant is treated as a pseudo-first order constant. The observed rate constants were found to be $k_{H_2O} = 6.0 \times 10^{-7}\ s^{-1}$ and $k_{OH^-} = 11.8 \pm 0.5\ M^{-1}s^{-1}$ and were determined from standard analysis of spectrophotometric data as a function of time.

The sonolytic acceleration of p-NPA hydrolysis has been reported previously by Kristol (31). He noted that several esters with widely different activation energies showed approximately the same relative enhancements in hydrolysis rates in the presence of ultrasound. Esters with substantially different activation energies for hydrolysis should show different relative rate enhancements, if these apparent enhancements were due only to the very high microscopic temperatures generated by cavitational bubble collapse. Our basic hypothesis, in this case, is that a change in the thermodynamics of the formation of the activated complex may account for changes in the observed reaction rates and reflect a change in either the microscopic environment and/or the mechanism. For a bimolecular reaction we can use the following activation parameters:

$$\Delta S^{\neq} = R\left(\ln A - \ln\left(\frac{k_B T}{h}\right) - 1\right) \tag{9}$$

$$\Delta H^{\neq} = E_a - RT$$

$$\Delta G^{\neq} = \Delta H^{\neq} - T\Delta S^{\neq} \qquad (11)$$

to characterize the overall rate of reaction, where E_a is the intrinsic activation energy, A is the pre-exponential factor, R = 8.31 J mol^{-1} K^{-1}, k_B = 1.38 x 10^{-23} J K^{-1} and h = 6.626 x 10^{-34} J s. E_a and A are determined experimentally from kinetic data.

The measured rate constant for hydrolysis of p-NPA at the bubble interface should be different from the rate constant determined from analysis of the bulk solution since the solution is not homogeneous. In order to determine a rate constant that is as close as possible to the intrinsic rate constant at the bubble interfaces, several other bulk solution parameters must be considered, including ionic-strength, co-solvent effects, and pH.

Given that the interface between the hot gas in the bubble and the surrounding cooler liquid is hydrophobic (32), organic compounds will partition to that region much more effectively than ions. Thus, a variation in the ionic strength of the bulk solution should have a negligible influence on the hydrolysis rate constant. As shown in Fig. 3, the observed hydrolysis rate constants do not vary appreciably over a NaCl concentration range of 0.0 and 0.3M.

Methanol, when used as a co-solvent can be present at a large excess compared to p-NPA. Under these conditions, methanol may preferentially accumulate at the bubble interface. In this way, a methanol co-solvent is predicted to slow down the rate of sonolysis of most organic molecules. This prediction is supported by the data shown in Fig. 4 which provides a comparison of the rate constants observed in irradiated solutions in the absence (◊, □) and presence (x, +) of 0.25% (v/v) methanol. The rate constants are found to be significantly larger in solutions that were prepared without methanol.

Over a pH range of 3 to 8, the overall first-order rate constants are essentially invariant in a sonicated solution as shown in Fig. 5. This pH-dependency is consistent with the tendency for water in a dense supercritical state to have a higher ion activity

product relative to normal-phase water; a higher value for K_W should result in a higher concentration of both OH^- and H^+ for a given set of conditions. Thus, we expect that the $k_{OH^-}[OH^-]$ term of k_{obs} (Eq. 8) should be enhanced significantly in the presence of transient SCW. Selected properties of supercritical water and water under ambient conditions compared in Table IV.

The optimal set of conditions for determination of intrinsic rate constants proved to be an unbuffered solution of 100 μM p-NPA in the absence of a co-solvent. The amount of NO_2^- and NO_3^- produced during p-NPA sonolysis was insignificant. This indicates that the main reaction pathway for p-NPA was hydrolysis of the ester linkage rather than pyrolytic denitration of the nitro group. Fig. 6 compares the relative values of k_{obs} in the presence of different saturating gases. The hydrolysis rate constants vary from 9.8×10^{-5} s^{-1} to 3.8×10^{-4} s^{-1}, depending on the nature of the dissolved gas.

The uncertainties associated with the calculation of the rate constant for the sonolytic hydrolysis of p-NPA are not large. As shown in Fig. 7, the rate of disappearance of p-NPA in an Ar-saturated solution at pH 6.4 and $[p\text{-NPA}]_i$ = 100 μM is reproducible over the course of five repetitions of the experiment. The average value of the rate constant is 1.58 min^{-1} with a standard deviation of 2.2×10^{-4}.

The Arrhenius plots for sonicated and unsonicated solutions are shown in Figs. 8 and 9. Using the overall activation energies determined from these plots, the respective activation parameters can be calculated. As shown in Table III, the activation free energy, $\Delta G^{\neq}$, for hydrolysis appears to increase in the sonicated system compared to the unsonicated solution primarily due to an increase in the value of $\Delta H^{\neq}$. The higher value of $\Delta H^{\neq}$ in the sonicated system may result in part from its correlation with heat capacity which is a function of temperature. The heat capacity of water greatly increases in the supercritical regime (13) and thus may contribute to an increase in $\Delta H^{\neq}$ during sonolysis. However, the corresponding reaction rate constant is also higher because of the net effect of an increasing effective reaction temperature. On the other hand $\Delta S^{\neq}$ for hydrolysis

appears to decrease in the presence of ultrasound. The apparent change in $\Delta S^{\neq}$ can be explained by considering changes in both the transition state and reactant interactions with the solvent, which are affected by the lower density and dielectric constant of the supercritical phase. Because the solute molecules are further apart in the supercritical domain, fewer are available for solvation of the polar transition state compared to the number which can cluster near the transition state in water at its normal density. In addition, the lower dielectric constant implies that when the organic solute is introduced into the supercritical phase, disruption of the solvent structure should be less compared to the disruption in the hydrogen bonds when an organic solute is introduced into liquid water.

MODEL FOR FORMATION OF THE TOTAL AMOUNT OF SUPERCRITICAL WATER DURING SONOLYSIS

In light of the above results, we now proceed to estimate the fraction of an individual cavitating bubble, and total fraction of a cavitating solution, that is in the transient supercritical regime.

Flint and Suslick (12) and Sehgal et al. (10) have clearly demonstrated that temperatures and pressures within a collapsing cavitation bubble exceed the critical point of water. Based on previously estimated temperatures within a collapsed bubble and a smaller layer of surrounding liquid (33), we now attempt to describe the spatial and temporal temperature distribution around a bubble just after its collapse. In order to obtain a simple first-order approximation of the heat transport from the interior of a hot bubble to the surrounding bulk liquid we need to make several severe assumptions. Thus, we caution that this model should be viewed as a qualitative estimation rather than a precise description of the real physical phenomenon. Our goal is to show qualitatively, conditions occur around a collapsed bubble that are in accord with existence of

supercritical water as suggested by our experimental results and to estimate the total volume of supercritical water present in a typical solution exposed to ultrasound.

The hydrodynamic life of the bubble before collapse is excluded from this analysis. Thus, we assume that the collapsed bubble is an instantaneous point source of heat embedded in an infinite matrix at ambient temperatures, as shown in Fig. 10. Furthermore, we assume that conduction provides the only means of heat transfer, and thus we ignore heat transport by convection and radiation. We also assume that the bubble retains its spherical shape after collapse. The heat capacity, thermal conductivity and density of the collapsed bubble are assumed to be the same as of the surrounding water at room temperature. In addition we assume that a uniform temperature is attained within the bubble immediately after collapse.

The following values for the physical properties of liquid water at 303 K are used in the calculation. The heat capacity, C_p, 4178.4 J/kg K, the thermal conductivity, λ, 0.6154 J/s m K, the density, ρ, 995.65 kg/m^3 were taken from the Handbook of Chemistry and Physics (34). The initial radius, a = 150 μm and the initial temperature of the collapsed bubble, T_0 = 5000 K have previously been estimated by Suslick (12,33). The temperature of the water surrounding the collapsed bubble, T_{med} = 300 K.

Given all these assumptions, we can write the heat transport equation as

$$\frac{\partial T}{\partial t} = k\nabla^2 T \tag{13}$$

where the thermal diffusivity, k, in units of [m^2/s] is given as $\lambda/(\rho\, C_p)$. The Laplacian, written in spherical polar coordinates

$$\nabla^2 = \frac{1}{r^2}\frac{\partial}{\partial r}\left[r^2\frac{\partial}{\partial r}\right] + \frac{1}{r^2\sin\theta}\frac{\partial}{\partial\theta}\left[\sin\theta\frac{\partial}{\partial\theta}\right] + \frac{1}{r^2\sin^2\theta}\frac{\partial^2}{\partial\phi^2} \tag{14}$$

can be simplified, since we have assumed that the collapsed bubble retains its spherical shape and that it has a uniform initial temperature T_0. The resulting temperature distribution, T(r), is, therefore, only a function of the distance from the bubble center and is independent of the angles θ and ϕ. With these assumptions we can write:

$$\frac{1}{k}\frac{\partial T}{\partial t} = \frac{\partial^2 T}{\partial r^2} + \frac{2}{r}\frac{\partial T}{\partial r} \tag{15}$$

For the initial conditions, $T = T_0$, for $t = 0$, $0 < r < a$ and $T = T_{med}$, for $t = 0$, $r > a$ and the boundary condition T = finite, for $r = 0$, the solution to Eq. 14 is given (35,36) as:

$$T_{red} = \frac{1}{2}\left[\operatorname{erf}\left(\frac{\frac{r}{a}+1}{2\sqrt{k\frac{t}{a^2}}} \right) - \operatorname{erf}\left(\frac{\frac{r}{a}-1}{2\sqrt{k\frac{t}{a^2}}} \right) \right] \ldots$$

$$\ldots - \frac{a}{r\sqrt{\pi}}\sqrt{k\frac{t}{a^2}}\left[\exp\left(-\left(\frac{\frac{r}{a}-1}{2\sqrt{k\frac{t}{a^2}}} \right) \right) - \exp\left(-\left(\frac{\frac{r}{a}+1}{2\sqrt{k\frac{t}{a^2}}} \right) \right) \right] \tag{16}$$

where the error function is given by

$$\operatorname{erf}(x) = \frac{2}{\sqrt{\pi}}\int_0^x \exp\left[-y^2\right] dy \tag{17}$$

while the reduced temperature is defined as

$$T_{red} = \frac{T - T_{med}}{T_0 - T_{med}} \tag{18}$$

In Eq. 17 T_0 is the initial temperature of the collapsed bubble, T_{med} is the initial temperature of the surrounding water, T_{red} is the reduced temperature as a function of the distance from the center of the bubble, r, at an elapsed time, t. The actual temperature can be calculated from the definition of the reduced temperature. In Fig. 11 we show a plot of T_{red} versus r/a, obtained from the numerical solution of Eq. 15. The maximum radius of a shell around the collapsed bubble with a temperature exceeding the critical value T_c = 647 K can also be calculated for each given time interval after collapse. The times and corresponding reduced distances are given in Table V. The estimated lifetime and spatial extent of the supercritical phase at a single cavitation site are on the order of milliseconds and microns. After 10 msec the radius of the supercritical region around a collapsed bubble extends about 40 % farther into the bulk solution than the original cavity. The radius of the supercritical shell expands up to 160 % of the original bubble radius at 50 msec after collapse.

We can also estimate the fraction of the total volume of a sonified aqueous solution that is actually in the supercritical state. The volume $V_{shell}(t_i)$ of the hot layer, where $T > T_c$, around a collapsed cavity can now be calculated as a function of time.

$$V_{shell}(t_i) = \frac{4}{3}\pi a^3\left[\left(\frac{r(t_i)}{a}\right)^3 - 1\right] \tag{19}$$

If N is the number of cavities that collapse per unit volume per unit time, the fraction of the aqueous solution that is in the supercritical state, x_{scw}, is given as

$$\frac{V_{scw}}{V_{total}} \equiv x_{scw} = N\sum_i V_{shell}(t_i)\left[t_i - t_{i-1}\right] \tag{20}$$

The number density of nuclei and their size distribution has been measured by Katz and Acosta (37). However there are no experimental data for the number density of nuclei or

actual cavitation bubbles in water during ultrasonic irradiation. Suslick and Hammerton (14) give an estimate for the number of collapsing bubbles per time and volume. If we use their estimate of $N = 4 \times 10^8$ $sec^{-1}m^{-3}$, we determine that $x_{scw} = 0.0015$.

Our simple model predicts that approximately 0.15 percent of the irradiated water is in the supercritical state at any point in time. Depending on the extent to which supercritical water accelerates chemical reactions, this fraction may represent a substantial contribution to reaction rate enhancements that have been reported previously for chemical reactions in the presence of ultrasound.

Conclusions

p-NPA hydrolysis in an ultrasonically irradiated solution exhibits an observed rate constant which is enhanced by about two orders of magnitude in comparison to the same hydrolysis under ambient conditions at 25 ^oC (as indicated when Figs. 2 and 5 are inspected). Furthermore k_{obs} is found to be relatively insensitive to the solution pH in the presence of ultrasound while k_{obs} under ambient conditions is a strong function of pH, i. e., $k_{obs} = k_o + k_{OH^-}[OH^-]$. The latter result is distinct from that observed in unsonified solutions and suggests that the reaction rate enhancement occurs at the cavitation bubble interface. Both the enhanced hydrolysis rate and its pH independence may be explained by the existence of supercritical water around the collapsing cavitation bubbles. Hydrolysis may be accelerated, in part, by a higher concentration of OH^- at the hot bubble interface, which results from the higher ion-product, K_w, of SCW. The apparent decrease of $\Delta S^{\neq}$ in the presence of ultrasound suggests that the rate enhancement might be due to a physical change in the microscopic environment surrounding the substrate. In addition to our experimental evidence, a simple heat transfer model predicts that approximately 0.15% of the irradiated water is in the supercritical state at any point in time, giving further evidence for the proposed existence of SCW in cavitating aqueous

solutions. Based on these experimental findings and our semi - quantitative calculations, we argue that supercritical water represents a potentially important component of sonochemistry, in addition to the free-radical reactions and thermal/pyrolytic effects (1-3) that have been demonstrated previously.

The existence of the SCW phase during acoustic cavitation has significant implications for hydrolysis reactions of environmental interest. Because the reaction occurs at or close to the bubble/water interface, compounds more hydrophobic than p-NPA are expected to exhibit even higher hydrolysis rate enhancements because the compound that is concentrated around the bubble will, once the bubble collapses, be embedded in supercritical water. The sonolysis of parathion at 25 ^{o}C results in complete hydrolysis within 30 min (3), whereas at 20 ^{o}C and pH 7.4 the non-catalyzed hydrolysis has a half-life of 108 days (38).

Finally, the existence of the supercritical phase in an ultrasonically irradiated solution suggests a modification of the conventional view of the reactive area at a cavitation site. This region is normally considered to consist of two discrete phases: a high temperature, low density gas phase, and a more condensed and lower temperature liquid shell. An alternative description would include a structural change of the collapsing bubble due to the existence of SCW with properties more characteristic of water vapor than liquid water. The presence of SCW in a collapsing bubble may help to explain the observed fragmentation of a single bubble into a bubble cloud consisting of many smaller bubbles (39).

The application of SCW oxidation to wastewater treatment has been investigated in recent years (21-23). One drawback of the large scale application of SCW oxidation is the inherently aggressive nature of water in the supercritical state, which results in extensive corrosion of reaction vessels. Corrosion of the reactor chamber lessens the economic feasibility of this method. We believe that the treatment of hazardous organic compounds with ultrasound could be a possible alternative to oxidation processes in bulk

supercritical water. Due to the local confinement of supercritical water as generated during the collapse of gas cavities, the bulk solution remains at ambient pressures and temperatures, thus avoiding extensive damage to the reaction vessel.

Acknowledgments: The authors are grateful to EPRI (contract # RP8003-36) and ARPA (Grant # NAV 5HFMN N0101492J1901) for generous financial support. We appreciate the support and encouragement of Drs. Ira Skurnick and Myron Jones and the helpful discussions provided by Professor Kenneth Suslick.

References

1. Kotronarou, A.; Mills, G.; Hoffmann, M. R., *J. Phys. Chem.*, **1991**, *95*, 3630-3638.

2. Kotronarou, A.; Mills, G.; Hoffmann, M. R., *Environ. Sci. Technol.*, **1992**, *26*, 2420-2428.

3. Kotronarou, A.; Mills, G.; Hoffmann, M. R., *Environ. Sci. Technol.*, **1992**, *26*, 1460-1462.

4. Petrier, C.; Micolle, M.; Merlin, G.; Luche, J. L.; Reverdy, G., *Environ. Sci. Technol.*, **1992**, *26*, 1639-1642.

5. Wu, J. M., Huang, H. S., Livengood, C. D., *Environ. Prog.*, **1992**, *11*, 195-201.

6. Rayleigh, L., *Philos. Mag.*, **1917**, *34*, 94-98.

7. Noltingk, B. E., and Neppiras, E. A., *Proc. Phys. Soc. B. (London)*, **1950**, *63B*, 674-685.

8. Neppiras, E. A., Noltingk, B. E., *Proc. Phys. Soc. B (London)*, **1951**, *64B*, 1032-1038.

9. Mason, T. J.; Lorimer, J. P. *Sonochemistry: Theory, Applications and Uses of Ultrasound in Chemistry*; Ellis Horwood Ltd.: Chichester, 1988, pp. 252.

10. Seghal, C., Steer, R. P., Sutherland, R. G., Verrall, R. E., *J. Chem. Phys.*, **1979**, *70*, 2242-2248.

11. Flint, E. B., Suslick, K. S., *J. Am. Chem. Soc.*, **1989**, *111*, 6987-6992.

12. Flint, E. B.; Suslick, K. S., *Science*, **1991**, *253*, 1397-1399.

13. Gutiérrez, A., Henglein, A., Fischer, Ch.-H., *Int. J. Radiat. Biol.*, **1986**, *50*, 313-

321.

14. Suslick, K. S., Hammerton, D. A., *IEEE Trans Ultrasonics Ferroelec Freq. Contr.*, **1986**, *UFCC-33*, 143-147.

15. Gutiérrez, M., Henglein, A., Ibañez, F., *J. Phys. Chem.*, **1991**, *95*, 6044-6047.

16. Shaw, R. W., Brill, T. B., Clifford, A. A., Ecker, C. A., Franck, E. U., *Chem. Eng. News*, **1991**, *69*, 26-39.

17. Marshall, W. L., Franck, E. U., *J. Phys. Chem. Ref. Data*, **1981**, *10*, 295-304.

18. Li, L. L., Egiebor, N. O., *Energy and Fuels*, **1992**, *6*, 35-40.

19. Lee, D. S., Gloyna, E. F., *Environ. Sci. Technol.*, **1992**, *26*, 1587-1593.

20. Klein, M. T., Mentha, Y. G., Torry, L. A., *Ind. Eng. Chem.*, **1992**, *31*, 182-187.

21. Townsend, S. H., Abraham, M. A., Huppert, G. L., Klein, M. T., Paspek, S. C., *Ind. Eng. Chem. Res.*, **1988**, *27*, 143-149.

22. Yang, H., Eckert, C. A., *Ind. Eng. Chem. Res.*, **1988**, *27*, 2009-2014.

23. Thornton, T. D., LaDue, III, D. E., Savage, P. E., *Environ. Sci. Technol.*, **1991**, *25*, 1507-1510.

24. Harrold, M. P., Wojtusik, M., Riviello, J., Henson, P., *J. Chrom.*, **1993**, *640*, 463-471.

25. Tsang, W., Robaugh, D., Mallard, G. W., *J. Phys. Chem.*, **1986**, *90*, 5968-5973.

26. Kaye, G. W. C., Labye, T. H. *Tables of Physical and Chemical Constants and Some Mathematical Functions;* 14 ed.; Longman Group Limited: London, 1973, pp. 386.

27. Braker, W., Mossman, A. *Gas Data Book;* 6 ed.; Matheson Gas Products Inc.:

Secaucus, NJ, 1980.

28. Young, F. R., *J. Acoust. Soc. Am.,* **1976**, *60*, 100-104.

29. Kondo, T., Kirschenbaum, L. J., Kim, H., Riesz, P., *J. Phys. Chem.,* **1983**, *97*, 522-527.

30. Makino, K., Mossoba, M., Riesz, P., *J. Phys. Chem.,* **1983**, *87*, 1369-1377.

31. Kristol, D. S., Klotz, H., Parker, R. C., *Tett. Letts.,* **1981**, *22*, 907-908.

32. Henglein, A., Kormann, C., *Int. J. Radiat. Biol.,* **1985**, *48*, 251-258.

33. Suslick, K. S.; Hammerton, D. A.; Cline, R. E., *J. Am. Chem. Soc.* , **1986**, *108*, 5641-5642.

34. *CRC Handbook of Chemistry and Physics*; 71 ed.; Lide, D. R., Ed.; CRC Press: Boca Raton, 1990.

35. Crank, J. *The Mathematics of Diffusion;* 1 ed.; Clarendon Press: Oxford, 1956, pp. 347.

36. Carslaw, H. S., Jaeger, J. C. *Conduction of Heat in Solids;* 2 ed.; Clarendon Press: Oxford, 1959, pp. 510.

37. Katz, J., Acosta, A., *Appl. Sci. Res.,* **1982**, *38*, 123-132.

38. Faust, S. D., Gomaa, H. M.,, *Environ. Lett.,* **1972**, *3*, 171-201.

39. Neppiras, E. A., Coakley, W. T., *J. of Sound and Vibration,* **1976**, *45*, 341-373.

Figure Captions

Figure 1: First-order plot of p-NP degradation in a sonicated solution with different saturating gases. Rate constants in units of [s^{-1}]: a) Kr: 7.5 x 10^{-4}, b) Ar: 5.2 x 10^{-4}, c) He: 1.4 x 10^{-4}. Also, a = absorbance at 400 nm at time t after start of sonication, and a_i = initial absorbance at 400 nm.

Figure 2: pH dependence of k_{obs} [s^{-1}] for the hydrolysis of p-NPA under ambient conditions.

Figure 3: Effect of ionic strength on hydrolysis kinetics. Initial ester concentration, $[p\text{-NPA}]_i$ = 100 μM.

Figure 4: Effect of co-dissolved methanol on hydrolysis kinetics. Initial ester concentration, $[p\text{-NPA}]_i$ = 100 μM.

Figure 5: p-NPA hydrolysis rate constant as a function of pH during sonolysis. The rate constant, k, is in units of min^{-1}.

Figure 6: First-order plot of p-NPA hydrolysis in a sonicated solution with different saturating gases. Rate constants in units of [s^{-1}]: a) Kr: 3.8 x 10^{-4}, b) Ar: 2.5 x 10^{-4}, c) He: 9.8 x 10^{-5}. Also, a = absorbance at 272 nm at time t after start of sonication, and a_i = initial absorbance at 272 nm.

Figure 7: Reproducibility of p-NPA hydrolysis during ultrasonic irradiation. Ar-saturated solution; $pH_i = 6.4$; $[p\text{-}NPA]_i = 100\ \mu M$. Average value of the rate constant = $1.56 \times 10^{-2}\ min^{-1}$. Standard deviation: $\sigma = 2.2 \times 10^{-4}$. Standard error : $\sigma/\sqrt{N} = 9.8 \times 10^{-5}$. N = 5. The slopes of the curve fits represent the sonolytic hydrolysis rate constants, [min^{-1}].

y = -0.0498 + -0.0156x R= 0.993

y = -0.0449 + -0.0162x R= 0.991

——— y = -0.0383 + -0.0158x R= 0.996

y = -0.0631 + -0.0160x R= 0.988

y = -0.0216 + -0.0158x R= 0.998

Figure 8: Arrhenius plot of hydrolysis rate constants of p-NPA in sonicated solution. Initial pH, $pH_i = 6.1$, initial ester concentration, $[p\text{-}NPA]_i = 100\ \mu M$. k is in units of inverse seconds.

Figure 9: Arrhenius plot of hydrolysis rate constants of p-NPA in unsonicated solutions. Initial pH, $pH_i = 6$. Ionic strength, I = 0.4 M (NaCl). Initial ester concentration, $[p\text{-}NPA]_i = 100\ \mu M$. k is in units of inverse seconds.

Figure 10: Schematic of the heat transfer model with initial conditions

Figure 11: Plot of the reduced temperature, T_{red}, versus the distance from the center of the bubble, r, for various times after bubble collapse.

Table I.

Physical Properties of Selected Gases Used During Sonolysis.

Gas	Polytropic Index, κ	*Thermal Conductivity, λ [mW/m K]	Solubility in Water [m^3/m^3]
Kr	1.66	17.1	0.0594
Ar	1.66	30.6	0.0320
He	1.63	252	0.00860

* @ 600 K

Table II.

Calculated Effective Temperature from Comparative Rate Thermometry With p-NP as Reacting System.

Dissolved Gas	Rate Constant, [s^{-1}]	Calculated Temperature, [K]
Kr	7.5×10^{-4}	779
Ar	$5.2. \times 10^{-4}$	772
He	1.2×10^{-5}	750

Table III.

Thermodynamics of p-NPA Hydrolysis in Sonicated and Unsonicated Solutions.

Thermodynamic Property	Sonicated	Unsonicated
$\Delta S^{\neq}$	-47 J/mol K	-107 J/mol K
$\Delta H^{\neq}$	211 kJ/mol	71.5 kJ/mol
$\Delta G^{\neq}$	248 kJ/mol	155 kJ/mol

*Quantities calculated using representative interfacial temperature of 780 K.

Table IV.

Selected Properties of Different Phases of Water.

Temperature, [K], and Pressure, [bar]	ρ, [g/ml]	ε	log K_w, [mol^2/L^2]	μ, [mPa/s]	Comments
T= 647, P = 221	0.3	~6	*-16.0	~10^2	Critical Point
T = 973, P = 10^4	0.95	~8	*-7.54	~10^2	Supercritical
T = 1073, P = 5 x 10^5	0.7	~20	*-9.05	~10^2	Supercritical
T = 298, P = 1	1	78.5	-14.0	~10^3	Ambient

ρ = density, ε = dielectric constant, K_w = ion-activity product, μ = viscosity

*Calculated from equation in (17). All other values from (16).

Table V.

Reduced radii and volumes of the hot layer around a collapsed cavity and corresponding elapsed times.

No, i	Time elapsed since collapse [msec]	Reduced distance from center, $r(t_i)/a$, with $T > T_c$	Volume of hot shell $V_{shell}(t_i)$ [pL]
0	0	1.000	0
1	1	1.147	7.2
2	2	1.200	10.3
3	5	1.307	17.4
4	10	1.400	24.7
5	15	1.467	30.5
6	30	1.573	40.9
7	50	1.613	45.2
8	70	1.573	40.9
9	90	1.467	30.5
10	110	1.307	17.4
11	120	1.200	10.3
12	130	1.067	3.04

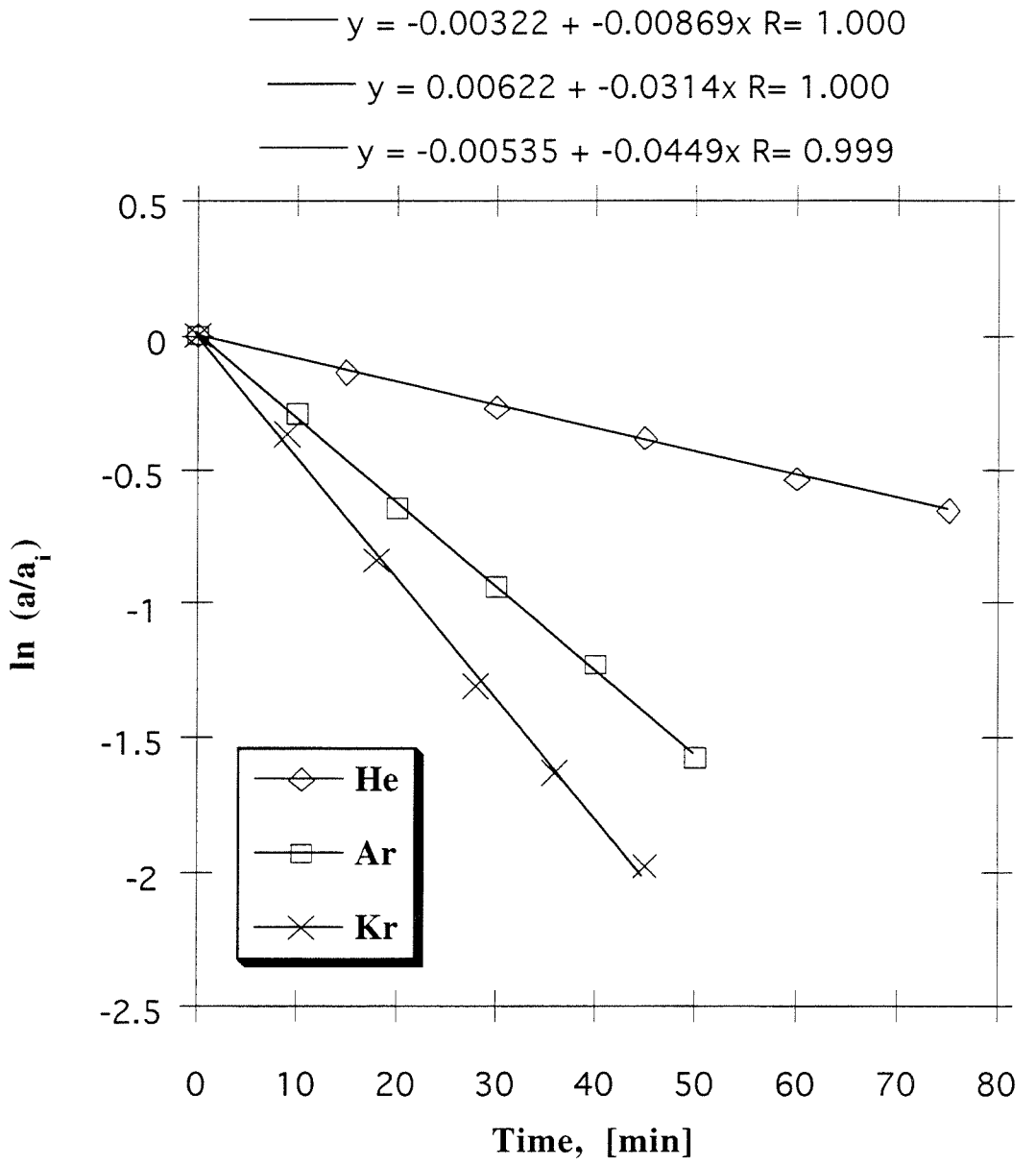

Fig. 1: First-Order plot of p-NP degradation with different saturating gases. Rate constants (s^{-1}): a)Kr: 7.5 x 10^{-4} b)Ar: 5.2 x 10^{-4} c)He: 1.4 x 10^{-4}. a=absorbance at 400 nm at time, t, of sonication. a_i = absorbance at 400 nm, t = 0.

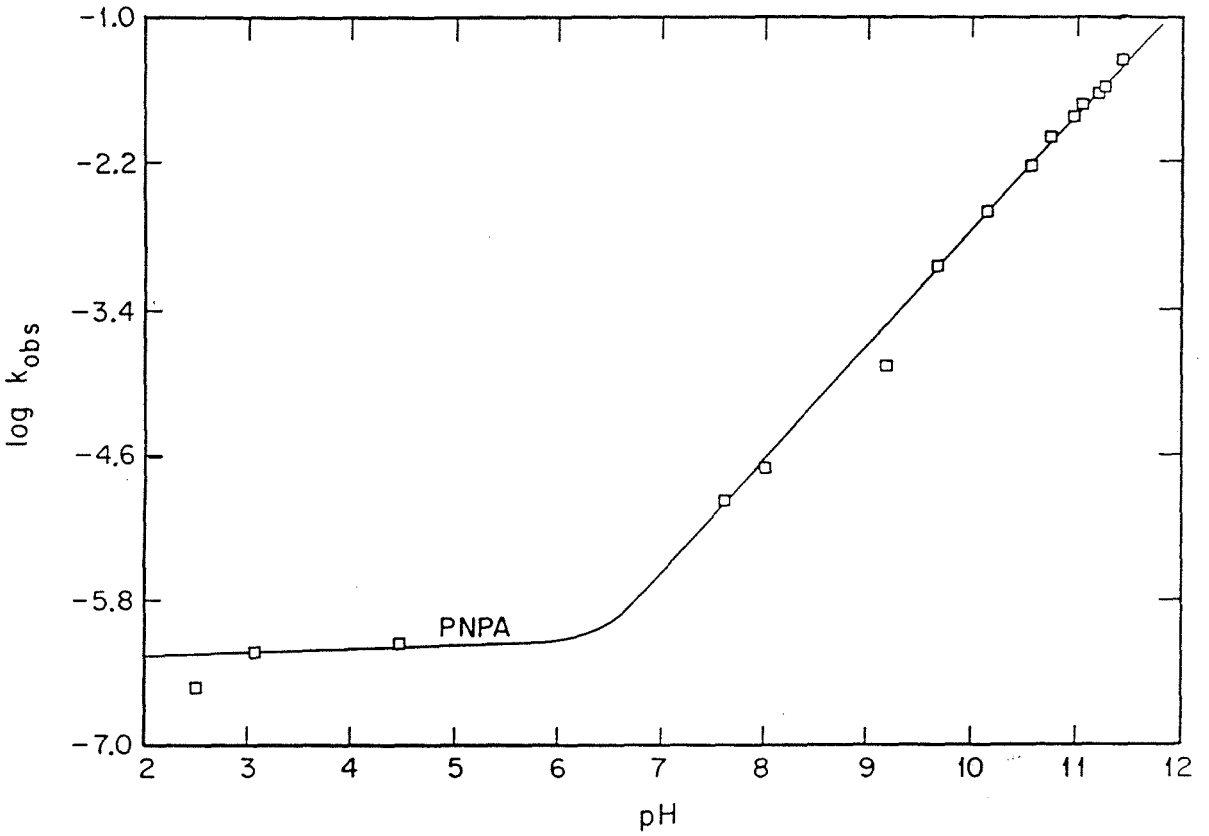

Fig. 2: pH dependence of k_{obs} [s^{-1}] for the hydrolysis of p-NPA under ambient conditions.

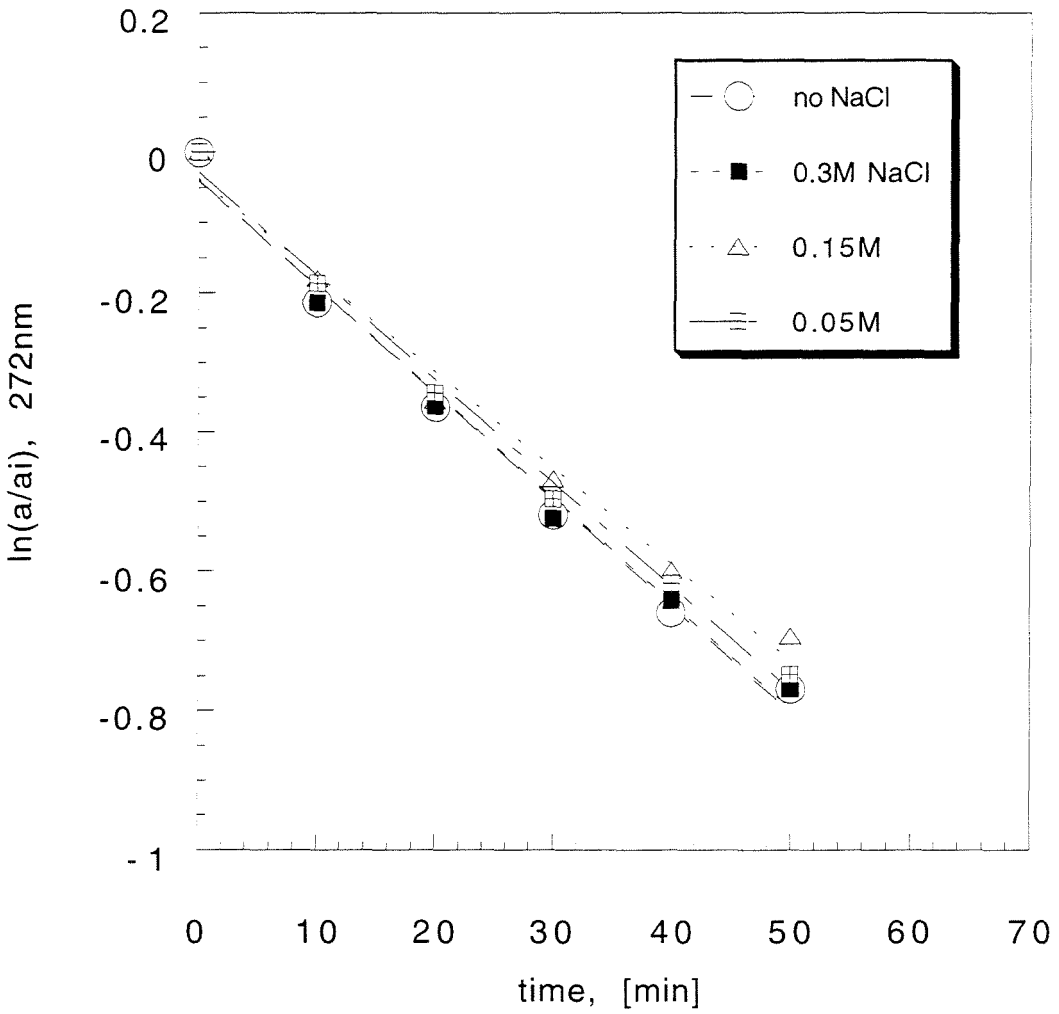

Fig. 3: Effect of ionic strength on hydrolysis kinetics. $[p\text{-NPA}]_i$ = 100 μM and T = 25 °C for all experiments.

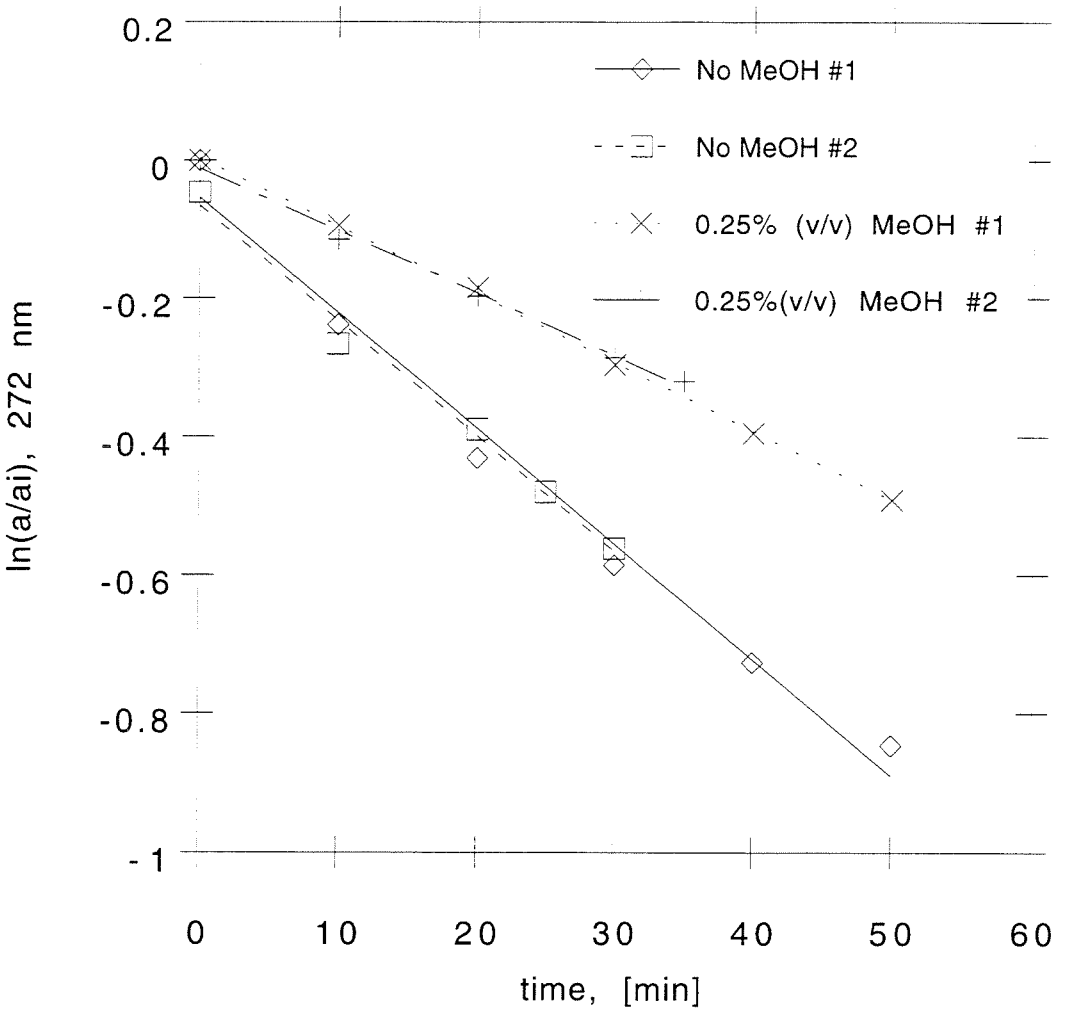

Fig. 4: Effect of co-dissolved methanol on hydrolysis kinetics. $[p\text{-NPA}]_i = 100\ \mu M$. Ar saturated solution.

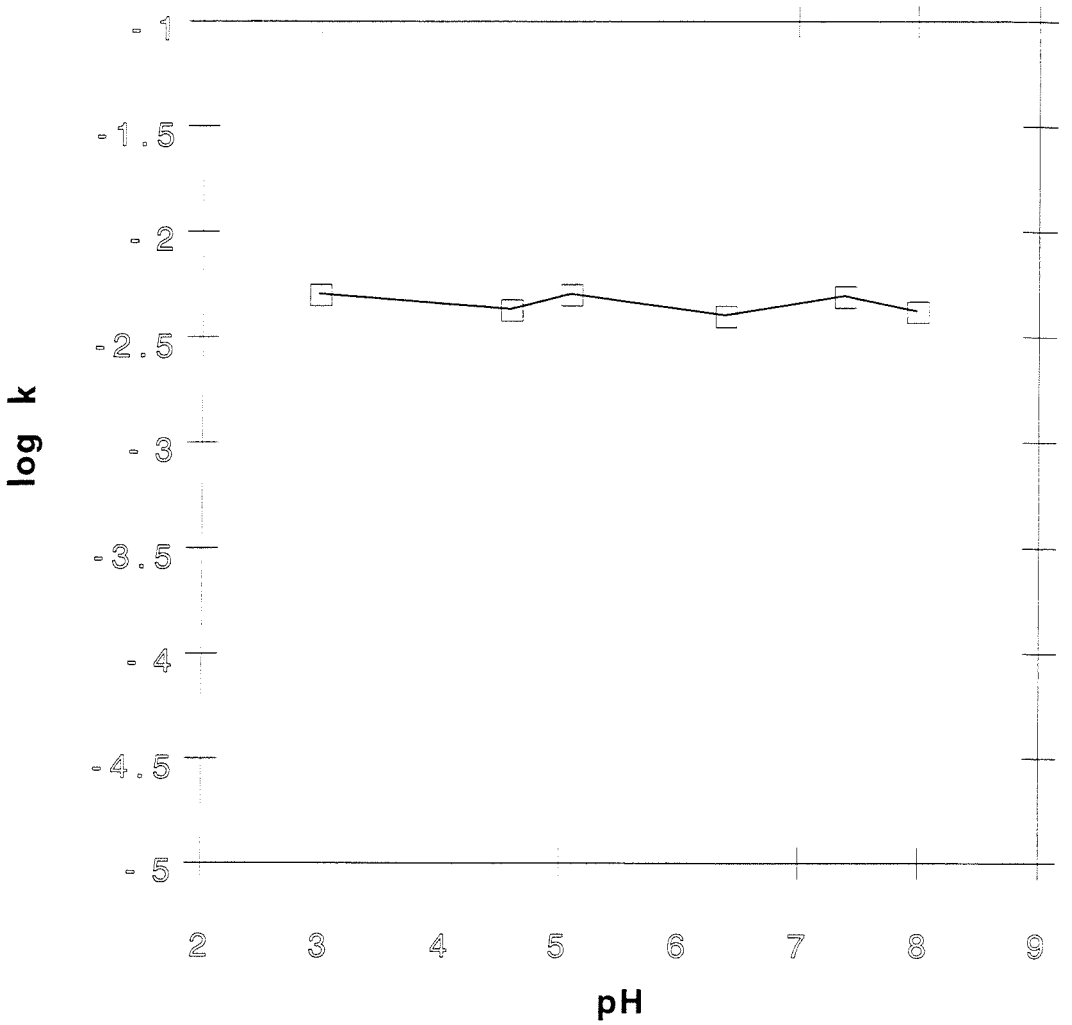

Fig. 5: p-NPA hydrolysis rate constant as a function of pH. The rate constant, k, is in units of min^{-1}.

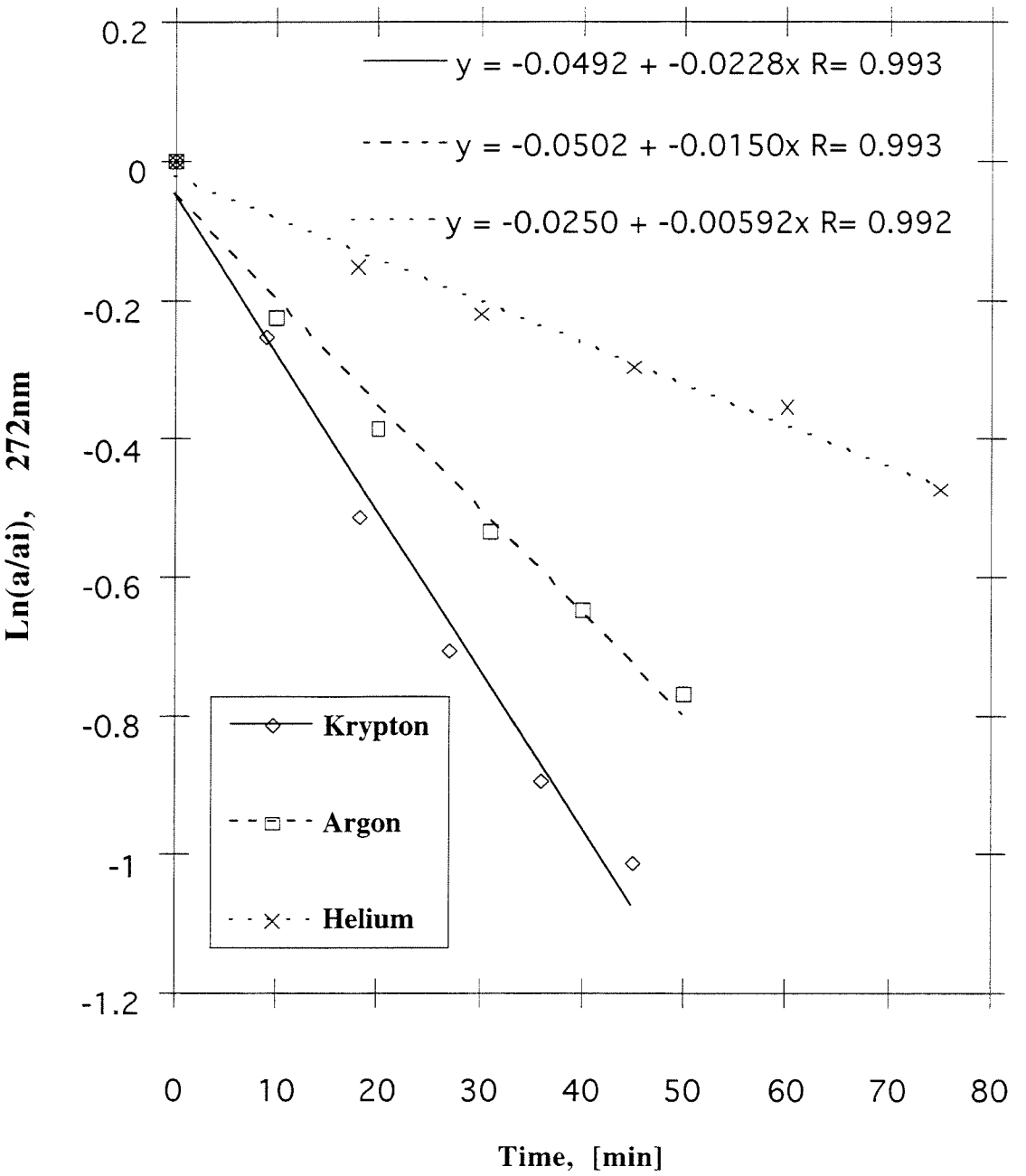

Fig. 6: First order plot of p-NPA hydrolysis in a sonicated solution with different saturating gases. Rate constants (s^{-1}): a)Kr: 3.8 x 10^{-4} b)Ar: 2.5 x 10^{-4} c)He: 9.8 x 10^{-5}. a = absorbance at 272 nm at time, t. a_i = absorbance at 272nm at t=0.

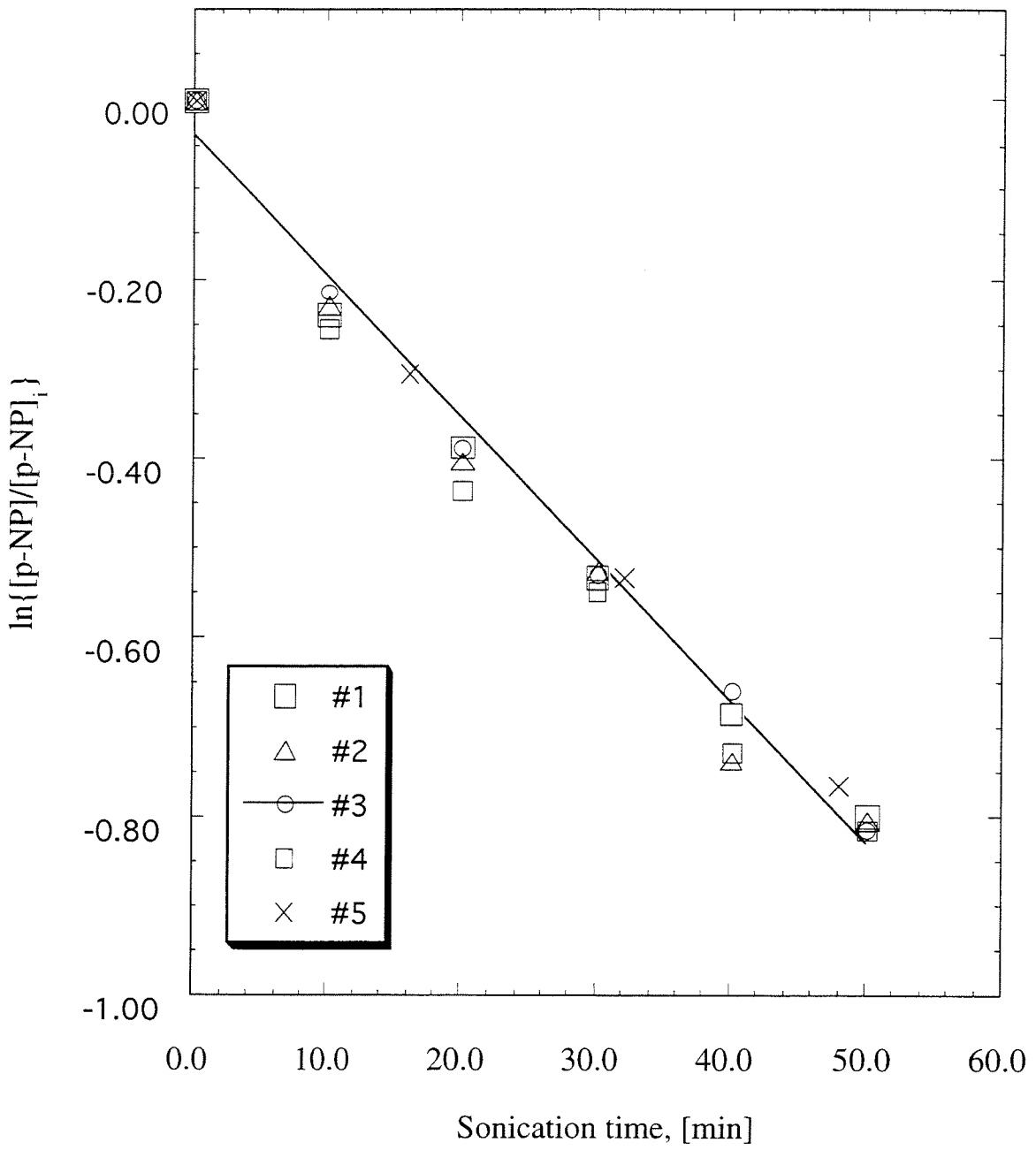

Fig. 7: Reproducibility of p-NPA hydrolysis during ultrasonic irradiation. Ar-saturated solution; $pH_i = 6.4$; $[p\text{-NPA}]_i = 100\ \mu M$. Average value of the rate constant = 1.56×10^{-2} min^{-1}. Standard deviation: $\sigma = 2.2 \times 10^{-4}$. Standard error : $\sigma/\sqrt{N} = 9.8 \times 10^{-5}$. N = 5.

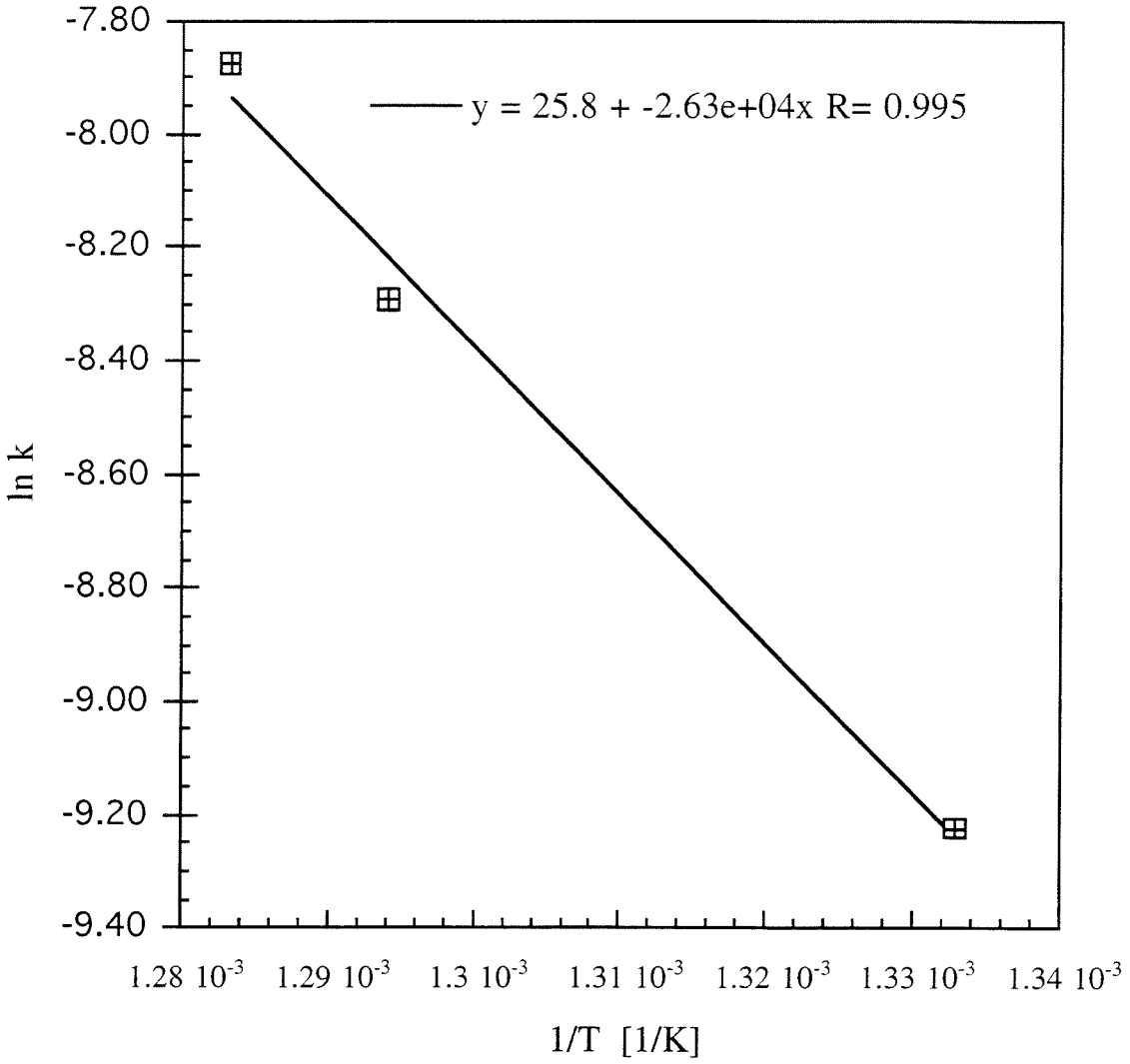

Fig. 8: Arrhenius plot of kinetics of hydrolysis of p-NPA in a sonicated solution. pH_i = 6.1, $[p\text{-NPA}]_i$ = 100 μM. k is in units of inverse seconds.

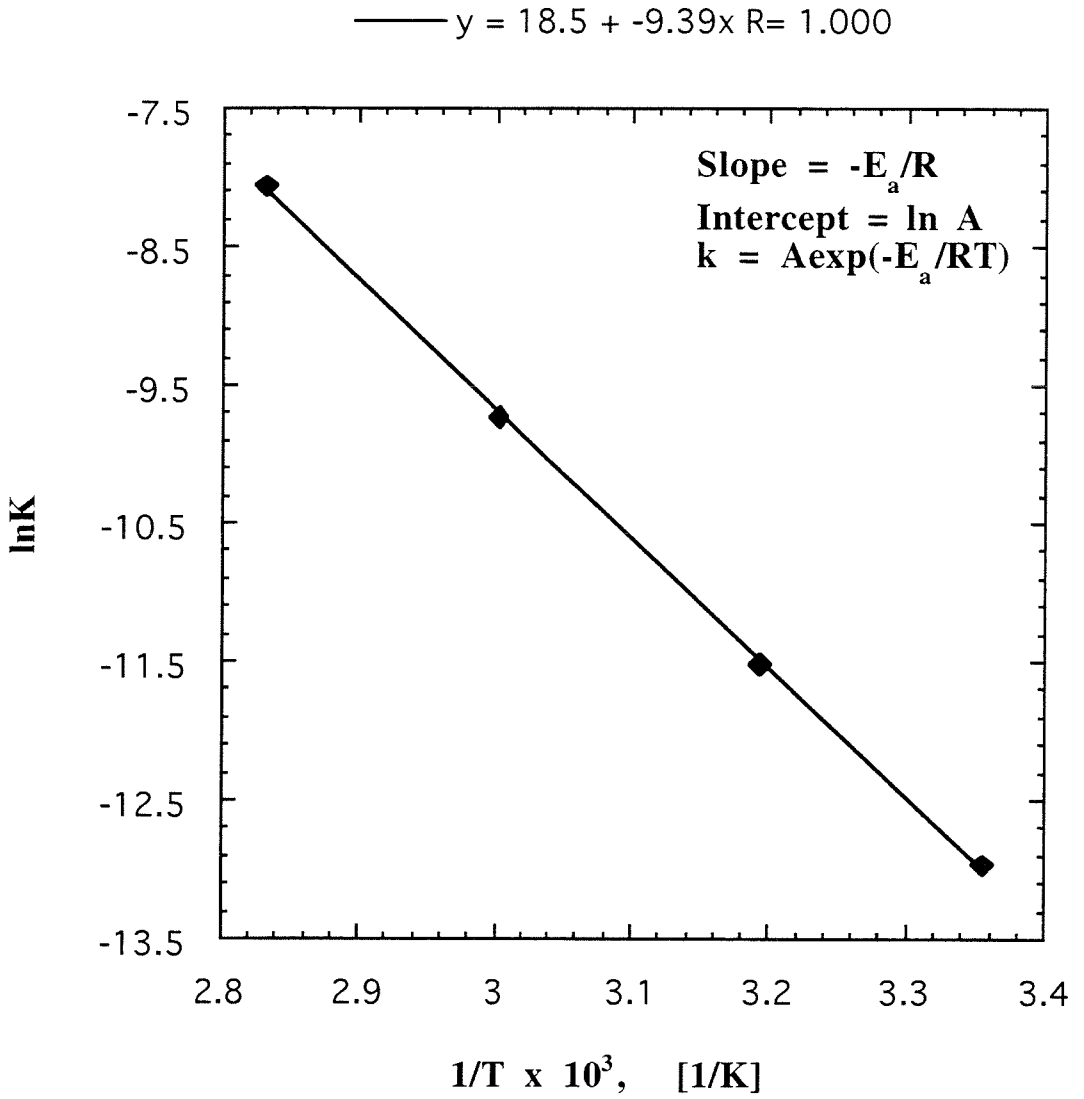

Fig. 9: Arrhenius plot of kinetic data for hydrolysis of p-NPA in an unsonicated solution. $[p\text{-NPA}]_i$ = 100 μM, I = 0.4M (NaCl), pH = 6. k is in units of inverse seconds.

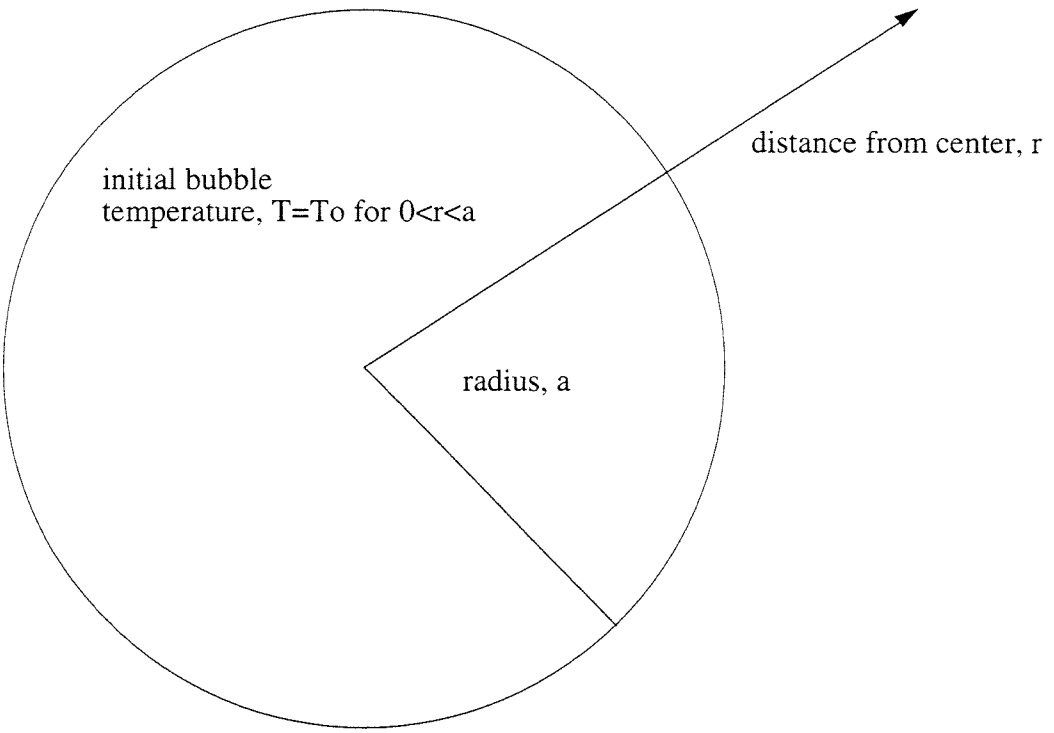

Figure 10: Schematic of the heat transfer model with initial conditions.

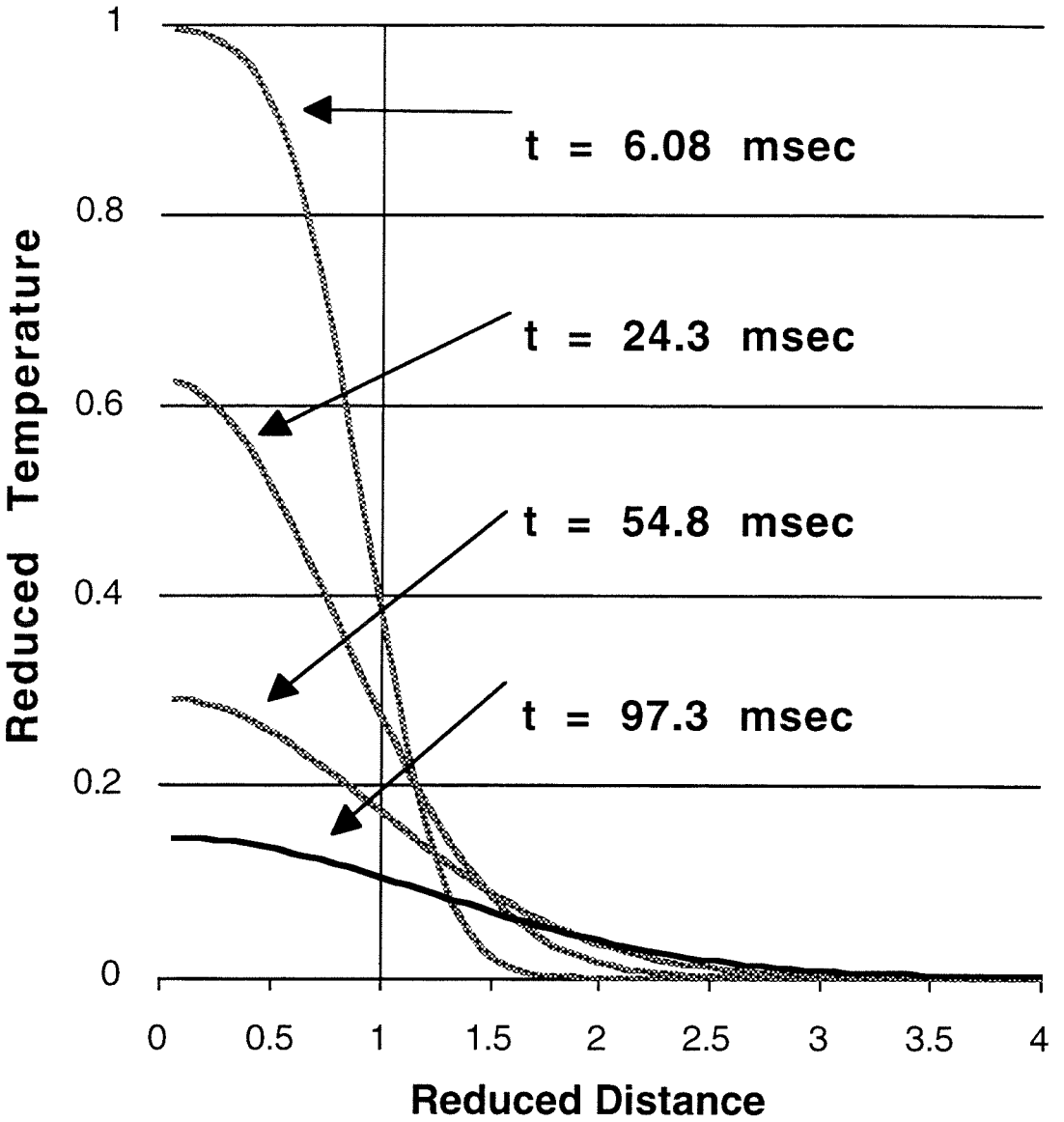

Figure 11: Plot of the reduced temperature, T_{red}, versus the distance from the center of the bubble, r, for various times after bubble collapse.

Chapter 3:

The Sonochemical Degradation of p-Nitrophenol in a Parallel-plate Near-field Acoustical Processor

[Hua, I., Höchemer Ralf H., Hoffmann, M. R., *Environmental Science and Technology*, **1995**, 11, *2790-2796*]

Abstract

The sonochemical degradation of p-nitrophenol (p-NP) in a near-field acoustical processor (NAP) is investigated. The pseudo first-order rate constant, k, for p-NP degradation increases proportionally from $1.00\times10^{-4}s^{-1}$ to $7.94\times10^{-4}s^{-1}$ with increasing power-to-volume ratio (i.e, power density) over the range of 0.98-7.27 W/cm^3. An increase in the power-to-area ratio (i.e., sound intensity), results in an increase in k up to a maximum value of 8.60×10^{-4} s^{-1} at a sound intensity of 1.2 W/cm^2. A mathematical model for a continuous-flow loop reactor configuration is required in order to extract k from the experimentally observed rate constant, k_{obs}, which is a function of the relative volumes of reactor and reservoir.

The nature of the cavitating gas (Ar, O_2) is found to influence the overall degradation rate and the resulting product distribution. The rate constant for p-NP degradation in the presence of pure O_2, $k_{O_2} = 5.19\times10^{-4}s^{-1}$, is lower than in the presence of pure Ar, $k_{Ar} = 7.94\times10^{-4}s^{-1}$. A 4:1 (v/v) Ar/$O_2$ mixture yields the highest degradation rate, $k_{Ar/O_2} = 1.20\times10^{-3}s^{-1}$.

Results of these experiments demonstrate the potential application of large-scale, high power ultrasound to the remediation of hazardous compounds present at low concentrations. The NAP is a parallel-plate reactor which allows for a lower sound intensity but a higher acoustical power per unit volume than conventional probe-type reactors.

INTRODUCTION

The sonochemical degradation of a variety of chemical contaminants in aqueous solution has been previously reported (1-16). Substrates such as chlorinated hydrocarbons, pesticides, phenols, and esters are transformed into short-chain organic acids, CO_2, and inorganic ions as the final products. Time scales of treatment in simple batch reactors are reported to range from minutes to hours for complete degradation (3,4,9). For example, the total elimination of H_2S at pH 7 was achieved within 10 minutes (4) while parathion required 120 min to achieve complete degradation (6). Ultrasonic irradiation appears to be an effective method for the destruction of organic contaminants in water because of localized high concentrations of oxidizing species such as hydroxyl radical and hydrogen peroxide in solution, high localized temperatures and pressures (7,13), and the formation of transient supercritical water (2).

The use of sonochemical reactors for practical waste water treatment applications has not been addressed to date. However, ultrasonic irradiation has been demonstrated to be effective in several industrial processes such as sludge-dewatering (17), coal benefication (18), fossil fuel recovery (19,20), de-foaming (21) and the cleaning of jet-engine parts (18). Martin (22) has identified important design parameters for sonochemical reactors (e.g., volume of the cavitating zone and the liquid flow-rate) and compared the effectiveness of a batch-scale probe reactor with a cylindrical duct reactor for the hydrolysis of methyl benzoate.

In addition to the conventional vibrating probe is another reactor configuration, the near-field acoustical processor (NAP), in which the flowing solution is irradiated between two vibrating, parallel plates. Also in use are pentagonal or hexagonal tube reactors with magnetostrictive transducers mounted on each side of the polygon (23).

In this paper we demonstrate the feasibility of utilizing an alternative reactor geometry for the degradation of chemical contaminants in water. The effects of the ultrasonic power-to-area and power-to-volume densities on the degradation rate of p-nitrophenol (p-NP) and the effects of the physical and chemical properties of dissolved gases are explored. The net energy efficiency of the NAP is compared to a conventional probe reactor.

EXPERIMENTAL METHODS

- Chemical Procedures

p-NP (Aldrich, 99%+), phosphoric acid (EM Science) and NaOH (EM Science) were used as received. Solutions of p-NP were made with water obtained from a MilliQ-UV-Plus System (R = 18.2 MΩ cm^{-1}). All experiments were performed on 3-5 L of 100 μM p-NP in water. The pH was adjusted to the range of 4.5-5.0 with phosphoric acid. Solutions were saturated with the appropriate gas (flow rate 1.9 L min^{-1}) by bubbling the gas through four glass fritted dispersion tubes (Kontes, New Jersey), which were immersed into the liquid, for at least 20 minutes before and during sonication. Ar and O_2 and a mixture of the two gases were used as the saturating gases. The flow rates of O_2 and Ar in the gas mixture were 688 mL min^{-1} and 2434 mL min^{-1}, respectively. The solution temperature within the reactor reservoir was maintained at 22-25 ^oC during the course of sonication. 10 mL aliquots of solutions were removed from the reservoir at appropriate time intervals (ranging from 15 to 60 min) and adjusted to pH 11 with 100 μL of 5N NaOH, filtered through 0.2 μm PFTE filters (Gelman), and analyzed spectrophotometrically (Hewlett-Packard UV/Vis, 8452A). The degradation of p-NP was followed at λ = 400 nm (ε = 17,900 M^{-1} cm^{-1}), and the formation of 4-nitrocatechol (4-NC) was followed at λ = 512 (ε = 12,300 M^{-1} cm^{-1}). The absorbance at λ = 400 nm is

corrected for interference by 4-NC by subtracting the relatively small absorbance due to the by-product ($\varepsilon = 6500\ M^{-1}\ cm^{-1}$) at 400 nm.

- The Near-Field Acoustical Processor (NAP)

In a near-field acoustical processor (Lewis Corporation, Oxford, CT) the vibrational energy is transferred to the reaction mixture via two parallel stainless steel plates which are bolted together (Fig. 1). Each plate is vibrationally driven by seven magnetostrictive transducers that are bonded onto each plate. The transducers convert the electrical energy which is delivered by two power generators, operating at 16 and 20 kHz respectively, into the mechanical energy of vibration. The total sonoactive area is 1261.8 cm^2, and the length and width are 81.25 and 7.76 cm respectively.

A stainless steel spacer is placed between the two vibrating plates, in order to define the reaction volume, V_S. The seal between spacer and plates is provided by a Gore-tex gasket. Spacers of different thicknesses were employed to study the apparent reaction rate as a function of volume (244-1807 mL), and thus at different power-to-volume densities.

Power input into the two frequency generating units was varied from 0 W to 1775 W in order to investigate the dependence of degradation rates on power per area. Due to energy transformation losses within the system, the acoustical power transferred to the reaction mixture is less than the overall power put into the power generators (i.e., the power drawn from the wall supply). Efficiency calculations were based on the total power drawn from the wall outlet. The NAP reactor was maintained at constant temperature (30 ^oC) using a VWR Scientific (Model 1176) refrigeration unit.

Since the NAP system does not allow for direct cooling of the plates and transducers, the reaction mixture flowing through the reactor itself is thermostated externally (Fig. 1). This reactor configuration involves the continuous flow of the reaction solution from the reservoir through the NAP and back into the reservoir. A Pyrex glass

vessel holding up to 8 L of reactant solution is used as reservoir. Stainless steel cooling coils were immersed into the reservoir solution to attain temperature control during sonication. Various ports in the top lid of the reservoir vessel allow for purging of the reaction mixture with the background gases during an experiment as well as sample withdrawal. NAP and reservoir were connected by a corrugated Teflon tubing (3/8'' i.d.). The reaction mixture is continuously circulated through the system via a peristaltic pump (Masterflex, model 7591-50) operating with Viton tubing. Throughout the study a volumetric flow rate of 3.2 L min^{-1} was maintained.

RESULTS

Even though the reactor configuration of Fig. 1 can be viewed as a pseudo-batch reactor, observed kinetic data may depend on the time a given volume element actually resides within the irradiation zone and thus on the relative volume of NAP and its reservoir, and on the actual residence-time distribution (24-26) .

By choosing a flow through mode as opposed to a true batch mode, in which all of the solution would remain in one vessel and is at all times exposed to the ultrasonic irradiation, we introduce several additional reactor parameters. These parameters include the volumetric flow rate, Q, and the volumes of the reservoir, V_R, and the NAP, V_S. In order to obtain empirical rate constants for p-NP degradation that are independent of these three parameters (i.e., to extract first-order rate constants, k, from the observed rate constants, k_{obs}), we need to understand the dynamic behavior of the reactor system. A mathematical model is needed to give the concentration of p-NP as a function of time in both the reservoir and the NAP.

In order to obtain a convenient mathematical description of the reactor system of Fig. 1, we can consider two ideal reactors according to general reactor design principles (24-26). We assume that the reservoir is a continuously stirred tank reactor (CSTR). This

assumption is justified, since the solution in the reservoir vessel is vigorously stirred via a magnetic stirrer during the course of all experiments, ensuring efficient mixing. Control experiments show that there is no degradation occurring in the reservoir; thus it appears to be a perfect mixer without chemical reaction.

For reactions with a kinetic order ≥ 1, the conversion per pass through a reactor is a function of the residence-time distribution. We address this problem by considering the NAP to be two ideal reactors, that exhibit opposite extremes of residence time distributions (i.e., the CSTR and the plug flow reactor, PFR) and incorporate them into two different models. If both modeling approaches predict the same temporal behavior of the p-NP concentration in the reservoir (i.e., the same k_{obs} for a given reaction rate constant, k), then the residence time distribution of the NAP has no important influence on the system dynamics in this particular case and either approach may be used to find the k_{obs} to k conversion factor.

Our first approach is to assume the NAP to be an ideal CSTR (CSTR model) and then assume it to be an ideal PFR (PFR model) and subsequently solve the resulting differential equations for both cases.

- CSTR Model

The mass balance equation for the reservoir is given as

$$\frac{dC_R(t)}{dt} = \frac{Q}{V_R}\left[C_S(t) - C_R(t)\right] \qquad (1)$$

where $C_R(t)$ and $C_S(t)$ are the concentrations of p-NP in the reservoir and in the NAP respectively and Q is the volumetric flow rate of the reaction mixture. Assuming ideal CSTR-behavior, the mass balance equation for the NAP is given as

$$\frac{dC_S(t)}{dt} = \frac{Q}{V_S}\left[C_R(t) - C_S(t)\right] + \nu r(k,c) \tag{2}$$

where V_S is the sonicated volume in the NAP, $\nu = -1$ is the stoichiometric coefficient for the reactant p-NP, and r(k, c) is the first order reaction rate, which is given as:

$$r(k, C_S) = kC_S(t) \tag{3}$$

where k is the intrinsic first-order rate constant for the rate-limiting step in the degradation reaction as shown by (5)

$$HOC_6H_4NO_2 \xrightarrow{k,\Delta} HOC_6H_4O^{\bullet} + NO \tag{4}$$

The initial conditions for Eqns. (1, 2) are given as $C_R(t = 0) = C_S(t = 0) = C_0$.

We can make the problem non-dimensional as follows:

$$\tau \equiv kt, \quad \gamma \equiv \frac{V_S}{V_R}, \quad g \equiv \frac{C_R}{C_0}, \quad f \equiv \frac{C_S}{C_0}, \quad \alpha \equiv \frac{1}{Da} = \frac{Q}{kV_S}, \tag{5}$$

where Da is the Damkoehler number. Da represents the ratio of the mean hydrodynamic residence time, V_S/Q, over the characteristic time constant of the reaction, k^{-1}, under the NAP entrance conditions (24).

With these terms Eqs. (1, 2), can be written in dimensionless form as follows:

$$\dot{g}(\tau) = \gamma\left[f(\tau) - g(\tau)\right] \tag{6}$$

$$\dot{f}(\tau) = \alpha g(\tau) - (1 + \alpha) f(\tau) \tag{7}$$

The dimensionless initial conditions are thereby given as $g(\tau = 0) = f(\tau = 0) = 1$, with the solution for g being

$$g(\tau) = \frac{1}{\lambda_2 - \lambda_1}\left[\lambda_2 \exp(\lambda_1) - \lambda_1 \exp(\lambda_2)\right] \tag{8}$$

and with λ_i given by

$$\lambda_1 = -\frac{\tau}{2}\left[1 + \alpha(1+\gamma) - \sqrt{\alpha^2(1+\gamma)^2 + 2\alpha(1-\gamma) + 1}\right] \tag{9}$$

$$\lambda_2 = -\frac{\tau}{2}\left[1 + \alpha(1+\gamma) + \sqrt{\alpha^2(1+\gamma)^2 + 2\alpha(1-\gamma) + 1}\right] \tag{10}$$

The actual operation conditions for volumetric flow rate, reaction rate constants and volume of NAP and reservoir allow us to simplify Eq.(8). For $\tau \geq \frac{10}{\alpha}$ and $\alpha >> 1$ (i.e. Da << 1) g (i.e., the dimensionless p-NP concentration in the reservoir) can be written in terms of γ:

$$g(\tau) = \exp\left\{-\left(\frac{\gamma}{1+\gamma}\right)\tau\right\} \tag{11}$$

In dimensional form Eq. (11) is given as

$$\frac{C_R(t)}{C_0} = \exp\left[-\left(\frac{V_S}{V_S + V_R}\right)kt\right] \tag{12}$$

where the observed first-order rate constant for p-NP degradation, k_{obs}, given by:

$$k_{obs} = \frac{V_S}{V_S + V_R} k \tag{13}$$

Eq. (13) relates the observed rate constant, k_{obs}, to the intrinsic rate constant in Eq. (4), k.

- PFR Model

Assuming ideal plug-flow behavior for the NAP, its mass balance equation is given by the partial differential equation

$$\left(\frac{\partial C_S(V,t)}{\partial t}\right)_{V=const} = -Q\left(\frac{\partial C_S(V,t)}{\partial V}\right)_{t=const} + vr(V,t) \tag{14}$$

and the mass balance equation for the reservoir is given by Eq. (1).

Using the same dimensionless quantities as above, Eq. (5), and by defining

$$f_\tau(x,\tau) \equiv \left(\frac{\partial f(x,\tau)}{\partial \tau}\right)_{x=const} \text{ and } f_x(x,\tau) \equiv \left(\frac{\partial f(x,\tau)}{\partial x}\right)_{\tau=const} \tag{15}$$

the mass balances for the reservoir and the NAP, Eqns (1, 12), respectively, can be written in dimensionless form as

$$\dot{g}(\tau) = \gamma[f(\tau) - g(\tau)] \tag{16}$$

$$f_x(x,\tau) + Da\, f_t(x,\tau) = -Da\, f(x,\tau) \tag{17}$$

with initial conditions $g(\tau = 0) = f(\tau = 0) = 1$, and the boundary condition of

$f(x,\tau) = g(\tau)$. Employing the method of characteristics, the differential equations can be solved analytically to obtain an expression for g,

$$g(\tau) = e^{-\lambda\tau} \tag{18}$$

where $$\lambda = 1 + \frac{1}{Da}\ln\left(1 + Da\frac{\lambda}{\gamma}\right) \tag{19}$$

For $Da\frac{\lambda}{\gamma} << 1$ we expand Eq. (19) into a MacLaurin series yielding a series expression for λ.

$$\lambda = \frac{\gamma}{1+\gamma} + O(Da) \tag{20}$$

Eq. (18) can be written in dimensional form by substituting Eq. 20 for λ,

$$C_R(t) = C_0 \exp\left[-\left(\frac{V_S}{V_S + V_R}\right)kt\right] \tag{21}$$

The relation between the intrinsic rate constant, k, and the observed rate constant, k_{obs}, is found to be given as:

$$k_{obs} = \frac{V_S}{V_S + V_R}k \tag{22}$$

which is identical to Eq. (13). We conclude, that by assuming the NAP to exhibit ideal PFR-behavior versus ideal CSTR-behavior we do not affect the final mathematical relationship between k_{obs} and k under the given conditions for Da and γ. Therefore, the

interpretation of the present results is possible without incorporating a residence time distribution within the NAP.

The initial reactions (5) in the degradation pathway of p-NP in an ultrasonically irradiated solution are shown below :

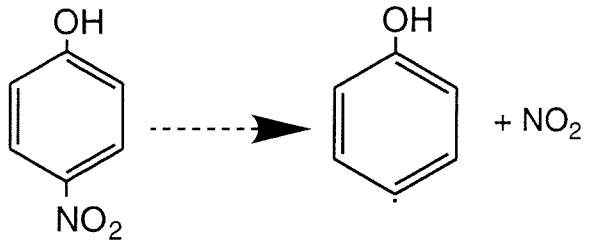

(23)

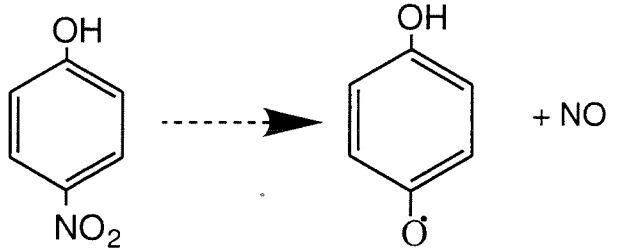

(24)

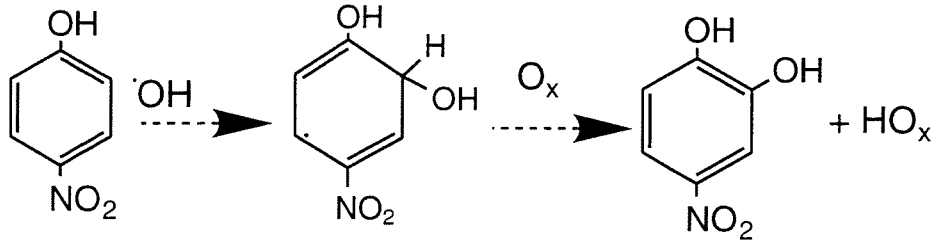

(25)

The predominant step, inferred from shock-tube studies (27) of analogous compounds is pyrolytic cleavage of the C-NO_2 bond which occurs at the hot bubble interface. Attack by hydroxyl radical (28-32) and subsequent reaction with other oxidizing species can lead to the formation of 4-NC and benzoquinone. A detailed discussion of the degradation by-products of p-NP in a sonicated solution is provided by Kotronarou et al (5)

First-order plots of ln[p-NP] vs. time for an Ar saturated solution of p-NP sonicated at a gap-width of 1.45 mm are shown in Fig. 2. The rate constants for three identical runs were reproducible within 3-5 %.

A second set of experiments was performed to examine a variable gap-width between the plates (i.e., a variable reaction volume), with a constant power input of 1775 W. This variation allowed for a range of power per unit volume while the power per unit area (i.e., sound intensity) was maintained constant. The energy required to expand a population of bubbles in solution can be estimated with Eq. (26) (33):

$$E = \frac{4}{3} P N R_{max}^3 \tag{26}$$

where P = the magnitude of the hydrostatic and acoustic pressure; N = number of bubbles in solution; R_{max} = the maximum radius of the bubble before it collapses. Because P and therefore R_{max} vary only when the intensity changes, increasing the power per unit volume in this set of experiments increases N, the number of bubbles which are forced to expand and then implode. Eq. (26) predicts that the number of bubbles will increase linearly with power density. Although the number of chemical events per bubble is not known, it is reasonable to expect a linear correlation of chemical reactivity with the amount of energy transferred into solution. Fig. 3 illustrates the linear correlation of the observed degradation rate constant of p-NP with the power density in an Ar saturated solution. The data for two initial concentrations is compared. The value of k ranges from $1.00 \times 10^{-4} s^{-1}$ at the lowest power-to-volume ratio (0.98 W mL^{-1}) to $7.94 \times 10^{-4} s^{-1}$ at the highest power-to-volume ratio (7.27 W mL^{-1}). Faster degradation rates at higher power densities result from a higher number of reactive sites (i.e., cavitation events) in solution. Sonication of solutions with $[p\text{-}NP]_i$ = 25 μM resulted in degradation rates constants which were about twice as large as those observed in solutions with $[p\text{-}NP]_i$ = 100 μM. The

slower degradation rate at a higher initial concentration demonstrates that the cavitation sites approach saturation with increasing bulk solute concentrations.

In order to examine the dependence of k on the power per unit area, the NAP reactor was operated at a fixed gap - width of 1.45 mm, while the power output was varied. Fig. 4 shows the variation of k as a function of the power per unit area. k increases with increasing sound intensity until a maximum value is obtained at 1.2 W/cm^2 and then k decreases with further increases in intensity. This behavior has been observed previously, in both aqueous (33-35) and organic (36) solutions. The intensity, or power per unit area, is correlated with the acoustic amplitude of the ultrasonic wave, Eq. (27) (7), as follows:

$$I = \frac{P_A^2}{2\rho c} \tag{27}$$

where I = amount of energy emitted per unit area per unit time, P_A = acoustic pressure amplitude, ρ is the density of water, and c is the speed of sound in water (~1500 m/s). The importance of the acoustic amplitude in determining the final temperature and pressure within the collapsed bubble can be estimated with Eqs. 28-29 (7,13).

$$P_{max} = P\left(\frac{P_m(K-1)}{P}\right)^{K/(K-1)} \tag{28}$$

$$T_{max} = T_o\left(\frac{P_m(K-1)}{P}\right) \tag{29}$$

where P_m = pressure in the liquid at the moment of collpase; P = pressure in the bubble at is maximum radius; $K = C_p/C_v$, the adiabatic index of the saturating gas; T_o = the temperature of the bulk liquid. P_m = is the sum of the hydrostatic and acoustic pressures. During the

compression cycle a higher pressure amplitude will result in a more complete implosion and thus more extreme final conditions. This translates into higher reactivity at each bubble as the acoustic amplitude increases. However, the cavitation intensity cannot be increased without limit because as the vibrational amplitude increases, decoupling occurs between the vibrating plate and the solution; thus the energy transfer efficiency decreases (37). Also, the formation of a bubble shroud (13) may occur at the surface of the vibrating plates at high intensities, resulting in attenuation of the sound wave.

The effect of dissolved gases on k was determined. Since the chemical reactivity at a cavitation site is determined by the final temperature and pressure of bubble collapse (7,13) as well as the nature of the oxidizing species produced, k should depend on the nature and properties of the dissolved gases. In the presence of Ar, water vapor in the high - temperature regions decomposes as follows (38):

$$H_2O \rightarrow H^{\bullet} + HO^{\bullet} \tag{30}$$

$$2\ HO^{\bullet} \rightarrow H_2O_2 \tag{31}$$

$$2\ H^{\bullet} \rightarrow\ H_2 \tag{32}$$

to produce $^{\bullet}OH$ and H_2O_2.

In addition to pyrolytic decomposition of water, the following reactions also occur in oxygen saturated solutions:

$$O_2 \rightarrow 2\ O^{\bullet} \tag{33}$$

$$O^{\bullet} +\ O_2 \rightarrow O_3 \tag{34}$$

$$H^{\bullet} + O_2 \rightarrow HO_2^{\bullet} \tag{35}$$

Thus, a solution saturated only with Ar would be expected to favor pyrolytic reactions (39,40) because of the higher final temperature, whereas an oxygen saturated solution would result in a greater number of oxidizing radicals but a lower temperature upon bubble collapse. The variation of k as a function of background gas compositions is shown in Fig. 5. The degradation of p-NP occurs most rapidly in a solution saturated with a 80%/20% (v/v) Ar/O_2 mixture and least rapidly in a solution saturated only with oxygen. This result is reasonable because the initiation of p-NP degradation occurs in two parallel reactions: pyrolytic cleavage of the $C\text{-}NO_2$ moiety and attack by $^{\bullet}OH$. In a solution saturated with either Ar or O_2 alone, only one of the parallel pathways is accelerated. In a solution containing both gases, more extreme conditions can be achieved, as well as higher concentrations of oxidizing species and thus, the overall reaction rate constant increases.

The effect of the saturating gas on the formation of 4-nitrocatechol, a reaction intermediate, is less predictable. In Fig. 6 a plot of the fraction of p-NP degraded to 4-NC as a function of the percentage of p-NP degraded is shown. In an Ar saturated solution, the fraction of p-NP degraded to yield 4-NC is the highest. However, in solutions saturated with O_2 or the Ar/O_2 mixture, 4-NC is present in much lower concentrations. These lower concentrations of 4-NC most likely result from faster degradation due to attack by $HO_2^{\bullet}$, which is formed in significant quantities only in the presence of oxygen.

DISCUSSION

A summary of the rate constants and reactor conditions is given in Table I. The power-to-area ratio was maintained constant while the power-to-volume ratio was varied. The observed first-order degradation rate constant increases as the power density and intensity are increased up to a saturation value. Manipulation of these macroscopic parameters leads to enhancement of the cavitation chemistry as the number of cavitation

bubbles and the chemical events at each bubble are varied. A seven-fold increase in power density results in an approximately equivalent increase in observed rate constant for degradation, whereas k reaches a maximum value upon increasing the intensity four-fold. Simultaneous acceleration of pyrolytic and free-radical reaction pathways results in the maximum rate observed in solutions saturated in an Ar/O_2 mixture. Hart (41) and Büttner (42) have studied free-radical formation in Ar/O_2 mixtures and also found an optimal percentages of each gas for oxidation of different substrates.

The energy efficiency of an advanced oxidation technology must be determined in order to determine its practical potential for hazardous waste treatment. In order to make this comparison, we employ the concept of efficiency, measured in terms of a G-value, which is often used in radiation chemistry (43,44). The G-value is defined for our purposes as the number of molecules degraded per unit of energy input into the system:

$$G - \text{value} = \frac{\Delta C \times N_0 \times V}{\Delta T \times W} \text{[molecules/kJ]} \qquad (34)$$

ΔC = change in the solute concentration over a given time interval ΔT; $N_0 = 6.023 \times 10^{23}$ molecules/mol; V = volume of solution; W = wall voltage. It should be noted that the G-value does not include any other chemical reaction, such as simultaneous degradation of the various by-products. Furthermore, the energy input is based on the wall-voltage, and the energy transduction process is not 100% efficient. Therefore, the G-values calculated in this study (Table II, Fig. 7) represent a lower limit of energy efficiency in the NAP reactor. A calorimetric method for the determination of the actual energy transferred into solution could also be used to calculate the energy efficiency.

The G-values for p-NP degradation in a probe reactor and NAP reactor under various conditions are compared in Table II. The standard bench top reactor configuration for sonochemistry consists of a vibrating horn (or 'probe') immersed in solution. This configuration was chosen for comparison to the NAP. Experimental methods for collection

of this data are described in Hua et al. (2) and specific reactor conditions are listed in the table. The G-value for the probe reactor is approximately an order of magnitude less than in the NAP although the rate constants are of the same order of magnitude. This is due to the more even dispersal of energy in the NAP system. Because of the larger emitting area of the plates in a NAP, all of the reactant solution is directly exposed to ultrasound whereas in the probe reactor, the actual cavitating volume represents a small fraction of the total solution (37). In addition, attenuation of the sound wave in the NAP is minimal because the distance at any point in the solution from the emitting surface is only several mm or at most ~1.25 cm. Finally, because the NAP operates at two different frequencies, a greater number of bubbles in a given population can be excited. Sound waves emitted from two opposing plates can undergo constructive interference, given the superposition principle (45). The amplitude of the resulting wave can be larger than the two individual sound waves, resulting in more intense cavitational collapse. Given two waves travelling in opposite directions, with amplitude A, frequencies ω_1 and ω_2 and wavenumbers k_1 and k_2, the behavior of the resulting wave as a function of time, t and position, x can be derived from the superposition principle, Eq. 37:

$$f(x,t) = 2A\cos\left[\frac{(k_1 + k_2)x + (\omega_1 - \omega_2)t}{2}\right]\cos\left[\frac{(k_1 - k_2)x + (\omega_1 + \omega_2)t}{2}\right] \qquad (37)$$

The NAP reactor operates at two different frequencies, but the sound field is the result of complex interactions.

The sonochemical degradation of p-NP in aqueous solutions can be successfully scaled-up from laboratory scale bench-top volumes to more practical operational volumes. The G-value obtained in the larger-scale NAP reactor is approximately 20 times higher than in a conventional probe reactor. The reaction rate retains its overall first-order character, and the observed rate constant exhibits an inverse relation to the initial substrate concentration similar to that observed in the probe system. The parallel-plate design of the

NAP reactor allows for a lower sound intensity but higher irradiation energy per unit volume. Furthermore, this configuration results in a more even distribution of cavitation events in the solution flowing through the NAP.

Optimization of p-nitrophenol degradation rates within the NAP can be achieved by adjusting the energy density, the energy intensity; and the nature and physical properties of the saturating gas in solution. The observed first-order degradation rate constant increases as the energy density and intensity are increased up to a saturation value. Manipulation of these macroscopic parameters leads to enhancement of the cavitation chemistry as the number of cavitation bubbles and chemical events at each bubble are varied. A seven-fold increase in energy density results in an approximately equivalent increase in observed rate constant for degradation, whereas k reaches a maximum value upon increasing the intensity four-fold. The specific nature of the saturating gas incluences the relative proportion of pyrolytic or free-radical reaction steps. Simultaneous acceleration of these pathways results in the maximum rate observed in solutions saturated in an Ar/O_2 mixture.

In our present investigations, the NAP reactor was integrated into a recycle system due to the need for temperature control which could only be achieved by thermostating the reaction mixture itself outside the reactor. The need for continuous recycling at a relatively high volumetric flow-rate together with the reactor volume and the first-order rate constants leads to small Damkoehler numbers, $D_a = \frac{kV_R}{Q} << 1$. The mathematical analysis of the reactor system shows that for small Da (i.e., small conversion per pass), the residence time distribution of the NAP has no influence on the observed rate constants. This result justifies the use of the simple volume correction factor in determining k from k_{obs}. Increasing the rate constant and/or the reactor volume, and decreasing the volumetric flow rate result in an increased Damkoehler number. Under these conditions, the residence time distribution of the NAP has to be known in order to extract k from k_{obs}.

Increasing the rate constant and/or the reactor volume, and decreasing the volumetric flow-rate result in an increased Damkoehler number. Under these conditions,

the residence time distribution of the NAP has to be known in order to extract k from k_{obs}. To operate the NAP as a steady-state continuous flow reactor, a higher conversion per pass is needed by either decreasing the volumetric flow-rate or increasing the reactor volume.

The degradation of p-NP by ultrasonic irradiation compares favorably to other modern treatment methods, including bacterial reduction (46) or oxidation (47), carbon adsorption (48), membrane solvent extraction (49), ozonolysis (50), and the Fenton reaction (51). Because reactor configurations (batch vs. flow-through) and reactor volumes vary greatly amond these studies, direct comparison of rate constants cannot be made. Most of the techniques resulted in >90% degradation or removal of p-NP on the time scale of hours. However, ultrasonic irradiation offers the advantage over carbon adsorption and membrane extraction of complete compound destruction. Degradation occurs over concentration ranges varying by orders of magnitude (5), unlike certain biological systems (47) which are inhibited by relatively low substrate concentrations. Furthermore, the cavitation chemistry of p-NP does not exhibit complex pH effects which are observed during ozonolysis of the substrate (50) .

Acknowledgments: The authors wish to thank Sayuri Desai for preliminary experiments and the power input measurements and Douglas A. Varela for his assistance with solving the partial differential equation. Financial support from the Advanced Research Projects Agency, ARPA, (Grant # NAV 5HFMN N0001492J1901), the Office of Naval Research, ONR, and the Electric Power Institute, EPRI, (Grant # RP 8003-37) is gratefully acknowledged.

References

1. Cost, M.; Mills, G.; Glisson, P.; Lakin, J., *Chemosphere,* **1993**, *27*, 1737-1743.

2. Hua, I.; Höchemer, R. H.; Hoffmann, M. R., *J. Phys. Chem.,* **1995**, *99*, 2335-2342.

3. Koskinen, W. C.; Sellung, K. E.; Baker, J. M.; Barber, B. L.; Dowdy, R. H., *J. Environ. Sci. Health Part B,* **1994**, *29*, 581-590.

4. Kotronarou, A.; Mills, G.; Hoffmann, M. R., *Environ. Sci. Technol.,* **1992**, *26*, 2420-2428.

5. Kotronarou, A.; Mills, G.; Hoffmann, M. R., *J. Phys. Chem.,* **1991**, *95*, 3630-3638.

6. Kotronarou, A.; Mills, G.; Hoffmann, M. R., *Environ. Sci. Technol.,* **1992**, *26*, 1460-1462.

7. Mason, T. J.; Lorimer, J. P. *Sonochemistry: Theory, Applications and Uses of Ultrasound in Chemistry*; Ellis Horwood Ltd.: Chichester, 1988.

8. Olson, T. M.; Barbier, P. F., *Wat. Res.,* **1994**, *28*, 1383-1391.

9. Petrier, C.; Micolle, M.; Merlin, G.; Luche, J. L.; Reverdy, G., *Environ. Sci. Technol.,* **1992**, *26*, 1639-1642.

10. Petrier, C.; Lamy, M. F.; Francony, A.; Benahcene, A.; David, B.; Renaudin, V.; Gondrexon, N., *J. Phys. Chem.,* **1994**, *98*, 10514-10520.

11. Serpone, N.; Terzian, R.; Colarusso, P.; Minero, C.; Pelizzetti, E.; Hidaka, H., *Res. Chem. Intermed.,* **1992**, *18*, 183-202.

12. Serpone, N.; Terzian, R.; Hidaka, H.; Pelizzetti, E., *J. Phys. Chem.,* **1994**, *98*, 2634-2640.

13. *Ultrasound: Its Chemical, Physical and Biological Effects*; Suslick, K. S., Ed.; VCH Publishers, Inc.: New York, 1988.

14. Weissler, A. C., H. W., Snyder, S., *J. Am. Chem. Soc.*, **1950**, *72*, 1769-1775.

15. Wu, J. M., Huang, H. S., Livengood, C. D., *Environ. Prog.*, **1992**, *11*, 195-201.

16. Price, G., Matthias, P., Lenz, EJ, *Process Safety and Environmental Protection: Transactions of the Institution of Chemical Engineers Part B,* **1994**, *72*, 27-31.

17. Bien, J., *Acustica,* **1991**, *74*, 279-283.

18. Hunicke, R. L., *Ultrasonics,* **1990**, *28*, 291-294.

19. Lin, J.-R.; Yen, T. F., *Energy and Fuels,* **1993**, *7*, 111-118.

20. Sadeghi, K. M.; Lin, J. R.; Yen, T. F., *Energy Sources,* **1994**, *16*, 439-449.

21. Berlan, J.; Mason, T. J., *Ultrasonics,* **1992**, *30*, 203-212.

22. Martin, P. D.; Ward, L. D., *Chem. Eng. Res. Des.*, **1992**, *70*, 296-303.

23. Mason, T. J., *Ultrasonics,* **1992**, *30*, 192-196.

24. Baerns, M., Hofmann, H., Renken, A. *Chemische Reaktionstechnik;* 1 ed.; Georg Thieme Verlag: Stuttgart, New York, 1987; Vol. 1, pp. 428.

25. Denbigh, K. G. *Chemical Reactor Theory*; University Press: Camebridge, 1965.

26. Dialer, K., Loewe, A. *Chemische Reaktionstechnik*; Carl Hanser Verlag: Muenchen, Wien, 1975, pp. 108.

27. Tsang, W.; Robaugh, D.; Mallard, W. G., *J. Phys. Chem.*, **1986**, *90*, 5968-5973.

28. O'Neill, P., Steenken, S., Van Der linde, H., Schulte-Frohlinde, D., *Radiat. Phys. Chem.*, **1978**, *12*, 13-17.

29. Volkert, O., Termens, G., Schulte-Frohlinde, D., *Z. Phys. Chem. N F*, **1967**, *56*, 261-267.

30. Grässlin, D., Merger, F., Schulte-Frohlinde, D., Volkert, O., *Z. Phys. Chem. N F*, **1966**, *51*, 84-94.

31. Suarez, C. L., F.;Günther, K.; Eiben, K., *Tetrahedron Lett*, **1970**, 575-578.

32. Cercek, B.; Ebert, M., *Adv. Chem. Ser.*, **1968**, *81*, 210-221.

33. Shutilov, V. A. *Fundamental Physics of Ultrasound*; OPA: Amsterdam, 1988, pp. 378.

34. Couppis, E. Z., Klinzing, G. E., *AIChE. J.*, **1974**, *20*, 485-491.

35. Henglein, A., Gutierrez, M., *J. Phys. Chem.*, **1990**, *94*, 5169-5172.

36. De Souza Barboza, J. C.; Petrier, C.; Luche, J. L., *J. Org. Chem.*, **1988**, *53*, 1212-1218.

37. Mason, T. J. *Practical Sonochemistry: User's Guide to Applications in Chemistry and Chemical Engineering*; Ellis Horwood: Chichester, 1991, pp. 186.

38. *Advances in Sonochemistry*; Mason, T. J., Ed.; JAI Press Ltd.: London, 1990; Vol. 1.

39. Kondo, T.; Riesz, P., *Free Radical Biol. Med.*, **1989**, *7*, 259-268.

40. Kondo, T.; Kirschenbaum, L. J.; Kim, H.; Riesz, P., *Abstr. A C S Meeting*, **1992**, *204*, 246-INOR.

41. Hart, E. J., Henglein, A., *J. Phys. Chem.*, **1985**, *89*, 4342-4347.

42. Büttner, J., Gutiérrez, M., Henglein, A., *J. Phys. Chem.*, **1991**, *95*, 1528-1530.

43. Armstrong, W. A., Humphreys, W. G., *Can. J. Chem.*, **1965**, *43*, 2576-2584.

44. Todd, J. H., *Ultrasonics,* **1970**, *8*, 234-238.

45. Ohanian, H. C. *Physics*; W. W. Norton and Co., Inc.: New York, 1985; Vol. 1, pp. 594.

46. Gurevich, P.; Oren, A.; Sarig, S.; Henis, Y., *Water Sci. Technol.*, **1993**, *27*, 89-96.

47. Spain, J. C.; Gibson, D. T., *Appl. Environ. Microbiol.*, **1991**, *57*, 812-819.

48. Calleja, G.; Serna, J.; Rodríguez, J., *Carbon,* **1993**, *31*, 691-697.

49. Tompkins, C. J.; Michaels, A. S.; Peretti, S. W., *J. Membr. Sci.*, **1992**, *75*, 277-292.

50. Beltrán, F. J.; V., G.-S.; Durán, A., *Wat. Res.*, **1991**, *26*, 9-17.

51. Kochany-Lipczynska, E., *Chemosphere,* **1992**, *24*, 1369-1380.

Figure Captions

Figure 1: Schematic diagram of the reactor system.

Figure 2: Reproducibility of p-NP degradation in the NAP reactor. First-order plot for p-NP degradation in an Ar saturated solution irradiated at 100 % (1775 W) power and a gap width of 1.45 mm. $[p\text{-}NP]_0$ = 100 μM, T = 30 ± 2 °C, pH = 5.0 ± 0.2, μ < 30 μM.

——— y = 0.0446 + -0.0466x R= 0.999

- - - - - y = 0.0191 + -0.0477x R= 1.000

- - - - - y = -0.0155 + -0.0490x R= 1.000

Figure 3: p-NP degradation rate constant as a function of ultrasound power-to-volume ratio at different initial concentrations. Variable reaction volume with constant power (1775 W). $[p\text{-}NP]_0$ = 100 and 25 μM, T = 30 ± 2 °C, pH = 5.0 ± 0.2, μ < 30 μM.

——— y = -1.69e-06 + 0.000113x R= 0.992

- - - - - y = -3.47e-05 + 0.000231x R= 1.000

Figure 4: p-NP degradation rate constant as a function of ultrasound power-to-area ratio. Variable power with constant reaction volume (244 mL). $[p\text{-}NP]_0$ = 100 μM, T = 30 ± 2 °C, pH = 5.0 ± 0.2, μ < 30 μM.

Figure 5: First-order plot of p-NP degradation in solutions saturated with different

gases at 1775 W power and 1.45 mm gap width. $k_{O_2} = 5.19 \times 10^{-4} s^{-1}$, $k_{Ar} = 7.94 \times 10^{-4} s^{-1}$, $k_{Ar/O_2} = 1.20 \times 10^{-3} s^{-1}$. $[p\text{-NP}]_0 = 100\ \mu M$, $T = 30 \pm 2\ ^{o}C$, pH = 5.0 ± 0.2, $\mu < 30\ \mu M$.

Figure 6: Fraction of degraded p-NP which has been transformed into p-NC as a function of the fraction of p-NP degraded. Reactions conditions same as in Fig. 4.

Figure 7: The effect of cavitating gas on the energy efficiency of p-NP degradation.

Table I.

First-Order Rate Constants for Different Power-Densities with Argon as Background Gas

Rate Constants, [10^{-4} s^{-1}]	Gap-Width, [mm]	Irradiated Volume, [mL]	Power/Area Ratio, [W cm^{-2}]	Power/Volume Ratio, [W mL^{-1}]
7.94	1.45	244	1.41	7.27
5.39	3.25	376	1.41	4.72
3.93	6.30	568	1.41	3.12
1.98	9.50	834	1.41	2.12
1.00	25.17	1807	1.41	0.98
8.16	1.45	244	1.41	7.27
8.50	1.45	244	1.33	6.86
8.60	1.45	244	1.23	6.35
6.50	1.45	244	0.93	4.80
4.00	1.45	244	0.55	2.82
1.99	1.45	244	0.33	1.74

Table II.

Energy Efficiencies of the NAP and Probe Systems

Reactor	Power Density, W/mL	Power Intensity, W/cm^2	G-value x 10^{-15}, molecules/kJ	k, s^{-1}
Probe*	4.8	10	2.3	5.2×10^{-4}
NAP** (Ar)	7.27	1.4	43	7.9×10^{-4}
NAP (Ar/O_2)	7.27	1.4	64	1.2×10^{-3}
NAP (O_2)	7.27	1.4	37	5.19×10^{-4}

*For an Ar saturated solution; pH ~5 and $[p\text{-NP}]_i = 100\ \mu M$. Probe reactor manufactured by Sonics and Materials: Model VCX-400; operated at an average output of 130 W; sonicated volume 25 mL; T = 30 °C.

**Values for the NAP are given for different saturating gases.

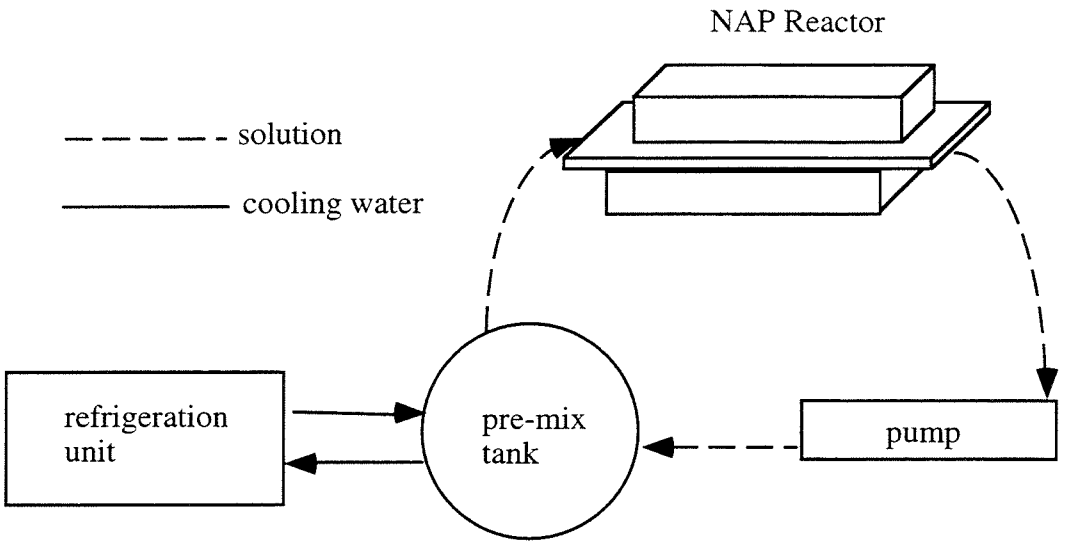

Fig. 1: Schematic diagram of the reactor system.

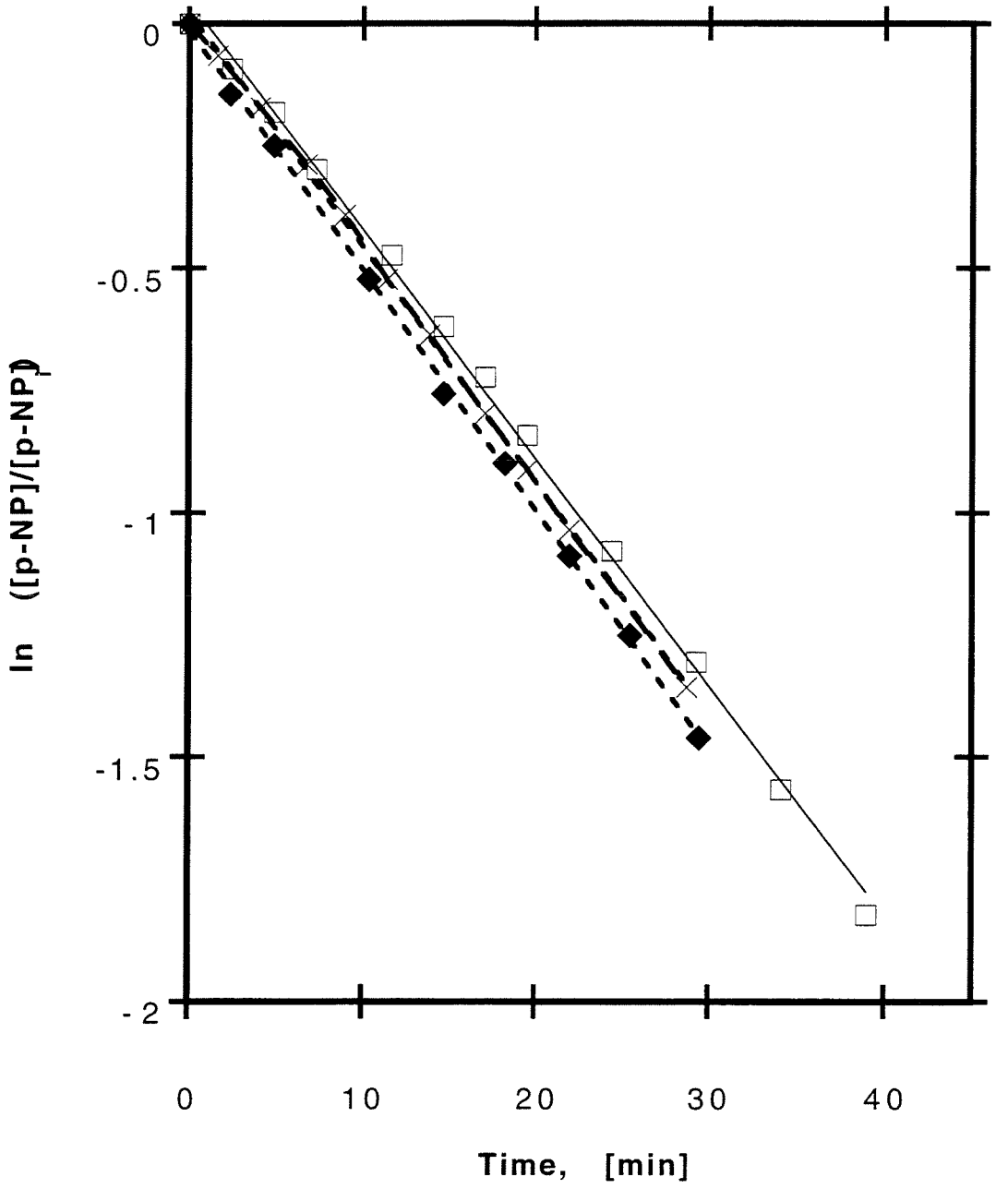

Fig. 2: Reproducibility of p-NP degradation in the NAP reactor. First-order plot for p-NP degradation in an Ar saturated solution irradiated at 100 % (1775 W) power and a gap width of 1.45 mm. $[p\text{-}NP]_0$ = 100 μM, T = 30 ± 2 °C, pH = 5.0 ± 0.2, μ < 30μM.

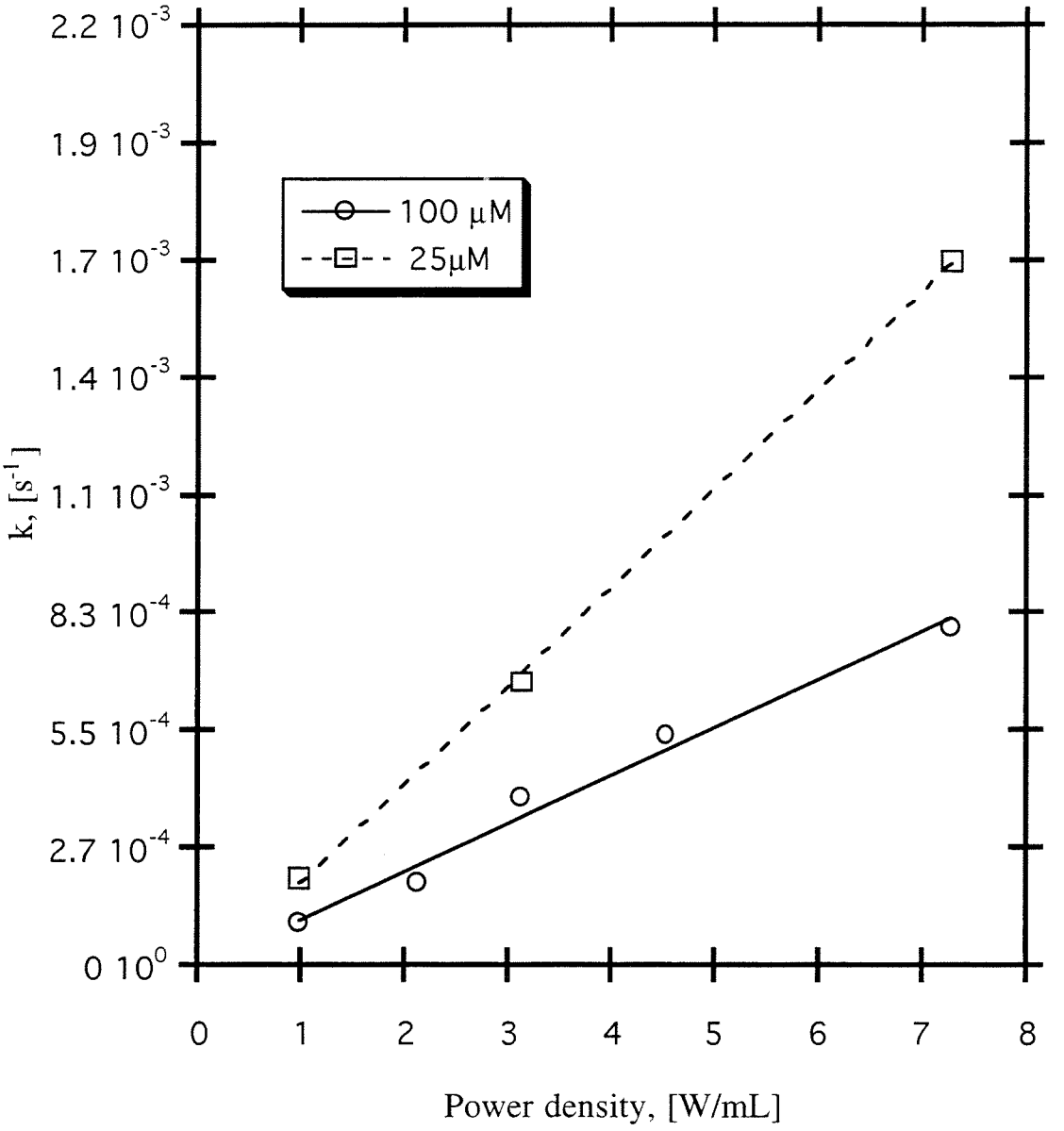

Fig. 3: p-NP degradation rate constant as a function of ultrasound power density at different initial concentrations. Variable reaction volume with constant power (1775 W). $[p\text{-}NP]_0$ = 100 and 25 µM, T = 30 ± 2 °C, pH = 5.0 ± 0.2, µ < 30 µM.

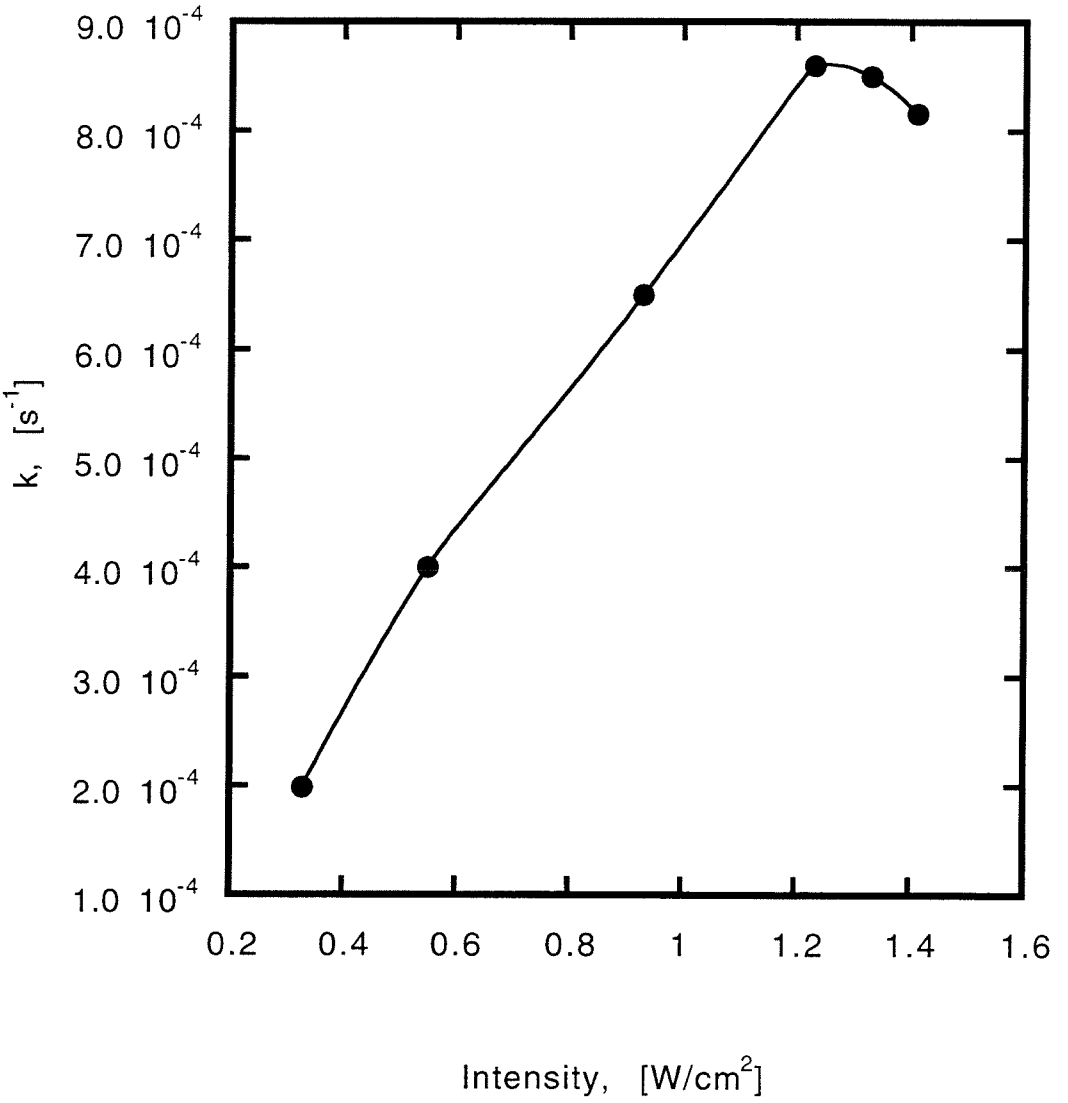

Fig. 4: p-NP degradation rate constant as a function of ultrasound power-to-area-density. Variable power with constant reaction volume (244 mL). $[p\text{-}NP]_0 = 100\ \mu M$, $T = 30 \pm 2\ ^{\circ}C$, $pH = 5.0 \pm 0.2$, $\mu < 30\ \mu M$.

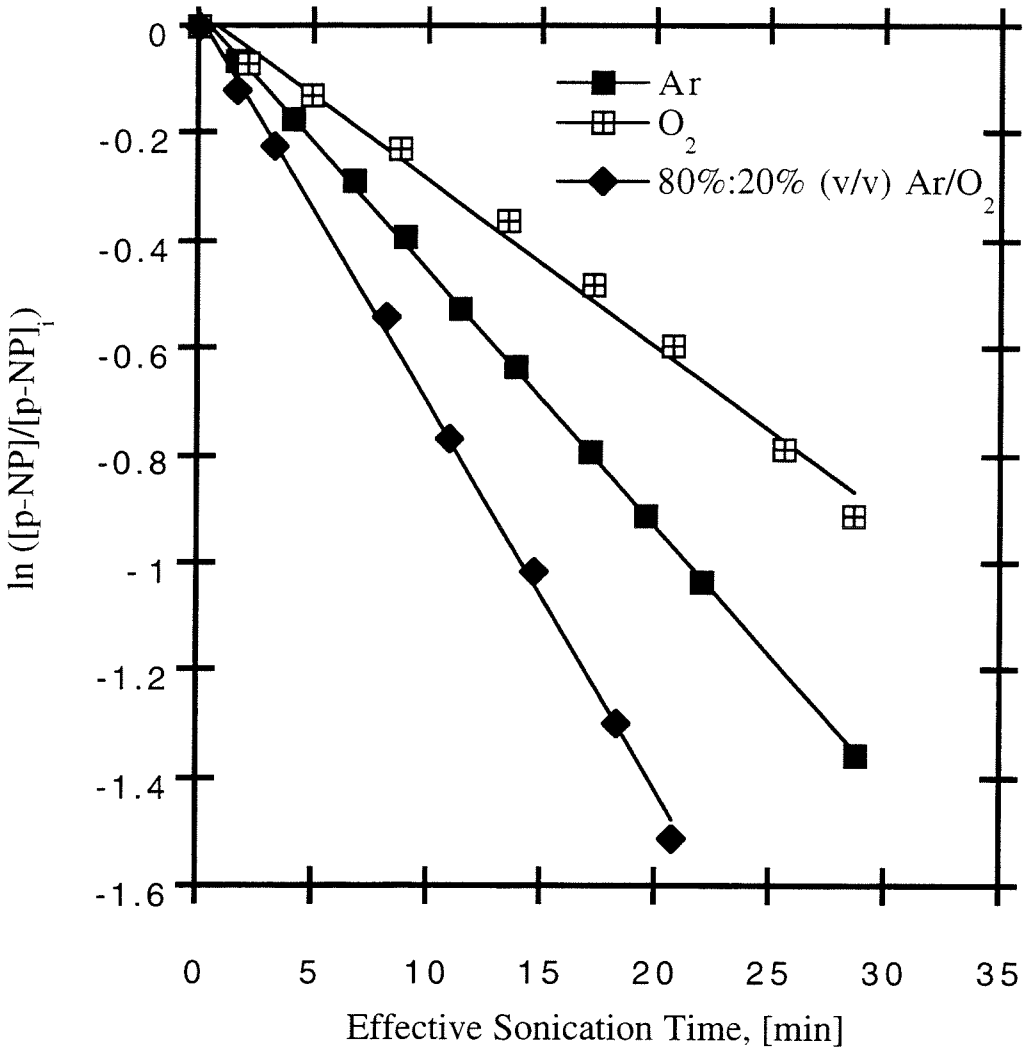

Fig. 5: First-order plot of p-NP degradation in solutions saturated with different gases at 1775 W power and 1.45 mm gap width. $k_{O_2} = 5.19 \times 10^{-4} s^{-1}$, $k_{Ar} = 7.94 \times 10^{-4} s^{-1}$, $k_{Ar/O_2} = 1.20 \times 10^{-3} s^{-1}$. $[p\text{-NP}]_0 = 100\ \mu M$, $T = 30 \pm 2\ ^{o}C$, pH = 5.0 ± 0.2, $\mu < 30\ \mu M$.

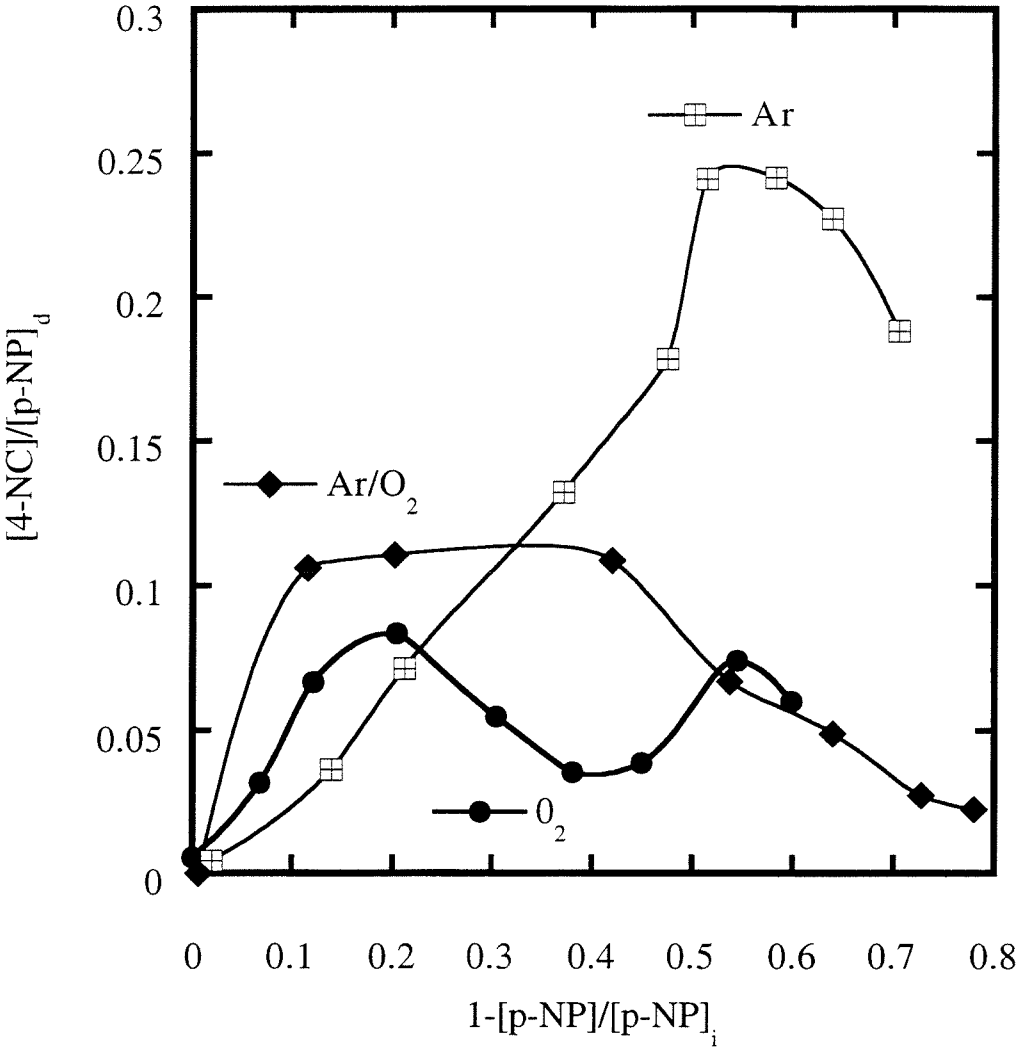

Fig. 6: Fraction of degraded p-NP which has been transformed into 4-NC as a function of the fraction of p-NP degraded. Reaction conditions same as in Fig. 5.

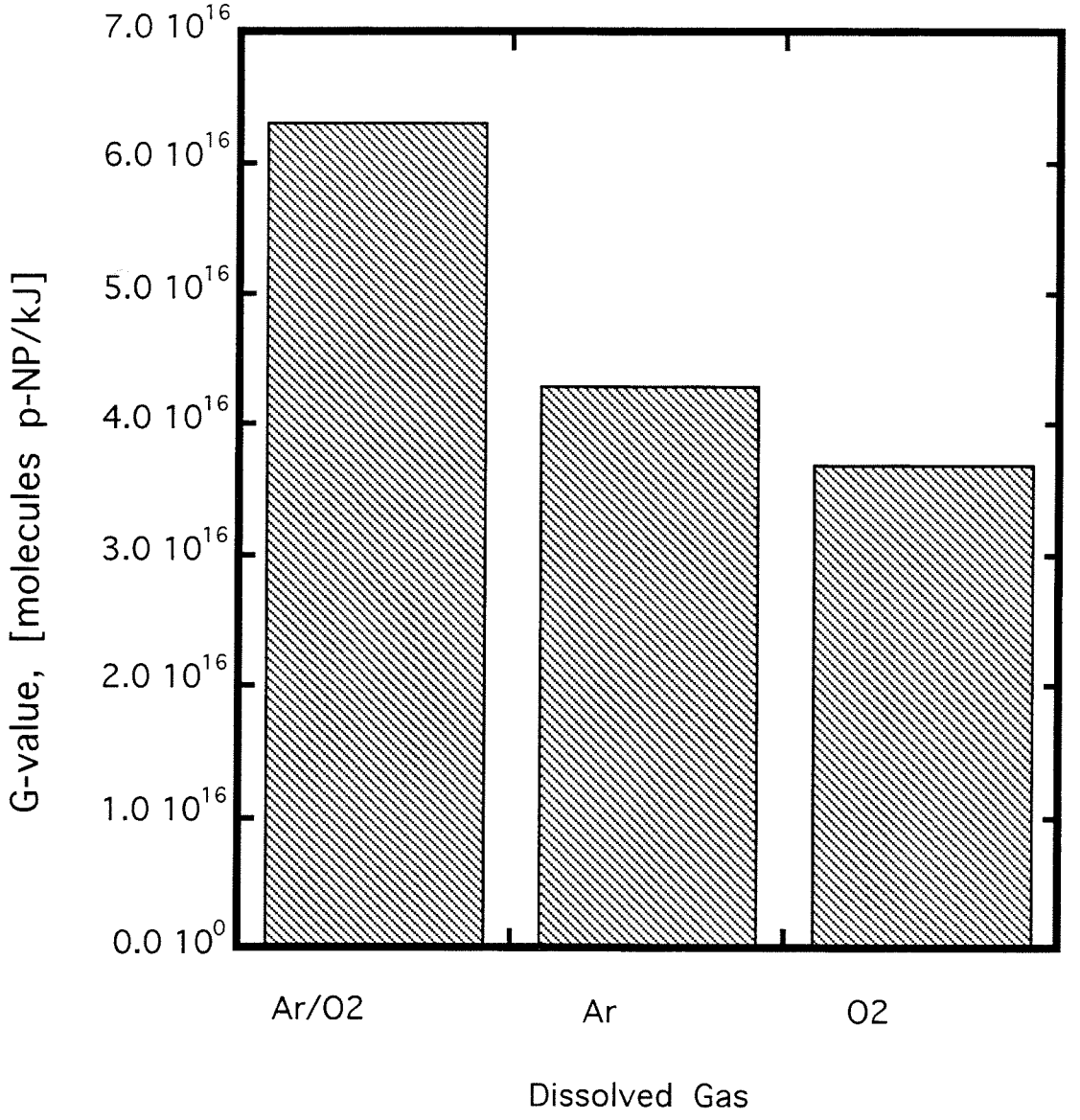

Fig. 7: The effect of cavitating gas on the energy efficiency of p-NP degradation.

Chapter 4:

Kinetics and Mechanism of the Sonolytic Degradation of CCl_4: Intermediates and By-Products

[Hua, I., Hoffmann, M. R., *Environmental Science and Technology,* **in press**]

Abstract

The sonolytic degradation of aqueous carbon tetrachloride is investigated at a sound frequency of 20 kHz and 135 W (112.5 W cm^{-2}) of power. The observed first-order degradation rate constant in an Ar saturated solution is 3.3 x 10^{-3} s^{-1} when the intitial CCl_4 concentration, $[CCl_4]_i$, is 1.95 x 10^{-4} mol L^{-1} and increases slightly to 3.9 x 10^{-3} s^{-1} when $[CCl_4]_i$ = 1.95 x 10^{-5} mol L^{-1}. Low concentrations (10^{-8} - 10^{-7} mol L^{-1}) of the organic by-products, hexachloroethane and tetrachloroethylene, are detected, as well as the inorganic products, chloride ion and hypochlorous acid (HOCl). The chlorine mass balance after sonolysis is determined to be >70%. The reactive intermediate, dichlorocarbene, is identified and quantified by means of trapping with 2,3-dimethyl-2-butene. The presence of ozone in the sonicated solution does not significantly effect the rate of degradation of carbon tetrachloride; however O_3 inhibits the accumulation of hexachloroethane and tetrachloroethylene. Ultrasonic irradiation of an aqueous mixture of p-nitrophenol and carbon tetrachloride results in the acceleration of the sonochemical degradation of p-nitrophenol. The sonolytic rate of degradation of p-NP appears to be enhanced by the presence of hypochlorous acid which results from the sonolysis of CCl_4.

INTRODUCTION

Carbon tetrachloride (CCl_4) contamination in the environment is widespread due to its refractory nature and its large-scale production. Under ambient conditions, CCl_4 does not degrade readily (1,2). However, CCl_4 is reduced by H_2S in the presence of mineral surfaces (3,4) and over cobalt catalysts (5). CCl_4 is unreactive towards hydroxyl radical (half-life >330 y) (6), but degrades via direct photolysis in the stratosphere (7,8) where it is thought to play a minor role in the depletion of stratospheric ozone (9,10). The persistence of CCl_4 in the environment is of concern because of its short-term and chronic human health effects and because it is a suspected human carcinogen and an EPA priority pollutant (11). The mechanisms of CCl_4 toxicity (12-17), its physical properties and its environmental fate (18,19) have been studied.

Numerous methods have been applied to the degradation of gas-phase CCl_4 such as catalytic decomposition over mixed metal oxide/porous carbon catalysts (20), incineration (21,22), reduction over metallic iron (23), and electron-beam plasmas (24,25). The treatment of aqueous phase CCl_4 has been explored using anaerobic activated carbon reactors (26), UV photolysis (27), and high-pressure (20 MPa) liquid water hydrolysis (28).

Ultrasonic irradiation of aqueous solutions of halogenated hydrocarbons, including chlorofluorocarbons (29) and CCl_4 (30-34) has been reported. The extreme temperatures and pressures generated during cavitation result in solute thermolysis as well as the formation of hydroxyl radical and hydrogen peroxide (35,36). The decomposition of aqueous CCl_4 during sonication was first reported by Weissler (37); CCl_4 sonolysis was also shown to result in enhanced sonoluminescence (38,39). The sonolysis of CCl_4 in the presence of iodide (40), magnesium chloride (41) and di-*n*-butyl sulfides (42) has also been examined. The results of these studies indicate that the decomposition of CCl_4 during ultrasonic irradation is significant, with first-order rate constants ranging from 10^{-2} to 10^{-3}

s^{-1}. The effect of reaction variables such as initial concentration, steady-state temperature and power intensity has been investigated. However, quantitative data on by-product analysis and intermediate formation is lacking.

In this paper, we examine the kinetics and mechanism of the ultrasonic irradiation of CCl_4 in aqueous solution with a particular focus on the Cl^- balance, reaction intermediates and reaction by-products. The effects of ozone and *p*-nitrophenol on CCl_4 degradation are also explored.

EXPERIMENTAL METHODS

High purity carbon tetrachloride (Calibration Standard; Supelco, Bellefonte, PA), hexachloroethane (98%; Aldrich, Milwaukee, WI), tetrachloroethylene (99.9%; Sigma-Aldrich, St. Louis, MO and Milwaukee, WI), 2,3-dimethlybutene (Aldrich), p-nitrophenol (Aldrich, 98%), 5,5',7-indigotrisulfonic acid (Sigma Chemical Co.) and pentane (Omnisolv grade, EM Science, New Jersey) were used as received. All aqueous solutions were made in water purified with a MilliQ UV Plus System (R = 18.2 mΩ). Reproducible concentrations of CCl_4 in water were obtained by adding a specific volume of the solute into a vial filled with water and sealing the vial with zero-headspace. The vial was then shaken at ~285 rpm at room temperature for 12 h to achieve complete dissolution. The solutions were then diluted in Ar-saturated water to the appropriate concentration and adjusted to pH 11.8 with NaOH. Buffers were not used to control the pH because many buffers (e. g. carbonate or bicarbonate) are effective radical scavengers (43) and would interfere with degradation of the target solute. Saturated solutions were made by stirring excess CCl_4 with water.

Sonications at 20 kHz were done with a VCX-400 Vibracell™ (Sonics and Materials, Inc., Danbury, CT) operated at 30% power amplitude and an average output of 135W as measured with a built-in wattmeter. The titanium tip of the probe was polished and the transducer tuned before every use to give a minimal power ouptut when vibrating in air. 95 mL of solution was transferred into a water-jacketed glass cell, which was closed to

the atmosphere (total volume, 110 mL). The bottom of the glass reactor (Fig. 1) had a one cm indentation in the center for reflection of the sound-waves and for even distribution of the cavitation bubbles in the solution. The reactor was made air-tight with two O-ring seals in the threaded Teflon® collar connecting the glass cell to the stainless steel probe. In addition, sampling ports were sealed with Teflon® valves and covered with rubber septa. Cooling water was circulated through the system by a Haake A80 Cooler/Recirculator in order to maintain a constant temperature. 1.0 mL aliquots were withdrawn with a Hamilton syringe and mixed with 0.5 mL pentane. 0.5 μL of the pentane extract was then analyzed with an HP 5880A Gas Chromatograph/Electron Capture Detector (GC/ECD) operated in the splitless mode and equipped with an HP-5 column (cross-linked 5% Phenyl Methyl Siloxane, 25 m x 0.32 mm x 1.05 μm film thickness). The instrument was calibrated by standard solutions of carbon tetrachloride, hexachloroethane and tetrachloroethylene in pentane. Ion-selective electrodes were used to quantify chloride ion and hypochlorous acid (Orion, Model # 96-17B and # 97-70).

All experiments with ozone were performed with an Orec Model V10-0 Ozonator (Ozone Research and Equipment Corporation, Phoenix, AZ) operated at 9 psi and a flow-rate of 4.5 LPM. Water was placed in a gas-dispersion bottle and bubbled with ozone at a flow-rate of 20 mL/min. Ozone-saturated water was used to dilute 140 mL of an Ar saturated CCl_4 solution to 250 mL. Any residual ozone in the aliquots withdrawn during sonication was quenched by adding 200μL of 1 mmol 5,5',7-indigotrisulfonic acid (Indigo Blue), following standard procedures (44). Pentane extracts were analyzed as described above.

Intermediates were trapped by sonicating a CCl_4 solution in the presence of 2,3-dimethyl-2-butene and Ar. Sample volume and extraction methods were the same as above. The detection of the 1,1-dichloro-2,2,3,3-tetramethylcyclopropane was achieved with a Hewlett - Packard 5890 Series II Gas Chromatograph (HP-5 column, 3 μL injection volume, He carrier gas) connected to a Hewlett - Packard 5972 Series Mass Selective Detector operated in the Single Ion Mode. A characteristic peak at 131 amu was used for

quantification. Confirmation of 1,1-dichloro-2,2,3,3-tetramethylcyclopropane was obtained by comparing the mass spectrum of the sonicated sample to the spectrum of the authentic compound.

Sonication of 100 μM p-NP in a solution saturated with CCl_4 and Ar was performed in an identical fashion as described above. Quantification of the p-NP was achieved with a Hewlett-Packard 8452a UV/Vis spectrophotometer as described previously (45,46).

RESULTS

As shown in Fig. 2 the sonochemical reactor was determined to be gas-tight. A solution of CCl_4 was stirred and maintained at 25 ^{o} C and liquid samples were sequentially withdrawn and analyzed. None of the dissolved CCl_4 appeared to be lost from the solution over a period of 90 min. Thus, even with a small headspace in the reactor, loss of CCl_4 due to volatization during sonolysis is negligible.

A first-order plot of $[CCl_4]$ vs. time during sonolysis is shown in Fig. 3. At two different initial concentrations, 195 μM and 19.5 μM, the reaction exhibits apparent first-order kinetics for approximately four half-lives. The first-order rate constant did not differ significantly over this concentration range; it was slightly higher ($3.9 \times 10^{-3} \pm 0.19\ s^{-1}$) when the initial concentration was 19.5 μM than at 195 μM ($3.3 \times \pm 0.23\ 10^{-3}\ s^{-1}$). In both cases, the concentration of carbon tetrachloride was reduced by 90% within 12 minutes of sonication.

A mass balance of chlorine atoms during CCl_4 sonolysis was determined as follows:

$$\text{chlorine atom yield} = \frac{[Cl^-] + [HOCl] + 4[C_2Cl_4] + 6[C_2Cl_6] + 4[CCl_4]_f}{4([CCl_4]_i - [CCl_4]_f)} \qquad (1)$$

Table I lists values for the observed by-products after ultrasonic irradiation. A typical chlorine balance was >70% with Cl^- found to be the dominant product. Hexachloroethane and tetrachloroethylene are the only organic by-products detected and are not present when the initial CCl_4 concentration is low (19.5 μM). Thus, despite the known degassing effect (47) of ultrasound; in a closed system, volatile solutes re-enter the treated solution and the observed losses are due to chemical reaction and not to volatization.

The formation of the reactive intermediate, dichlorocarbene, was confirmed by utilizing the following reaction:

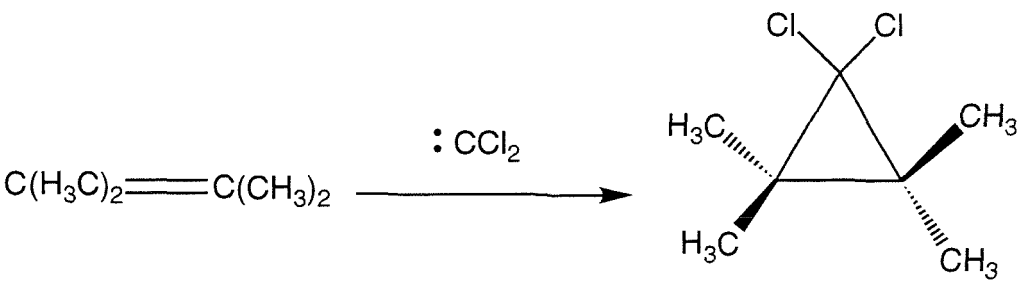

(2)

to form 1,1,-dichloro-2,2,3,3-tetramethylcyclopropane. A peak concentration of 2.8 μM was observed after 15 minutes of sonication, as shown in Fig. 4. This concentration allows a lower limit to be placed on the dichlorocarbene concentration in solution during sonication. Fig. 5 provides a comparison of the mass spectrum of an authentic sample of 1,1-dichloro-2,2,3,3-tetramethylcyclopropane and that of the compound detected during the sonication of carbon tetrachloride. The chromatographic retention times of the peaks in each sample were in agreement to within 0.36 s. Furthermore, the correct distribution of abundances and ratios was observed for several characteristic fragments: 131, 95, and 77 AMU. The representative abundances and mass fragments are summarized in Table II.

In a separate set of experiments, the effect of ozone on the degradation kinetics of carbon tetrachloride was determined. Under ambient conditions, ozone does not react appreciably with carbon tetrachloride (Fig. 6) because the central carbon atom is already fully oxidized. Sonication of CCl_4 in the presence of a 56%:44% (v/v) Ar/O_3 mixture (Fig.

7) does not result in enhanced degradation of CCl_4, as would be expected if the initial degradation step is a thermal cleavage of the C-Cl bond.

However, the formation of C_2Cl_4 and C_2Cl_6 was found to be strongly inhibited in ozone saturated solutions, as shown in Fig. 8. The maximum concentrations of both by-products were attained during the early stages of the reaction, regardless of the saturating gas mixture. However, the maximum concentration was substantially less in the presence of ozone.

The results presented in Fig. 9 demonstrate the apparent acceleration of p-NP degradation during sonolysis in a CCl_4 saturated system. In the absence of ultrasonic irradiation, p-NP does not degrade in a saturated solution of CCl_4. However, addition of CCl_4 during sonication of p-NP in an Ar saturated solution enhances the rate constant of p-NP degradation by a factor of 4.5 compared to sonication without CCl_4. The formation of 4-nitrocatechol, an aromatic degradation product, is inhibited in the presence of CCl_4.

DISCUSSION

The weak influence of the initial concentration on the first-order rate constant for the sonolytic degradation of CCl_4 has also been observed by other investigators (34). In contrast, the degradation rate constant of p-NP is inversely correlated to its intitial concentration during sonication (46). CCl_4 appears to undergo pyrolysis in the gas-phase at the center of the bubble as well as in the interfacial region, whereas p-NP reacts predominantly at the interface. The volume of the gas-phase is estimated to be ~2 x 10^4 larger than the volume of the interfacial region (48). Thus, more molecules of CCl_4 than p-NP can react during a single cavitation event. Table III lists the relevant properties of the two substrates. Based on its higher K_{OW}, CCl_4 partitions more effectively to the hydrophobic (49,50) cavitation bubble interface. Furthermore, with a higher vapor pressure and lower boiling point, a greater fraction of CCl_4 will react in the gas-phase.

• Gas-Phase Reactivity of Carbon Tetrachloride

The reaction pathways of CCl_4 during sonolysis can be inferred from combustion and shock tube studies. The thermal dissociation of CCl_4 in an Ar gas-phase is known to produce two chlorine atoms for every molecule of CCl_4; fission of the second chlorine is thought to occur at approximately 10 percent of the rate of primary fission (51). The initial steps of CCl_4 degradation during sonolysis appear to be as follows:

$$CCl_4 \xrightarrow{\Delta} {}^{\cdot}CCl_3 + {}^{\cdot}Cl \qquad (3)$$

$${}^{\cdot}CCl_3 \rightarrow {}:CCl_2 + {}^{\cdot}Cl \qquad (4)$$

Formation of dichlorocarbene, $:CCl_2$ is also thought to occur by the simultaneous elimination of two chlorine atoms (52):

$$CCl_4 \rightarrow {}:CCl_2 + Cl_2 \qquad (5)$$

A third mechanism for dichlorocarbene formation is disproportionation of the trichloromethyl radical which can be inferred from an analogous reaction between the trifluoromethyl radical and the hydrodifluoromethyl radical (53) :

$${}^{\cdot}CCl_3 + {}^{\cdot}CCl_3 \rightarrow CCl_4 + {}:CCl_2 \qquad (6)$$

All three pathways are possible at the hot center of the imploding bubble. The trichloromethyl radical can also couple to form hexachloroethane (54):

$${}^{\cdot}CCl_3 + {}^{\cdot}CCl_3 \rightarrow C_2Cl_6 \qquad (7)$$

The relative rate of disproportionation to that of combination depends on the radical species, but is usually less than one (55). The recombination of the trichloromethyl radical in the gas-phase has been studied, and at 298 K and 1 atm (in Ar) the rate constant of formation of hexachloroethane is approximately an order of magnitude less than the re-formation of CCl_4 (56).

In the presence of oxidizing species, the trichloromethyl radical can act as a scavenger of hydroxyl radical:

$$\dot{C}Cl_3 + \dot{O}H \rightarrow HOCCl_3 \qquad (8)$$

or molecular oxygen: (57):

$$\dot{C}Cl_3 + \dot{O}\text{-}\dot{O} \rightarrow \dot{O}\text{-}OCCl_3 \qquad (9)$$

The relative concentrations of trichloromethyl radical and hydroxyl radical in the gas-phase of a cavitation bubble can be estimated by comparing the carbon-chlorine bond-strength in carbon tetrachloride, 73 kcal mol^{-1} (58), to the hydrogen-oxygen bond-strength in a water molecule, 119 kcal mol^{-1} (59). Thus, sufficient quantities of trichloromethyl radical are formed such that recombination and radical scavenging occur in parallel. At high trichloromethyl radical concentrations in an Ar atmosphere, self-reaction of two CCl_3 radicals appears to be a likely primary reaction.

Based on analogous gas-phase mechanisms, the reactive intermediate $HOCCl_3$ appears to rapidly react to yield phosgene and other products as follows:

$$HOCCl_3 \rightarrow HCl + COCl_2 \qquad (10)$$

$$COCl_2 + H_2O \rightarrow CO_2 + HCl \qquad (11)$$

$$\dot{O} - OCCl_3 + H_2O \rightarrow COCl_2 + HOCl \quad (12)$$

Phosgene hydrolyis in water is rapid (60) under ambient conditions; and the rate constant is positively correlated with temperature (61). Thus, the hydrolysis of this intermediate can be enhanced by the occurrence of supercritical water (45) during cavitional bubble collapse:

$$COCl_2 + H_2O \rightarrow HCl + CO_2 \quad (13)$$

The dichlorocarbene can couple to form tetrachloroethylene:

$$2 :CCl_2 \rightarrow C_2Cl_4 \quad (14)$$

or hydrolyze to carbon monoxide and hydrochloric acid:

$$:CCl_2 + H_2O \rightarrow CO + 2\ HCl \quad (15)$$

Chlorine atoms can combine to form molecular chlorine, which hydrolyzes to hypochlorous acid and chloride ion:

$$2\ \dot{C}l \rightarrow Cl_2 \rightarrow HOCl + Cl^- \quad (16)$$

Chlorine atom recombination in the gas-phase is a termolecular process. If molecular chlorine is the third body, then the recombination rate constant at 298 K is larger ($k = 2.0 \times 10^{10}$ $L^2mol^{-1}s^{-1}$) than when Ar is the third body ($k = 4.4 \times 10^{10}$ $L^2mol^{-1}s^{-1}$) (62). Thus, during a cavitational event, the rate of molecular chlorine formation will vary as the relative ratio of molecular chlorine and Ar atoms varies.

The detection of dichlorocarbene in a sonicated, aqueous solution of CCl_4 confirms the validity of extrapolating gas-phase reaction mechanisms to those occurring in the hottest

regions of the cavitation bubble. Sonolysis of aqueous CCl_4 appears to include similar pathways to those occurring during sonolysis of pure CCl_4 and $CHCl_3$. Spin-trapping studies (63) during ultrasonic irradation of pure CCl_4 indicated the formation of $^{\cdot}Cl$. The formation of a carbene intermediate was also postulated (64) during the sonication of $CHCl_3$. The standard bi-phasic reaction ($NaOH/CHCl_3$) for generating dichlorocarbene in the aqueous phase is enhanced by sonolysis (65), most likely due to enhanced mixing. Characterization of intermediates during sonolysis of aqueous CCl_4 may allow further insight into the mechanism by which CCl_4 enhances sonoluminescence.

The possible enhancement of sonolytic processes by the addition of ozone has been investigated in both chemical and biological systems (66-70). The use of ozone in conjunction with ultrasonic irradiation in this study demonstrates the efficacy of simultaneous treatment processes. The initial refractory compound, CCl_4 is transformed into more reactive species via pyrolysis. Degradation by-products such as C_2Cl_4 can then be attacked by ozone. Various different reaction pathways can be enhanced in a single reactor by combining advanced treatment technologies.

Ozone can react directly with solute molecules, and also decomposes in the gas-phase to yield oxygen atoms and hydroxyl radical as follows: (66):

$$O_3 \rightarrow O_2 + O \tag{17}$$

$$^{\cdot}O + H_2O \rightarrow 2\ ^{\cdot}OH \tag{18}$$

Aqueous ozone decomposition in solution is strongly influenced by pH and results in a variety of reactive species, including superoxide radical and hydrogen peroxide (71). These species may also react with both tetrachloroethylene and hexachloroethane concentrated at the cavitation bubble interface. Ozone and its decomposition products most likely accelerate the decomposition of C_2Cl_4 (72-74) during sonolysis. Direct reaction of ozone with alkenes is facile (75):

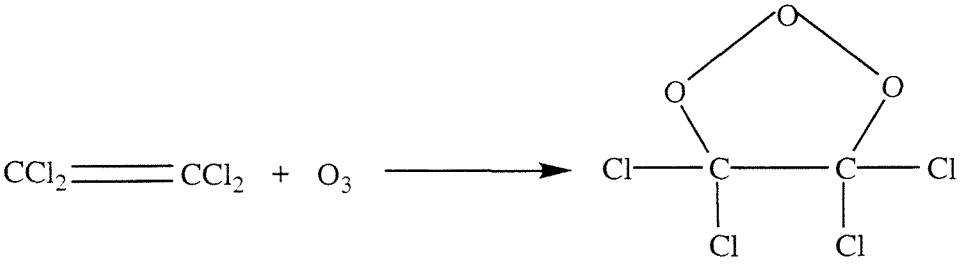

(19)

Rearrangement of the molozonide to the ozonide and subsequent hydrolysis yields phosgene and hydrogen peroxide:

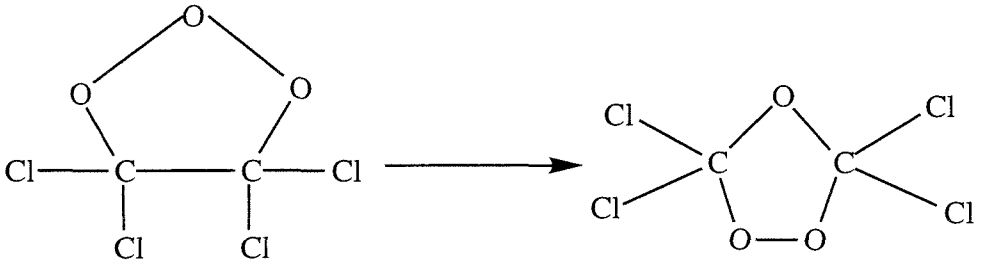

(20)

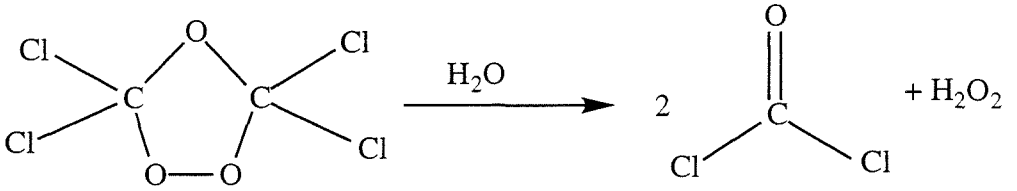

(21)

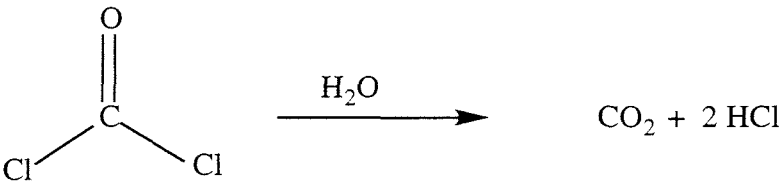

(22)

Hydrolysis of phosgene to carbon dioxide and hydrochloric acid is the final step leading to mineralization.

On the other hand, the decomposition of hexachloroethane is not expected to be influenced by ozone. Thus, a lower concentration of hexachloroethane in an ozone-

saturated, sonicated solution is observed because a greater fraction of the trichloromethyl radical is scavenged before it can couple to form hexachloroethane.

In the absence of ozone, hexachloroethane and tetrachloroethylene (76,77) can react thermally. Because the C-C bond strength is 145 ± 5 kcal mol^{-1} (78) whereas the C-Cl bond strength is 93 kcal mol^{-1} (79), the further degradation of hexachloroethane is probably dominated by thermal cleavage of a C-Cl bond. At pH 6.5, tetrachloroethylene reacts rapidly with hydroxyl radical ($k = 2.8 \times 10^9$ $Lmol^{-1}s^{-1}$) (43,80).

Acceleration of p-NP degradation could occur in several different regions of the sonicated solution. The formation of hypochlorous acid is rapid during sonication of CCl_4. This by-product is highly oxidizing and most likely reacts directly with p-NP in the bulk solution. Micromolar concentrations of chloropicrin (CCl_3NO_2) are obtained when 3-nitrophenol is exposed to 200 μM chlorine (81), while 2-nitrophenol and 2,4-dinitrophenol concentrations are reduced by 76% and 12%, respectively, during chlorination (82).

Reactions at the cavitation bubble interface may involve intermediates from the degradation of both molecules. For example, hydroquinone could react with dichlorocarbene in a similar fashion as 2,3-dimethyl-2-butene:

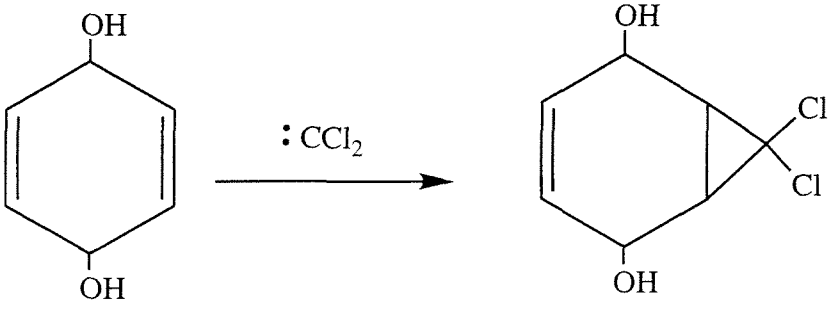

(23)

The results of this investigation suggest that sonolysis is a particularly suitable method for degrading volatile, hydrophobic molecules because these compounds are reactive in the largest region of the cavitation bubble (i.e., the gas-phase). CCl_4 was significantly degraded during sonolysis: 90% reduction was observed after ~12 minutes, and 99% reduction occurred after ~90 min. The quick reduction of CCl_4 is important in

scale-up operations because it allows for a shorter residence time when operating in a continuous-flow mode.

The reactive pathways of CCl_4 in a sonicated, aqueous solution are in agreement with those observed during sonolysis of the pure liquid. Furthermore, detection of dichlorocarbene during sonolysis is important for confirming the mechanism of the formation of tetrachloroethylene. The self-reaction of dichlorocarbene is a likely pathway for the formation of tetrachloroethylene. In addition, the self-coupling reactions of dichlorocarbene and trichloromethyl radicals indicates that both species maybe present in excess of gas-phase oxidizing species, such as hydroxyl radical.

The weak correlation of the apparent first-order degradation rate constant with the initial concentration suggests that despite the high concentration of CCl_4 in the center of the imploding bubble, the final collapse temperature is not significantly reduced at higher solution concentrations. Furthermore, although ozone should also decrease the final collapse temperature because of its lower polytropic index (K_{O_3} = 1.2 vs. K_{Ar} = 1.66), it does not appear to have a significant effect when mixed in the proportion used during this investigation. The influence of the nature of the saturating gas on the temperature at the center of a collapsed cavitation bubble is given by:

$$T_{max} = T_o \left\{ \frac{P_m(K-1)}{P} \right\} = T_o \left(\frac{R_o}{R_{min}} \right)^{3(K-1)} \qquad (24)$$

where T_o = temperature of the bulk solution, K = polytropic index of the gas, P = pressure in the bubble at its maximum size, P_m = pressure in the bubble at the moment of transient collapse (83,84). The effect on sonochemical degradation rates of varyiable Ar/O_3 mixtures should be similar to variations in Ar/O_2 mixtures, which results in a maximum rate of I^- oxidation at a discrete mixture proportion, 70% Ar/30% O_2 (85).

Multi-component wastestreams are a more realistic matrix to consider for practical treatment situations. The sonication of a mixture of CCl_4 and p-NP results in the

enhancement of p-NP degradation and demonstrates that ultrasound is not limited to single solute solutions. Because of the variety of reaction pathways and reactive regions which occur during cavitation, competition between different solutes is minimized. The effect of CCl_4 in a mixed wastestream is particularly interesting because it releases a residual oxidant, which can continue to attack other refractory molecules in solution, after the ultrasonic irradiation is halted.

ACKNOWLEDGMENTS:

The authors wish to thank Wonyong Choi for help with the carbene trapping experiments. Financial support from the Advanced Research Projects Agency, ARPA, (Grant # NAV 5HFMN N0001492J1901), the Office of Naval Research, ONR, and the Electric Power Institute, EPRI, (Grant # RP 8003-37) is gratefully acknowledged.

References

(1) McCarty, P. L., Bouwer, E. J., *App. Env. Microbiol.*, **1983**, *45*, 1286-1294.

(2) Mabey, W., Mill, T., *J. Phys. Chem. Ref. Data,* **1978**, *7*, 383-415.

(3) Kriegman-King, M. R., Reinhard, M., *Environ. Sci. Technol.*, **1992**, *26*, 2198-2206.

(4) Kriegman-King, M. R., Reinhard, M., *Environ. Sci. Technol.*, **1994**, *28*, 692-700.

(5) Ukrainczyk, L., Chibwe, M., Pinnavaia, T. J., Boyd, S. A., *Envriron. Sci. Technol.*, **1995**, *29*, 439-445.

(6) Cox, R. A., Derwent R. G., Eggleton, A. E. J., *Atmos. Environ.*, **1976**, *10*, 305-308.

(7) Davis, D. D., Schmidt, J. F., Neeley, C. M., Hanrahan, R. J., *J. Phys. Chem.*, **1975**, *79*, 11-16.

(8) Molina, M. J., Rowland, F. S., *Geophys. Res. Lett.*, **1974**, *1*, 309-213.

(9) Rhodes, W. J., *J. Air Waste Manage. Assoc.*, **1991**, *41*, 1579-1584.

(10) Tominaga, T., *Pure and Appl. Chem.*, **1992**, *64*, 529-536.

(11) *Handbook of Toxic and Hazardous Chemicals and Carcinogens*; 3rd ed.; Sittig, M., Ed.; Noyes Publishers: Park Ridge, New Jersey, 1991; Vol. 1, pp 848.

(12) Recknagel, R. O., *Pharmacol. Thera.*, **1989**, *12*, 139-154.

(13) Ruch, R. J., Klaunig, J. E., Schultz, N. E., Askari, A. B., Lacher, D. A., Pereira, M. A., Goldblatt, P. J., *Environ. Health Per.*, **1986**, *69*, 310-305.

(14) Slater, T. F., Cheeseman, K. H., Ingold, F. R. S., K U., *Phil. Trans. R. Soc. Lond.*, **1985**, *B311*, 633-645.

(15) Tezuka, M., Momiyama, K., Edano, T., Okada, S., *J. Inorg. Biochem.*, **1991**, *42*, 1-8.

(16) Waller, R. L., Glende, Jr., E. A., Recknagel, R. O., *Biochem. Pharmacol.*, **1983**, *32*, 1613-1617.

(17) Pohl, L. R., George, J. W., *Biochem. Biophys. Res. Comm.*, **1983**, *117*, 367-371.

(18) *Handbook of Environmental Fate and Exposure Data for Organic Chemicals*; Howard, P. M., Ed.; Lewis Publishers, Inc.: Chelsea, 1990; Vol. II, pp 546.

(19) Mackay, D., Shiu, W. Y., Ma, K. C. *Illustrated Handbook of Physical-Chemical Properties and Environmental Fate for Organic Chemicals*; Lewis Publishers: Chelsea, Michigan, 1993; Vol. III, pp. 916.

(20) Petrosius, S. C., Drago, R. S., Young, V., Grunewald, G. C., *J. Am. Chem. Soc.*, **1993**, *115*, 6131-6137.

(21) Taylor, P. H., Dellinger, B., Tirey. D. A., *Int. J. Chem. Kin.*, **1991**, *23*, 1051-1074.

(22) Xiong, T.-Y., Fleming, D. K., Weil, S. A. In *Emerging Technologies in Hazardouse Waste Management II*; W. Tedder Pohland, F. G., Ed.; American Chemical Society: Washington DC, 1991; Vol. 468; pp 12-28.

(23) Matheson, L. J., Tratnyek, P. G., *Environ. Sci. Technol.*, **1994**, *28*, 2045-2053.

(24) Bromberg, L., Cohn, D. R., Koch, M., Patrick, R. M., Thomas, P., *Phys. Lett. A*, **1993**, *173*, 293-299.

(25) Rosocha, L. A., Secker, D. A., Smith, J.D. In *Emerging Technologies for Hazardous Waste Management*; W. Tedder Pohland, F. G., Ed.; American Chemical Society: Washington DC, 1994; Vol. 554; pp 184-196.

(26) Narayanan, B., Suidan, M. T., Gelderloos, A. B., Brenner, R. C., *Wat. Res.*, **1993**, *27*, 181-194.

(27) Loraine, G. A., *Haz. Waste Haz. Mat.*, **1993**, *10*, 185-194.

(28) Elliott, D. C., Phelps, M. R., Sealock, Jr., L. J., Baker, E. G., *Ind. Eng. Chem. Res.*, **1994**, *33*, 566-574.

(29) Cheung, H. M., Kurup, S., *Environ. Sci. Technol.*, **1994**, *28*, 1619-1622.

(30) Bhatnagar, A.; Cheung, H. M., *Environ. Sci. Technol.*, **1994**, *28*, 1481-1486.

(31) Cheung, H. M.; Bhatnagar, A.; Jansen, G., *Environ. Sci. Technol.*, **1991**, *25*, 1510-1512.

(32) Inazu, K., Nagata, Y., Maeda, Y., *Chem. Lett.*, **1993**, 57-60.

(33) Lur'e, Y. Y., Kandzas, P. F., Mokina, A. A., *Russ. J. Phys. Chem.*, **1963**, *37*, 6-8.

(34) Wu, J. M., Huang, H. S., Livengood, C. D., *Environ. Prog.*, **1992**, *11*, 195-201.

(35) Mason, T. J.; Lorimer, J. P. *Sonochemistry: Theory, Applications and Uses of Ultrasound in Chemistry*; Ellis Horwood Ltd.: Chichester, 1988.

(36) *Ultrasound: Its Chemical, Physical and Biological Effects*; Suslick, K. S., Ed.; VCH Publishers, Inc.: New York, 1988.

(37) Weissler, A. C., H. W., Snyder, S., *J. Am. Chem. Soc.*, **1950**, *72*, 1769-1775.

(38) Chendke, P. K.; Fogler, H. S., *J. Phys. Chem.*, **1983**, *87*, 1362-1369.

(39) Finch, R. D., *Ultrasonics*, **1963**, *1*, 87-98.

(40) Alippi, A.; Cataldo, F.; Galbato, A., *Ultrasonics*, **1992**, *30*, 148-151.

(41) Voglet, N.; Mullie, F.; Lepoint, T., *New J. Chem.*, **1993**, *17*, 519-521.

(42) Spurlock, L. A., Reifsneider, S. B., *J. Am. Chem. Soc.*, **1970**, *92*, 6112-6117.

(43) Buxton, G. V., Greenstock, C. L., Helman, W. P., Ross, A. B., *J. Phys. Chem. Ref. Data*, **1988**, *17*, 513-886.

(44) Hoigné, J., Bader, H., *Wat. Res.*, **1981**, *15*, 449-456.

(45) Hua, I.; Höchemer, R. H.; Hoffmann, M. R., *J. Phys. Chem.*, **1995**, *99*, 2335-2342.

(46) Kotronarou, A.; Mills, G.; Hoffmann, M. R., *J. Phys. Chem.*, **1991**, *95*, 3630-3638.

(47) Mason, T. J. *Practical Sonochemistry User's Guide to Applications in Chemistry and Chemical Engineering*; Ellis Horwood: West Sussex, England, 1991, pp. 186.

(48) Suslick, K. S., Hammerton, D. A., *Ferroelec. Freq. Cont. UFCC-33*, **1986**, *2*, 143-147.

(49) Henglein, A., Kormann, C., *Int. J. Radiat. Biol.*, **1985**, *48*, 251-258.

(50) Kondo, T., Riesz, P., *Free Rad. Biol. Med.*, **1989**, *7*, 259-268.

(51) Michael, J. V., Lim, K. P., Kumaran, S. S., Kiefer, J. H., *J. Phys. Chem.*, **1993**, *97*, 1914-1919.

(52) Songlin, X., Harmony, M. D., *Chem. Phys. Lett.*, **1993**, *205*, 502-507.

(53) Pritchard, G. O., Perona, M. J., *Int. J. Chem. Kinetics,* **1969**, *1*, 413-425.

(54) Matheson, I. A., Sidebottom, H. W., Tedder, J. M., *Int. J. Chem. Kinetics,* **1974**, *6*, 493-506.

(55) Nonhebel, D. C., Walton, J. C. *Free-radical Chemistry*; Cambridge University Press: Cambridge, 1974, pp. 572.

(56) Ellermann, T., *Chem. Phys. Lett.*, **1992**, *189*, 175-181.

(57) Slater, T. F. In *Biological Reactive Intermediates: Chemical Mechanisms and Biological Effects*; R. Snyder Parke, D. V., Kocsis, J., Jollow, D. J., Gibson, G. G., Ed.; Plenum Publishing Co.: New York, 1982; pp 575-609.

(58) Cox, J. D., Pilcher, G. *Thermochemistry of Organic and Organometallic Compounds*; Academic Press: London, 1970.

(59) *Handbook of Chemistry and Physics*; 56th ed.; Weast, R. C., Ed.; CRC Press: Ohio, 1975.

(60) Manogue, W. H., Pigford, R. L., *Am. Inst. Chem. Eng. J.*, **1960**, *6*, 494-.

(61) Mertens, R., von Sonntag, C., Lind, J., Merenyi, G., *Angew. Chem. Int. Ed. Engl.*, **1994**, *33*, 1259-1261.

(62) Clyne, M. A. A., Stedman, D. H., *Trans. Faraday Soc.*, **1968**, *64*, 2698-2707.

(63) Rosenthal, I., Mossoba, M. M., Riesz, P., *J. Mag. Res.*, **1981**, *45*, 359-361.

(64) Henglein, A., Fischer, C. H.,, *Ber. Bunsen-Ges. Phys. Chem.*, **1984**, *88*, 1196-1199.

(65) Regen, S. L.; Singh, A., *J. Org. Chem.*, **1982**, *47*, 1587-1588.

(66) Hart, E. J., Henglein, A., *J. Phys. Chem.*, **1986**, *90*, 3061-3062.

(67) Olson, T. M.; Barbier, P. F., *Wat. Res.*, **1994**, *28*, 1383-1391.

(68) Sierka, R. A., *Ozone Sci. E Vol,* **1984**, *6*, 275-290.

(69) Sierka, R. A., Amy, G.L., *Ozone Sci. E Vol,* **1985**, *7*, 47-62.

(70) Lozier, J. C., Sierka, R. A., *Journal AWWA,* **1985**, *78*, 60-65.

(71) *Ozone in Water Treatment Application and Engineering*; Langlais, B., Reckhow, D. A., Brink, D. R., Ed.; Lewis Publishers, Inc.: Chelsea, Michigan, 1991, pp 569.

(72) Gehringer, P., Proksch, E., Szinovatz, W., Eschweiler, H., *Wat. Res.,* **1988**, *22*, 645-646.

(73) Kusakabe, K., Aso, S., Wada, T., Hayashi, J. I., Morooka, S., Isomura, K., *Wat. Res.,* **1991**, *25*, 1199-1203.

(74) Peyton, G. R., Huang, F. Y., Burleson, J. L., Glaze, W. H., *Environ. Sci. Technol.,* **1982**, *16*, 448-453.

(75) Streitweisser, A. J., Heathcock, C. H. *Introduction to Organic Chemistry;* Third ed.; Macmillan Publishing Co.: New York, 1985, pp. 1197.

(76) Tirey, D. A., Taylor, P. H., Kasner, J., Dellinger, B., *Combust. Sci. and Tech.,* **1990**, *74*, 137-157.

(77) Yasuhara, A., *Chemosphere,* **1993**, *26*, 1507-1512.

(78) Darwent, B. d. B. "Bond Dissociation Energies in Simple Molecules," National Bureau of Standards, 1970.

(79) Kent, R. A., Margrave, J. L., *J. Am. Chem. Soc.,* **1965**, *87*, 3582-3585.

(80) Itoh, N., Kutsuna, S., Ibusuki, T., *Chemosphere,* **1994**, *28*, 2029-2040.

(81) Thibaud, H., De Laat, J., Dore, M. In ; R. L. Jolley Condie, L. W., Johnson, J. D., Katz, S., Minear, R. A., Mattice, J. S., Jacobs, V. A., Ed.; Lewis Publishers, Inc.: Chelsea, Michigan, 1987; Vol. 6; pp 681-690.

(82) Lee, Y. S., Hunter, J. V. In ; R. L. Jolley Bull, R. J., Davis, W. P., Katz, S., Roberts, M. H. Jr., Jacobs, V. A., Ed.; Lewis Publishers, Inc.: Chelsea, Michigan, 1985; Vol. 5; pp 1515-1526.

(83) Noltingk, B. E., and Neppiras, E. A., *Proc. Phys. Soc. B. (London),* **1950**, *63B*, 674-685.

(84) Neppiras, E. A., Noltingk, B. E., *Proc. Phys. Soc. B (London),* **1951**, *64B*, 1032-1038.

(85) Hart, E. J., Henglein, A., *J. Phys. Chem.,* **1985**, *89*, 4342-4347.

(86) Howard, P. M. *Handbook of Environmental Fate and Exposure Data for Organic Chemicals: Large Production and Priority Pollutants*; Lewis Publishers: Chelsea, Michigan, 1989; Vol. I, pp. 574.

(87) Schwarzenbach, R. P., Stierl, R., Folsom, B. R., Zeyer, J., *Environ. Sci. Technol.,* **1987**, *22*, 83-92.

Figure Captions

Figure 1: Schematic diagram of a gas-tight glass reactor cell with a Teflon® collar for attachment to stainless steel sonication probe.

Figure 2: Change in concentration of CCl_4 as a function of time in a stirred solution at 25 ° C without sonication.

Figure 3: Variation of the degradation rate constant with initial carbon tetrachloride concentration.

Figure 4: Concentration of 1,1-dichloro-2,2,3,3-tetramethylcyclopropane as a function of sonication time.

Figure 5: **a.** Mass spectrum of 100 μM 1,1-dichloro- 2,2,3,3-tetramethylcyclopropane. **b.** Mass spectrum of an aliquot withdrawn after 15 min. of sonication of an aqueous solution saturated with CCl_4, 2,3-dimethylbutene and Ar.

Figure 6: Ozonolysis of CCl_4 under ambient conditions. pH ~6, T = 25 ° C.

Figure 7: Effect of ozonolysis on the degradation of carbon tetrachloride during sonolysis.

Figure 8: Effect of ozonolysis on the accumulation of C_2Cl_6 and C_2Cl_6 in a sonicated solution of aqueous CCl_4.

Figure 9: Enhancement of p-NP sonolytic degradation by addition of CCl_4.

——— y = -0.0182 + -0.0190x R= 0.995

- - - - - y = 0.0131 + -0.00425x R= 0.988

Table I

Final Distribution of Chlorine Atoms in a Sonicated Solution of CCl_4 After 90 min of Sonolysis

Species	Initial concentration, μM	Final concentration, μM
CCl_4	4.0×10^2	4.0
C_2Cl_4	ND*	3.1×10^{-3}
C_2Cl_6	ND	8.4×10^{-2}
Cl^-	ND	1.1×10^3
HOCl	ND	1.3×10^2

*Not detected

Table II

Abundances of Major Mass Fragments for Identification of Dichlorocarbene

Sample	131 amu	95 amu	77 amu
**$C_7H_{12}Cl_2$	7.09×10^4	2.36×10^4	3.59×10^4
*sonicated sample	9.78×10^2	3.98×10^2	5.44×10^2

** 100 μM 1,1-dichloro-2,2,3,3-tetramethylcyclopropane

*Sonication of an aqueous solution saturated with CCl_4, C_6H_{12}, and Ar.

Table III

Selected Physical Properties of Carbon Tetrachloride and *p*-Nitrophenol

Compound	Log K_{OW}	Vapor Pressure, mmHg	Boiling Point,°C
CCl_4	2.83	114	77
p-NP	1.91	1.00×10^3	2.8×10^2 (dec)

Data in this table was taken from Ref. (18,86,87).

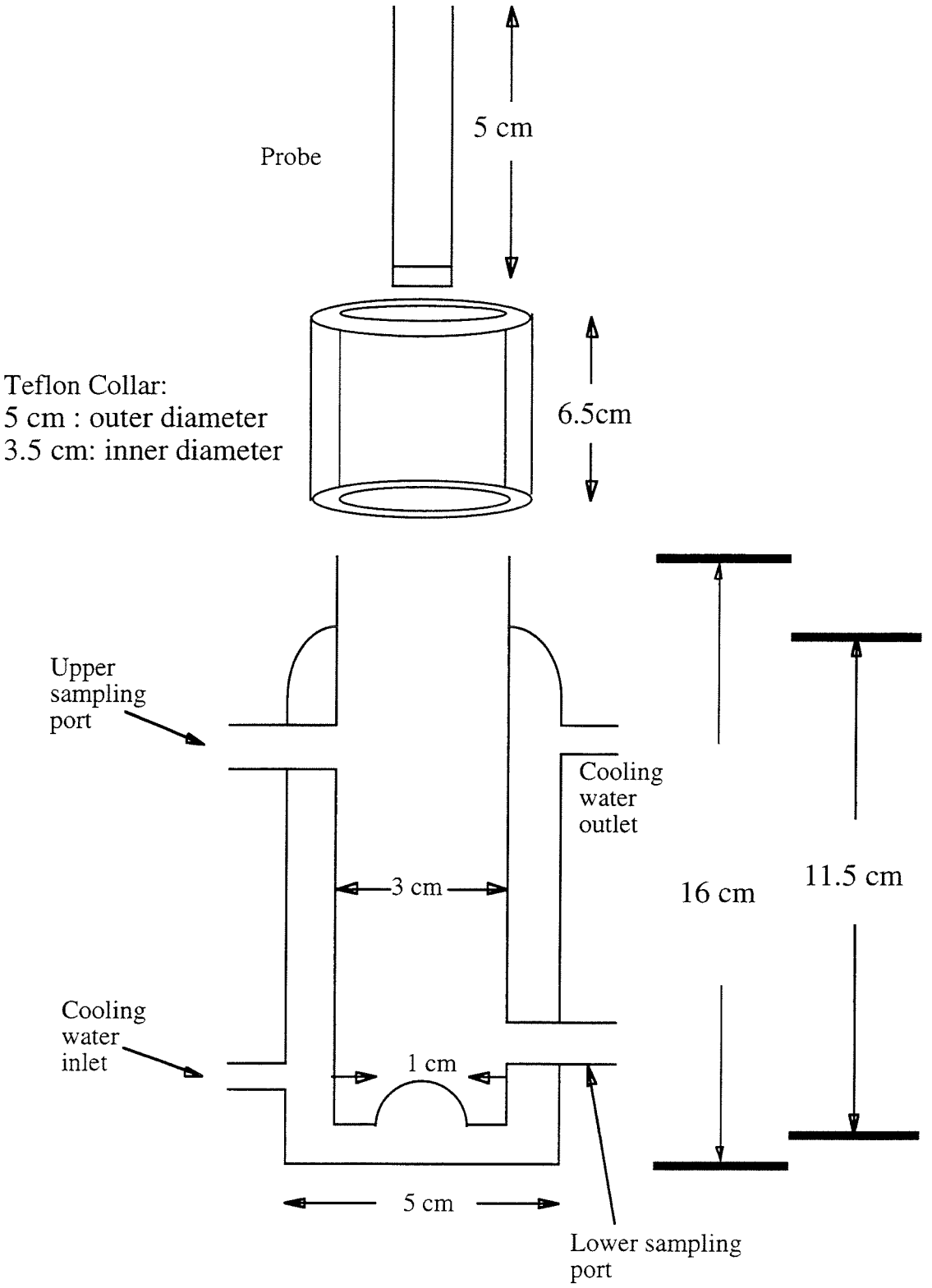

Fig. 1: Schematic diagram of a gas-tight glass reactor cell with a Teflon® collar for attachment to stainless steel sonication probe.

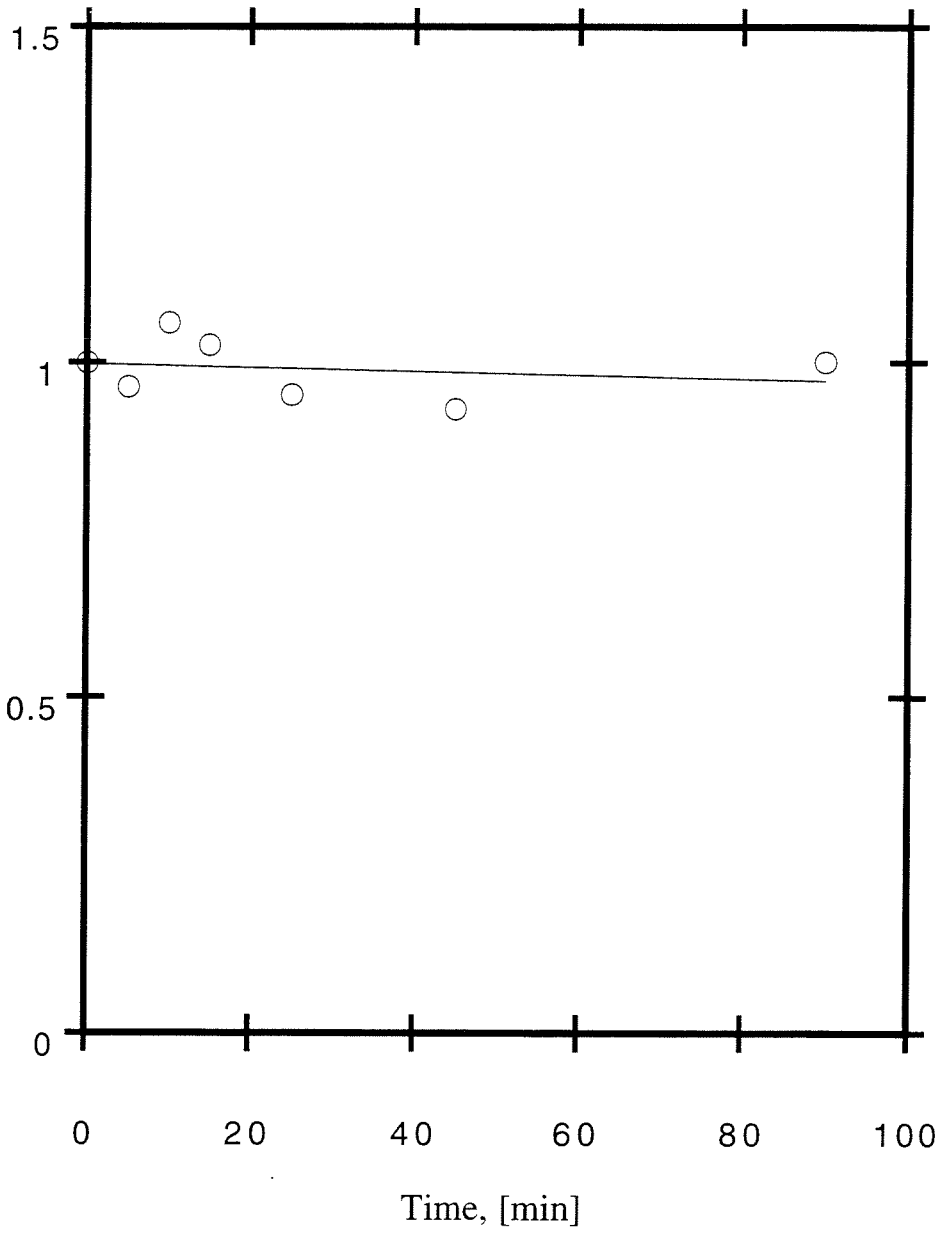

Fig. 2: Change in concentration of CCl_4 as a function of time in a stirred solution at 25 ^{o} C without sonication.

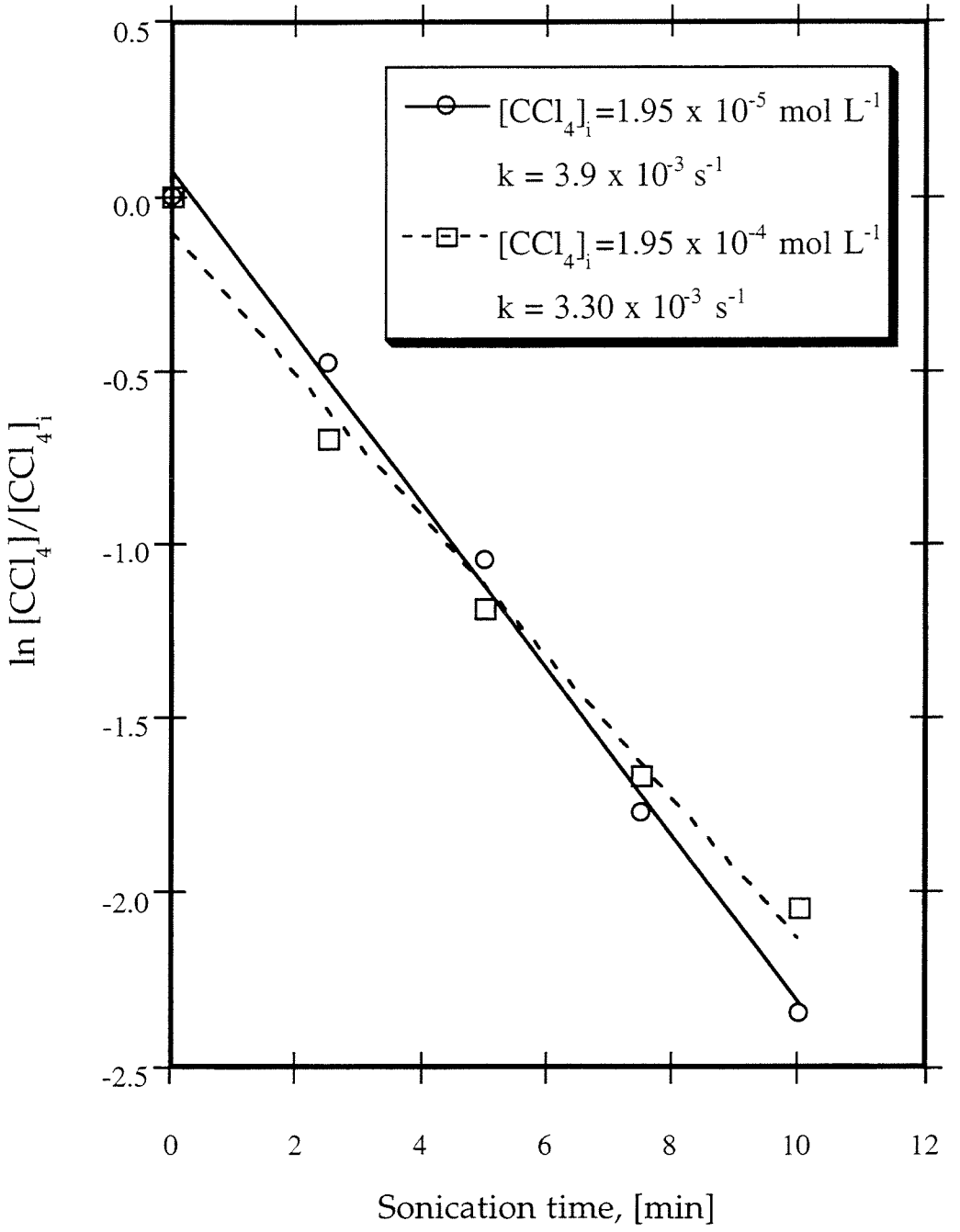

Fig. 3: Variation of the degradation rate constant with initial carbon tetrachloride concentration.

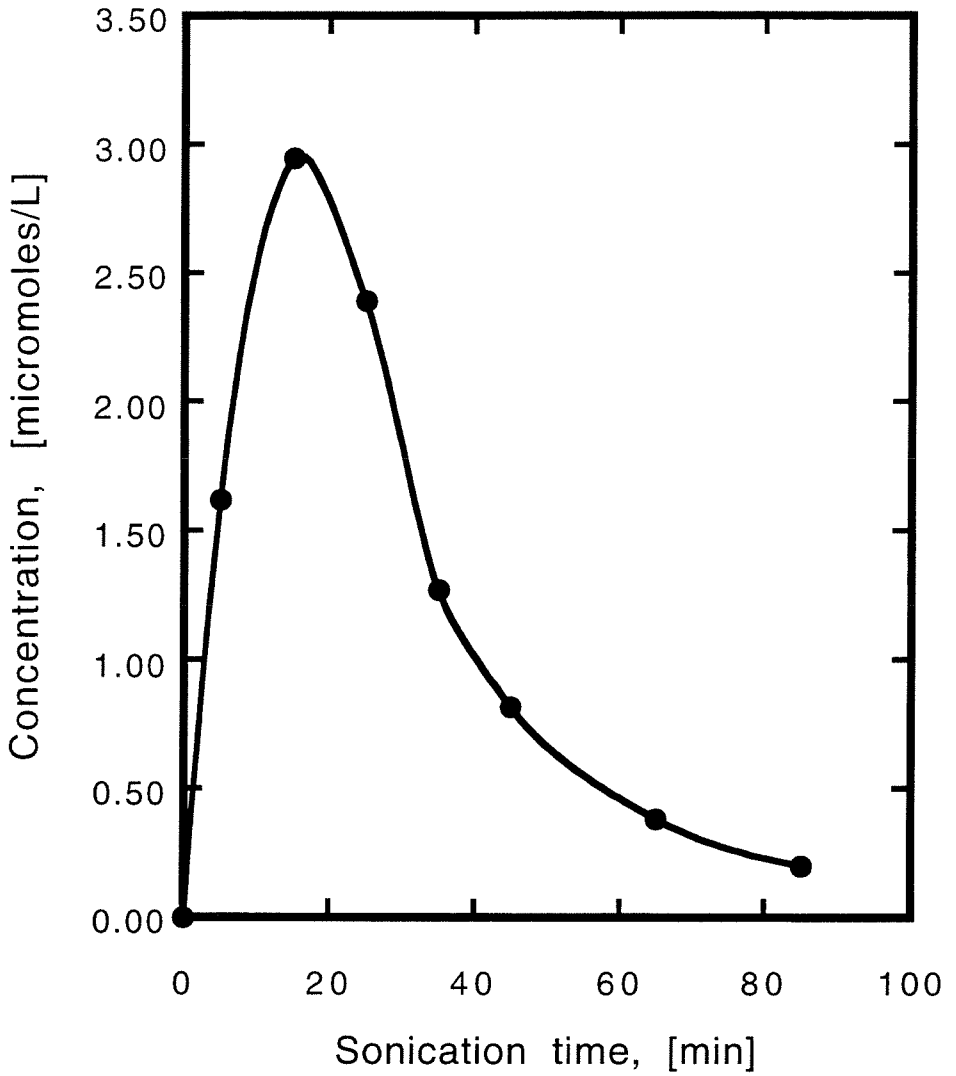

Fig. 4: Concentration of 1,1-dichloro-2,2,3,3-tetramethylcyclopropane as a function of sonication time.

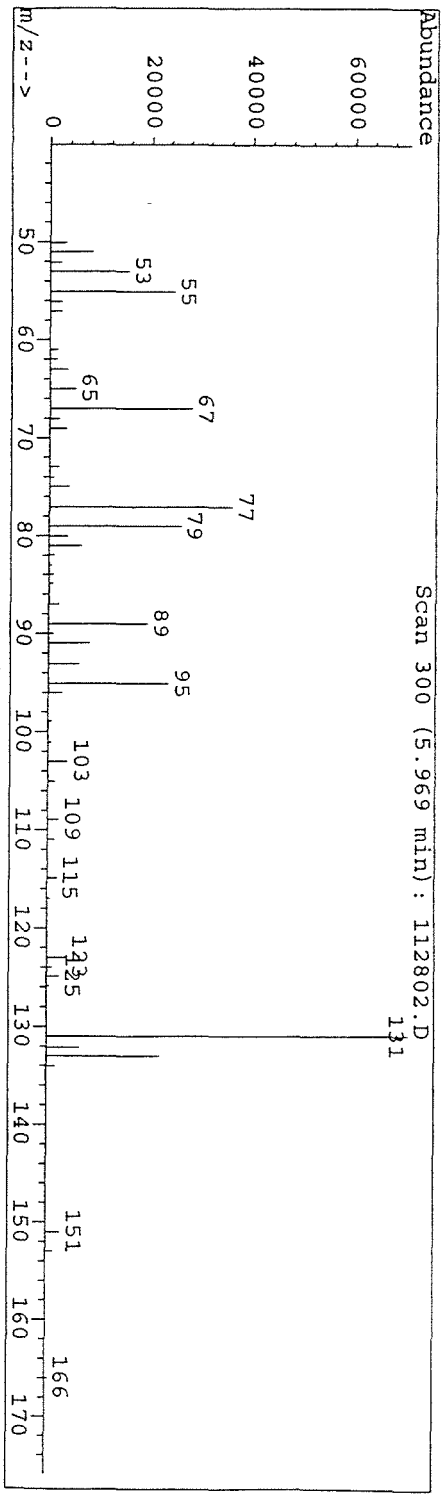

Fig. 5a: Mass spectrum of 100 µM 1,1-dichloro- 2,2,3,3-tetramethylcyclopropane.

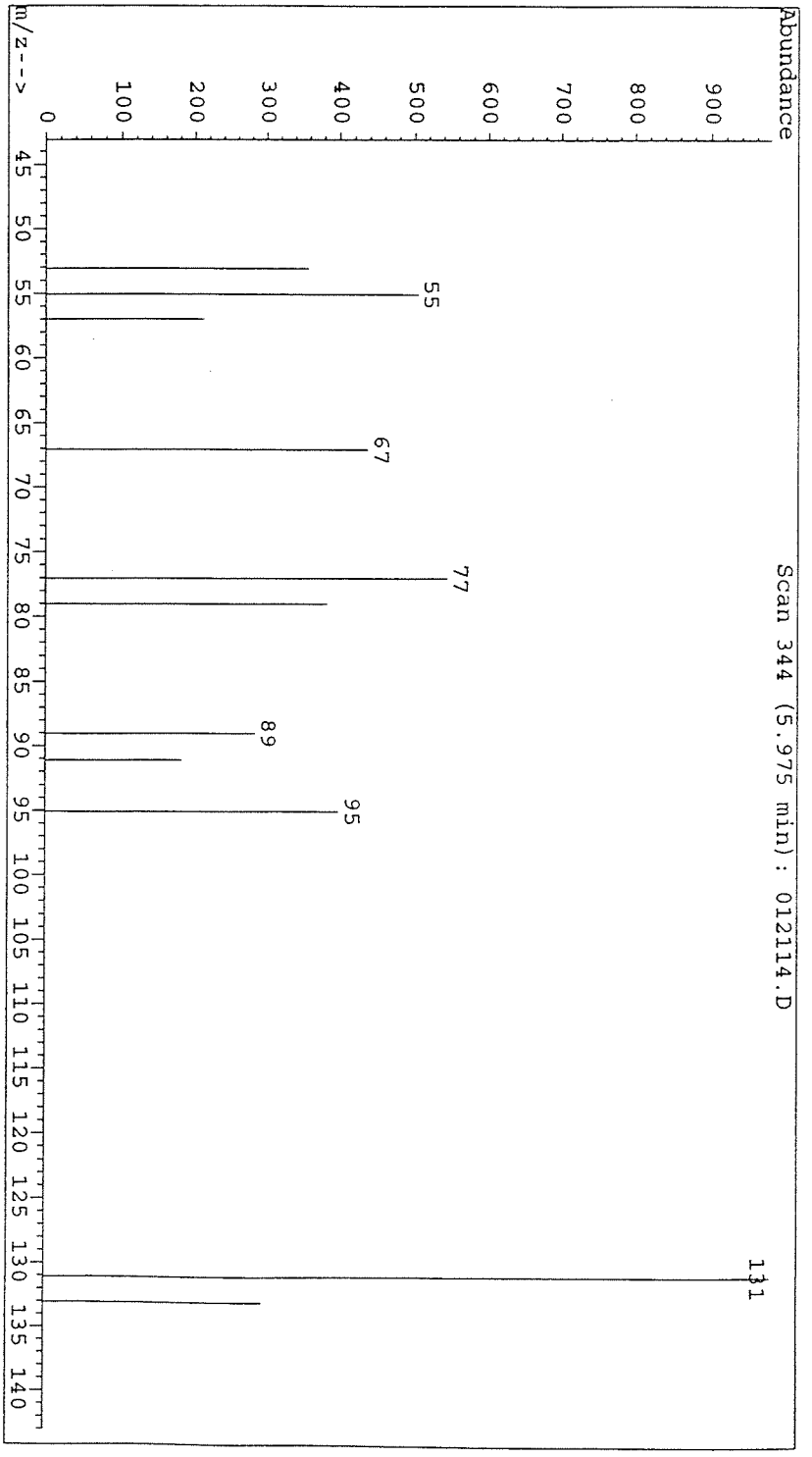

Fig 5b: Mass spectrum of an aliquot withdrawn after 15 min. of sonication of an aqueous solution saturated with CCl_4, 2,3-dimethylbutene and Ar.

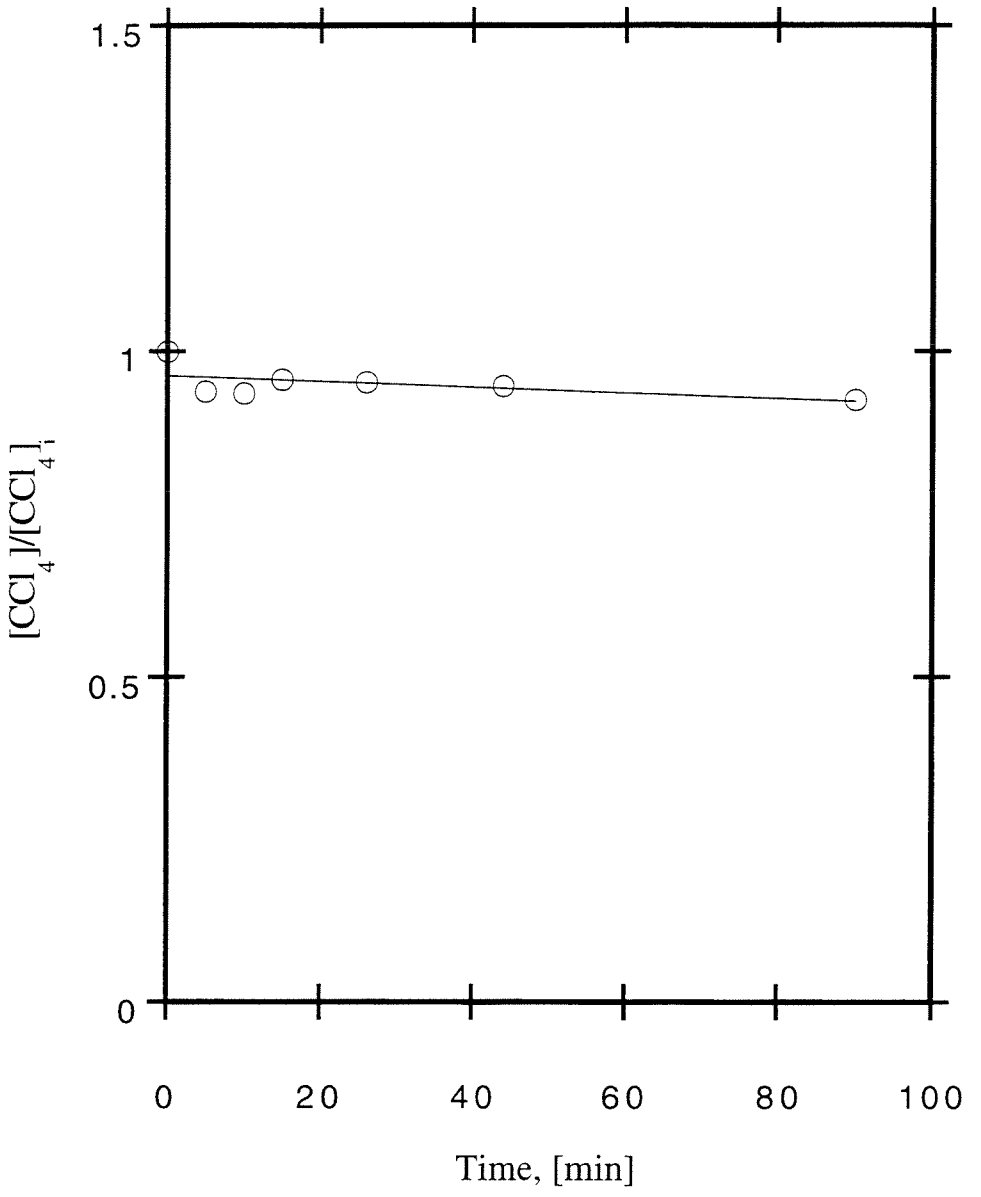

Fig. 6 : Ozonolysis of CCl_4 under ambient conditions. pH ~6, T = 25 ^{o} C.

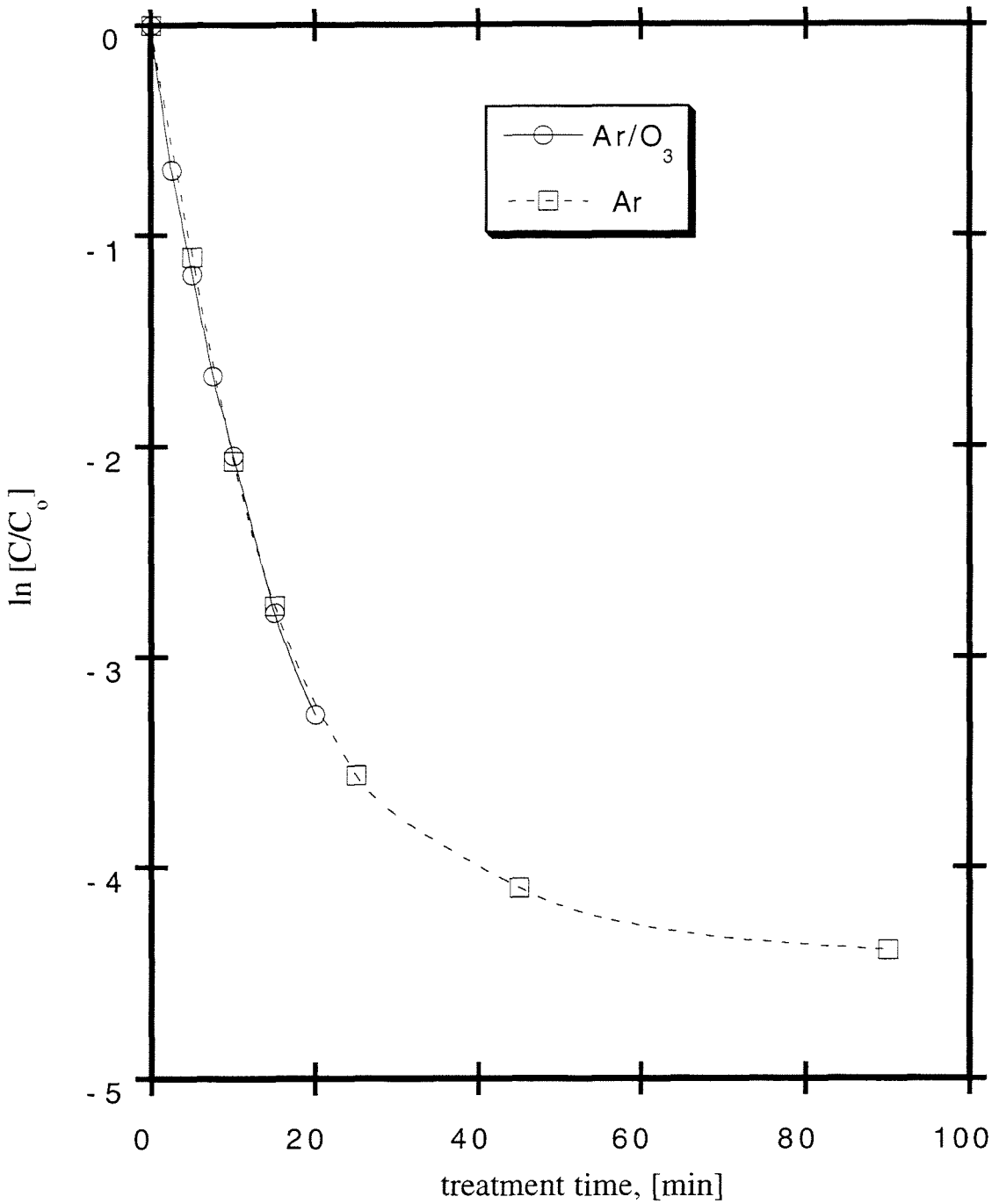

Fig. 7: Effect of ozonolysis on the degradation of carbon tetrachloride during sonolysis.

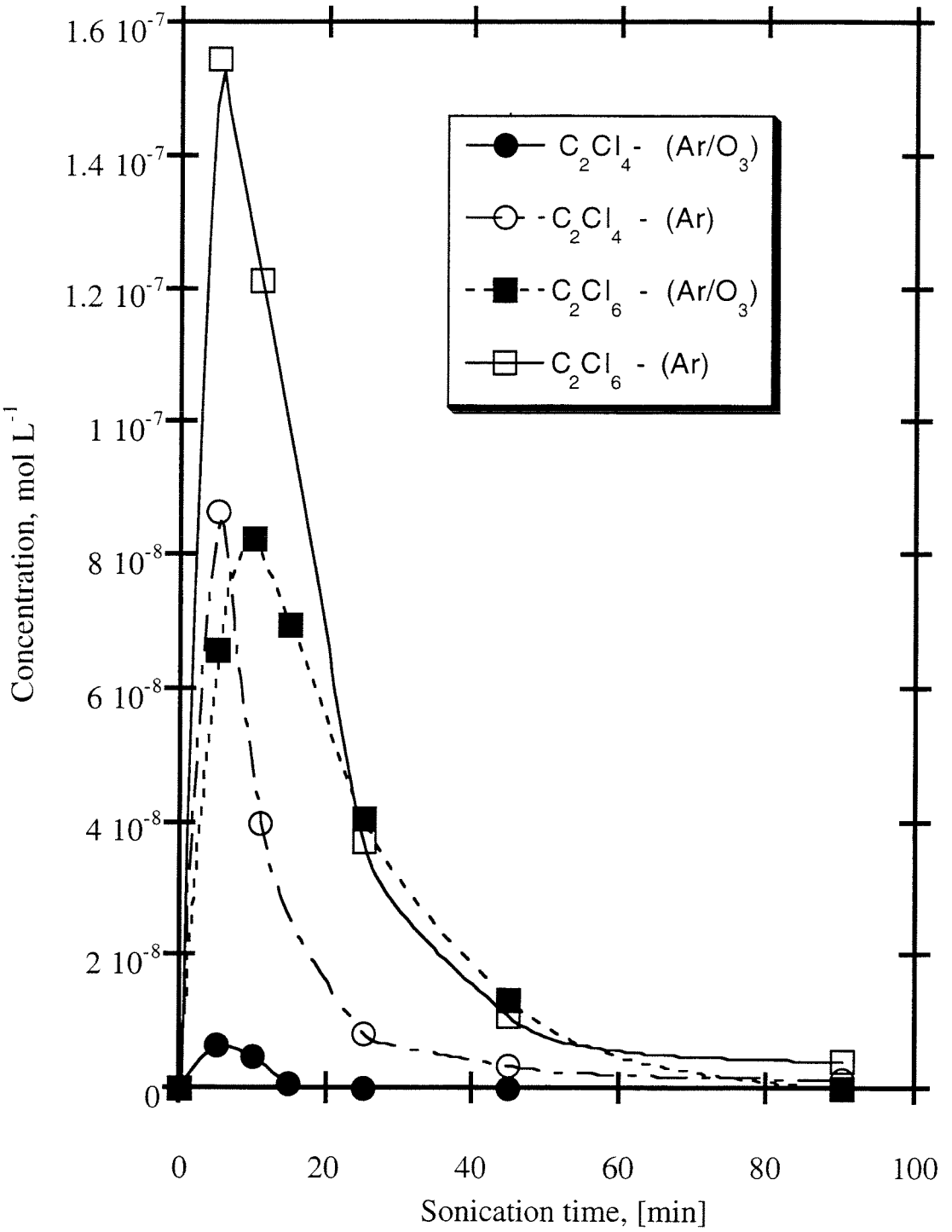

Fig. 8 : Effect of ozonolysis on the accumulation of C_2Cl_4 and C_2Cl_6 in a sonicated solution of aqueous CCl_4.

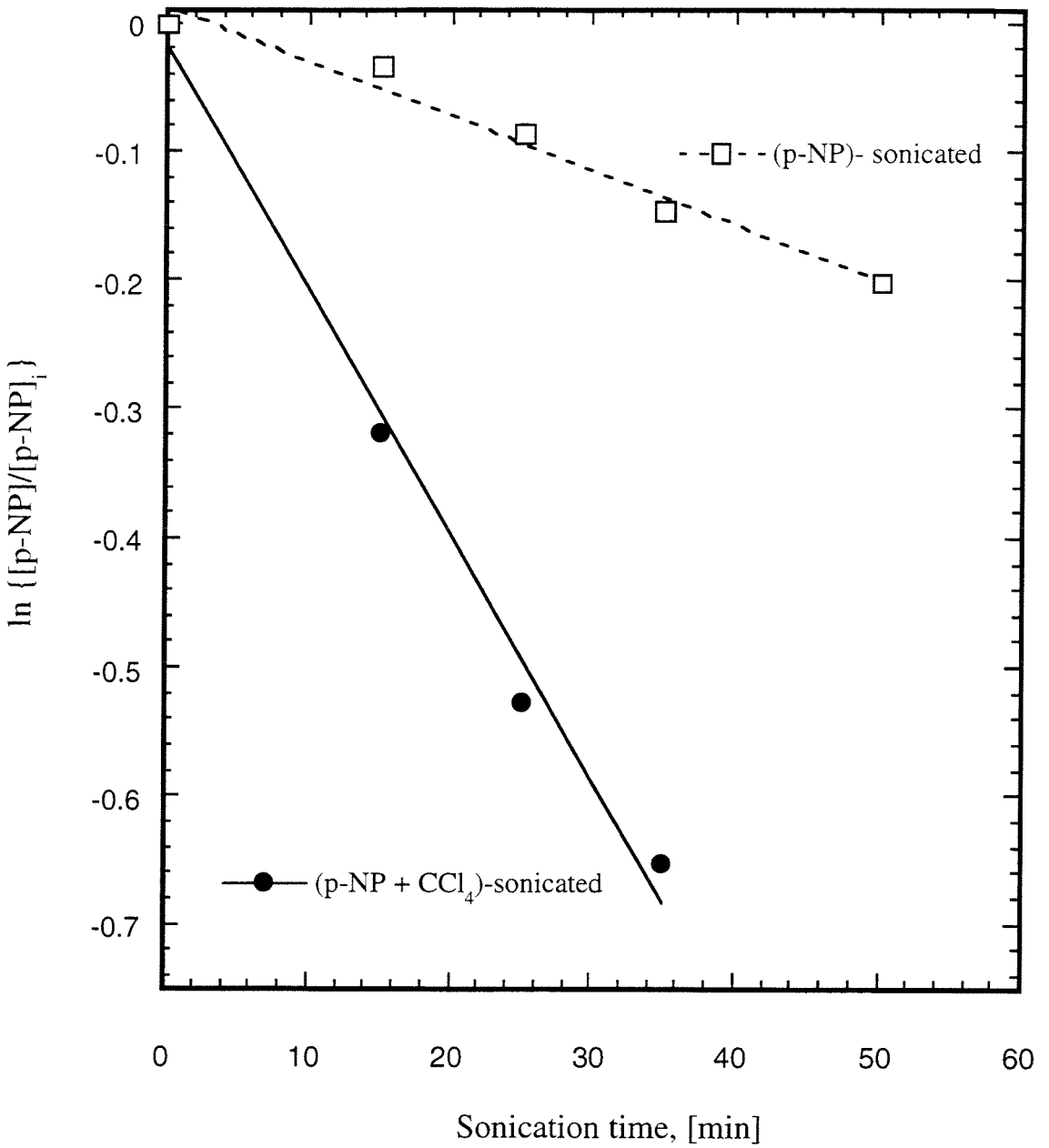

Fig. 7: Enhancement of p-NP sonolytic degradation by addition of CCl_4.

——— y = -0.0182 + -0.0190x R= 0.995

- - - - - y = 0.0131 + -0.00425x R= 0.988

Chapter 5:

Sonochemical Production of Hydroxyl Radical and Hydrogen Peroxide: The Effect of Frequency and Saturating Gas

[Inez Hua and Michael R. Hoffmann, submitted to *J. Phys. Chem.* 1995]

Abstract

The sonolytic production of hydrogen peroxide (H_2O_2) and hydroxyl radical ($^{\bullet}OH$) has been investigated at ultrasonic frequencies of 20, 40, 80 and 500 kHz and with four saturating gases (Kr, Ar, He, O_2) at each frequency. The largest rate constants for the production of H_2O_2 at pH 7 (3.57 $\mu M\ min^{-1}$) and $^{\bullet}OH$ at pH 11 (0.47 $\mu M\ min^{-1}$) are observed during irradiation of Kr-saturated solutions at 500 kHz. Irradiation of He-saturated solutions at 20 kHz yields the slowest production rate constants for both H_2O_2 and $^{\bullet}OH$: 0.05 $\mu M\ min^{-1}$ and 0.031 $\mu M\ min^{-1}$, respectively.

Both the frequency and the saturating gas significantly influence the sonochemical rates of production of $^{\bullet}OH$ and H_2O_2. At 20 kHz, the rate contants for production of H_2O_2 varied over an order of magnitude when different saturating gases were employed (0.05 $\mu M\ min^{-1}$ to 1.31 $\mu M\ min^{-1}$). In contrast, at 80 kHz, the rate constants ranged from (0.76 $\mu M\ min^{-1}$ to 2.24 $\mu M\ min^{-1}$) Similar trends were observed for the production of $^{\bullet}OH$ at the same frequencies and under the same saturating gases. The diminishing differences between the saturating gases at higher frequencies are attributed to the change in bubble dynamics as the resonant radius decreases. The resonant radii are approximately 177, 88, 44, and 7μm at 20, 40, 80 and 500 kHz. The change in bubble size influences the time required for bubble collapse and may result in near isothermal behavior for smaller bubbles.

The production rates for each species were found to increase with increasing frequency. Sonication at 500 kHz or 80 kHz resulted in faster production rates than sonication at 20 or 40 kHz, regardless of the saturating gas.

INTRODUCTION

Acoustic cavitation is the cyclical growth and collapse of cavitation bubbles during the irradiation of liquids with ultrasound. As a result of bubble implosion, extreme temperatures and pressures exist at the center of the bubble which facilitate enhanced chemical reactivity (1,2). Reactions in organic solvents as well as in aqueous solutions have been studied (3,4), and electrochemical methods have been utilized to examine the hydrodynamics of cavitation (5-7). The efficient degradation of various organic contaminants in aqueous solution has been demonstrated (8-24), and results from the extreme physical conditions and the production of oxidizing species. However, sonochemical effects need to be optimized by manipulation of the physics of cavitation. In particular, maximizing the production of oxidizing species, such as hydroxyl radical and hydrogen peroxide, would benefit the application of ultrasonic irradiation to remediation problems.

The role of ultrasonic frequency in determining cavitation bubble physics and chemistry has not been systematically investigated until recently (25-31). Recent reports indicate that reaction rates are more generally enhanced by irradiating with higher frequencies than with standard frequencies used in chemical laboratories (i.e., 16-20 kHz). The rate of potassium iodide production is reported to be higher at 900 kHz than at 20 kHz (30), while the degradation of phenol (25) was determined to be approximately ten times higher at 487 kHz than at 20 kHz. Other investigators have compared the oxidation rate of potassium iodide (29) at 20, 40 and 60 kHz.

Sonoluminescence, the emission of light from cavitating bubbles, is also affected by the ultrasonic frequency. Both the intensity and emission spectrum of sonoluminscence are altered when cavitation is induced with different ultrasonic frequencies (32-35). The total sonoluminscence intensity in an Ar-saturated solution was found to be maximal at 337 kHz, compared to 1.1 MHz and 22 kHz. This is of interest because emission by hydroxyl

radical is implicated in multiple-bubble sonoluminescence (36). The significance of ultrasonic frequency is further implicated by the strong correlation between sonoluminscence intensity and reaction rate enhancement during cavitation (37).

In this paper, we examine the rates of production of hydroxyl radical and hydrogen peroxide in aqueous solution during sonolysis at four ultrasonic frequencies: 20, 40, 80 and 500 kHz in the presence of four saturating gases (Kr, Ar, O_2, and He). Our working hypothesis is that both the ultrasonic frequency and the physico-chemical properties of the saturating gas determine the optimal production rates of $^{\bullet}OH$ and H_2O_2.

EXPERIMENTAL METHODS

Ultrapure water was obtained from a MilliQ Plus UV System, and had a minimum resistance of 18.2 mΩ. All reagents were reagent grade and used as received. Potassium hydroxide pellets and ammonium molybdate were obtained from Mallinckrodt. Potassium iodide and potassium biphthalate were obtained from JT Baker. 0.1N sodium hydroxide, sodium phosphate dibasic, and 30% hydrogen peroxide were obtained from EM Science while phosphate buffer capsules (pH 7) were obtained from Microessential Laboratory. Terephthalic acid (98%) and 2-bromoterephthalic acid (97%) were obtained commercially (Aldrich Chemical Company) while hydroxyterephthalic acid was synthesized following standard procedures.(38) Compressed gases were obtained from Air Liquide (Walnut Creek, CA).

Sonications were performed with an Undatim Sonoreactor® (20, 40, 80 kHz) or an Undatim power generator, built for the 500 kHz transducer. (Undatim Ultrasonics S. A., Louvain-La-Neuve, Belgium). The temperature of the sonicated solutions was maintained at 25-30 °C with a Haake A80 Refrigerated Bath and Circulator (Haake Inc., Saddle Brook, New Jersey). The temperature of the cooling water was maintained at 20.0± 0.1 °C. Replaceable titanium tips (20 and 40 kHz transducers) were polished with wetted

sand-paper as needed and tightened before each use to prevent solvent intrusion into the cavity. The peizoelectric transducers were maintained at a constant temperature by passing a stream of compressed air through a plastic fitting inserted into the housing. Because of differences in the reactor configurations, sonications performed at 80 kHz were done with 100 mL of solution, those at 20 and 40 kHz were done with 200 mL of solution, and irradiations at 500 kHz were done with 600 mL of solution. Table I contains information about the physical dimensions of the transducers at each of the four frequencies used during this study. Figs. 1-2 illustrate the different reactor configurations used for each frequency. Sonications were performed with four different saturating gases at each of four frequencies. Solutions were pre-sparged for 30 min. at a flow-rate of approximately 80 mL/min, before and during each sonication. In order to facilitate gas and heat transfer, solutions were stirred during the pre-sparge stage and during sonication with a Teflon® stir-bar and a magnetic stirring motor.

Calorimetry measurements were performed at each of the four frequencies, and at the given power settings and solution volumes used during sonications. The power output was calculated from the change in temperature, as described elsewhere (3). Results and specific conditions are given in Table II.

Hydroxyl radical was trapped by direct reaction with terephthalic acid. Terephthalic acid solutions (1.5 mM) were prepared in a phosphate buffer (6.8×10^{-4} M sodium hydroxide and 4.1×10^{-3} M sodium phosphate dibasic) at pH of 10.9 ± 0.1. Optimal pH and concentration ranges were determined previously (39). At various time intervals during sonication, 3.0 mL samples were taken and transferred to a quartz fluorescence cell in the fluorimeter. Samples irradiated at the lower frequencies (20 and 40 kHz) were filtered with Acrodisc® 0.2 mM PFTE syringe filters (Gelman Sciences). Fluorescence measurements were made with a Shimadzu Spectrofluorophotometer, RF-540 and a Shimadzu Data Record DR-3. The slit width for the excitation and emission beams was 5 nm and 2nm, respectively. It should be noted that the fluorescence response factor, and

thus the senstivity of the method, will vary depending on the slit widths chosen. The ordinate multiplier was four. Solutions of sonicated terephthalate were excited at 310 nm and the emission measured at 425 nm.

Electron paramagnetic resonance (EPR) measurements were performed with an E-line Century X-band spectrometer (Varian) equipped with a multipurpose cavity maintained at 298 K. 25 ml of an Ar-saturated, 10^{-2} M aqueous solution of 2,2,6,6-tetramethyl-4-piperidone monohydrate (TMPone) was placed in a water-jacketed stainless steel reactor cell and sonicated at 20 kHz with a Sonics and Materials VCX-400 Vibracell™ (Sonics and Materials, Inc.) at 30% (135 W) of the total power output . The solution temperature was maintained at 25 C. ~200 μL of the sonicated solution was tranferred to a glass tube and placed in the ESR cavity for analysis. Filtration with a PFTE 0.2 μm filter did not affect the quality of the spectra, thus eliminating the possibility of interfering titanium ions from the sonication probe tip.

Hydrogen peroxide was detected by the method of Kormann et al (40). pH 7 buffer (4.8×10^{-3} M sodium hydroxide and 8.3×10^{-3} M potassium phosphate monobasic) was sonicated at each frequency. At appropriate time intervals during the sonication, 2.0 mL of sample was withdrawn, filtered if necessary, and mixed in a quartz cuvette with 1.0 mL 0.1M potassium biphthalate and 0.75 mL of a solution containing 0.4 M potassium iodide, 0.06M sodium hydroxide, and ~2 $\times 10^{-4}$ M ammonium molybdate. The mixed solutions (total volume = 3.75 mL) were allowed to stand for 2 min. before the absorbance was read. Absorbance measurements were made at 298 K with a Hewlett-Packard 8452a Diode Array Spectrophotometer and 89090A Temperature Controller.

CAVITATION CHEMISTRY IN AQUEOUS SOLUTION

- Sonolytic Production of H_2O_2 and $^{\bullet}OH$

The generation of oxidizing species during sonolysis of aqueous solutions is initiated by the thermolysis of water (Eq. 1) as follows:

$$H_2O \xrightarrow{\Delta} {}^{\bullet}OH + {}^{\bullet}H \qquad (1)$$

The production of $^{\bullet}OH$ and $^{\bullet}H$ during sonolysis under a variety of physical and chemical conditions has been directly determined using electron spin resonance (41-43). The presence of $^{\bullet}OH$ is also indicated by the hydroxylation of aqueous benzoic acid (44) and terephthalic acid (27,45-48) during sonication. The G-value (molecules produced per 100 eV, or 1.6×10^{-17} J) for the formation of $^{\bullet}OH$ during sonolysis has been estimated to be 0.35 by using the Fricke dosimeter (49) .

After the initial splitting of H_2O, further reactions depend on other species present in the gas-phase. 80% of the formed $^{\bullet}OH$ and $^{\bullet}H$ has been estimated to recombine (50). However, $^{\bullet}OH$ can self-react to form hydrogen peroxide:

$$2\ {}^{\bullet}OH \rightarrow H_2O_2 \qquad (2)$$

Recombintation of $^{\bullet}OH$ to form H_2O_2 most likely occurs at the collapsing bubble interface (51). The recombination rate constant measured in water under ambient conditions is 5.5×10^9 $Lmol^{-1}s^{-1}$ (52). The rate constant for the self-reaction at the interface should be at least as large. $^{\bullet}H$ does not appear accumulate outside the cavitation bubble (53).

If O_2 is present in the vapor phase of the bubble, it can also undergo thermolysis as follows:

$$O_2 \rightarrow 2\ O^{\bullet} \qquad (3)$$

Cleavage of the O-O bond during sonolysis has been demonstrated by isotopic exchange experiments (54). Because the dissociative bond energies in the gas-phase for water and oxygen are both 119 kcal mol^{-1} (55), thermolysis of these molecules in cavitation bubbles is an important process during sonication of O_2-saturated solutions. Since H_2 is not detected during sonolysis of an O_2-saturated solution (56) it appears that O_2 efficiently scavenges $^{\bullet}H$:

$$^{\bullet}H + O_2 \rightarrow HO_2^{\bullet} \qquad (4)$$

An alternate pathway for production of $^{\bullet}OH$ in an O_2-saturated solution is as follows (54):

$$H^{\bullet} + O_2 \rightarrow {}^{\bullet}OH + {}^{\bullet}O \tag{5}$$

Both H_2O_2 and $^{\bullet}OH$ are strong oxidants, and have aqueous reduction potentials at pH 7 of 1.35V and 2.31V, respectively (E^O, V vs. NHE) (57). The kinetics of $^{\bullet}OH$ reactions with organic compounds have been studied extensively in both the gas-phase (58) and in aqueous solution (52) .

The production rates of $^{\bullet}OH$ and H_2O_2 during sonolysis will be affected by the final collapse temperature, T_{max} and pressure, P_{max} within the bubble. These quantities can be estimated from an approximate solution to the Rayleigh-Plesset Equation, assuming adiabatic bubble collapse, as follows (1) :

$$T_{max} = T_o\left\{\frac{P_m(K-1)}{P}\right\} \tag{6}$$

$$P_{max} = P\left\{\frac{P_m(K-1)}{P}\right\}^{\left(\frac{K}{K-1}\right)} \tag{7}$$

where P_m = pressure in the liquid at the time of collapse, P = pressure in the bubble at its maximum size, and $K = C_p/C_v$, the ratio of specific heats. The polytropic index, K, is correlated to the heat released upon compression of a gas. Also important are the thermal conductivity and solubility of a gas. The influence of K (59) and the thermal conductivity on the sonochemical production of free-radicals has been demonstrated experimentally (60) In addition, sonoluminescence is influenced by the thermal conductivity of the background gas (61-64). Various physico-chemical properties of the four gases used in this investigation are listed in Table III. From this data, we see that Kr is the least heat

conducting and most soluble of the gases; thus, collapse of a bubble containing Kr is expected to yield the most extreme transient temperatures.

The ultrasonic frequency will affect the reaction environment by determining the resonant bubble radius (65):

$$\rho\omega_r^2 R_r^2 = 3KP_o \qquad (8)$$

where ρ = density of water, ω_r = resonance frequency, R_r = resonant radius, P_o = pressure in the liquid, usually taken to be 1 atm, and K = polytropic index, as defined before. This expression is valid when surface tension effects are small. Differences in bubble radii will result in variable bubble collapse times (66,67) as well as surface area-to-volume ratios. Tables IV-V illustrate these differences. Although the radius is slightly influenced by the nature of the saturating gas, the most significant influence is the frequency. The resonant radius ranges from ~7 microns at 500 kHz to ~170 microns at 20 kHz. However, it should be noted that the cavitating solution will contain a bubble population with a distribution of radii.

RESULTS AND DISCUSSION

The standard response curves for hydrogen peroxide (H_2O_2) and hydroxyterephthalic acid (HTA) are shown in Fig. 3-4. In each case, we see a linear response over the concentration range of interest. The reproducibility of $^{\bullet}OH$ production and detection (Fig. 5) is demonstrated for sonolysis at 39W and 500 kHz in an Ar-saturated solution at 25 ^{o} C; variation in the magnitude of the rate constant of HTA production does not exceed 5% from one experiment to the next.

• Influence of Saturating Gas

The kinetic data illustrating the effects of different saturating gases at each frequency are shown in Figs. 6-9 and Figs. 11-14. The slopes of the linear regression lines yield the uncorrected rate constants for production of $^{\bullet}OH$ and H_2O_2. In order to determine the effect of frequency on the reaction rates, the rate constants are normalized by correcting for the differences in the acoustic energy densities.

H_2O_2 production during sonication at 20 kHz as a function of the saturating gases is illustrated in Fig. 6. The apparent kinetics are zero-order, with the rate constants ranging from 5.4×10^{-2} μM min^{-1} for He to 1.3 μM min^{-1} for Kr. The difference in rates in Kr-saturated solutions versus Ar-saturated solutions can be inversely correlated with the difference in thermal conductivity and solubility of each gas (a factor of ~2). The observed production rate in the presence of He is slower than would be predicted solely by its low water solubility, but faster than predicted by its high thermal conductivity. Differences in the polytropic index, K, affect the production rate in O_2-saturated solutions. Less heat is released during the implosion of a cavitation bubble in O_2-saturated solutions. The lower collapse temperature decreases the $^{\bullet}OH$ production rate and leads to a slower formation rate for H_2O_2. However, the lower value of K does not appear to influence the production rate as significantly as the higher thermal conductivity of He.

H_2O_2 production during irradiation at 40 kHz is shown in Fig.7. At this frequency, there is a weaker correlation between the measured rate constants in Ar- and Kr-saturated solutions (1.27 μM min^{-1} and 0.709 μM min^{-1}, respectively) and their respective thermal conductivities. The differences in thermal conductivity and solubility appear to have a lesser effect at 40 kHz.

At 80 kHz (Fig. 8), the differences in thermal conductivity and K with respect to the production rate of H_2O_2 are minimal. In this case, all the rate constants are of the same

order of magnitude (0.101 μM min^{-1} to 0.325 μM min^{-1}). The apparent rate constants differ by 10% in Ar-and Kr-saturated solutions (0.325 μM min^{-1} vs. 0.288 μM min^{-1}). Furthermore, the production rate in an O_2-saturated solution (0.160 μM min^{-1}) is only ~50% less than that observed in Ar- and Kr-saturated solutions, while the rate is 66% less under He (0.101 μM min^{-1}). These results imply that differences in the polytropic index are minimized at 80 kHz or that scavenging of $^{\bullet}H$ by O_2 occurs more readily in smaller bubbles.

The analogous trends during sonication at 500 kHz (Fig. 9) appear to be intermediate between those observed at 20 and 40 kHz and those observed at 80 kHz. The differences in H_2O_2 production rate in solutions saturated with the three noble gases do not correlate very strongly with the corresponding differences in thermal conductivity, with the exception of He. The three highest rate constants are within 50% of each other (k_{Kr} = 2.9 μM min^{-1}, k_{Ar} = 1.9 μM min^{-1}, k_{O_2} = 1.6 μM min^{-1}) although there is an order of magnitude difference between the lowest rate constant (k_{He}= 0.28 μM min^{-1}) and the highest rate constant.

The data of Figs. 6-9 are summarized in Fig. 10, in which the ratios of rate constants are compared at each frequency. The He/Kr and Ar/Kr ratios reflect the influence of changing thermal conductivities and solubilities of the dissolved gases on the production rate for H_2O_2 at each frequency. The O_2/Ar ratio reflects changes in the rate constant due to a variable K, as well as the higher-temperature reactions of O_2. The highest variability for H_2O_2 production rates with different saturating gases is found at 20 kHz (i.e., the rate constant ratios are <1). As the frequency increases, the value of the rate constants converge, with the ratios approaching unity. Under O_2, the rate constant ratios steadily increase as the frequency increases, indicating that the difference in polytropic indices between O_2 and the noble gases is less important at the higher frequencies. An important implication of these decreasing differences with increasing frequency is that the reaction site is more homogeneous under certain conditions. Larger bubbles require longer times for

heat to flow with respect to an actual acoustic period (68); thus, the temperature and pressure gradients may be most severe at 20 kHz. Smaller bubbles may exhibit behavior more isothermal behavior.

Similar trends are noted for the production of $^{\bullet}OH$ with the same saturating gases and ultrasonic frequencies. Interpretation of these apparent rate constants is complicated by several factors. First, terephthalic acid must diffuse to the bubble surface in order to trap the $^{\bullet}OH$, which is present at a much lower concentration than in the hotter vapor-phase region of the imploded bubbles. Second, hydroxyterephthalic acid (HTA), the hydroxyl radical addition product, may react further with $^{\bullet}OH$ before it diffuses away from the bubble surface. Therefore, quantifying $^{\bullet}OH$ production via hydroxyterephthalic acid represent a lower limit for the actual $^{\bullet}OH$ production rate under a given set of conditions.

The differences in production rate of $^{\bullet}OH$ at 20 kHz are shown in Fig. 11. The rate constants range from 0.031 $\mu M\ min^{-1}$ to 0.146 $\mu M\ min^{-1}$. Even though the production rates with different dissolved gases are correlated with the thermal conductivities of the gases, the correlation is not as strong as that observed for hydrogen peroxide production at this frequency. Sonication at 40 kHz (Fig. 12) yields similar trends to those observed at 20 kHz (Fig. 11).

During ultrasonic irradiation at 80 kHz (Fig. 13), the apparent $^{\bullet}OH$ formation rate constants are all of the same order of magnitude (i.e., 1.08×10^{-2} $\mu M\ min^{-1}$ to 5.28×10^{-2} $\mu M\ min^{-1}$). The difference between the rates observed in Ar-saturated solutions compared to Kr-saturated solutions (5.28×10^{-2} $\mu M\ min^{-1}$ vs. 5.18×10^{-2} $\mu M\ min^{-1}$) is ~10%, which is much less than the difference among the various physical properties of the gases. Furthermore, the production rate in O_2-saturated solutions (3.78×10^{-2} $\mu M\ min^{-1}$) is ~30% lower than in solutions saturated with either Ar or Kr. The reduced variability of $^{\bullet}OH$ production rates with different saturating gases at 80 kHz is very similar to the trends observed at this frequency for H_2O_2 production.

The differences among Ar, Kr, and O_2 are smallest when solutions are irradiated at 500 kHz (Fig. 14). At this frequency, the three highest rates are within ±8% (3.31×10^{-1} μM min^{-1} to 3.92×10^{-2} μM min^{-1}). However, $^{\bullet}OH$ production in He-saturated solutions (7.16×10^{-2} μM min^{-1}) is 18% of that observed in the presence of Kr. From these observations we conclude that at 500 kHz, a large difference in thermal conductivity can still influence the production of $^{\bullet}OH$ and the subsequent physicochemical conditions during cavitational bubble collapse. Furthermore, because the production rates in the presence of O_2 (K = 1.41) are comparable to those observed in the presence of Ar or Kr (K = 1.66), the difference among the K values is minimized and this implies that the amount of heat released from each of the three gases results in similar final temperatures at 500 kHz.

The trends in $^{\bullet}OH$ production rates are summarized in Fig. 15. Selected rate constant ratios are plotted as a function of the ultrasonic frequency. In this case, we see that the difference in $^{\bullet}OH$ production rate in He- and Kr-saturated solutions is large regardless of the irradiation frequency. This may imply that the trapping efficiency of terephthalic acid for $^{\bullet}OH$ does not depend on the surface area-to-volume ratio under these conditions. H_2O_2 production, on the other hand, most likely occurs at the cooler interfacial region. Even though a smaller number of $^{\bullet}OH$ radicals is produced during the implosion of He-saturated bubbles, a greater fraction appears to self-react to form H_2O_2 as the surface area-to-volume ratio increases with decreasing bubble size.

Although EPR was not used for quantifying the production of hydroxyl radical, the method allows for direct confirmation of the presence of hydroxyl radical in aqueous solution. The first derivative EPR spectrum at 298 K of a sonicated solution of TMPone is shown in Fig. 16. The solution had been exposed to ultrasonic irradiation for 5 min. before the spectrum was recorded. This is in agreement with the the expected spectrum of the paramagnetic compound (2,2,6,6-tetramethyl-4-piperidone-N-oxyl) shown below:

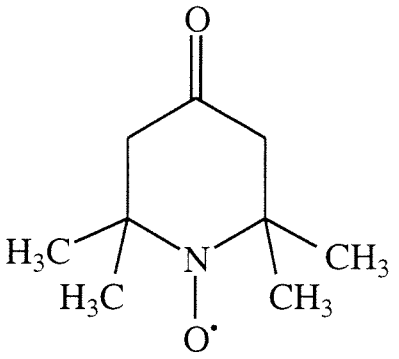

The transformation mechanism by which this structure is formed from the parent molecule, TMPone, is described by Petrier et al (26).

Additional insight is obtained by examining the relative production rates of $^{\bullet}OH$ and H_2O_2 as a function of frequency and background gas (Fig. 17). In all cases, the steady-state production of H_2O_2 is greater than that of $^{\bullet}OH$. This is due in part to the fact that the observed rate of $^{\bullet}OH$ accumulation is lower than the true rate of production within the center of the bubble. The largest difference in the production rates of $^{\bullet}OH$ and H_2O_2 appears in Ar- and Kr-saturated solutions at 40 kHz, whereas this maximum appears in He-saturated solutions at 80 kHz . In O_2-saturated solutions, the difference monotonically increases with frequency, indicating a better efficiency of $^{\bullet}H$ scavenging by O_2 at higher frequencies.

The corrrelations of H_2O_2 production rate ratios with the thermal conductivity or solubility ratios of the background gas are shown in Figs. 18-19. Irradiations of O_2-saturated solution are not included because the $H^{\bullet}$ scavenging reactions leading to $HO_2^{\bullet}$ would bias the results. As the relative difference in thermal conductivity decreases, the production rates become closer in magnitude and the ratios increase towards unity. However, the relative changes in thermal conductivity have the least effect at 80 kHz. In the latter case, all the rate ratios are ≥ 0.3.

Hydroxyl radical production is also influenced in a similar fashion by frequency and saturating gas (Figs 20-21). At 20 kHz, the correlation between solubility and rate

ratio is linear. Gas-solubility influences the extent to which a bubble will collapse. For example, a higher solubility gas is more easily forced back into solution. The longest compression cycle and collapse times are required at 20 kHz, therefore, the solubility would be expected to have a greater influence on reaction rates at this frequency than at the other frequencies. At the lower frequencies (20 and 40 kHz), the production rates of $^{\bullet}OH$ appear to be less sensitive to the differences in thermal conductivity and solubility compared to the senstivity of H_2O_2 production rates, as reflected by higher production rate ratios.

The rate constants for the production of H_2O_2 and $^{\bullet}OH$ at each of the four frequencies in solutions saturated with each gas are tabulated in Tables VI and VII. Because the experiments were carried out at different total power outputs, the rate constants were normalized for comparison. The ratio of the energy density (acoustic energy per unit volume) at each frequency to that at 20 kHz was used as a correction factor to the observed rate constants (Eqn. 9).

$$k_{corr,\,f} = k_{obs,f}\left(\frac{P_{f_S}}{P_f}\right) \tag{9}$$

where $k_{corr,\,f}$ and $k_{obs,\,f}$, are the corrected and the observed rate constants at the irradiation frequency, f. P_f is the power per unit volume at that frequency. P_{f_S} is the power per unit volume at the standard ultrasonic frequency, f_S, chosen to be 20 kHz.

The fastest production of H_2O_2 occured during sonolysis at 500 kHz of Kr-saturated solutions (k_{corr} = 3.57 $\mu M min^{-1}$), whereas the slowest production rate was observed during sonolysis at 20 kHz of He-saturated solutions (k_{corr} = 0.05 $\mu M min^{-1}$). Hydrogen peroxide formation occurs most rapidly in Kr-saturated solution at each frequency except at 80 kHz. Sonication at 500 kHz yields the fastest production rates, regardless of the saturating gas, except for He-saturated solutions, for which maximum

rates were observed at 80 kHz. In general, the apparent rate constants tend to increase with increasing frequency and surface area-to-volume ratios (Fig. 22).

A similar trend for the production of $^{\bullet}OH$ is seen is the data of Table 7, even though these rates represent a lower limit of the true rate of $^{\bullet}OH$ production by thermolysis of H_2O that occurs in the gas-phase of the bubble. Hydroxyl radical production is optimized during sonolysis of Kr-saturated solutions at 500 kHz and while it occurs mostly slowly during sonication at 20 kHz of He-saturated solutions (e.g., k_{corr} = 0.47μM min^{-1} and 0.031 μM min^{-1}, respectively). In addition, Kr-saturated solutions yield the highest rates of $^{\bullet}OH$ production regardless of the irradiation frequency and irradiations at 500 kHz appears to maximize the $^{\bullet}OH$ production rate, regardless of the nature of the dissolved gas. $^{\bullet}OH$ production rates are comparable at 20 and 40 kHz, but increase sharply at 80 kHz (Fig 23).

The larger observed rate constants at higher frequencies may indicate both a higher production rate for $^{\bullet}OH$ and a higher trapping efficiency of the terephthalic acid at the bubble interface. Petrier et al. (26) have suggested that at higher frequencies, hydroxyl radicals are ejected out of the bubble before they can recombine in the gas-phase because the collapse time at higher frequencies is shorter.

In addition, the increased efficiency of H_2O_2 and $^{\bullet}OH$ production at higher irradiation frequencies may also be due to variations in the acoustic pressure amplitude and in the surface tension. The acoustic pressure amplitude ranges from 4.9 atm at 20 kHz to 5.7 atm at 80 kHz while at 500 kHz, the pressure amplitude is 2.1 atm. This implies that a bubble may not collapse as completely at 500 kHz. Instead, at 500 kHz, a stable bubble will oscillate a greater number of times per second and will produce a greater flux of $^{\bullet}OH$. The surface tension, which is inversely correlated with bubble radius, is a collapsing force on the bubble. For a bubble in the absence of an acoustic field, (1) the pressure varies as follows:

$$P = P_h + \left(\frac{2\sigma}{R}\right) \quad (10)$$

where P = pressure which the bubble must maintain to avoid dissolution, P_h = hydrostatic pressure, σ = surface tension, R = bubble radius. A 44 μm (80 kHz) bubble will experience a surface tension which is approximately four-fold larger than a 177 μm (20 kHz) bubble, regardless of the acoustic pressure. Thus, at a given acoustic pressure (e.g., sound intensity), the total implosive force on a bubble at the resonant radius may be larger at higher frequencies, resulting in a more complete collapse and more extreme temperatures.

The cyclic growth and collapse of bubble clouds can also be altered as a function of frequency. Acoustic cavitation is induced by the excitation of a population of bubble nuclei to a resonant radius, at which point, the bubbles efficiently absorb energy from the sound waves. The bubbles grow by the process of rectified diffusion (69), which is a means by which gas diffuses into the bubble. When the bubble expands during a rarefaction half-cycle, the gas within the bubble expands and there is a flux of gas from the surrounding liquid into the bubble. During the compression half-cycle, the gas is compressed and results in an outward flux of gas into the bulk liquid. Because the surface area of the bubble during the expansion cycle is larger than during the compression cycle, there is a net increase of gas within the bubble at the end of each acoustic cycle. At higher frequencies, the resonant radius is calculated to be smaller and, therefore, fewer acoustic cycles are required before the bubble reaches resonant size. With a greater number of acoustic cycles per unit time at higher frequencies, rectified diffusion occurs more rapidly. Thus, a greater number of nuclei can reach resonance more quickly than at lower frequncies. The net effect is to produce a greater enhancement of sonochemical reactions.

Bubble cloud behavior can also be altered by the phenomenon of microstreaming, which involves the release of smaller bubbles from the surface waves of an oscillating bubble. The pressure amplitude required to produce surface waves on air bubbles is

0.0025 atm and 0.037 atm at 20 and 500 kHz, respectively (69), while the threshold amplitude required to produce microbubbles is about four times greater (70). These pressure amplitudes are well below those attained in our experiments. At higher frequencies, the effect of microstreaming should be amplified by the faster growth rates and produce a larger number of chemically active bubbles.

CONCLUSIONS

The sonolytic production of H_2O_2 at pH 7 and $^{\bullet}OH$ at pH 11 is influenced by the nature of the dissolved gases and the applied ultrasonic frequencies. A maximum production rate of H_2O_2 and $^{\bullet}OH$ (3.57 $\mu M\ min^{-1}$ and 0.47 $\mu M\ min^{-1}$, respectively) is observed during sonolysis of Kr-saturated solutions at 500 kHz. Kr- and Ar-saturated solutions appear to yield the fastest production rates for H_2O_2 and $^{\bullet}OH$, regardless of the frequency, while sonication at 500 kHz and 80 kHz yield faster rates than sonication at 20 kHz and 40 kHz for all saturating gases.

Even though the H_2O_2 and $^{\bullet}OH$ production rates at each frequency differ according to the nature of the background gas, the variability is less at higher frequencies since stable cavitation bubbles result in near isothermal conditions. In addition, the surface area-to-volume ratio of the bubbles appears to play a role in the production efficiency of H_2O_2. The effect of the different gases reaches a maximum for each species, except in the case of O_2-saturated solutions. The sonolytic production rates of both H_2O_2 and $^{\bullet}OH$ in O_2-saturated solution relative to Ar-saturated solutions increase monotonically with increasing frequency. The increasing isothermal character, as K approaches unity, of smaller bubbles may contribute to this trend. Furthermore, an improved scavenging efficiency of $^{\bullet}H$ by O_2 is implicated at higher frequencies.

The absolute production rates are also higher at each frequency: $k_{500} > k_{80} > k_{40} > k_{20}$ for most saturating gases. There are several reasons for enhanced sonochemistry at

higher frequencies, including the enhancement of the collapse intensity of individual bubbles due to surface tension effects. However, the bubble cloud may also be altered by differences in rectified diffusion and microstreaming at higher frequencies which result in a greater number of cavitating bubbles.

ACKNOWLEDGMENTS

The authors are grateful to EPRI (contract # RP8003-36) and ARPA (Grant # NAV 5HFMN N0101492J1901) for their generous financial support.

References

1. Mason, T. J.; Lorimer, J. P. *Sonochemistry: Theory, Applications and Uses of Ultrasound in Chemistry*; Ellis Horwood Ltd.: Chichester, 1988, pp. 252.

2. *Ultrasound: Its Chemical, Physical and Biological Effects*; Suslick, K. S., Ed.; VCH Publishers, Inc.: New York, 1988, pp. 336.

3. Mason, T. J. *Practical Sonochemistry User's Guide to Applications in Chemistry and Chemical Engineering*; Ellis Horwood: West Sussex, England, 1991, pp. 186.

4. *Current Trends in Sonochemmistry*; Price, G. J., Ed.; The Royal Society of Chemistry: Cambridge, UK, 1992, pp 183.

5. Hagan, C. R. S., Coury, L. A., *Anal. Chem.,* **1994**, *66*, 399-405.

6. Compton, R. G., Eklund, J. C., Page, S. D., *J. Phys. Chem.,* **1995**, *99*, 4211-4214.

7. Klima, J., Bernard, C., Degrand, C., *J. Electroanal. Chem.,* **1994**, *367*, 297-300.

8. Alippi, A.; Cataldo, F.; Galbato, A., *Ultrasonics,* **1992**, *30*, 148-151.

9. Bhatnagar, A.; Cheung, H. M., *Environ. Sci. Technol.,* **1994**, *28*, 1481-1486.

10. Bromberg, L., Cohn, D. R., Koch, M., Patrick, R. M., Thomas, P., *Phys. Lett. A,* **1993**, *173*, 293-299.

11. Cheung, H. M.; Bhatnagar, A.; Jansen, G., *Environ. Sci. Technol.,* **1991**, *25*, 1510-1512.

12. Cheung, H. M., Kurup, S., *Environ. Sci. Technol.,* **1994**, *28*, 1619-1622.

13. Hua, I.; Höchemer, R. H.; Hoffmann, M. R., *J. Phys. Chem.,* **1995**, *99*, 2335-2342.

14. Hua, I., Höchemer, R. H., Hoffmann, M. R., *Environ. Sci. Technol.*, **1995**, *29*, 2790-2796.

15. Hua, I., Hoffmann, M. R., *Environ. Sci. Technol. in press*, **1995**,

16. Inazu, K., Nagata, Y., Maeda, Y., *Chem. Lett.*, **1993**, 57-60.

17. Jennings, B. J. ;. T., S. N., *J. Phys. Chem.*, **1961**, *65*, 1574-1579.

18. Kotranarou, A.; Mills, G.; Hoffmann, M. R., *Environ. Sci. Technol.*, **1992**, *26*, 2420-2428.

19. Kotronarou, A.; Mills, G.; Hoffmann, M. R., *J. Phys. Chem.*, **1991**, *95*, 3630-3638.

20. Kotronarou, A.; Mills, G.; Hoffmann, M. R., *Environ. Sci. Technol.*, **1992**, *26*, 1460-1462.

21. Petrier, C.; Micolle, M.; Merlin, G.; Luche, J. L.; Reverdy, G., *Environ. Sci. Technol.*, **1992**, *26*, 1639-1642.

22. Serpone, N.; Terzian, R.; Colarusso, P.; Minero, C.; Pelizzetti, E.; Hidaka, H., *Res. Chem. Intermed.*, **1992**, *18*, 183-202.

23. Serpone, N.; Terzian, R.; Hidaka, H.; Pelizzetti, E., *J. Phys. Chem.*, **1994**, *98*, 2634-2640.

24. Wu, J. M., Huang, H. S., Livengood, C. D., *Environ. Prog.*, **1992**, *11*, 195-201.

25. Petrier, C., Lamy, M. F., Francony, A., Benahcene, A., David, B., Renaudin, V., Gondrexon, N., *J. Phys. Chem.*, **1994**, *98*, 10514-10520.

26. Petrier, C., Jeunet, A., Luche, J. L., Reverdy, G., *J. Am. Chem. Soc.*, **1992**, *114*, 3148-3150.

27. Zhao, Y., Bates, D. M., Lorimer, J. P., Mason, T. J., *Ultrasonics Sonochemistry,* **1994**, *1*, S91-S95.

28. Berlan, J., Trabelsi, F., Delmas, H., Wilhelm, A. M., Petrignani, J. F., *UltrasonicsSonochemistry,* **1994**, *1*, s97-s102.

29. Cum, G.; Galli, G.; Gallo, R.; Spadaro, A., *Ultrasonics,* **1992**, *30*, 267-270.

30. Entezari, M. H., Kruus, P., *Ultrasonics Sonochemistry,* **1994**, *1*, s75-s79.

31. Cum, G., Gallo, R., Spadaro, A., Galli, G., *J. Chem. Soc. Perkins. Trans. 11,* **1988**, 376-383.

32. Seghal, C., Sutherland, R. G., Verral, R. E., *J. Phys. Chem.,* **1980**, *84*,

33. Taylor, K. J., Jarman, P.D., *Aust. J. Phys.,* **1970**, *23*, 319.

34. Didenko, Y. T., Nastitch, D. N., Pugach, S. P., Polovinka, Y. A., Kvochka, V. I., *Ultrasonics,* **1994**, *32*, 71-76.

35. Wu, C. C., Roberts, P. H., *Proceedings of the Royal Society of London Series A-Mathematical and Physical Sciences,* **1994**, *445*, 323-349.

36. Matula, T. J., Roy, R. A., Mourad, P. D., McNamara III, W. B., Suslick, K. S., *Phys. Rev. Lett.,* **1995**, *75*, 2602-2605.

37. Chendke, P. K., Fogler, H. S., *J. Phys. Chem.,* **1983**, *87*, 1362-1369.

38. Field, L., and Engelhardt, P. R., *J. Org. Chem.,* **1970**, *35*, 3647-3655.

39. Price, G. J., Lenz, E. J., *Ultrasonics,* **1993**, *31*, 451-6.

40. Kormann, C., Bahnemann, D. W., Hoffmann, M. R., *Environ. Sci. Technol.,* **1988**, *22*, 798-806.

41. Makino, K., Mossoba, M., Riesz, P., *J. Phys. Chem.,* **1983**, *87*, 1369-1377.

42. Riesz, P.; Christman, C. L., *Federation Proceedings,* **1986**, *45*, 2485-2492.

43. Riesz, P.; Kondo, T., *Free Radical Biology And Medicine,* **1992**, *13*, 247-270.

44. Parke, A. V. M., Taylor, D., *J. Chem. Soc.,* **1956**, 4442-4450.

45. Barreto, J. C., Smith, G. S., Strobel, N. H. P., McQuillin, P. A., Miller, T. A., *Life Sciences,* **1995**, *56*, PL89-96.

46. Brandenburg, K., Moll, H., *Radiat. Phys. Chem.,* **1984**, *23*, 431-434.

47. Matthews, R. W., *Rad. Res.,* **1980**, *83*, 27-41.

48. McLean, J. R., Mortimer, A. J., *Ultrasound Med Biol,* **1988**, *14*, 59-65.

49. Todd, J. H., *Ultrasonics,* **1970**, *8*, 234-238.

50. Fischer, C.-H., Hart, E. J., Henglein, A., *J. Phys. Chem.,* **1986**, *90*, 3059-3060.

51. Henglein, A., Kormann, C., *Int. J. Radiat. Biol.,* **1985**, *48*, 251-258.

52. Buxton, G. V., Greenstock, C. L., Helman, W. P., Ross, A. B., *J. Phys. Chem. Ref. Data,* **1988**, *17*, 513-886.

53. Hart, E. J., Henglein, A., *J. Phys. Chem.,* **1987**, *91*, 3654-3655.

54. Fischer, C.-H., Hart, E. J., Henglein, A., *J. Phys. Chem.,* **1986**, *90*, 1954-1956.

55. *CRC Handbook of Chemistry and Physics*; 71 ed.; Lide, D. R., Ed.; CRC Press: Boca Raton, 1990.

56. Hart, E. J., Henglein, A., *J. Phys. Chem.,* **1985**, *89*, 4342-4347.

57. Sawyer, D. T. *Oxygen Chemistry*; Oxford University Press: New York, 1991; Vol. 26, pp. 223.

58. Atkinson, R., *Chem. Rev.*, **1985**, *85*, 69-201.

59. Riesz, P., Kondo, T., Carmichael, A. J., *Free Rad. Res. Comms.*, **1993**, *19*, S45-S53.

60. Kondo, T., Kirschenbaum, L. J., Kim, H., Riesz, P., *J. Phys. Chem.*, **1993**, *97*, 522-527.

61. Hiller, R., Weninger, K., Putterman, S. J., Barber, B. P., *Science*, **1994**, *266*, 248-250.

62. Didenko, Y. T., Gordeychuk, T. V., Koretz, V. L., *J. Sound Vibr.*, **1991**, *32*, 71-76.

63. Young, F. R., *J. Acoust. Soc. Am.*, **1976**, *60*, 100-104.

64. Ciuti, P., Iernetti, G., Tomasini, F., *Acustica*, **1991**, *73*, 277-282.

65. Minnaert, M., *Phil. Mag.*, **1933**, *16*, 235.

66. Khoroshev, G. A., *Sov. Phys. Acoust.*, **1963**, *9*, 273.

67. Rayleigh, L., *Phil. Mag.*, **1917**, *34*, 94.

68. Crum, L. A., *J. Acoust. Soc. Am.*, **1983**, *73*, 116-120.

69. Young, F. R. *Cavitation*; McGraw-Hill Book Company (UK) Limited: Berkshire, 1989, pp. 418.

70. Neppiras, E. A., *Ultrasonics*, **1980**, *18*, 201-209.

71. Tchobanoglous, G., Schroeder, E. D. *Water Quality*; Addison-Wesley Publishing Company: Reading, MA, 1985, pp. 768.

List of Figure Captions

Fig. 1: Reactor configuration for sonications at 20, 40, and 80 kHz.

Fig. 2: Reactor configuration for sonications at 500 kHz.

Fig.3 : Hydrogen peroxide standard curve.

——— y = -0.00102 + 0.0236x R= 1.000

Fig. 4: Hydroxyterephthalic acid standard curve.

——— y = 0.0548 + 0.513x R= 1.000

Fig. 5: Reproducibility of $^{\bullet}OH$ production and detection at 500 kHz in an Ar-saturated solution.

——— y = -0.101 + 0.39x R= 0.999

- - - - - y = -0.0843 + 0.403x R= 0.998

— — - y = 0.062 + 0.407x R= 0.996

Fig. 6: Production of H_2O_2 at 20 kHz in Kr, Ar, O_2 or He-saturated solutions.

——— y = -1.39 + 1.31x R= 0.999

– – – – y = -2.39 + 0.718x R= 0.995

– – – – y = -0.424 + 0.204x R= 0.999

— – – y = 0.0407 + 0.0541x R= 0.995

Fig. 7: Production of H_2O_2 at 40 kHz in Kr, Ar, O_2 or He-saturated solutions.

——— y = -1.36 + 1.27x R= 0.999

– – – – y = -1.42 + 0.709x R= 0.999

– – – – y = 0.397 + 0.219x R= 0.997

— – – y = 0.649 + 0.0847x R= 0.995

Fig. 8: Production of H_2O_2 at 80 kHz in Kr, Ar, O_2 or He-saturated solutions.

——— y = 0.204 + 0.298x R= 0.995

– – – – y = -1.80 + 0.325x R= 0.997

– – – – y = -0.0145 + 0.160x R= 0.995

— – – y = 0.0960 + 0.101x R= 0.992

Fig. 9: Production of H_2O_2 at 500 kHz in Kr, Ar, O_2 or He-saturated solutions.

——— y = -0.0463 + 2.95x R= 1.000

– – – – y = 1.67 + 1.93x R= 1.000

– – – – y = 1.05 + 1.65x R= 0.999

— – – y = -0.905 + 0.288x R= 0.998

Fig. 10: Ratio of rate constants of hydrogen peroxide formation at different frequencies and with variable saturating gas.

Fig. 11: $^{\bullet}OH$ production at 20 kHz in Kr, Ar, O_2 or He-saturated solutions.

——— y = -0.0441 + 0.146x R= 0.997

– – – – y = 0.502 + 0.103x R= 0.996

– – – – – y = -0.0119 + 0.0700x R= 1.000

— – – y = -0.207 + 0.0310x R= 0.992

Fig. 12: $^{\bullet}OH$ production at 40 kHz in Kr, Ar, O_2 or He-saturated solutions.

——— y = 0.142 + 0.120x R= 0.998

– – – – y = -0.319 + 0.0920x R= 0.996

– – – – – y = -0.0959 + 0.0564x R= 0.998

— – – y = -0.0235 + 0.0173x R= 0.999

Fig. 13: $^{\bullet}OH$ production at 80 kHz in Kr, Ar, O_2 or He-saturated solutions.

——— y = -0.169 + 0.0518x R= 0.988

– – – – y = -0.0308 + 0.0528x R= 0.994

– – – – – y = 0.0221 + 0.0378x R= 0.991

— – – y = -0.0645 + 0.0108x R= 0.988

Fig. 14: $^{\bullet}OH$ production at 500 kHz in Kr, Ar, O_2 or He-saturated solutions.

——— y = 0.321 + 0.392x R= 0.996

– – – – y = -0.101 + 0.390x R= 0.999

– – – – y = 0.260 + 0.331x R= 0.999

— – – y = 0.000254 + 0.0716x R= 1.000

Fig. 15: Ratio of rate constants of $^{\bullet}OH$ formation at different frequencies and with variable saturating gas.

Fig. 16: First derivative EPR spectrum of an Ar-saturated solution of TMPone after 5 min. of ultrasonic irradiation.

Fig. 17: Ratio of H_2O_2 to $^{\bullet}OH$ production at different frequencies.

Fig. 18: Correlation of H_2O_2 production rate ratios with saturating gas thermal conductivity ratios.

Fig. 19: Correlation of H_2O_2 production rate ratios with saturating gas solubility ratios.

Fig. 20: Correlation of $^{\bullet}OH$ production rate ratios with saturating gas thermal conductivity ratios.

Fig. 21: Correlation of $^{\bullet}OH$ production rate ratios with saturating gas solubility ratios.

Fig. 22: Influence of bubble surface area-to-volume ratio on H_2O_2 production rates.

Fig. 23: Influence of bubble surface area-to-volume ratio on $^{\bullet}OH$ production rates.

Table I

Physical Dimensions of the Multi-Frequency Transducers

Frequency, kHz	Emitting Diameter, cm	Emitting Area, cm^2	Sonicated Volume,mL	%Total Power
20.2	1.41	1.57	2.00×10^2	40.0
39.4	1.25	1.23	2.00×10^2	60.0
80.6	0.406	0.129	1.00×10^2	60.0
513	5.70	25.5	6.00×10^2	60.0

Table II

Results of Calorimetry Measurements

Frequency, kHz	Power Output, W	Density, W/cm^3	Intensity, W/cm^2	*Acoustic Amplitude, atm
20.2	15.8	7.80×10^{-2}	10.0	5.40
39.4	13.5	6.70×10^{-2}	11.0	5.70
80.6	1.05	1.00×10^{-2}	8.10	4.90
513	39.0	6.50×10^{-2}	1.50	2.10

Table III

Physical Properties of Saturating Gases

Gas	Polytropic Index, K	Thermal Conductivity, mW/m-K	Water solubility, m^3/m^3
Kr	1.66	17.1	5.94×10^{-2}
Ar	1.66	30.6	3.37×10^{-2}
He	1.63	2.52×10^{2}	8.60×10^{-4}
Oxygen	1.41	48.1	3.05×10^{-4}

All data from refs. (55) and (71).

Table IV

Compression Half-Cycles and Bubble Collapse Times

Frequency, kHz	Compression half-cycle length, μs	*Collapse time, μs
20.2	25.0	16.2
39.4	12.5	8.10
80.6	6.80	4.10
513	1.00	6.49×10^{-1}

*For a bubble of resonant radius; assumed to be an 'empty void' with pressure in the liquid at 1 atm.

Table V

Influence of Frequency and Saturating Gas on Bubble Resonant Radius

a. He-saturated solution.

Frequency, kHz	Resonant Radius, μm	Surface Area, μm^2	Volume, nL	Surface area-to-volume ratio, μm^{-1}
20.2	176	3.89×10^5	22.8	1.70×10^{-2}
39.4	87.9	9.73×10^4	2.85	3.40×10^{-2}
80.6	43.9	2.43×10^4	0.356	6.81×10^{-2}
513	7.03	6.23×10^2	0.00146	4.26×10^{-1}

b. Ar- or Kr-saturated solution.

Frequency, kHz	Resonant Radius, μm	Surface Area, μm^2	Volume,nL	Surface area-to-volume ratio, μm^{-1}
20.2	178	3.96×10^5	23.4	1.68×10^{-2}
39.4	88.8	9.91×10^4	2.93	3.37×10^{-2}
80.6	44.4	2.48×10^4	0.366	6.75×10^{-2}
513	7.10	6.34×10^2	0.00150	4.22×10^{-1}

c. O_2-saturated solution.

Frequency, kHz	Resonant Radius, μM	Surface Area, μm^2	Volume,nL	Surface area-to-volume ratio, μm^{-1}
20.2	163	3.38×10^5	18.4	1.84×10^{-2}
39.4	81.9	8.84×10^4	2.30	3.66×10^{-2}
80.6	40.9	2.11×10^4	0.288	7.33×10^{-2}
513	6.5	5.40×10^2	0.00118	4.61×10^{-1}

Table VI

Rate Constants of Hydrogen Peroxide Production at 20, 40, 80 and 500 kHz*

Frequency, kHz	Kr	Ar	O_2	He
20.2	1.31	0.717	0.204	0.0541
39.4	1.48	0.832	0.256	0.0993
80.6	2.24	2.44	1.21	0.761
513	3.57	2.34	2.00	0.350

*Corrected for differences in total acoustic energy at each frequency.

Table VII

Rate Constant of Hydroxyl Radical Production at 20, 40, 80 and 500 kHz*

Frequency, kHz	Kr	Ar	O_2	He
20.2	0.146	0.103	0.0699	0.0310
39.4	0.141	0.108	0.0661	0.0203
80.6	0.389	0.396	0.283	0.0811
513	0.476	0.435	0.402	0.0870

*Corrected for differences in total acoustic energy at each frequency.

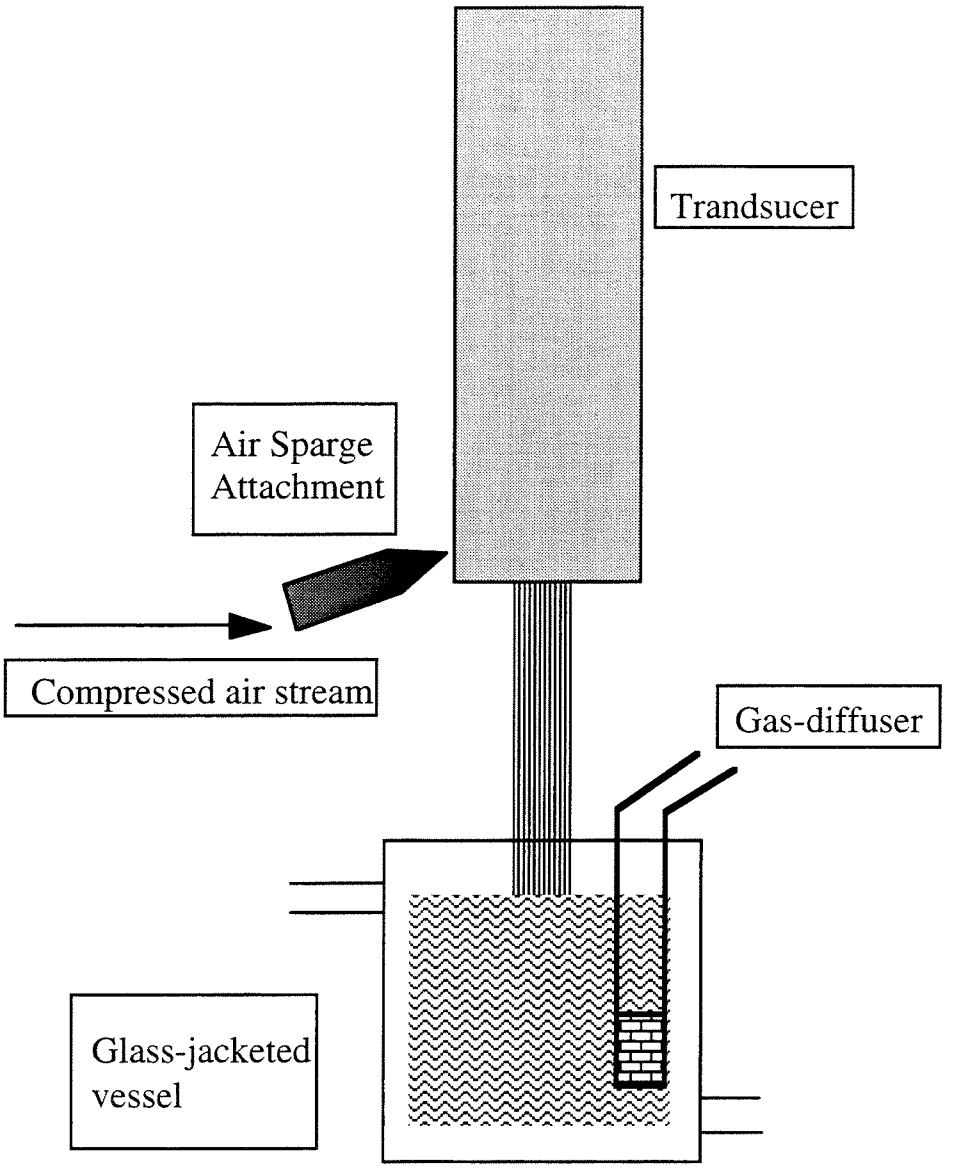

Fig. 1: Reactor configuration for sonications at 20, 40, and 80 kHz.

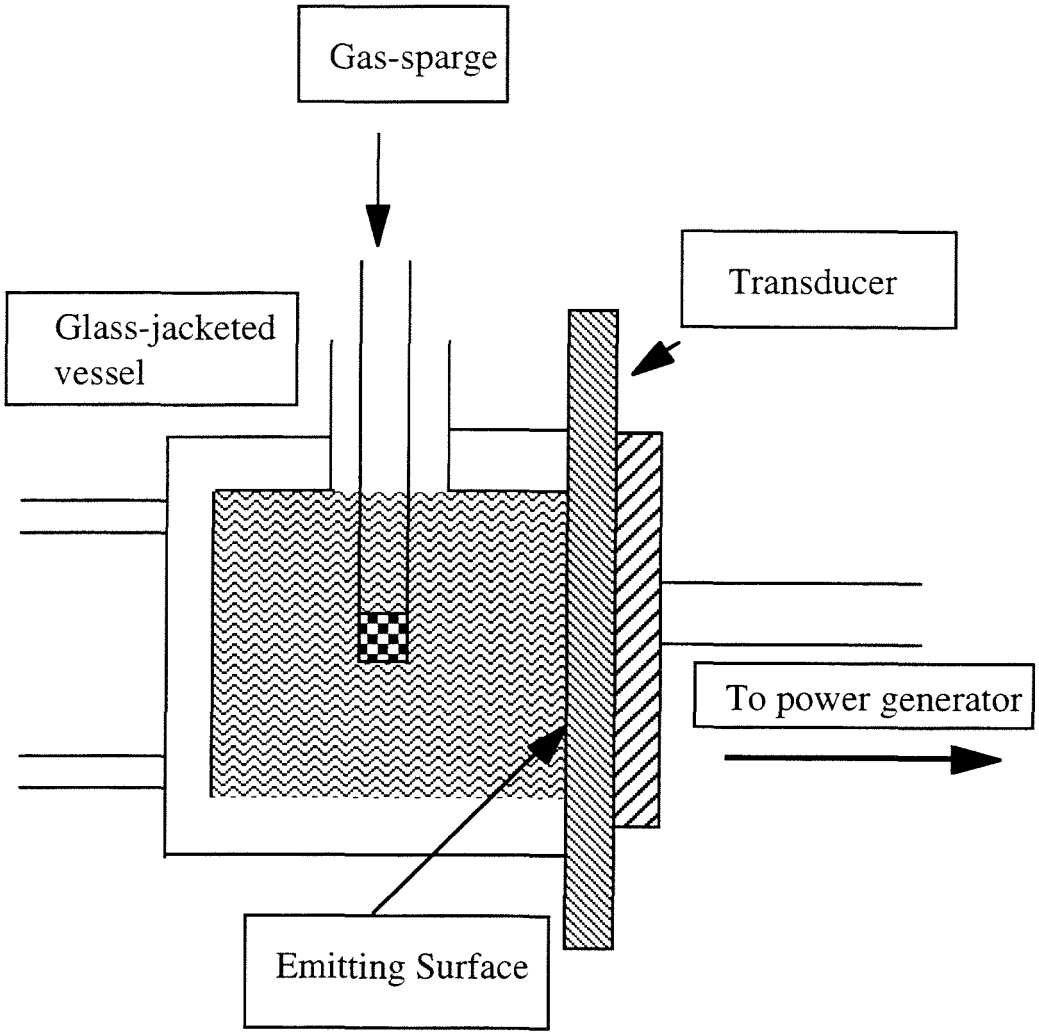

Fig. 2: Reactor configuration for sonications at 500 kHz.

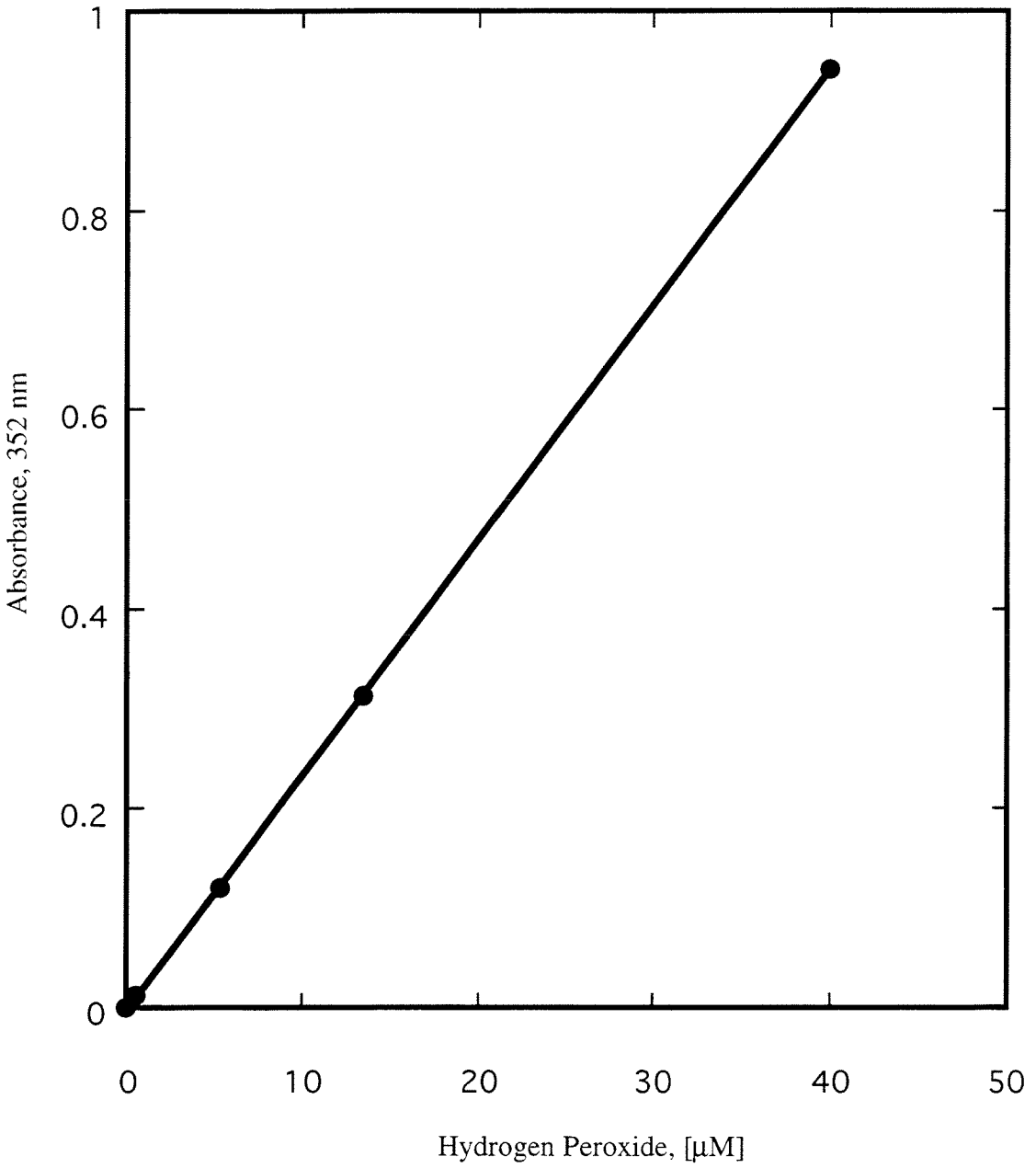

Fig.3 : Hydrogen peroxide standard curve

——— y = -0.00102 + 0.0236x R= 1.000

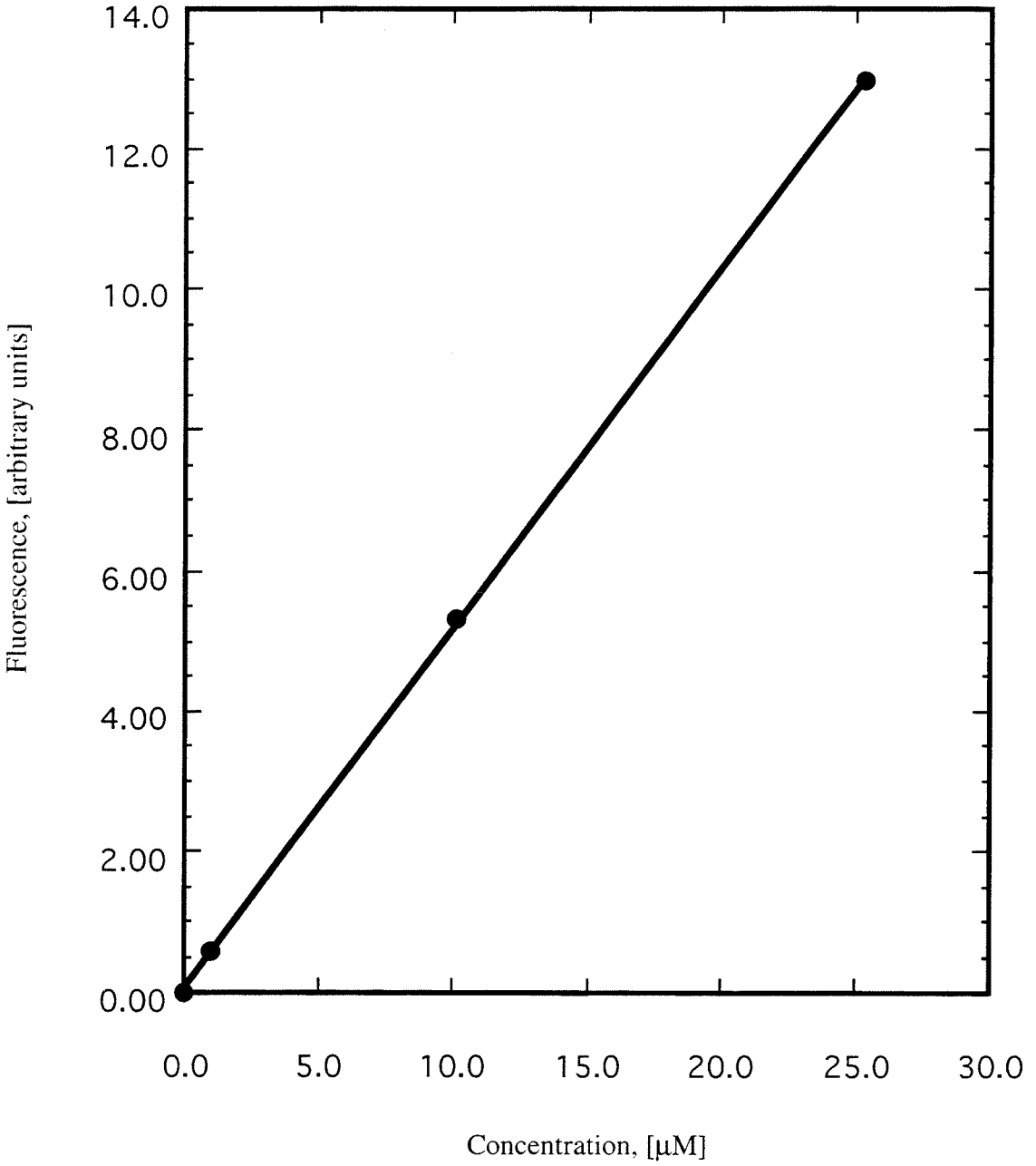

Fig. 4: Hydroxyterephthalic acid standard curve

——— y = 0.0548 + 0.513x R= 1.000

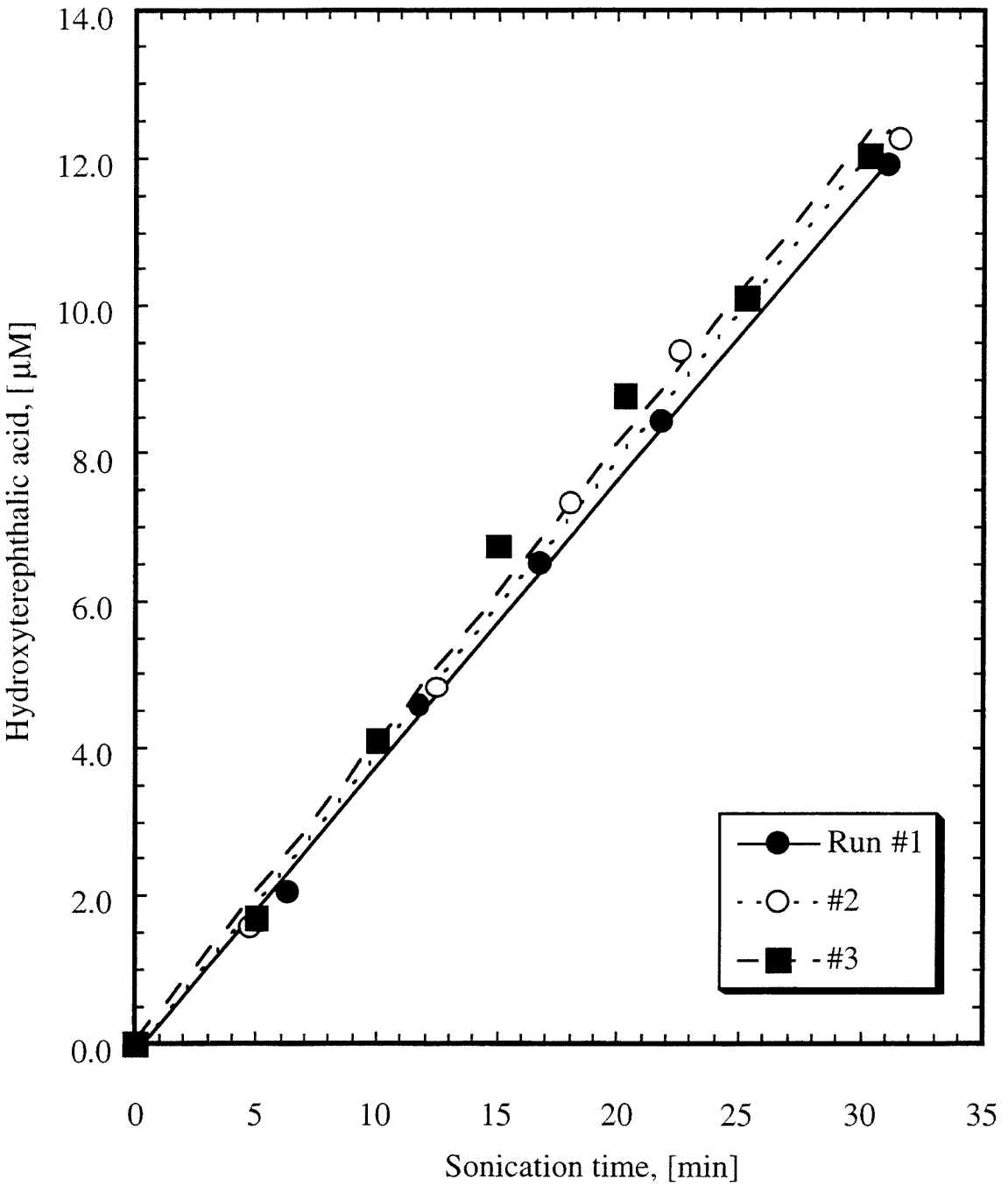

Fig. 5: Reproducibility of $^{\bullet}OH$ production and detection at 500 kHz in an Ar-saturated aqueous solution.

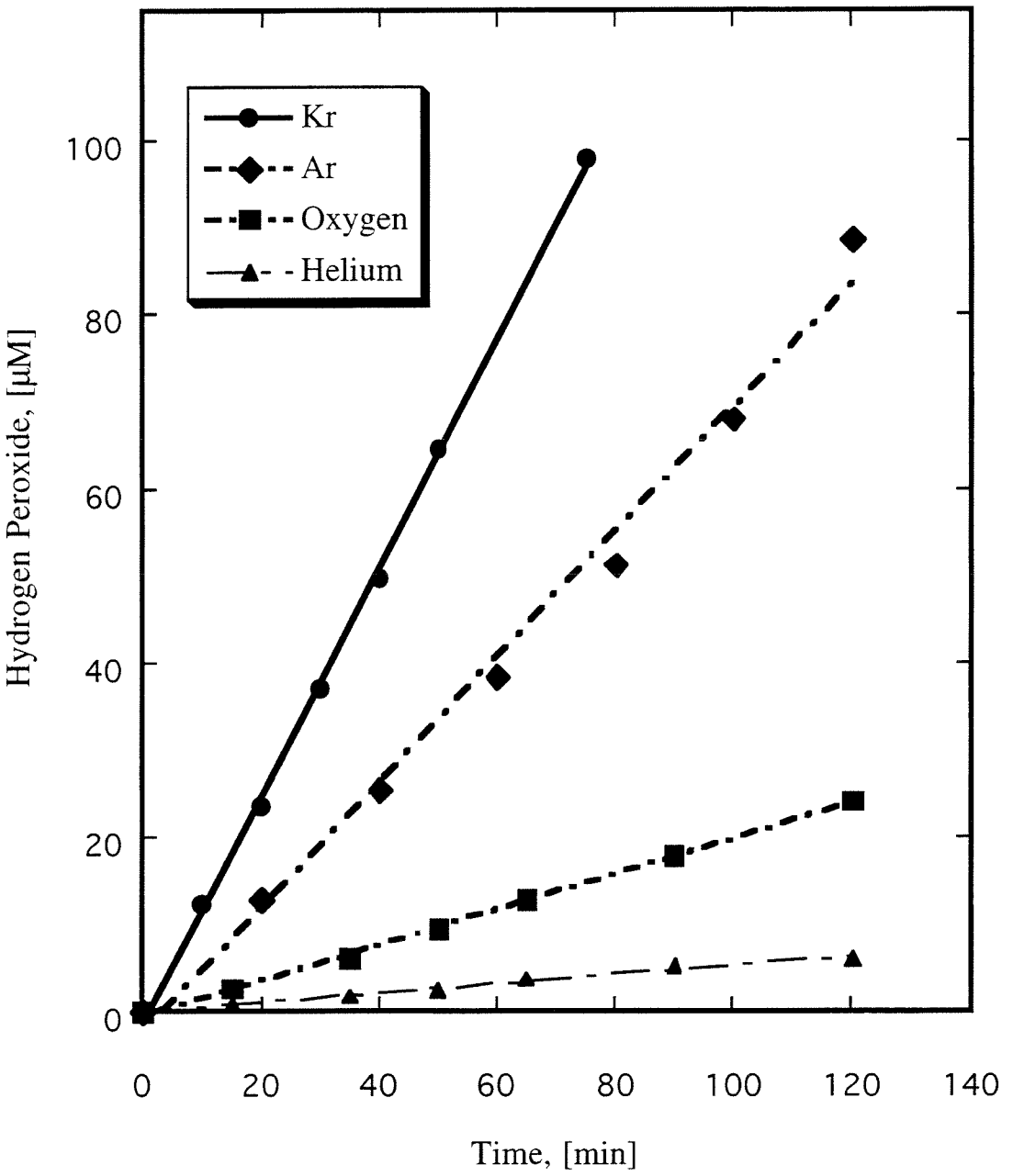

Fig. 6: Production of H_2O_2 at 20 kHz in Kr, Ar, O_2 or He-saturated solutions.

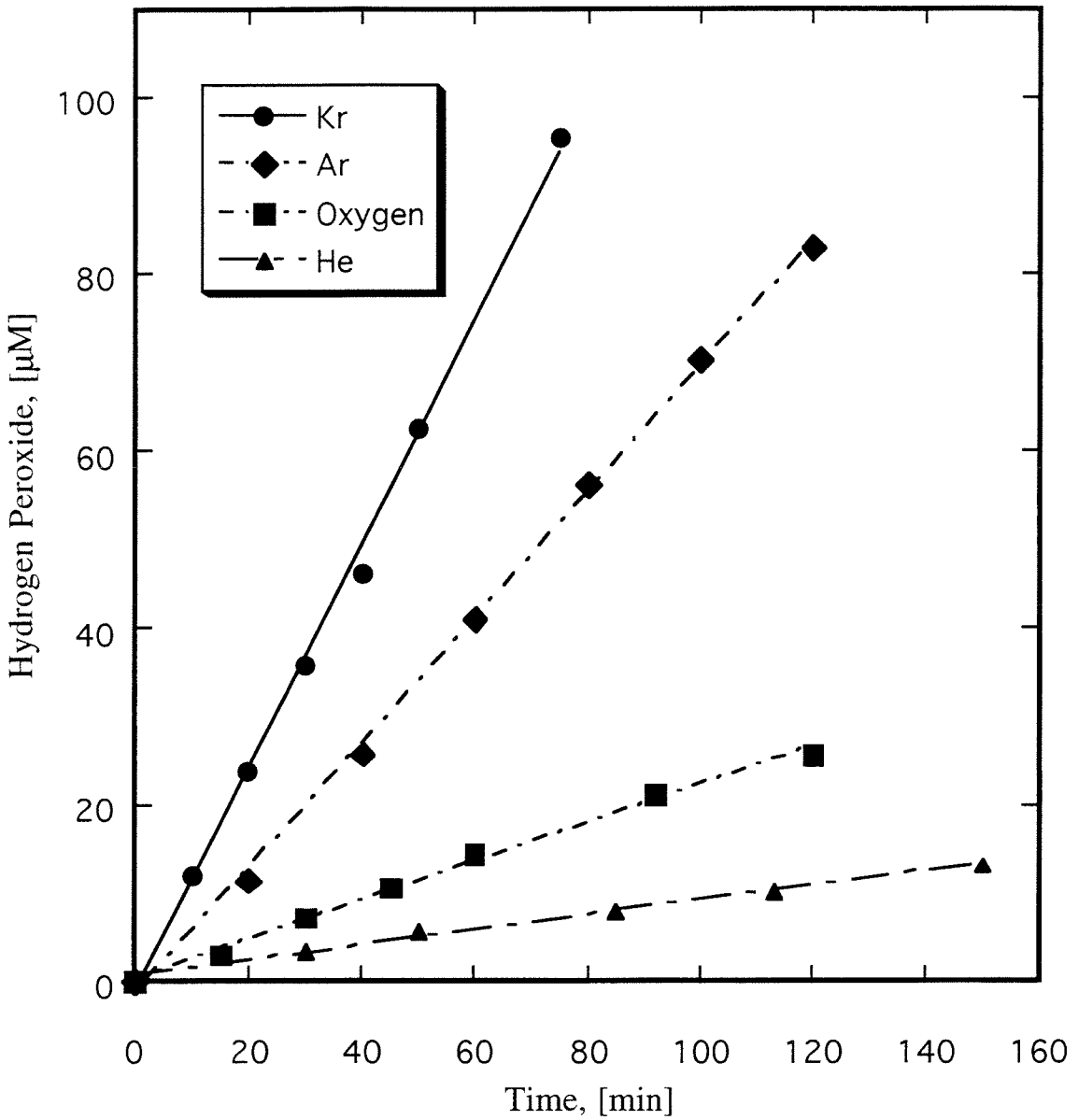

Fig. 7: Production of H_2O_2 at 40 kHz in Kr, Ar, O_2 or He-saturated solutions.

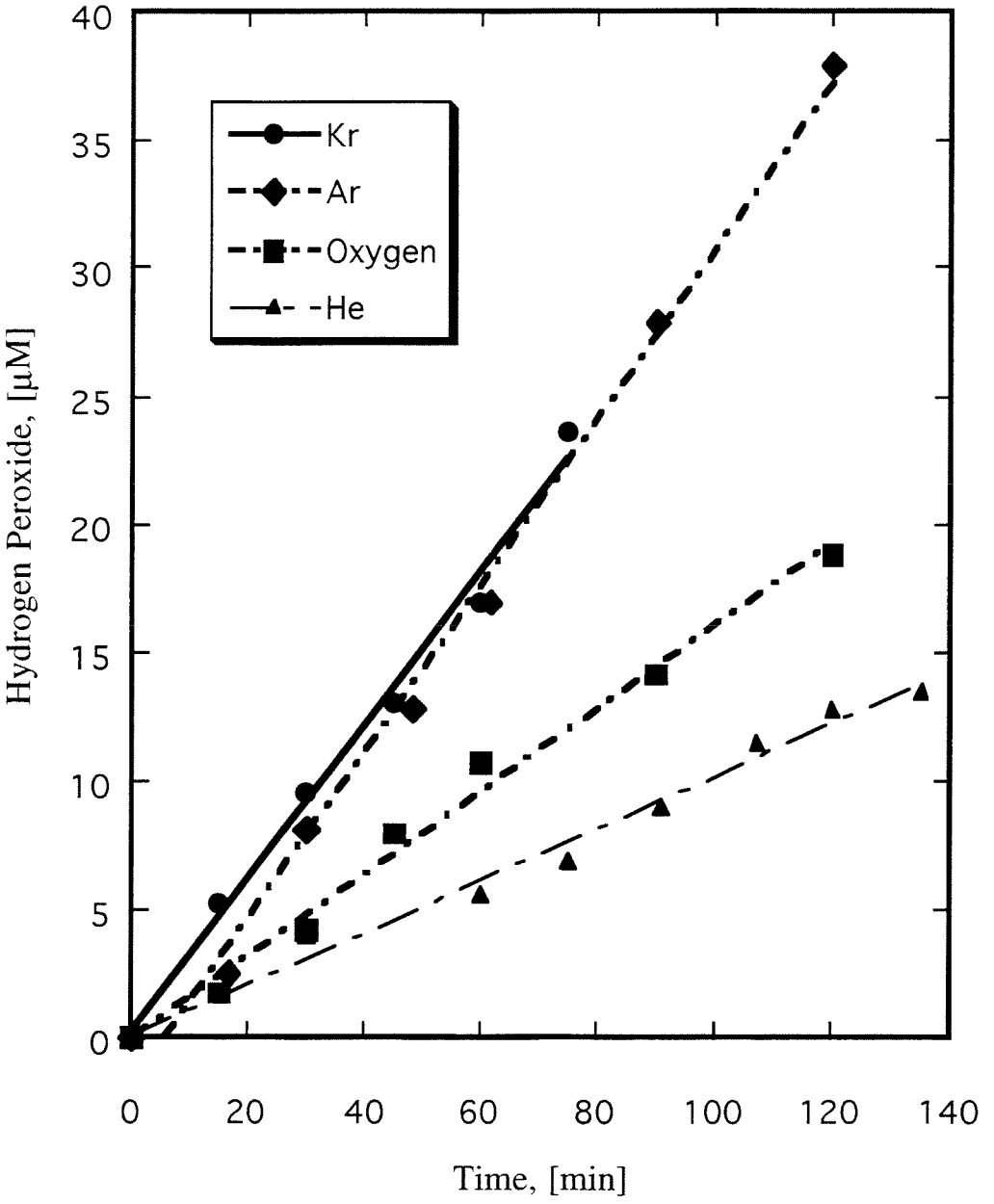

Fig. 8: Production of H_2O_2 at 80 kHz in Kr, Ar, O_2 or He-saturated solutions.

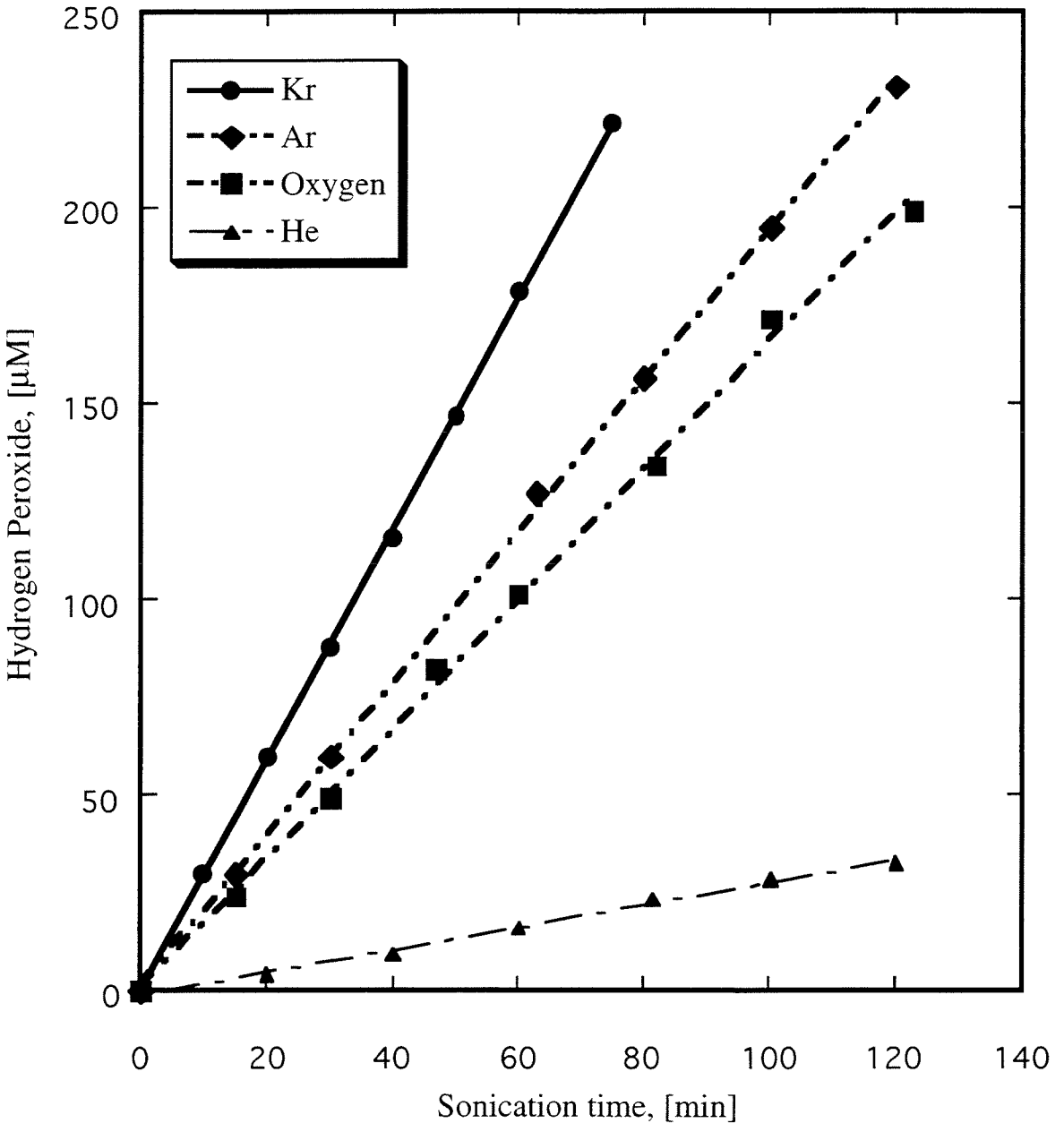

Fig. 9: Production of H_2O_2 at 500 kHz in Kr, Ar, O_2 or He-saturated solutions.

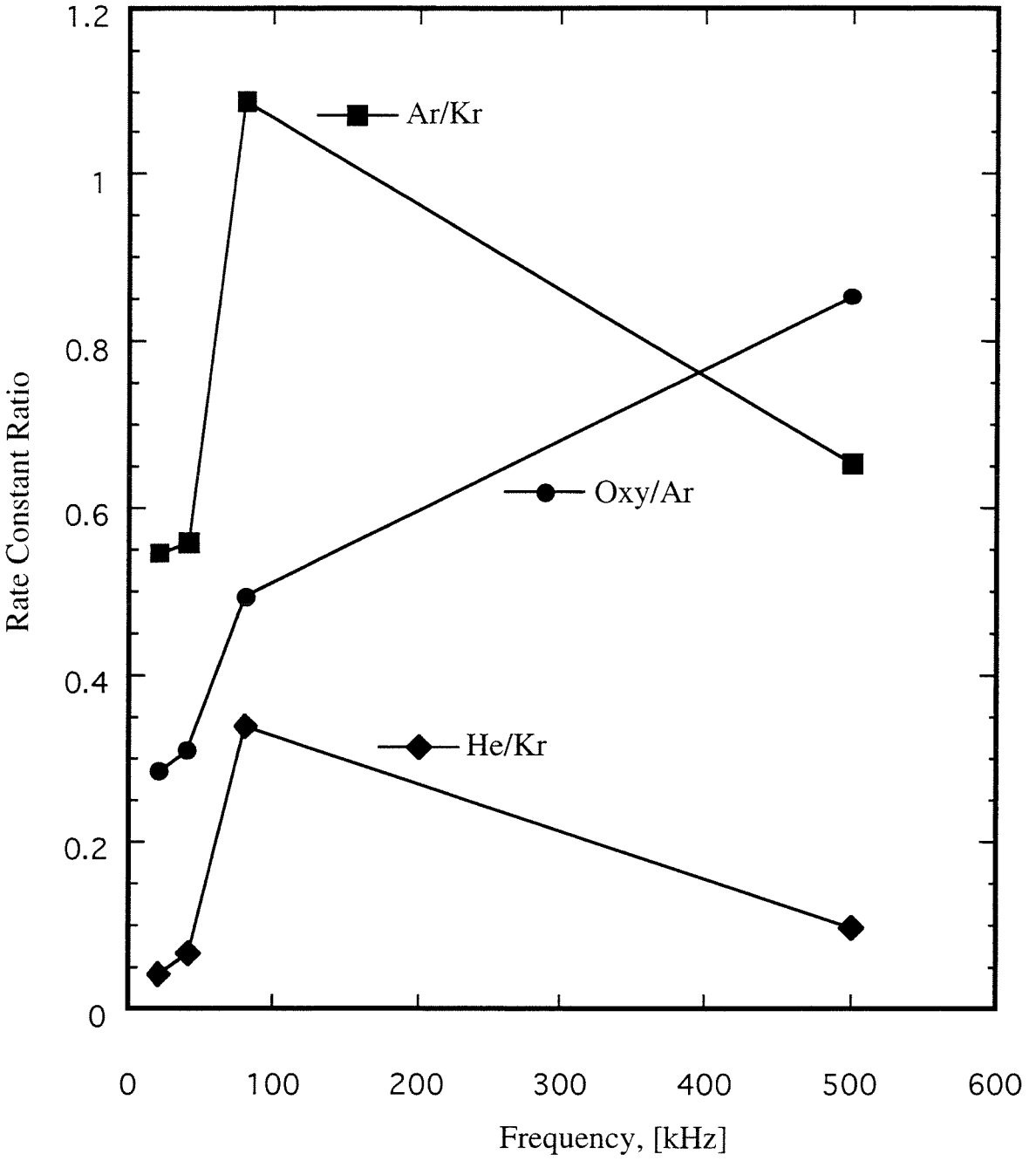

Fig. 10: Ratio of rate constants of hydrogen peroxide formation at different frequencies and with variable saturating gas.

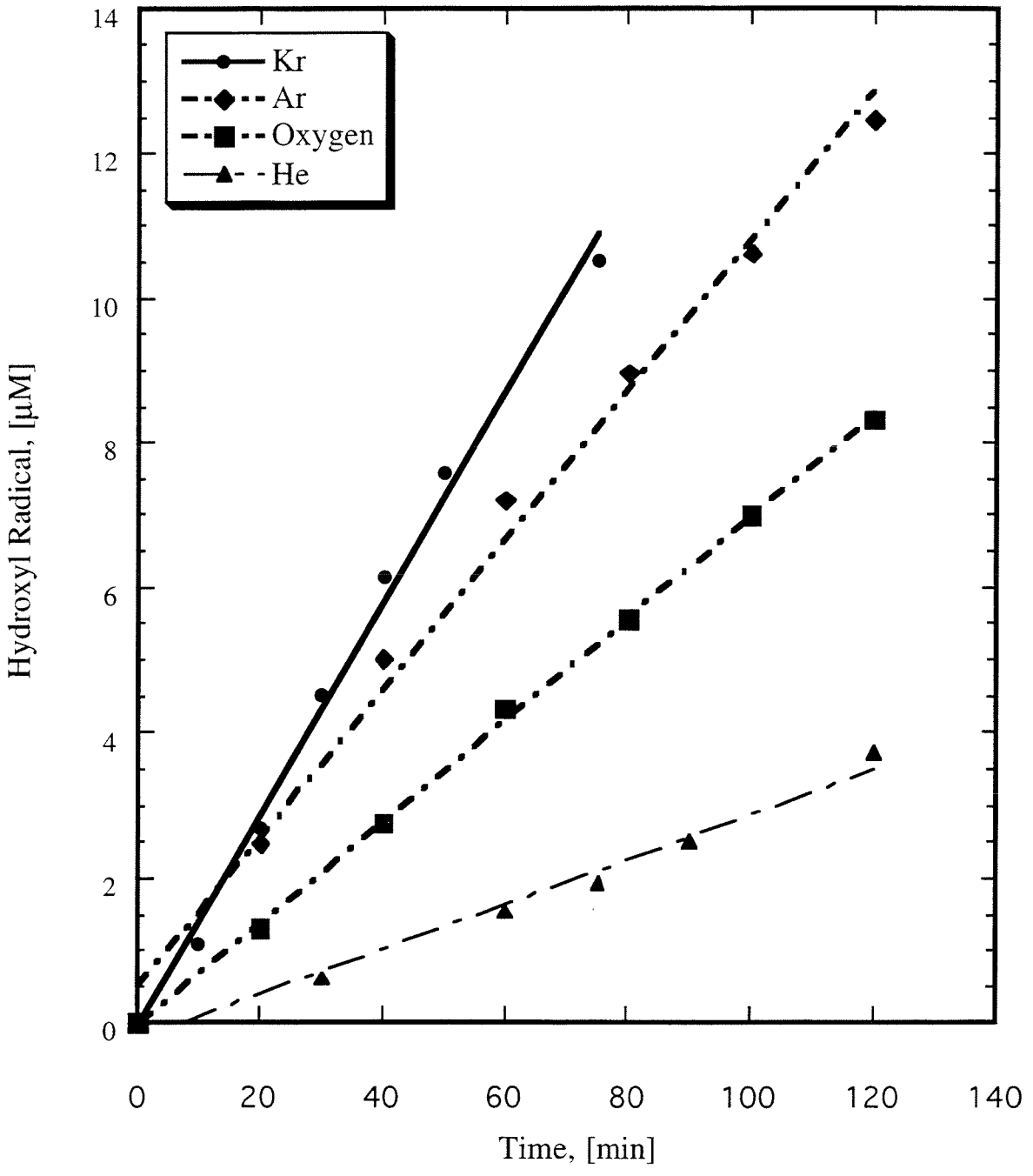

Fig. 11: $^{\bullet}OH$ production at 20 kHz in Kr, Ar, O_2 or He-saturated solutions.

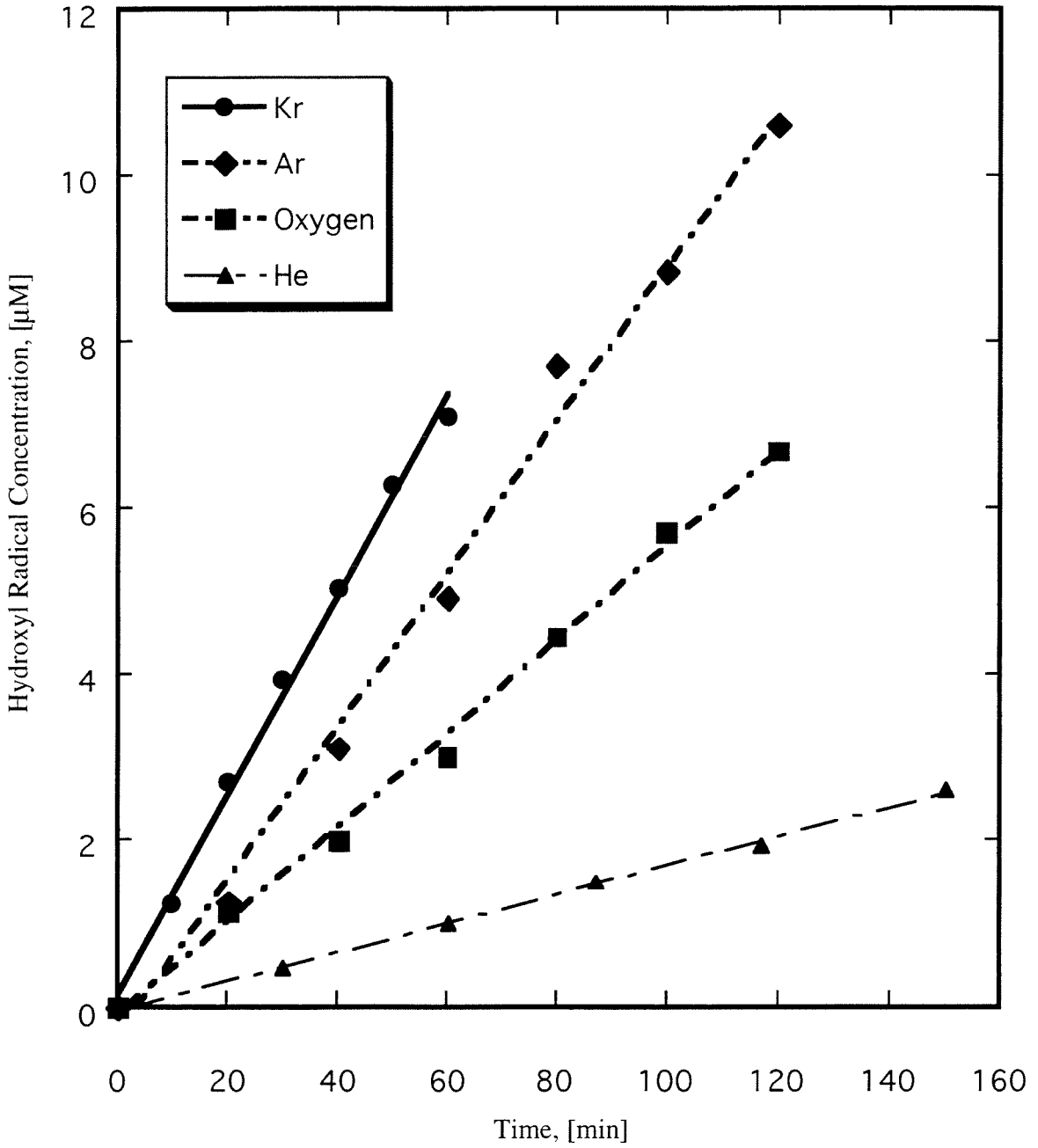

Fig. 12: $^{\bullet}OH$ production at 40 kHz in Kr, Ar, O_2 or He-saturated solutions.

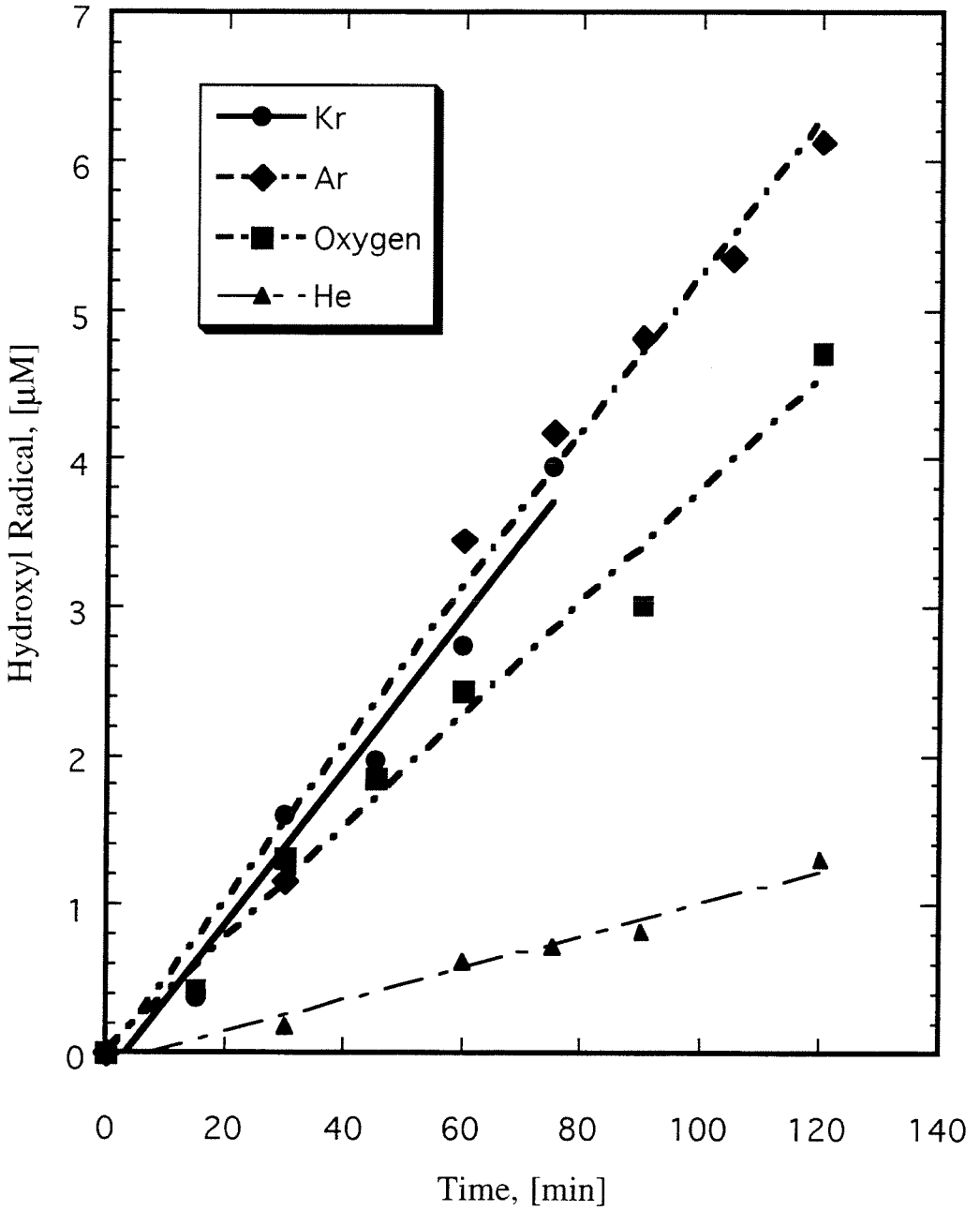

Fig. 13: $^{\bullet}OH$ production at 80 kHz in Kr, Ar, O_2 or He-saturated solutions.

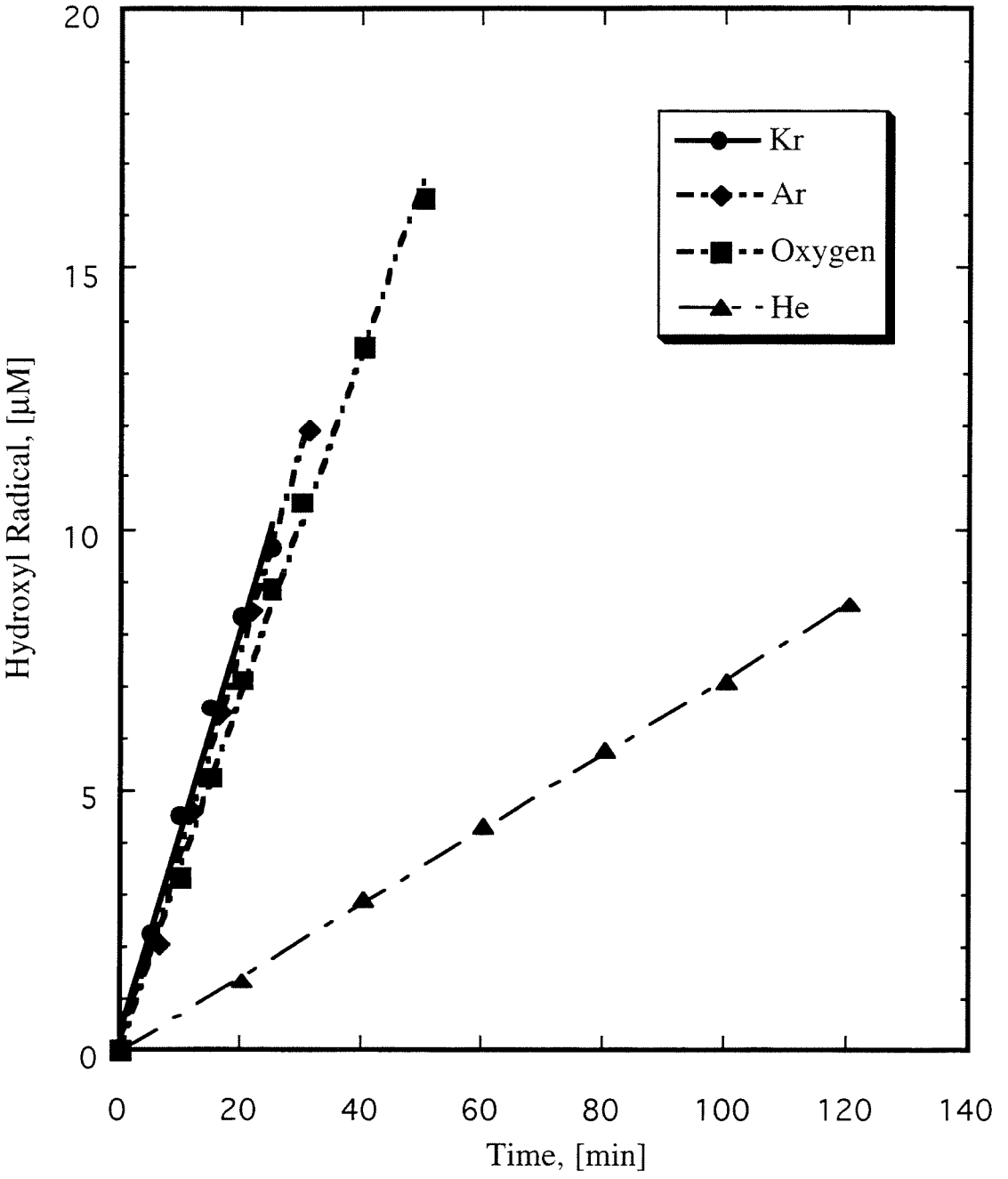

Fig. 14: $^{\bullet}OH$ production at 500 kHz in Kr, Ar, O_2 or He-saturated solutions.

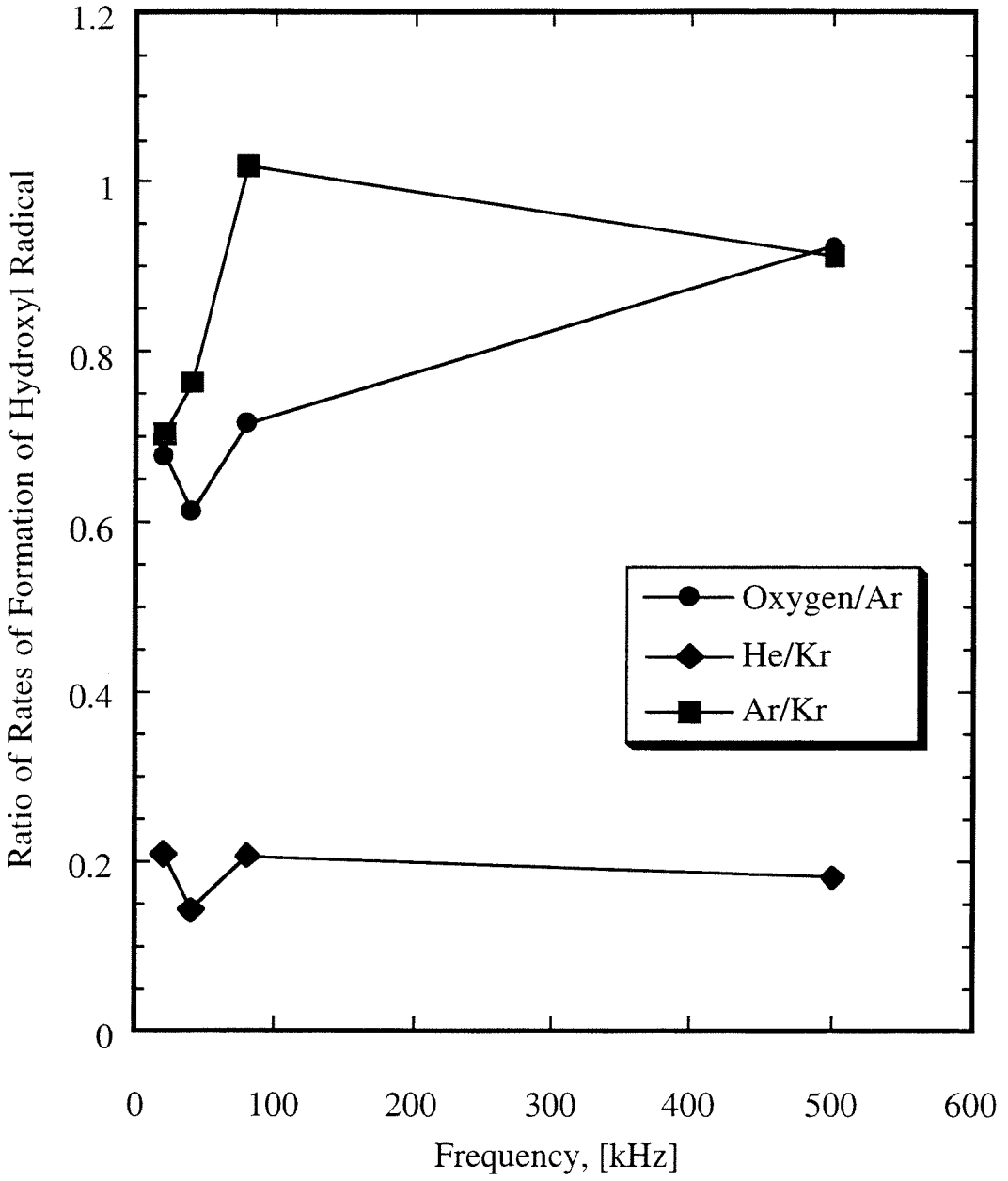

Fig. 15: Ratio of rate constants of $^{\bullet}OH$ formation at different frequencies and with variable saturating gas.

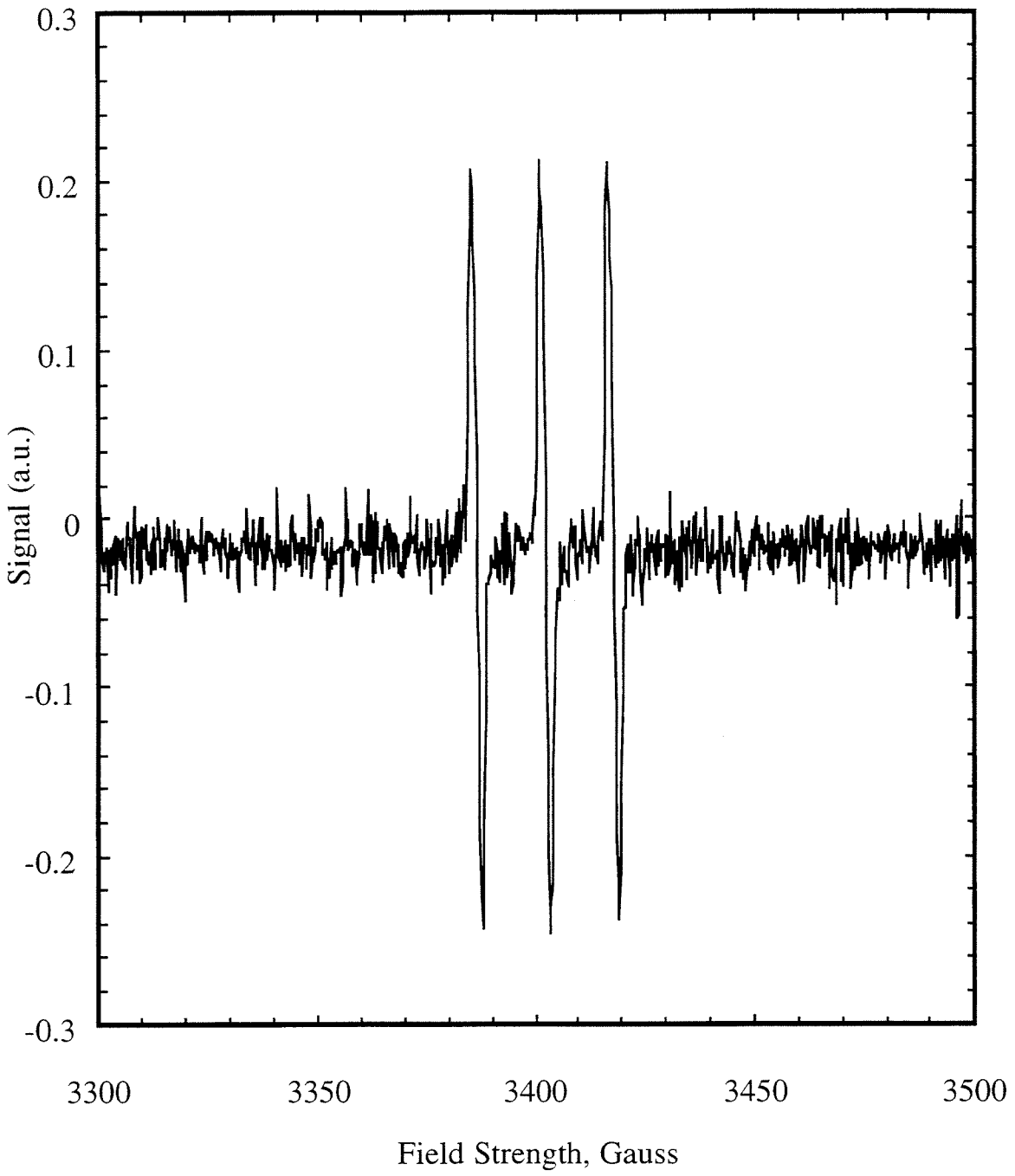

Fig. 16: First derivative EPR spectrum of an Ar-saturated solution of TMPone after 5 min. of ultrasonic irradiation.

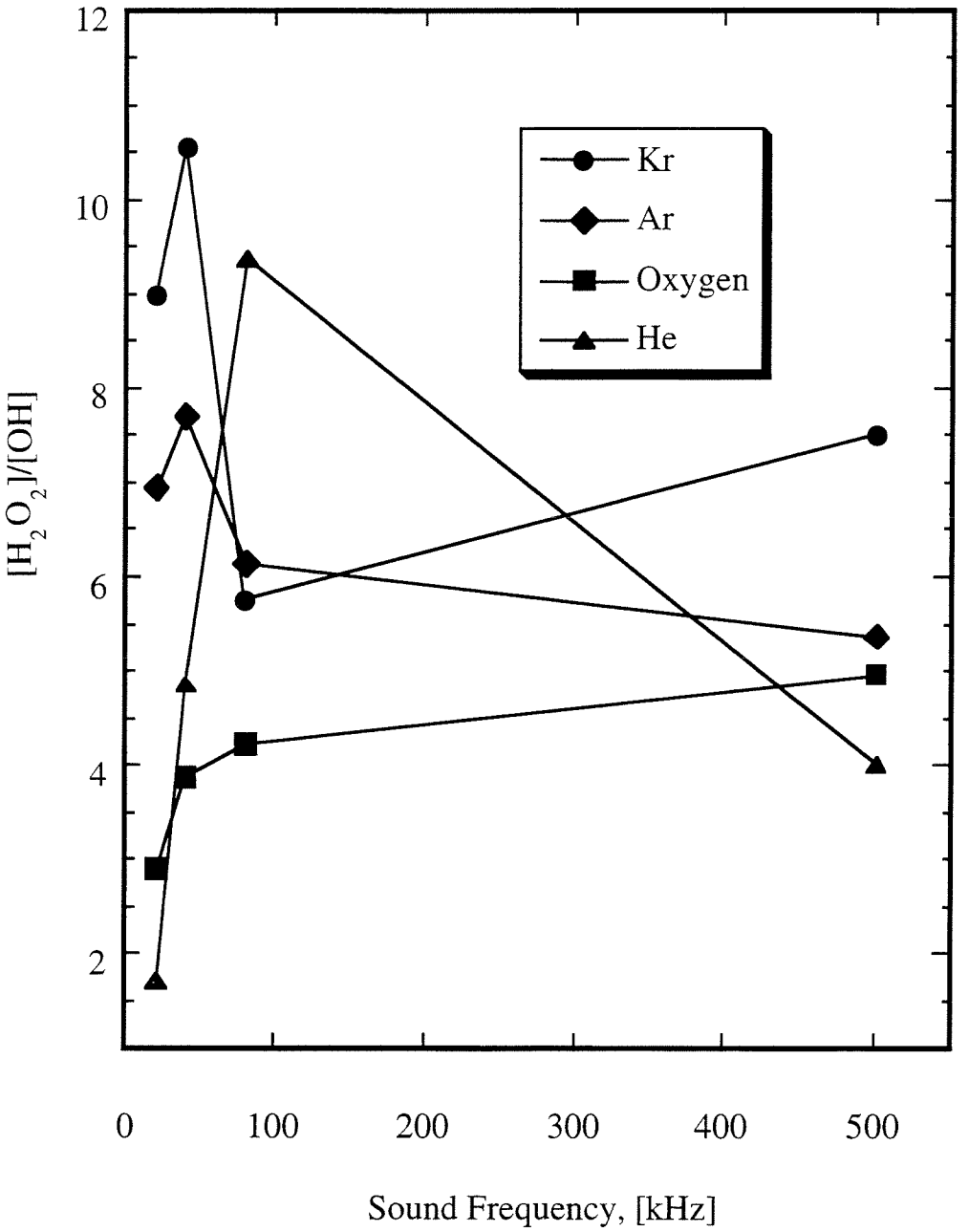

Fig. 17: Ratio of H_2O_2 to $^{\bullet}OH$ production at different frequencies.

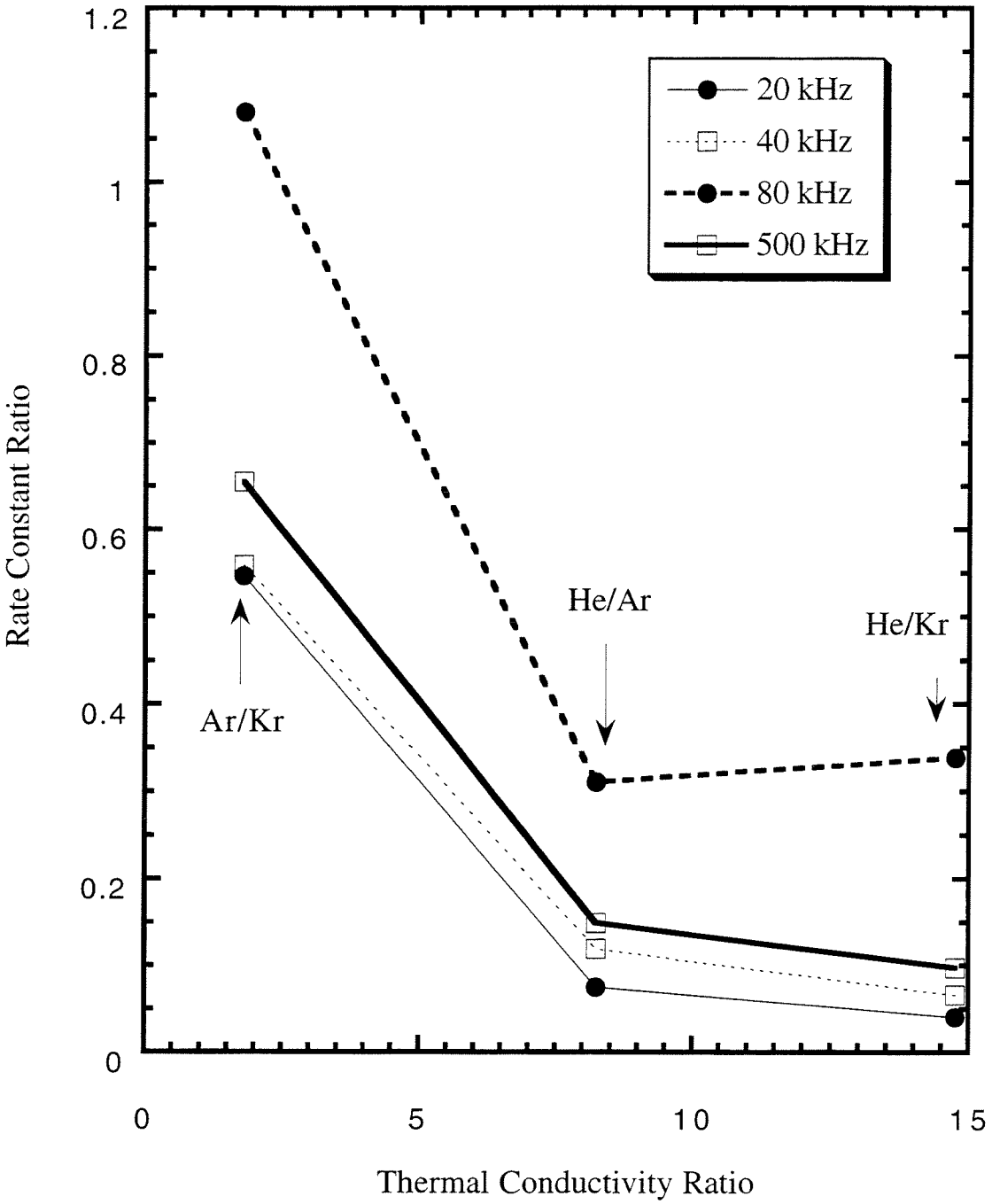

Fig. 18: Correlation of H_2O_2 production rate ratios with saturating gas thermal conductivity ratios.

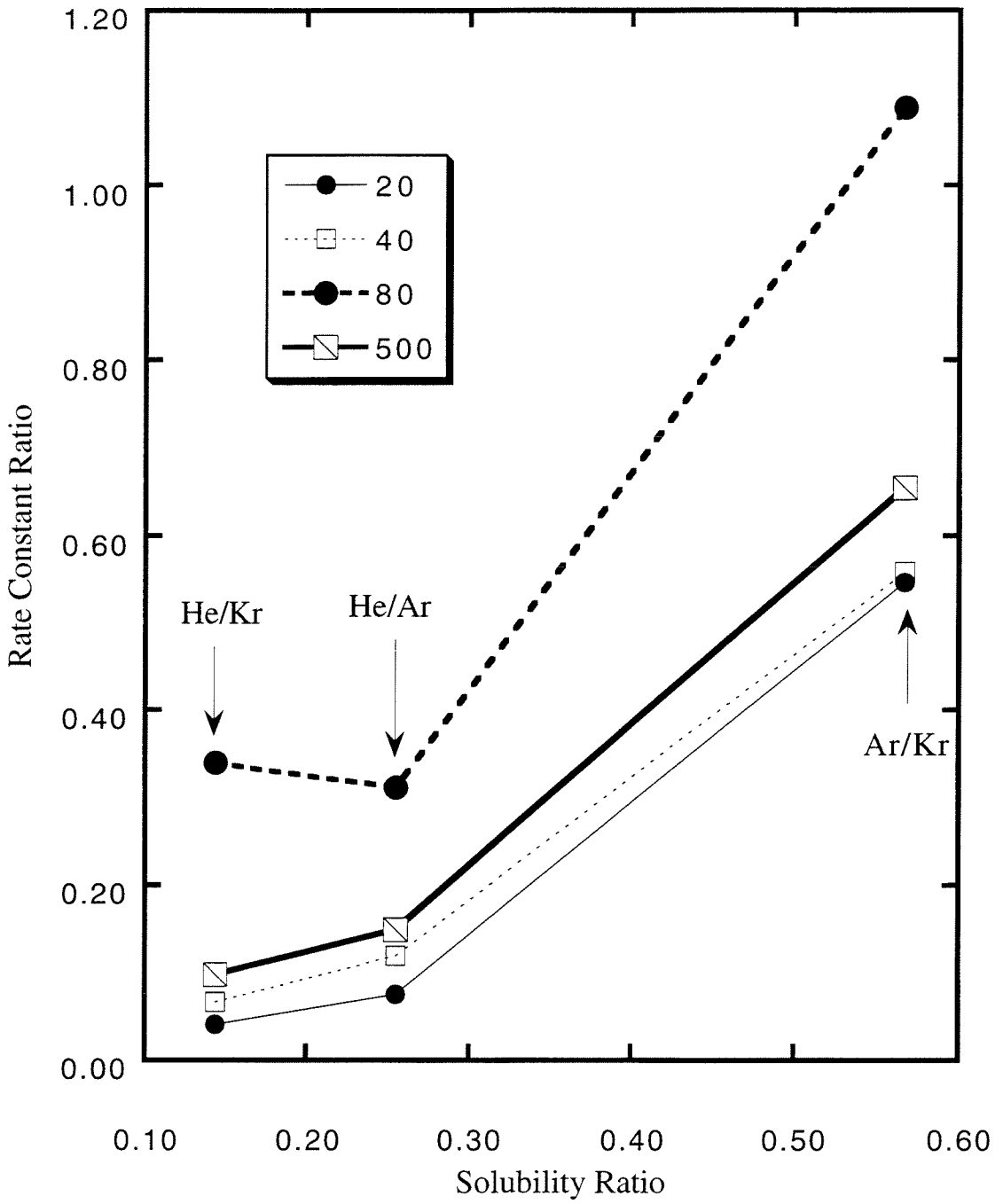

Fig. 19: Correlation of H_2O_2 production rate ratios with saturating gas solubility ratios.

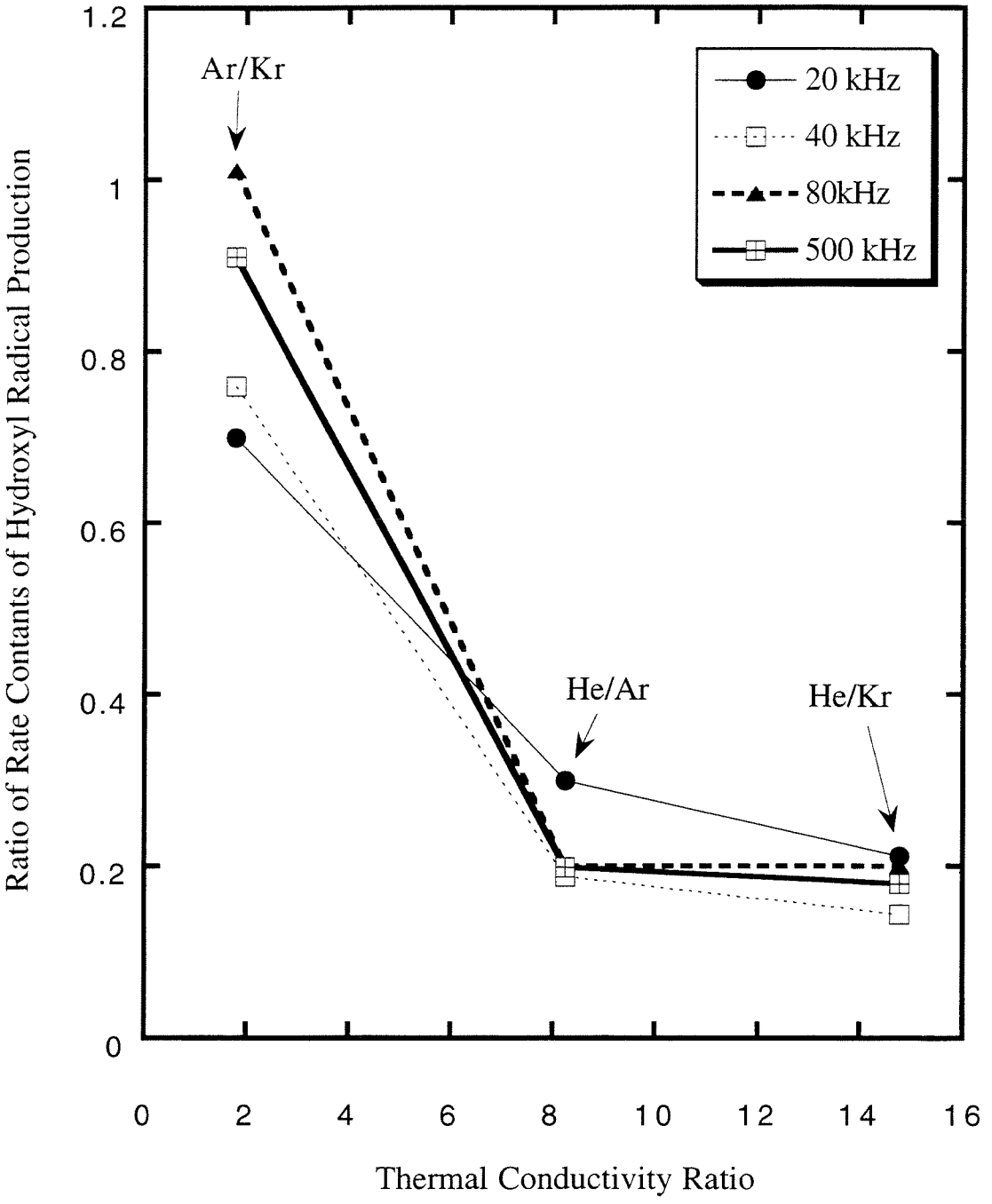

Fig. 20: Correlation of $^{\bullet}OH$ production rate ratios with saturating gas thermal conductivity ratios.

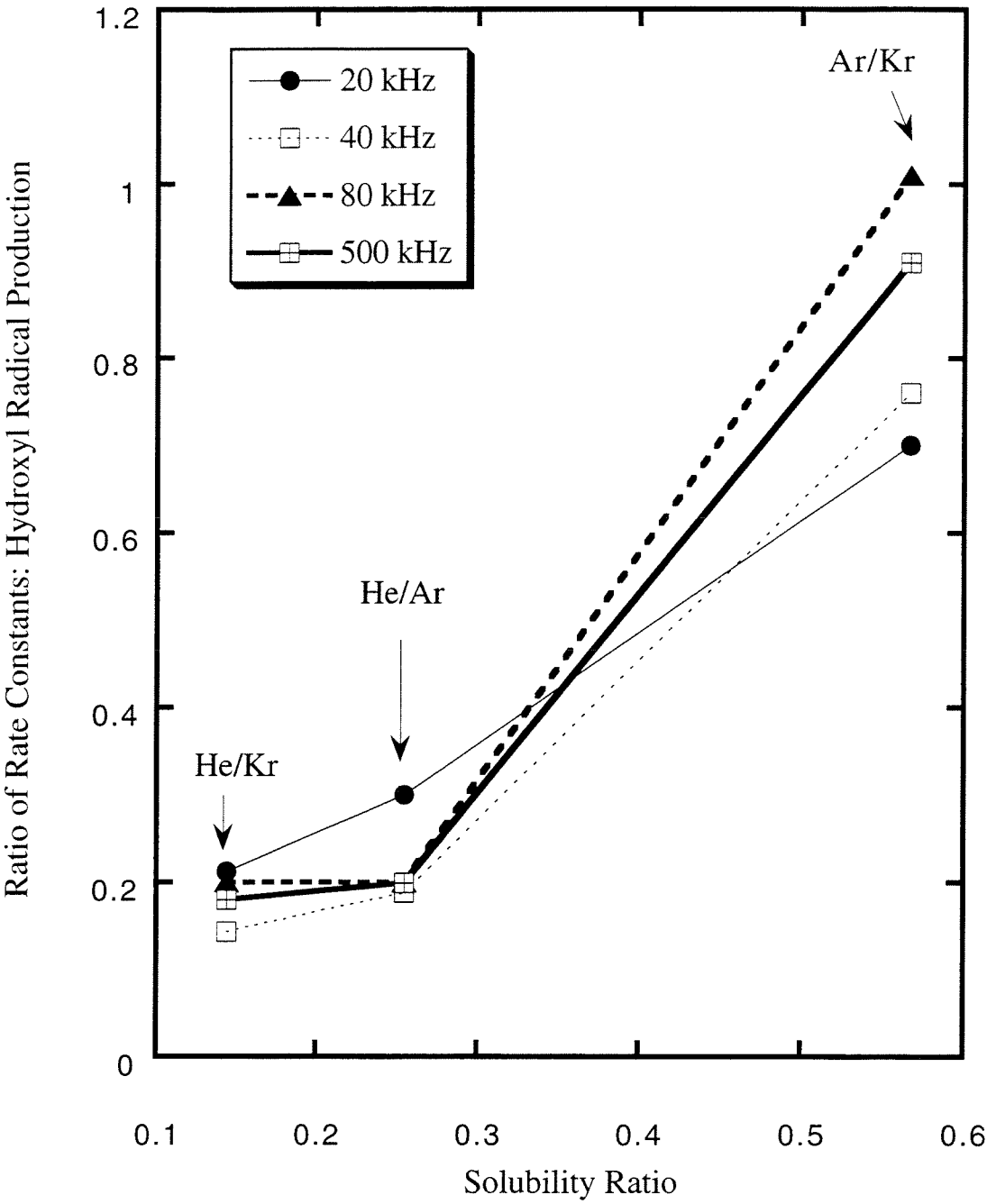

Fig. 21: Correlation of $^{\bullet}OH$ production rate ratios with saturating gas solubility ratios.

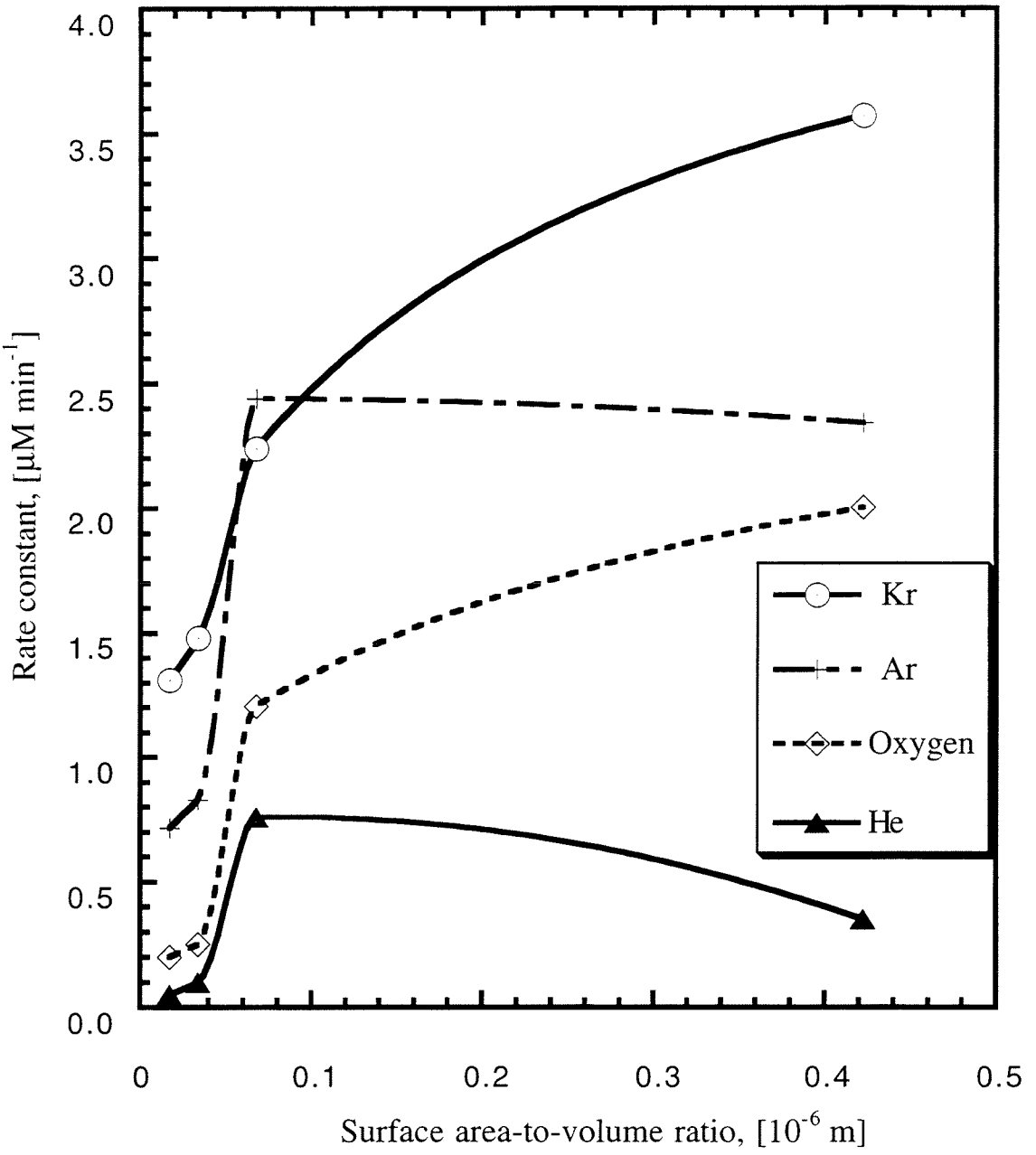

Fig. 22 Influence of bubble surface area-to-volume ratio on H_2O_2 production rates.

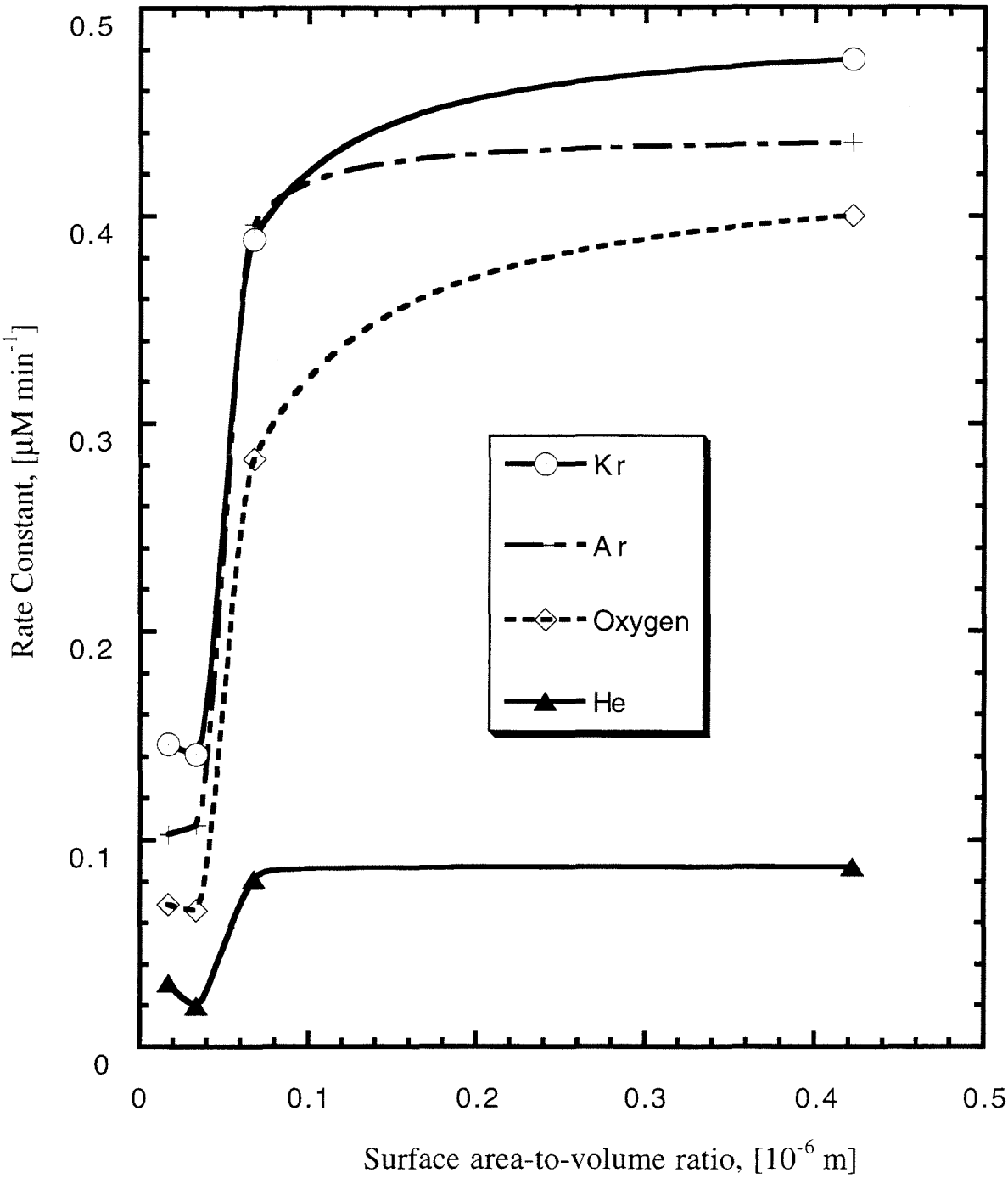

Fig. 23: Influence of bubble surface area-to-volume ratio on $^{\bullet}OH$ production rates.

Chapter 6:

Conclusions

Ultrasonic irradiation has been shown to enhance a variety of different chemical reactions in aqueous solution. The kinetics of sonolytic hydrolysis of p-NPA were analyzed to probe for the existence of transient supercritical water (SCW) during acoustic cavitation. The hydrolysis reaction was deduced to occur at the interfacial region of the cavitating bubble because of the insensitivity of sonolytic rates to the bulk pH and ionic strength. The rate enhancement may be due in part to a higher concentration of OH^- at the bubble interface which results from the higher ion-product, K_w, of SCW. Furthermore, the presence of a competing co-solvent, methanol, significantly decreased the hydrolysis of p-NPA during ultrasonic irradiation. A simple heat transfer model predicted that after 10 msec the radius of the supercritical region around a collapsed bubble extends about 40% farther into the bulk solution than the original cavity. The radius of the supercritical shell expands up to 160 % of the original bubble radius at 50 msec after collapse.

The existence of the supercritical phase during acoustic cavitation is significant for the application of sonolysis to remediation problems. Many compounds of environmental interest which are more hydrophobic than p-NPA may be present at an even higher concentration at the interface, and will be embedded in supercritical water upon bubble implosion. Depending on how much the supercritical phase enhances chemical reactions, the contribution to observed sonochemical effects of even a small volume fraction within the bulk phase maybe significant.

Finally, the existence of the supercritical phase in an ultrasonically irradiated solution suggests a modification of the conventional view of the reactive areas at a cavitation bubble. This region is normally considered to consist of two discrete phases: a high temperature, low density gas phase, and a more condensed and lower temperature liquid shell. An alternative description would include a structural change of the collapsing bubble due to the existence of SCW with properties more characteristic of water vapor than liquid water. The presence of SCW in a collapsing bubble may help to explain the

observed fragmentation of a single bubble into a bubble cloud consisting of many smaller bubbles (39).

Sonolytic degradation of p-NP with a parallel-plate, near-field acoustical processor (NAP) was found to be ~20 times more energy efficient than sonication with a conventional probe configuration, in which a horn was immersed into solution and the sound is transmitted through a relatively small area (~1 cm^2). The increased efficiency of a reactor with a larger emitting surface was due to the fact that a greater fraction of the solution was cavitating during sonication. Attenuation of the sound waves was minimal because the distance from any point in the solution to the emitting surface was on the order of mm or at most ~1.25 cm. Also, the NAP was operated at two slightly different frequencies. The top plate vibrated at 16 kHz and the bottom plate vibrated at 20 kHz. The presence of these two frequencies increased the number of bubbles in solution which can be excited and induced to cavitate.

Increasing the power-to-volume density in the NAP resulted in a linear increase in the degradation rate constant. Increases in the power-to-area ratio resulted in an increase up to a maximum value of the rate constant before it began to decrease. Enhancements of the rate constant were attributed to both an increased number of chemically active cavitation bubbles, and increased intensity of collapse of each bubble.

The nature of the saturating gas (Ar or O_2) determined the rate of disappearance of p-NP as well as the degradation intermediates. Sonolyis under a mixture of Ar and O_2 yielded the fastest rate of p-NP degradation. Sonolysis in the presence of pure O_2 yielded the lowest fraction of 4-nitrocatechol, a degradation intermediate resulting from attack of p-NP by hydroxyl radical. However, the p-NP degradation rate was also the slowest during ultrasonic irradiation of an O_2-saturated solution.

The reactions kinetics and by-products during ultrasonic irradiation of Ar- or O_3-saturated aqueous solutions of carbon tetrachloride (CCl_4) have been identified and quantified. A 90% reduction in the initial concentration was observed after ~12 minutes of

irradiation. Because of its higher volatility and hydrophobicity, CCl_4 partitioned more effectively to the cavitation bubble, and the net result was a faster observed degradation rate. Chloride ion and hypochlorous acid were the inorganic products; hexachloroethane and tetrachloroethylene were the organic by-products. The chlorine mass balance was typically greater than >70%. Ozone did not accelerate the degradation of CCl_4 but did inhibit the accumulation of tetrachloroethylene and hexachloroethane.

The detection of dichlorocarbene during sonolysis of aqueous CCl_4 confirmed the validity of extrapolating gas-phase reaction mechanisms to those occurring in the hottest regions of the cavitation bubble. Sonolysis of aqueous CCl_4 appeared to include similar pathways to those occurring during sonolysis of pure CCl_4 and $CHCl_3$.

The enhanced degradation of p-NP during sonication in the presence of CCl_4 demonstrated that effective degradation during ultrasonic irradiation was not limited to single solute solutions. Because of the variety of reaction pathways and regions which are present during acoustic cavitation, competition between different solutes was minimized. The effect of CCl_4 in a mixed waste stream was particularly interesting because it released a residual oxidant (HOCl) which can attack other refractory molecules in solution, after the ultrasonic irradiation is halted.

Quantification of hydrogen peroxide and hydroxyl radical production during sonolysis of aqueous solutions at four frequencies (20, 40, 80 and 500 kHz) with four saturating gases at each frequency (Kr, Ar, O_2, and He) allowed insight into how differences in bubble behavior can determine sonochemical effects. The absolute production rates were also higher at each frequency: $k_{500} > k_{80} > k_{40} > k_{20}$ for most saturating gases. There are several reasons for enhanced sonochemistry at higher frequencies, including the enhancement of the collapse intensity of individual bubbles due to surface tension effects. However, the bubble cloud may also be altered by differences in rectified diffusion and microstreaming at higher frequencies which result in a greater number of cavitating bubbles.

The thermal conductivity and solubility of the dissolved gas, as well as its polytropic index, K, could be correlated to the production rates of hydrogen peroxide and hydroxyl radical observed at each frequency. Faster rate constants were observed during sonolysis in the presence of gases with low thermal conductivity. However, the variability of the rate constants is less at higher frequencies since small, stably cavitating bubbles exhibit near isothermal behavior. In addition, the surface area-to-volume ratio of the bubbles appears to play a role in the production efficiency of hydrogen peroxide. The sonolytic production rates of both H_2O_2 and $^{\bullet}OH$ in O_2-saturated solution relative to Ar-saturated solutions increased monotonically with increasing frequency. The increasing isothermal character, as K approaches unity, of smaller bubbles may contribute to this trend. Furthermore, an improved scavenging efficiency of $^{\bullet}H$ by O_2 is implicated at higher frequencies.